Electronic Structure and Magnetic Properties of Graphene Derivatives and Graphene-based Composite Structures

Thesis Submitted for the Degree of

Doctor of Philosophy (Science)

In

Physics (Theoretical)

By

Nafday Dhani Milind

DEPARTMENT OF PHYSICS

UNIVERSITY OF CALCUTTA

SEPTEMBER 2018

ABSTRACT

Graphene, the 2-D allotrope of carbon, has created enormous sensation among condensed matter physicists and materials scientists in recent time, due to it's unique properties such as high carrier mobility and gate tunable carrier concentration. However the future application possibility of graphene is restricted by the facts that graphene is a zero gap semiconductor and nonmagnetic.

One of the major focus of the present thesis, is to explore computationally the ways in which the electronic and magnetic properties of graphene-based systems can be tailored. Employing ab intio calculations within the framework of density functional theory (DFT) and the model Hamiltonian approach, we have investigated three graphene derivatives, with an aim to engineer and manipulate magnetic properties *viz* a) adatom-bilayer graphene assembly, b) 0-D graphene nanoflakes and c) transition metal atom decorated holey graphene. The aim of these studies was to understand the mechanisms behind the formation of magnetic moments and an examination into the possibility of tuning the magnetic properties by external means. Our results highlight the fact that induction and manipulation of magnetism on and in graphene/graphene-derivatives can be obtained through external means like gating, substrate engineering, chemical modification through introduction of foreign atoms etc.

Another important aspect of modern day graphene research is use of graphene in a field effect transistor (FET) geometry, to be utilized as a probe to investigate the properties of various materials. In this context, motivated by recent experiments where graphene FET has been utilized to determine the out-of-plane polarization at the TiO_2 terminated surface of strontium titanate ($SrTiO_3$), we have also investigated the graphene/$SrTiO_3$ composite heterostructure with the aim to understand the microscopic origin behind the formation of the surface polarization, the influence of presence of graphene on the surface polarizability as well as the effect of an external electric field on the tunability of the value of surface polarization.

We hope that the computational results presented in the thesis will form a solid basis and useful guide for exploring novel functionalities of these graphene derivatives and

composite structures in future experiments.

(Nafday Dhani Milind)

Electronic Structure and Magnetic Properties of Graphene Derivatives and Graphene-based Composite Structures

Nafday Dhani Milind

Thesis Abstract

Graphene, the 2-D allotrope of carbon, has created enormous sensation among condensed matter physicists and materials scientists in recent time, due to it's unique properties such as high carrier mobility and gate tunable carrier concentration. However the future application possibility of graphene is restricted by the facts that graphene is a zero gap semiconductor and nonmagnetic.

One of the major focus of the present thesis, is to explore computationally the ways in which the electronic and magnetic properties of graphene-based systems can be tailored. Employing ab intio calculations within the framework of density functional theory (DFT) and the model Hamiltonian approach, we have investigated three graphene derivatives, with an aim to engineer and manipulate magnetic properties *viz* a) adatom-bilayer graphene assembly, b) 0-D graphene nanoflakes and c) transition metal atom decorated holey graphene. The aim of these studies was to understand the mechanisms behind the formation of magnetic moments and an examination into the possibility of tuning the magnetic properties by external means. Our results highlight the fact that induction and manipulation of magnetism on and in graphene/graphene-derivatives can be obtained through external means like gating, substrate engineering, chemical modification through introduction of foreign atoms etc.

Another important aspect of modern day graphene research is use of graphene in a field effect transistor (FET) geometry, to be utilized as a probe to investigate the properties of various materials. In this context, motivated by recent experiments where graphene FET has been utilized to determine the out-of-plane polarization at the TiO_2 terminated surface of strontium titanate ($SrTiO_3$), we have also investigated the graphene/$SrTiO_3$ composite heterostructure with the aim to understand the microscopic origin behind the formation of the surface polarization, the influence of presence of graphene on the surface polarizability as well as the effect of an external electric field on the tunability of the value of surface polarization.

We hope that the computational results presented in the thesis will form a solid basis and useful guide for exploring novel functionalities of these graphene derivatives and composite structures in future experiments.

(Nafday Dhani Milind)

ACKNOWLEDGEMENTS

*T*he *penning of this thesis brings down the curtain on what has been one of the most laborious and yet, undoubtedly, one of the most enriching endeavors of my life viz the pursuit of a Ph. D. This long journey, in terms of time (and also distance), would not have been possible without the support and encouragement of many people and it would be extremely remiss of me not to acknowledge the contributions of all those who have enhanced my efforts towards achieving this venture.*

First and foremost, I wish to express my sincere and heartfelt gratitude towards my respected supervisor Prof. Tanusri Saha-Dasgupta. The work presented in this thesis would have been impossible if not for her valuable expert guidance, constant push and prompt ideas. Her endless enthusiasm and dedication to science has made a deep impact on me and my approach to science. I have immensely benefited from the ample opportunities Prof Saha-Dasgupta has provided by inovlving me in a number of different collaborative projects which have greatly broadened my scientific horizons. The ease of adjustment in shifting from Pune to Kolkata was largely due to her readily availabe support from the very beginning.

I would also like to take the opportunity and thank all of my collaborators Prof Goutam Dev Mukherjee, Prof. Arindam Ghosh, Prof. Tamalika Banerjee, Prof. Maxim Mostovoy, Prof. Pushan Ayyub, Prof Lilia Boeri, Prof. D. G. Kanhere, Prof. Puru Jena, Dr Mukul Kabir, Dr Sajeev Chacko for their kind acceptance in working together with me and for sharing their experienced scientific knowledge which has greatly aided me to develop deeper understanding of the subject. I wish to sincerely thank Prof. Lilia Boeri for her gracious help and warm hospitality during my academic visit to Graz University of Technology, Graz, Austria. In particular, I am extremely grateful for the continued kind support of Prof. Goutam Dev Mukherjee and the Ministry of Earth Sciences by providing the funding crucial to the successful completion of my Ph. D. On that note, I would also like to extend my thanks to S. N. Bose National Centre of Basic Sciences for hosting and providing me a very comfortable stay for the duration of my Ph. D..

iii

was Prof. Kanhere who directed me to my current supervisor Prof. Tanusri Saha-Dasgupta for which he will always have my humble gratitude. His continual support as a honored teacher and collaborator has been a cornerstone of my academic life. My days at the Advanced Computing Lab (ACL) at the University of Pune, which he presided over, were made merrier by the enthusiasm and cheery demeanor of my taleneted co-workers and senior colleagues. I am sincerely thankful to Dr. Sajeev Chacko for taking the time to teach the basic ropes of computational physics in my initial days at the ACL. Getting the opportunity to work with him as a respected collaborator and friend, later on, during our simultaneous stay at S. N. Bose National Centre for Basic Sciences has been one of the memorable moments of Ph. D. journey. Those vibrant days spent in the company of Bhalchandra, the three spices of my life - Ideh(Cardamom), Aniruddha (Ginger) and Vaibhav (Habanero), Sandip and Soumyajyoti are valued memories as they along with Prof. Kanhere made me experience the genuine fun of research as well of things outside of research. I extend my genuine thanks to all of them for instilling in me the "Physics can be fun" paradigm and wish for their continued success on both professional fronts.

I am genuinely thankful to Kavitha, Supriya and Madhura who are my oldest friends and am extremely grateful for their presence of in my life and their continued support always delivered either by phone, email or person.

A sincere and humble thank you, cannot express my appreciation and love towards Aroop Kaka and Ranjitha Aunty. They have been the rock on which my life in Kolkata has been built. Their affection, concern for my well being and readily given support have been my anchor over the past six years. For being my second family away from home, I owe them a deep heartfelt gratitude.

Finally, I express my sincere gratitude towards my family: my mother, Mrs Aroona Nafday, my father Mr. Milind Nafday and my elder brother, Alap Nafday. Without their unconditional love, support and respect for my choices, it would have been impossible to start on this journey. Personally, I owe a great deal more to my parents that cannot be described in any words of any language. They have been the guiding beacon that has never let me astray in my life. It would be extremely audacious of me to try to articulate their significance in my life and it is with a deep sense of gratitude, love and affection I dedicate this thesis to them.

Dhani Nafday
Kolkata, India
September 2018

Publications Reported In The Thesis

(1) Magnetism of an adatom on bilayer graphene and its control: A first-principles perspective
Dhani Nafday and Tanusri Saha-Dasgupta
Phys. Rev. B 88, 205422 (2013)

(2) Exact diagonalization study in nanographene: Modulation of charge and spin, magnetic phase diagram, and thermodynamics
Sajeev Chacko, Dhani Nafday, Dilip Kanhere and Tanusri Saha-Dasgupta
Phys. Rev. B 90, 155433 (2014)

(3) Controlling adatom magnetism on bilayer graphene by external field
Dhani Nafday, Mukul Kabir and Tansuri Saha-Dasgupta
Phys. Rev. B 93, 045433 (2016)

(4) Out-of-plane dipoles and anti-hysteresis at the interface of graphene-strontium titanate hybrid transistor
Anindita Sahoo, Dhani Nafday, Tathagata Paul, Roald Ruiter, Arunesh Roy, Maxim Mostovoy, Tamalika Banerjee, Tansuri Saha-Dasgupta and Arindam Ghosh
npj 2D Materials and Applications 2(9), 1 (2018)

(5) Electronic and magnetic Properties of $3d$ transition metal atom embedded holey graphene
Dhani Nafday, Puru Jena and Tanusri Saha-Dasgupta (Under preperation)

Other Publications

(6) Manipulating the mechanical properties of Ti_2C MXene: Effect of substitutional doping
Poulami Chakraborty, Tilak Das, Dhani Nafday, Lilia Boeri and Tansuri Saha-Dasgupta
Phys. Rev. B 95, 184106 (2017)

(7) Properties at the interface of graphene and Ti_2C MXene
Pallabi Paul, Poulami Chakraborty, Tilak Das, Dhani Nafday, and Tansuri Saha-Dasgupta
Phys. Rev. B 95, 184106 (2017)

(8) Search for new magnetic materials : DFT predictions on Rh based double perovskites
Anita Halder, Dhani Nafday, Prabuddha Sanyal and Tansuri Saha-Dasgupta
npj Quantum Materials 3(17), 1 (2018)

(9) A reduction in particle size generally causes body-centered-Cubic metals to expand but face-centered-cubic metals to contract
Dhani Nafday, Subhrangshu Sarkar, Pushan Ayyub and Tanusri Saha-Dasgupta
ACS Nano 12(7), 7246 (2018)

TABLE OF CONTENTS

3   Field Tunable Magnetism of an adatom on bilayer graphene*   85

4   Magnetism driven by long-range Coulomb Interaction in Graphene Nanoflakes*   115

LIST OF TABLES

1

1.1 Two Dimensional Materials

Three-dimensional(3-D) layered materials are materials whose structure comprises of individual atomic layers stacked on top of each other. These materials are generally characterized by the presence of strong in-plane chemical bonds and a weak coupling between the layers such as Van-der Waals interactions, hydrogen bonds, etc. Today these class of materials encompasses a broad range of materials such as graphite, clays, ceramics, oxides, halides, chalcogenides and MAX phases, which leads to the possibility of cleaving these 3-D materials layer by layer to obtain their two dimensional (2-D) monolayer counterparts. For a long time, the existence of such two-dimensional (2-D) materials was thought not possible due to long held theoretical considerations which state that such 2-D materials are not stable due to thermal and quantum fluctuations[1, 2]

It was not until 2004, when Novoselov and Geim were able to synthesize for the very first time a 2-D allotrope of carbon known as "graphene" from the mechanical exfoliation of graphite by Scotch tape method, that interest in the field of 2-D materials was revived.[4–6] Since then the landscape of 2-D materials has been rapidly evolving and is currently one of the most active areas of research. Following the realization of graphene, advances in exfoliation techinques such as micromechanical cleavage, ion interaction, surface assissted ultrasonofication as well as development of alternative techniques such as chemical vapour deposition (CVD), epitaxial growth, etc have led to manufacturing of 2-D materials of monoatomic layer thickness beyond graphene as in
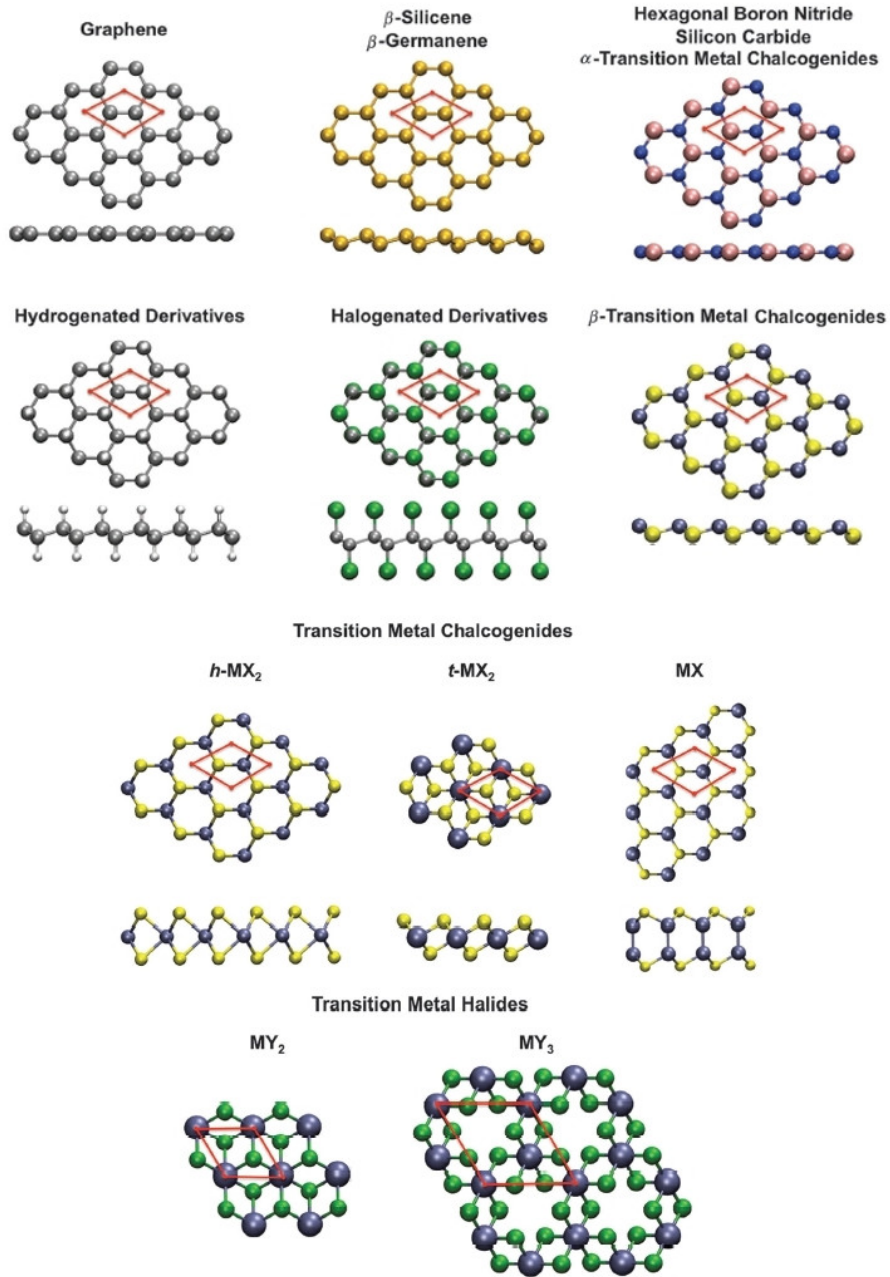
Figure 1.1: Structure of atomically thin 2D materials: graphene, silicene, germanene (and their derivatives), silicon carbide (SiC), hexagonal boron nitride (h-BN) and α,β transition metal chalcogenides (TMC) (top). Ultrathin 2D materials such as transition metal chalcogenides (TMC) (centre) and halides (TMH)(bottom). Unit cells are depicted in red. Colour code: metals in ice blue, halides in green, chalcogenides in yellow, nitrogen in blue, carbon in grey, silicon and germanium in gold, boron in pink and hydrogen in white.(Figure adapted from Ref[3]).

hexagonal boron nitrides, silicon carbide, transition metal dichalcogenides as well as halides, etc. Many more have been studied in the realm of theoretical simulations with the aid of robust first principles method like density functional theory. A concise pictorial overview of the 2-D material family is presented in Figure 1.1.

The enormous interest in 2-D materials is due to the host of unique properties possessed by these materials due to their reduced dimensionality. Due to the confinement of carriers responsible for electrical, thermal transport in a 2-D plane, a drastic change is observed in their electronic, thermal and optical properties for example graphene possesses high electrical and thermal conductivity while TMD's show enhanced photoluminescence relative to their bulk counterparts.[4–11] The electronic structure of 2-D materials also varies drastically depending on their composition with graphene being a zero gap semiconductor[12–14] and h-BN being an insulator with a large band gap of 5.97 eV.[15, 16] The family of 2-D TMD materials demonstrate a large variation in their conduction properties depending on the coordination and oxidation state of the metal atoms. Thus, TMD materials are classified as semiconductors (MoS_2, WS_2) , semi-metals (WTe_2, $SiTe_2$), true metals (NbS_2, VSe_2) and superconductors ($NbSe_2$, TaS_2).[17–23]

Since the surface crystal structure of 2-D materials show good compatibility with current thin-film techniques, it becomes possible for them to be placed on various substrates and be integrated in electronic devices. 2-D materials such as graphene and TMD's posses high electron mobility and excellent electrical properties[4–6, 19, 20], optical properties[24–26], mechanical flexibility and strength[27–29] that are suited for electronics and opto-electronics.[30–33] Furthermore, TMD's like MoS_2 monolayers show large optical absorption and enhanced photoluminescence which are of importance for opto-electronics.[34, 35] Due to their large surface area, graphene and TMD's also find applications as capacitors in batteries.[36–39] h-BN in addition to being atomically flat surface, has a wide band-gap, good dielectric characteristics and excellent thermal conductivity that has promise as an excellent substrate.[40]

In addition, there exists vast literature pointing towards the modification as well as tunability of the properties of 2-D materials by external means. Various studies have shown that carrier concentration and charge mobilities within 2-D materials can be tuned by application of electric field or by chemical doping.[4, 7, 41, 42] Band gap tunable by external means such as electric field, strain, etc has been observed in bi- as well as tri-layer graphene by various groups.[43–48] Transition from indirect band-gap to direct band-gap on reduction of size from bulk to monolayer respectively has been reported in the case of TMD's which lead to enhanced photoluminescence. This gives rise to the

possibility of thickness dependent photoluminescence properties of TMD's.[34, 35]

Magnetic and spin properties of 2-D materials are also of interest from spintronics point of view. Extensive study in this regard has been carried out within the context of graphene by using theoretical simulation as well as experimental study. These studies show that graphene possesses long spin lifetimes and diffusion lengths which are suited for spintronic applications.[49–51] Systematic study of defects such as vacancies as well as dopants of various types have shown that it is possible to introduce localized magnetic moments in graphene. Studies on TMD's show that MoS_2 and other TMD's posses strong spin-orbit coupling.[52–54] Investigations by Wei *et. al.*,[55] suggests ferromagnetic interactions in MoS_2 originating from strong interactions between Mo^{4+} and sulfur vacancies. The fact that magnetic semiconductors are crucial to the development spin-field effect transistors as proposed by Das and Dutta,[56] has made research on magnetism of 2-D materials essential.

In view of the above discussion, it is evident that 2D materials offers a rich playground to explore a variety of interesting physics for diverse and novel applications. In the following sections and subsections we discuss the various aspects of graphene, the 2-D material of interest in context of the present thesis.

1.2   Graphene

The start of the 21st century was marked by a significant breakthrough in materials science. In 2004, the first ever two-dimensional (2-D) material - graphene was synthesized by Novoselov and Geim.[4, 5] Now, almost 15 years since the pioneering discovery, the impact of graphene on the scientific community and society at large cannot be denied and this important discovery has been recognized by the Noble Prize in 2010.

Graphene to put simply, is a single layer of carbon atoms which are arranged in a planar honeycomb lattice as shown in Figure 1.2. The highly unusual electronic and mechanical properties of graphene results from the carbon-carbon bonding. The s, p_x and p_y orbitals of carbon undergo sp^2 hybridization to form the in-plane σ covalent bonds, while the unhybridized p_z orbitals form the out-of-plane π bonds. The strong in-plane σ bonds are responsible for the mechanical properties of graphene. The out-of-plane π bond network, on the other hand, is responsible for the unique band structure of graphene which plays a crucial role in determining it's electronic properties.
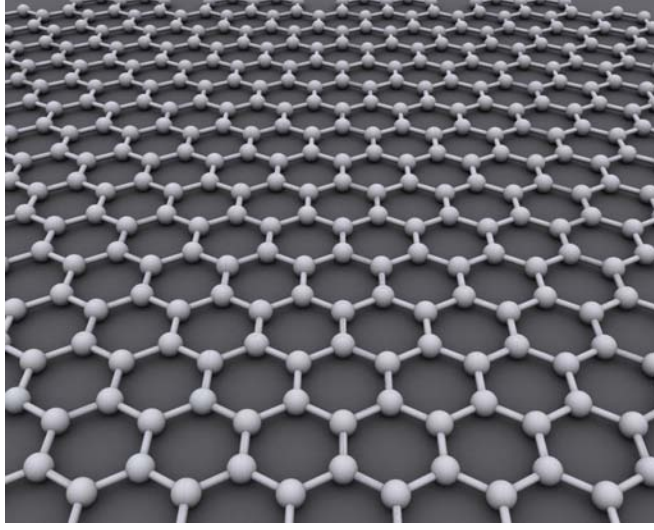
Figure 1.2: The honeycomb structure of two-dimensional graphene sheet.(Figure adapted from Wikipedia).

Crystal Structure

The lattice of graphene is not a Bravais lattice. However, it can be divided into two inequivalent triangular Bravais sublattices A and B. Therefore the honeycomb lattice of graphene can be treated as a triangular lattice with a two atom basis. Thus the primitive unit-cell of graphene, as shown in Figure 1.3(a), is a rhombus containing two carbon atoms A and B belonging to A sublattice and B sublattice respectively. The lattice vectors of the unit cell (refer Figure 1.3(b)) are

$$\vec{a_1} = \frac{a_0}{2}(3, \sqrt{3}); \quad \vec{a_2} = \frac{a_0}{2}(3, -\sqrt{3}) \tag{1.1}$$

where $a_0 = 1.42\text{Å}$ is the distance between the nearest neighbor carbon atoms and $\vec{a} = \sqrt{3}a_0 = 2.46\text{Å}$ is the lattice constant of graphene. Each carbon atom belonging to sublattice A has three carbon atoms belonging to sublattice B as it's nearest neighbor and vice versa. The nearest neighbor vectors are given by

$$\delta_1 = \frac{a_0}{2}(1, \sqrt{3}); \quad \delta_2 = \frac{a_0}{2}(1, -\sqrt{3}); \quad \delta_3 = -a_0(1, 0) \tag{1.2}$$

The reciprocal lattice of graphene is also a triangular lattice and is spanned by the lattice vectors

5
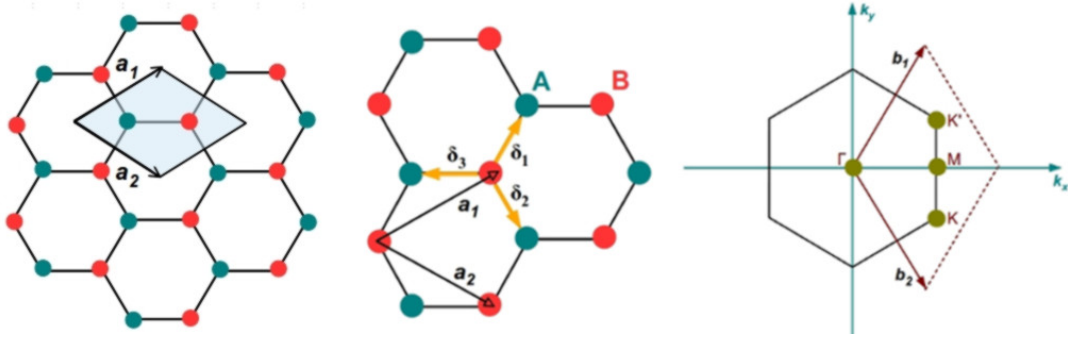
Figure 1.3: a) The primitve unit cell of graphene with two carbon atom basis (Turquoise(Red) circles represent carbon atoms belonging to A(B) sublattice.) b) The lattice vectors $\vec{a}_1, \vec{a}_2$ (black arrows) and the near-neighbour vectors $\delta_1, \delta_2, \delta_3$ (yellow arrows) are shown. c) The first Brillouin Zone (BZ) corresponding to the graphene unit cell is shown. The high symmetry Γ, M, K points (brown circles) are marked. The lattice vectors $\vec{b}_1, \vec{b}_2$ are shown by red arrows

$$(1.3) \qquad \vec{b}_1 = \frac{2\pi}{3a_0}(1, \sqrt{3}); \quad \vec{b}_2 = \frac{2\pi}{3a_0}(1, -\sqrt{3})$$

The first Brillouin zone (BZ) for graphene is a hexagon as shown in Figure 1.3(c). along with the high symmetry k points Γ, M, K. There are six corners of the Brillouin zone of which only two are inequivalent and represented by the points K and K' as

$$(1.4) \qquad K = \frac{2\pi}{3a_0}\left(1, \frac{1}{\sqrt{3}}\right); \quad K' = \frac{2\pi}{3a_0}\left(1, -\frac{1}{\sqrt{3}}\right)$$

The remaining four corners can then be obtained by translation of K or K' points by a reciprocal vector. The two inequivalent points K and K' are of important significance for the physics of graphene which will be discussed in the following section.

Electronic Structure of Graphene

The electronic band structure of graphene is rather unconventional. As stated previously, it's behavior is dictated by the out-of-plane π bond network and at low energies, the electronic spectrum of graphene shows a 'linear' dependence between the energy and wave vectors. The electronic band structure of graphene has been studied theoretically since 1947, decades before it was synthesized, when Wallace[12] first solved the problem within the tight binding approximation. On consideration of only the π energy bands of

graphene, the form of the tight binding Hamiltonian for graphene in nearest neighbor approximation is given by

(1.5)
$$H = -t \sum_{\langle i,j \rangle, \sigma} a^{\dagger}_{i,\sigma} b_{j,\sigma} + H.c$$

where t is the nearest neighbor hopping term, $a^{\dagger}_{i,\sigma}(b^{\dagger}_{i,\sigma})$ and $a_{i,\sigma}(b_{i,\sigma})$ are the creation and annihilation operators which create and annihilate an electron with spin $\sigma(\sigma = \uparrow, \downarrow)$ on site i of the sublattice A(B). The notation $\langle .,. \rangle$ denotes that only nearest-neighbor interactions are included and H.c. stands for the Hermitian conjugate term.

To derive the electronic band structure we recast Eqn (1.5) in k-space using Fourier transforms for the electron operators

(1.6)
$$a_{k\sigma} = \frac{1}{\sqrt{N}} \sum_{n} e^{ik.R^A_n} a_{n\sigma}; \quad b_{k\sigma} = \frac{1}{\sqrt{N}} \sum_{n} e^{ik.R^B_n} b_{n\sigma}$$

where N is the number of unit cells in the lattice, R^{α}_n is the position of the carbon atom in the nth unit cell of sublattice α (α = A,B) and the index n runs over all the unit cells in the lattice.

In this representation the Hamiltonian of Eqn (1.5) can be written as

(1.7)
$$H(\vec{k}) = -t \begin{pmatrix} 0 & S(\vec{k}) \\ S^*(\vec{k}) & 0 \end{pmatrix}$$

where $S(\vec{k})$ is given by

(1.8)
$$S(\vec{k}) = \sum_{i} e^{ik\delta_i} = e^{-ia_0 k_x} + 2e^{i\frac{a_0 k_x}{2}} cos(\frac{\sqrt{3}a_0 k_y}{2})$$

where δ_i are the nearest-neighbor vectors as in Eqn (1.2).

On diagonalizing the Hamiltonian matrix given in Eqn (1.7), we obtain the energy eigenvalues as

(1.9)
$$E_{\pm}(\vec{k}) = \pm t|S(\vec{k})| = \pm\sqrt{3 + f(\vec{k})}$$

where

7

(1.10)
$$f(\vec{k}) = 2cos(\sqrt{3}a_0 k_y) + 4cos(\frac{\sqrt{3}}{2}a_0 k_y)cos(\frac{3}{2}a_0 k_x)$$

From Eqn (1.9) and Eqn (1.10), it can clearly be noted that the condition for $E_{\pm}(\vec{k}) = 0$ is met only at the corners of the Brillouin zone i.e at the points K and K' and the resultant energy band is exactly symmetric about the point $E_{\pm}(\vec{k}) = 0$. The $+$ sign provides the bonding π energy band and $-$ sign provides the anti-bonding π^* band which as a result of Eqn (1.9) and Eqn (1.10) are degenerate at the points K and K'. Since the unit-cell of graphene contains two π electrons, these two π electrons completely occupy the lower π band, resulting in the density of states (DOS) vanishes at the Fermi level and making graphene a zero gap semiconductor. The points K and K' are conventionally called the Dirac points or neutrality points as the energy dispersion near these points shows a linear dependence with zero effective mass, similar to that of the relativistic massless Dirac fermions as shown in Figure 1.4.
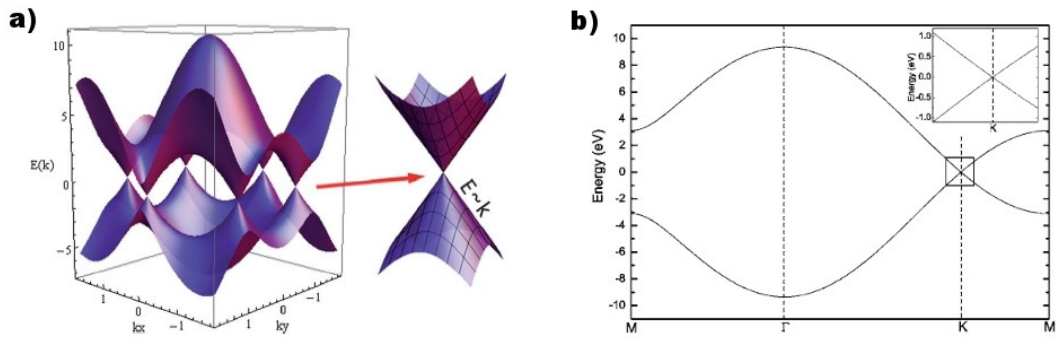
Figure 1.4: a) Plot of the π band structure of graphene, showing the conduction band and the valence band touching at the K points (Figure adapted from Ref[57]). The zoomed part at the right-hand side shows the linear dispersion in the region of the Dirac points. b)The band structure of a single graphene layer along MΓKM. The inset is an enlargement of the region indicated by the square around the K point.(Figure adapted from Ref[13])

The linear dispersion can be obtained from the band structure equations by performing a Taylor expansion of $S(\vec{k})$ around the K (K') points with $k = K + q$. The dispersion relation thus obtained for $|q| << |K|$ has the form

(1.11)
$$E_{\pm}(q) = \pm \hbar v_F |q|, \quad v_F = \frac{3}{2\hbar}a_0 t$$

where v_F is the Fermi velocity. Thus, at low energies the electronic spectrum of graphene consists of two Dirac cones located at the K and K' points of the Brillouin zone.

Synthesis and Characterization Tools for Graphene

Since it's discovery, various techniques have been developed to synthesize graphene of different shapes and sizes. The quality of graphene strongly depends on the synthesis technqiue and hence care has to be taken to choose the optimal technique to correspond with the requirements of the investigation. Graphene flakes upto $millimeter$-size can be obtained by micromechanical cleavage which consists of repeated peeling of graphite by scotch tape, followed by transference onto silicon dioxide (SiO_2) substrate.[4, 58, 59] Thermal annealing of silicon carbide (SiC) in ultra high vacuum at high temperatures leaves behind graphene layers on the insulating (SiC) substrate.[60, 61] Large graphene films of upto $centimeter$-size can be synthesized by epitaxially growing carbon on top of metal substrates by chemical vapor deposition.[62–64] Ultrasonic cleavage, used for micromechanical exfoliation of graphite flakes in proper solvents, can be used to produce stable suspensions of sub-micrometer graphene crystallites.[65, 66]

The characterization of graphene can be done using several different methods. Angle-resolved photoemission spectroscopy is primarily used to probe the electronic structure of graphene.[67, 68] Raman spectroscopy has been widely used to examine the number of layers, existence of dopants as well as disorders in graphene films.[69, 70] The presence of dopants and the level of doping can also be obtained from X-ray photoelectron spectroscopy. The quantities like electrical conductivities as well as resistance of undoped and doped graphene can be obtained through transport measurement by utilizing field effect devices.

Within the theoretical domain the different properties of graphene have ben studied $v$ia model Hamiltonians within the tight binding approach or by employing ab-$initio$ density functional theory which solves the many-body Schrödinger equation by mean field approach. For studying the effect of electron-electron correlations, the Hubbard model is the standard approach. Solutions of the Hubbard Hamiltonian in graphene problem can be achieved by various means such as exact diagonalization, mean-field approximation, quantum monte carlo technique, density matrix renormalization group, etc.

Properties and Applications of Graphene

The singular band structure of graphene having low-energy linear dispersion along with the strong in-plane covalent bonding enables graphene with highly attractive electronic and mechanical properties which could be exploited for future technological applications.

9

Graphene is a zero gap semiconductor and as such possesses high carrier density and high conductivity. Graphene is also known to show ambipolar characteristics *i.e.* the charge carriers in graphene can be tuned to provide hole conductance or electron conductance depending on the gate voltage.[4] A remarkably high electron mobility of 15000 $\text{cm}^2\text{V}^{-1}\text{s}^{-1}$ is observed for graphene at room temperatures.[4, 71] The anomalous quantum Hall effect observed at low temperatures in graphene is also a consequence of the linear dispersion of the band structure which leads to a Landau level spectrum proportional to $\pm\sqrt{N}$, where N is the index of the Landau level.[6, 72, 73] Additionally, since the spacing between the lowest Landau levels is large, it also allows for observation of the quantum Hall effect at room temperatures.[73] The charge carriers in graphene hardly encounter scattering and therefore have a average mean free path of about 1 μm which is orders of magnitude larger than the general average mean free path of carriers in materials which is the nanometer range.

Another consequence of the unique band structure is the ability of graphene to absorb 2.3% of incident light intensity which is unusual for material with only one atom thickness. This makes graphene nearly transparent.[24, 25] The thermal conductivity of graphene estimated to be 5000 $\text{Wm}^{-1}\text{K}^{-1}$ is rather high compared to that of copper, which is about 10 times lower.[8, 9, 11]

The mechanical properties of graphene are as extraordinary as it's electronic properties. Graphene is the strongest material to be discovered due to the stiffness of the in-plane covalent bonds. The breaking strength of graphene is about 42 N/m corresponding to an intrinsic strength of 130 GPa.[27] Graphene is also exceptionally light with a density of 0.77 mg/m^2. This makes graphene 1000 times lighter than paper and at the same time 1000 times stronger than steel. Graphene is also elastic with the estimates of spring constant and Young's modulus around 1-5 N/m and 1 TPa respectively.

The extraordinary properties of graphene have already driven research aimed at technological applications and have met with some success. The development of a working graphene field effect transistors is quite an achievement considering that intrinsically graphene does not possess a band gap.[30] Furthermore, integrated RF circuits employing graphene transistors have recently been realized. These RF circuits which work as frequency mixers operate at frequencies upto 10 GHz.[74] The property of variable resistance on modification of the carrier density by adsorption of gas molecules on graphene has been employed to build a micro-level gas sensor.[75]

As graphene is transparent and has good conductivity it is also an excellent candidate to replace iridium based electrodes in organic light emitting diodes (OLED's) which

are essential components of electronic device display screens. A functional graphene based touch screen has already been realized[76] Research is also ongoing to exploit the flexibility of graphene to produce flexible display screens. Graphene also has potential applications in optoelectronic devices such as photodetectors and solar cells.[31, 77, 78]

Applications exploiting the high surface-to-volume ratio of graphene are also being investigated. Composites made from graphene are prospective for lithium ion batteries. Use of graphene as surface coating of the anode in lithium-ion batteries is found to help in reducing the recharge time of the battery.[79] Graphene composites are also found to be suitable for applications in supercapcitors and fuel cells.[36, 37, 79, 80]

In the following section we will take up the issue of the magnetic properties that may be induced in graphene which otherwise is nonmagnetic. This will form one of the central topic of the present thesis.

1.3 Magnetism in Graphene Materials

Magnetism in light materials, like those based on carbon, have been studied since 1991 when the first experimental report of ferromagnetic ordering was observed in crystalline p-nitrophenyl nitronyl nitroxide (p-NPNN)[81, 82] and in complexes of fullerene (C60) and tetrakis dimethylamino ethylene (TDAE) below Curie temperatures (T_c) of 0.6 K and 16K, respectively.[83] In 2003, room temperature ferromagnetism was found in highly oriented pyrolitic graphite (HOPG) irradiated with high energy protons.[84] The experimental investigation revealed the magnetic order in HOPG originated from the carbon π electron system rather than the magnetic impurities. A year later in 2004, graphene was first synthesized and the interest in studying magnetism of carbon-based elements was revived.

The topic of magnetism in graphene holds considerable interest from the standpoint of basic physics and technological applications. Hitherto, magnetism in materials had been associated with the interactions between d- or f- electrons present in the system and which, by now, is quite well understood. Graphene, however, does not possess d- or f- electrons due to the absence of magnetic atoms. Hence the formation of magnetic moment arising from the p- electrons residing within the π network of graphene is a non-trivial problem from the view of basic physics.

From the technological viewpoint, the long spin life times and spin diffusion lengths[49–51] make graphene attractive for spintronic applications for example as a spin generator. In addition reports have suggested that materials involving $sp-$ elements possess high

spin-wave stiffness resulting in higher Curie temperatures[85, 86], display weak spin-orbit coupling and hyperfine coupling.[87–89] Hence graphene also holds promise for realizing transport of spin polarized currents. In fact, pure spin transport over long channel lengths was recently demonstrated in chemical vapor deposition grown graphene on SiO_2/Si substrate.[90]

Experimentally ferromagnetism has been excluded for defect free graphene upto temperatures of 2K.[91] However, theoretical calculations based on Quantum Monte Carlo (QMC) and Hartree-Fock calculations do predict an anti-ferromagnetic insulating ground state.[92, 93] While magnetic ordering in defect free graphene is still open to debate, ferromagnetic ordering has been found experimentally in nanographene[94, 95], disordered graphite samples[84, 96] and at grain boundaries of HOPG.[97] These studies emphasize the role of defects, edge terminations and finite-size effects in triggering magnetic order within the system.

Since it is bipartite lattice, magnetic moment formation in graphene follows Lieb's theorem[98] which states that the ground state magnetic moment is given by $|N_A - N_B|$ where N_A and N_B are the number of A and B sublattice sites. It is obvious that $|N_A - N_B|$ will have a non-zero value only if $N_A \neq N_B$ implying that a "sublattice imbalance" is necessary for magnetism to occur.

One possible way to generate sublattice imbalance is by adding an atom to the graphene lattice or by removing an atom from the graphene lattice, which leads to the formation of localized moments. In this regard the examples of a) magnetism induced by chemisorption of hydrogen on graphene as well as b) the formation of magnetic moments due to a single vacancy in graphene are benchmark cases in providing insights into the mechanism of defect induced magnetism.

Hydrogen induced magnetism in graphene was first predicted theoretically in 2007 by O. Yazyev and L. Helm [99] and only recently STM experiments by Herrero *et.al.*, have verified the validity of the claim.[100] Figure 1.5(a) shows the spin-polarized density of states for hydrogen chemisorbed on graphene. By forming a strong covalent bond with graphene, the hydrogen adatom removes one p_z orbital from the π band which effectively corresponds to removing a single carbon site thereby generating a sublattice imbalance. This leads to the formation of quasi-localized states near the Fermi energy level with a magnetic moment $1\mu_B$.

In contrast, the case of single vacancy defect in graphene is more complicated. Results from both theoretical[99, 101–103] and experimental[104, 105] investigations confirm that a single vacancy generates localized states within graphene which are spin polarized.
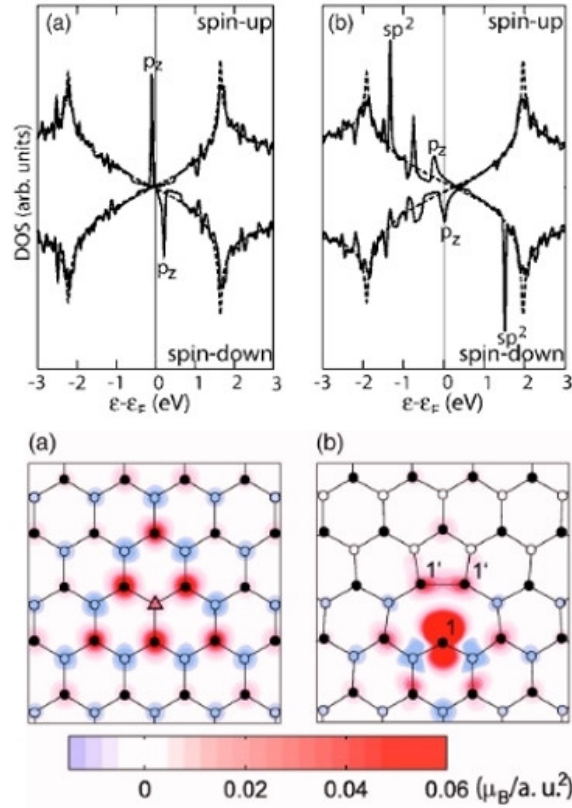
Figure 1.5: Top panel: Spin-polarized density of states plots for the systems with (a) hydrogen chemisorbed on graphene and (b) for a single vacancy defect introduced in graphene.The dashed line shows the density of states of the ideal graphene. Bottom panel: Spin-density projection (in $\mu_B/a.u.^2$) on the graphene plane around (a) the hydrogen chemisorption defect (Δ) and (b) the vacancy defect in the A sublattice. Carbon atoms corresponding to the A sublattice (open circles) and to the B sublattice (filled black circles) are distinguished.(Figure adapted from Ref[99])

Removal of a single carbon atom from graphene results in three dangling σ bonds and the loss of one p_z electron. Jahn-Teller distortion near the vacancy causes the dangling bond states to split, with one state being doubly occupied and lying deep below the Fermi energy and the other singly occupied state lying close to the Fermi energy as shown in the spin-polarized density of states in Figure 1.5(b). Thus a single vacancy introduces two types of states, a quasi-localized state due to the removal of one p_z orbital similar to the case of hydrogen adatom and a localized state originating from the dangling σ bond, each of which contributes a magnetic moment close to $1\mu_B$ as can be seen from the spin density plots and therefore a net magnetic moment of $2\mu_B$.

Over the years, defect induced magnetism in graphene has been extensively studied

13

within the theoretical framework of density functional theory as well as to a much lesser degree experimentally. An overview of these studies is presented as a background for the topics discussed in chapters 3 and chapter 6.

An alternative way to introduce magnetism in graphene is by cutting graphene along it's two different crystallographic directions 'armchair' and 'zigzag' to provide finite sized graphene fragments such as graphene nanoflakes and graphene nanoribbons. The "nanographene" differ in their electronic and magnetic properties from pristine 2-D graphene as a consequence of the finite size effect. In particular, studies have shown that opening of band gaps as well as magnetism is strongly dependent on the edge character (armchair or zigzag) and size of the system (e.g. width in nanoribbons).[106–110] Thus given the crucial role of edges in determining the properties of nanographene systems, their observation and characterization is of significant importance for investigating these systems. In this regard, substantial work has been done by the group of T. Enoki and other groups where tools such as scanning tunneling microscopy (STM) and Raman spectroscopy are used to differentiate between zigzag and armchair edges[111–113], x-ray absorption fine structure (NEXAFS) and electron spin resonance (ESR) are used to determine the magnetic edge states.[114] Recently, graphene nanoribbons with pre-defined zigzag and armchair edges were synthesized using STM nanolithography where atomic resolution images were used to identify the different crystallographic orientations and therefore control over the cutting directions.[115] Applications of nanographene in technological devices such as transistors require the edges to be well defined and defect free. Over the year various approaches such as lithographic patterning of graphene[116–118], sonochemical methods[119], chemical vapor deposition[120, 121], unzipping of carbon nanotubes[122, 123] and other approaches have been used to synthesize graphene nanoribbons with armchair and zigzag edges of various widths.

In providing a fundamental understanding of the observed properties of nanographene, theoretical simulations within either tight-binding models, Hubbard models or first principle calculations play a major role. These studies[106, 110, 124–126] have shown, that the source of magnetism within these nanographene structures is due to localized electronic states present at the so called zigzag edges due to the presence of unsaturated π bonds at these edges. No such localized states are attributed to armchair edges and therefore no magnetism is observed. A more detailed account of the effect of edge terminations on the electronic and magnetic properties of nanographene structures is discussed as a precursor to our study presented in chapter 4.

In the following we will discuss in detail the various graphene and graphene-derived

systems that have been studied in the present thesis.

1.4 Graphene Systems Discussed in the Thesis

In practice the use of graphene in many applications despite its novel properties, is hindered by the lack of a band gap. Though studies have shown that band gaps in graphene can be opened when placed on substrate, these gaps are still small for commercial applications such as transistors. This has fueled interest in research on alternative forms of graphene and their properties. Fortunately, graphene can be considered the parental building block for various forms of carbon materials. As shown in Figure 1.6, it can be wrapped to form zero-dimensional (0-D) bucky balls, rolled to form one-dimensional (1-D) carbon nanotubes or can be stacked layer by layer to form three-dimensional (3-D) graphite. The 2-D nature of graphene also allows for heterostructring with various other 2-D materials like $h-$BN or other kinds of substrate.
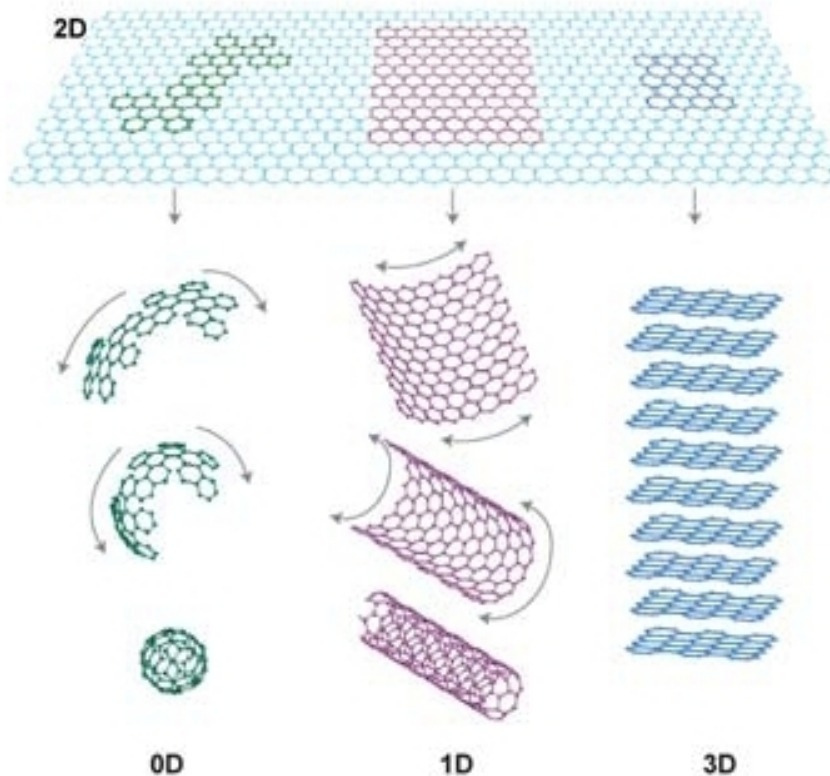
Figure 1.6: Graphene can be envisaged as a 2D parental unit for carbon materials among all other dimensionalities. It can be wrapped up into 0D buckyballs, rolled into 1D nanotubes or stacked into 3D graphite(Figure adapted from Ref[7]).

It has also been shown, that the properties of graphene as well as graphene-based derivatives can be tuned by various methods such as chemical functionalization, defects, mechanical strain, etc which can lead to realization of novel phenomenon like magnetism.

In this thesis we have employed density functional theory (DFT) to study the electronic and magnetic properties as well as the tunability of said properties for graphene systems belonging to four broad classes:

1. Few-Layer Graphene

2. Nanographene

3. Graphene Heterostructures

4. Graphene Nanomesh

A brief description of these system with respect to their attributes and general properties is provided below.

1.4.1 Few-Layer Graphene

Few-layer graphene (FLG) consists of single layers of graphene stacked on top of each other and held together by Van der Waals interaction. Depending on the number of graphene layers within the FLG, a variety of stacking sequences is possible. While it is estimated that for a FLG with N layers, 2^{N-2} stacking sequences are possible, the Bernal stacking sequence (ABA) and rhombohedral stacking sequence (ABC) as shown in Figure 1.7 have currently been observed for FLG[127–130] while bilayer graphene is known to be stable only for the Bernal (AB) stacking configuration.

The discovery of controlled opening of band gap by an electric field in bilayer graphene[132–134], the smallest unit of FLG, prompted considerable interest in FLG's as an alternative to graphene for future technologies. Various studies, experimental as well as theoretical, investigating the electronic properties of these FLG have concluded that the electronic structure of FLG's differ greatly from that of single layer graphene and show a strong dependence on the stacking sequence.[135–142]

Unlike the linear dispersion observed in graphene, the presence of interlayer coupling in FLG's gives rise to a parabolic dispersion of the low energy π bands in bilayer graphene [136, 143, 144] and a cubic dispersion for ABC trilayer graphene[137, 138, 145] as can be seen from the band structure plots of Figure 1.8. On application of electric field, the asymmetry between the on-site energies for the carbon atoms belonging to the A and B
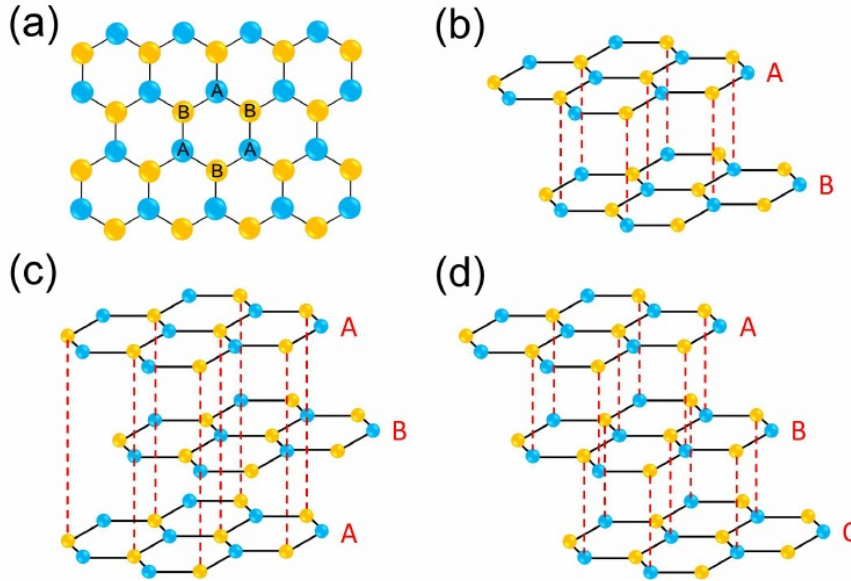
Figure 1.7: (a) Schematic of the hexagonal honeycomb lattice of single layer graphene consisting of two carbon sublattices. The carbon atoms in the A and B sublattices are colored in blue and yellow, respectively. (b) Schematic of the Bernal or AB stacked bilayer graphene. (c) Schematic of the ABA (Bernal) stacked trilayer graphene. (d) Schematic of the ABC (rhombohedral) stacked trilayer graphene.(Figure adapted from Ref[131])

sublattices causes a band gap to open at the Fermi energy in the case of bilayer graphene and ABC trilayer graphene, which can be tuned depending on the strength of the electric field.

The effect of stacking on the electronic structure of FLG can be appreciated from the marked difference in the band structures of ABC stacked trilayer graphene and ABA stacked trilayer graphene and the influence of external electric field on them. It is noted from Figure 1.8(b), that ABA stacked trilayer graphene remains semimetallic on application of electric field whereas the ABC stacked trilayer graphene becomes a semiconductor similar to the case of bilayer graphene.

In general ABA stacked FLG's can be considered as combinations of single layer and bilayer graphene. Thus a ABA stacked FLG with $2N$ (even) number of layers will consist of N sets of bilayer-like bands, while for $2N + 1$ (odd) number of layers it will have N subset of bilayer-like bands and one subset of monolayer-like band. In the case of ABA trilayer graphene this leads the low energy π bands to be a mixture of bilayer-like and monolayer-like bands with parabolic and linear dispersions respectively. The breaking of the mirror reflection symmetry with respect to the central layer on application of an external electric field causes hybridization between the linear and low
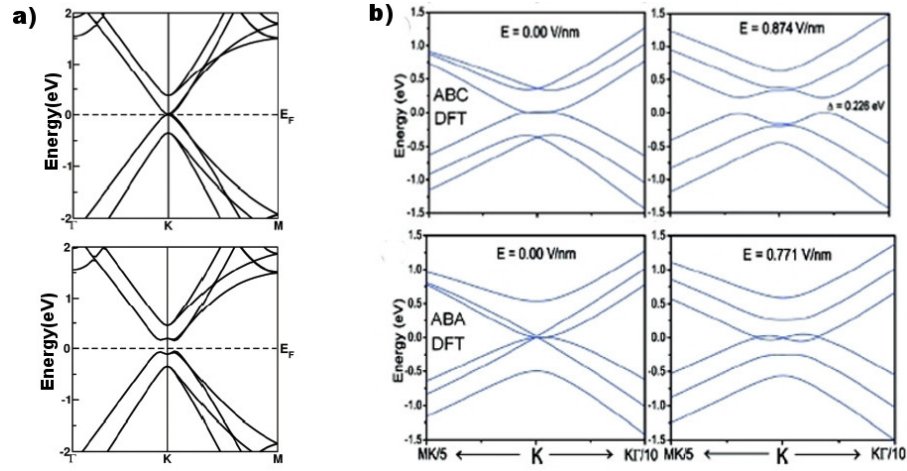
Figure 1.8: Band structure plots of the low energy π bands for a) Bernal stacked (AB) bilayer graphene without external electric field (top panel) and with electric field (bottom panel); b) for rhombohedral (ABC) stacked and Bernal (ABA) stacked trilayer graphene without electric field (left panels) and with electric field (right panels) (Figure adopted from Ref[46])

energy parabolic bands leading to band overlap near Fermi energy, the extent of the overlap being dependent on the strength of the electric field.

FLG's offer a diverse range of electronic properties with potential for device applications. The unique feature of band structure opens up the possibility of band gap engineering by control of the hopping parameters through stacking. While the band gap in FLG's is sensitive to the number of layers N and will reduce as N increases[138], it has been demonstrated that for a 'given' strength of electric field, the induced band gap increases with N. For example, for an electric field of 1 V/m which corresponds to the electric break down of SiO_2 dielectric layer, the induced band gap in AB bilayer graphene is ~ 0.17 eV [146] while in ABC trilayer graphene it is ~ 0.24 eV.

Alternatively, band gap opening in FLG's can also be achieved by surface adsorption of atoms/molecules on FLG's.[147–150] R. Quhe *et. al.*,[150] extensively investigated the effect of different metal adatoms on the electronic properties of graphene. It was reported that band gaps comparable to those achieved by external electric field can be achieved by surface adsorption of metal atoms, it being dependent on the coverage of adsorption. In the same study, *ab-inito* quantum transport simulations were carried out for a model of single gate Cu-adsorped ABC stacked trilayer FET. The calculations showed the existence of a transport gap for the model device with the theoretical implication that FLG with surface adsorption can serve as the channel of a single gated FET.

The thermal conductivity in FLG's also drops with the increasing number of graphene layers due to phonon coupling between the layers. However, the estimate of 1300 $Wm^{-1}K^{-1}$ for four layer thick FLG is still relatively high compared to bulk copper which has a thermal conductivity of 400 $Wm^{-1}K^{-1}$.[151, 152] This allows for the possibility of using FLG's for thermal management.

Long spin relaxation lengths exceeding 8 μm has also been reported for few-layer graphene which enhances it's suitability for use in spintronic devices as well.[153] In spite of the importance it has for spintronic application, the literature on the magnetic properties of FLG is highly limited. In chapter 3, we aim for understanding magnetism in FLG systems within the *ab-initio* simulations approach by investigating the formation of local magnetic moments in bilayer graphene (BLG) due to surface adsorption and it's tunability by application of an external electric field.

1.4.2 Nanographene

As mentioned in section 1.3, nanographene systems are finite sized fragments of graphene obtained by cutting graphene along it's two crystallographic axes termed as zigzag and armchair which are shown in Figure 1.9(a). By finite termination of graphene in either one or all possible directions one can obtain quasi one-dimensional (1-D) graphene nanoribbons (GNR) or zero dimensional (0-D) graphene nanoflakes as in Figure 1.9(b). Depending on the geometry of edges obtained on termination, nanographene can be classified into zigzag or armchair varieties. By convention the width is determined by the number of carbon dimer lines M across the nanographene which is different for armchair and zigzag edges.

Currently, synthesis of nanographene can be classified into two categories a) Top-down approach and b) Bottom-up approach. Top-down approach involves cutting of large graphene sheets into nanostructures of desired shape and size using diverse techniques such as etching of graphene sheets by an STM tip[118], by thermal activation of nanoparticles[156], epitaxial growth of graphene sheets patterned by lithographic techniques[116, 117], sonification of exfoliated graphene layers[119, 157] etc. However preparation of nanographene using above techniques results in irregular edge geometries and little control over the number of graphene layers. Bottom-up approaches involve building desired graphene nanostructures by attaching small molecular units together. These approaches consist of chemical vapor deposition (CVD)[158], molecular percursor based growth[159, 160], solution chemistry with growth on surfaces[120, 121, 161], pyrolyzing biodegradable composites[162], etc. Control over the size of the nanographene
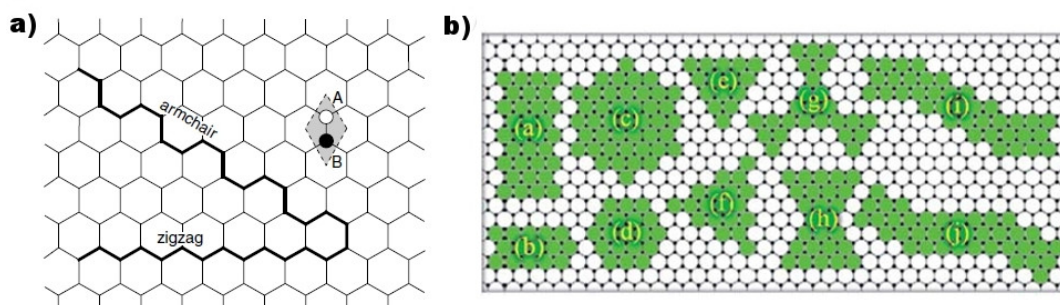
Figure 1.9: a) Two-dimensional crystalline lattice of graphene. The shaded area denotes the unit cell of graphene containing two carbon atoms which belong to the two sublattices of graphene, A (empty circle) and B (filled circle). The two high-symmetry directions of graphene lattice, armchair and zigzag, are highlighted (Figure adapted from Ref[154]); b) The schematic representation of different "nanographene"" of a variety of shapes, e.g., rectangular with (a) armchair and (b) zigzag edges, nanodiscs with (c) armchair and (d) zigzag edges, nanotriangles with (e) zigzag and (f) armchair edges, nanoflakes with (g) propeller and (h) sand clock structures, z-shaped structures with (i) zigzag/armchair/zigzag and (j) armchair/zigzag/armchair graphene nanoribbon junctions. (Figure adapted from Ref[155]

is also crucial as the electronic properties of the system is determined by it. Over the years, effort has been made to fabricate nanographene structures in sub-10 nm - 20 nm regime. In recent times, Dai *et. al.* have been successful in synthesizing graphene nanoribbons < 10 nm by using chemical sonication route and in the 10-20 nm regime by unzipping of carbon nanotubes.[119, 121]

Theoretical methods such as the tight binding approximation and Hubbard models, as well as first principle simulations based on density functional theory provide a microscopic understanding of the electronic and magnetic behavior of wide variety of materials and have been greatly used to shed light on some of the observed phenomenon for nanographene structures such as the previously mentioned existence of magnetic edge states which is discussed below.

As previously stated in section 1.3, the termination of graphene generates unsaturated p_z orbitals on carbon atoms along the edges. The zigzag edge consists of carbon atoms belonging to the same sublattice. Thus, the presence of unsaturated bonds along the zigzag edge introduces localized electronic states along the edge called as "edge states". This does not occur for the armchair edge where the presence of two carbon atoms belonging to different sublattices results in the formation of bond and therefore does not give rise to edge states. The different characteristics of the zigzag and armchair
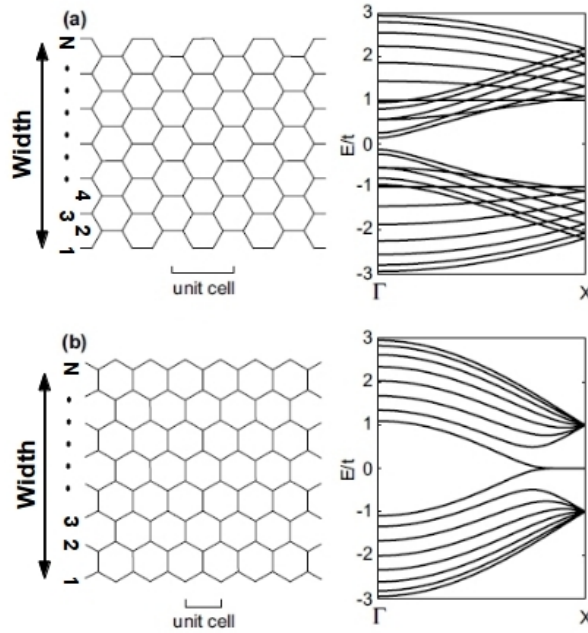
Figure 1.10: Atomic structures and tight-binding band structures of (a) armchair and (b) zigzag graphene nanoribbons. Unit cells of the graphene nanoribbons are shown.(Figure adapted from Ref[154])

edges affect the electronic properties of nanographene systems in different ways.

In Figure 1.10, the electronic band structure for wide armchair and zigzag graphene nanoribbons are shown. Tight binding model studies[106, 108, 109, 124, 163], solution of Hubbard models[124, 164] as well as first principle calculations[107, 110, 165, 166] probing the electronic and magnetic properties of these nanoribbons, predict opening of the band gap for graphene nanoribbons with armchair edges with the band gap varying inversely with the width of the nanoribbon. For certain widths the band gaps can become vanishingly small so that the corresponding armchair nanoribbon can be considered metallic. No magnetic order is predicted for armchair structures.

In contrast, in zigzag graphene nanoribbons, the presence of "edge states" along the zigzag edges give rise to flat bands at the the Fermi energy within the non spin-polarized approximation and hence a metallic character. These edge states are low energy states that decay rapidly inside the bulk.[106, 124, 163] The high density of states at the Fermi energy due to the presence of flat bands suggest instability towards magnetic order due to Stoner's criteria.[167] Figure 1.11 shows the spin-polarized band structure as well as spin density for zigzag nanoribbon. It is observed that in it's ground state, zigzag graphene nanoribbons show parallel alignment of localized spins within a given edge
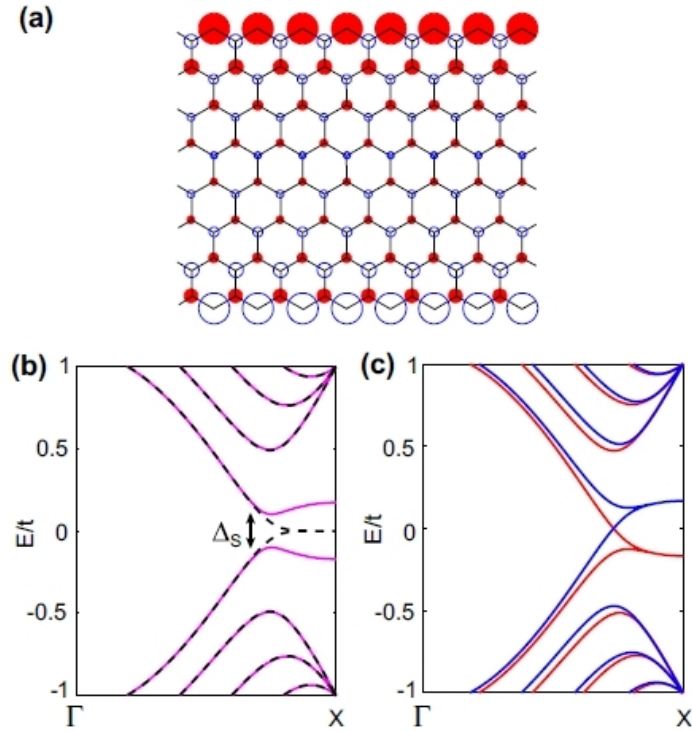
Figure 1.11: (a) Local magnetic moments in a zigzag graphene nanoribbon calculated using the mean-field Hubbard model (U/t = 1.2). Area of each circle is proportional to the magnitude of the local magnetic moment at each atom. Filled and empty circles correspond to spin-up and spin-down densities, respectively. (b) Mean-field Hubbard-model band structure (solid lines) compared with the tight-binding band structure (dashed lines) for the solution shown in panel (a). The band structures for spin-up and spin-down electrons are equivalent. (c) Mean-field Hubbard-model band structure for the same graphene nanoribbon with the ferromagnetic mutual orientation of the edge spins. The band structures for the majority-spin electrons and the minority-spin electrons are distinguished.(Figure adapted from Ref[154])

and anti-parallel alignment between spins belonging to opposite edges thus making the ground state anti-ferromagnetic (AFM). Futhermore, the AFM zigzag graphene nanoribbon shows a direct band gap which varies inversely with the ribbon width.

Additionally it has been shown that by application of electric field the band gap can be varied in both armchair and zigzag graphene nanoribbons. In both cases, the band gap decreases with increasing electric field. In fact first principle calculations show that zigzag graphene nanoribbons exhibit half-metallicity beyond certain critical value of electric field.[165, 168, 169] Alternatively, tuning of the electronic and magnetic properties can also be achieved by doping or modification of edges.[170–173]

The observation of edge magnetism as well as electric field control of band gap in nanoribbons have propelled investigations into the magnetic nature of other graphene nanostructures of various shapes known as graphene nanoflakes. Strictly speaking, finite sized graphene nanoribbons can be considered as nanoflakes of rectangular shape. Therefore in general, the effect of edges for these finite-sized graphene fragments are similar to that of graphene nanoribbons, with armchair edged nanostructures exhibiting no magnetism while magnetic order is found along the zigzag edge due to localized edge states. Unlike graphene nanoribbons however geometric considerations and finite-size effects play an important role in determining the electronic and magnetic properties of these nanoflakes. For zigzag nanoflakes, the total magnetic moment is given by the sublattice imbalance according to Lieb's theorem. Even for the cases where sublattice imbalance is zero, magnetic order can still be enforced by having a magnetic configuration with zero total moment but finite edge moments aligned in anti-parallel manner. Since the magnetism lifts the degeneracy of states at the Fermi energy, it is expected that electron-electron correlations will play an important role in determining the properties of these systems. Finite-size effect, in case of nanographene further strengthen the electron-electron correlation effect, handling of which may require a model beyond the standard Hubbard model considerations.

In chapter 4 we take up the task of studying the effect of electron-electron correlations on graphene nanoflakes with triangular and ribbon geometries within the extended Hubbard model approximations which take into account the on-site electron-electron Coulomb interaction (U) as well as inter-site electron-electron Coulomb interaction (V). The effect of (V) as well as doping (n) on the magnetic properties of the nanoflakes is studied to obtain a complete magnetic phase diagram in $n - V$ space.

1.4.3   Graphene Heterostructures

The novel properties of graphene which make it a material of interest for various applications have been obtained for free-standing, defect-free graphene. However, characterization of graphene properties as well as realization of graphene-based devices requires graphene to be supported by a dielectric substrate.

Often, the presence of substrate negatively affects the properties of graphene. For example the carrier mobility of graphene diminishes from $\sim 10^7$ cm^{2}V^{-1}s^{-1} for free standing graphene to about 25,000 cm^{2}V^{-1}s^{-1} [174–176] when supported by dielectric silicon dioxide (SiO$_2$) substrate. Reduced electrical and thermal conductivity has also been reported for graphene on substrates. Various investigations report that some of the

primary causes for the observed reduction are electron scattering from charged surface states and impurities[174, 175, 177], surface optical phonons[178–180], the roughness of the surface i.e., surface corrugations[181, 182] as well as substrate induced disorders which lead to creation of electron and hole puddles.[176, 183]

Thus it can be seen that the interfacial interaction between graphene and substrate play a crucial role in determining the various properties of supported graphene and their understanding is essential for building graphene heterostructures that can be used for novel functionalities.

Traditionally, graphene has been deposited on SiO_2 substrates or grown expitaxially on SiC substrates. In recent years, epitaxial growth of graphene on metal substrates such as Pt (111), Ru (0001), Ir(111) and Ni(111) have also been reported.[184–196] It has been found that depending on the type of adsorbtion the graphene-substrate interaction can be divided into types a) graphene can either be physisorbed onto the substrate as in the case of SiO_2[197–199], Pt(111)[200, 201] and Ir(111)[202–204] or b) graphene can be chemisorbed on to the substrate as in the case of SiC[205–207], Ru(0001)[208–211] and Ni(111)[212–215].

Vibrational spectroscopy studies[216–219] have shown that chemisorption of graphene on substrate leads to softening of the graphene phonon modes, in particular the out-of-plane vibrational modes with the corresponding force constants ~ 50% lower than bulk graphite. This implies that there exists strong interaction between graphene and substrate which leads to weakening of the in-plane C-C bonds. In contrast, physisorption of graphene leads to minimal changes in the phonon spectrum. Theoretical investigations show that the quenching of the out-of-plane flexural phonon modes and shorter phonon lifetimes is one of the main causes of the reported reduction in thermal conductivity in supported graphene.[220–222]

Interfacial interaction between graphene and substrate can also cause doping of graphene.[198, 201, 207, 223–225] A experimental and theoretical study by M. Gao *et.al.*[225], have reported that charge transfer between the graphene and Ni(111) substrate at the interface shifts the graphene Dirac point below the Fermi energy thus making the graphene doping *n*-type. On the other hand for graphene/Pt(111) interface, the Fermi energy lies below the Dirac point leading to *p*-type doping of graphene. The study also reports that graphene on Ru(0001) shows a curious spatially varying doping which occurs due to the buckling of graphene. Graphene is known to buckle when placed on the substrate and the degree of corrugation depends on the graphene-substrate interaction. Graphene chemisorbed on Ru(0001) shows a high degree of corrugation ~ 1.54Å

which causes some carbon atoms to lie farther from the substrate, top atoms, and others to lie near the substrate. This leads to charge transfer between the top and bottom atoms which effectively makes the top p-type and the bottom n-type which results in the spatial variation of the doping.

Strong bonding between graphene and substrate can also lead to opening of band-gaps in graphene as in the case of graphene on Ni(111) where strong covalency between the graphene π states and Ni d states strongly modifies the linear low energy spectrum of graphene. Interlayer coupling between the carbon buffer layer and graphene in graphene/SiC system is reported to be the cause for the opening of band gaps close to 0.26 eV[226]. Intercalation by metal atoms has also been reported to open band gaps in graphene. Recent photoemission and density functional theory investigations have reported a band gap of 0.29 eV being opened in graphene at room temperature when europium was intercalated between graphene and SiC substrate due to strong hybridization between the Eu $4f$ states and graphene π states[227]. It is inferred that such strong coupling breaks the sublattice symmetry between the carbon atoms within graphene which results in introduction of the band gap. Similar opening of band gaps has also been observed for intercalation of gold (Au) between graphene/Ru(0001)[228], silver(Ag) and copper (Cu) in graphene/Ni(111)[229–231] and also in bismuth (Bi), copper (Cu), iron (Fe) in graphene/Ir(111).[232–234]

From above it can be implied that tuning the interfacical interaction between graphene and substrate may lead to control of the electronic properties of graphene which may be of importance in developing graphene-heterostructures for new device functionalities.

In this regard, heterostructures of graphene with ferroelectric materials for designing graphene based FET's have gained attention over recent years due to their ultra high dielectric constants κ and nonlinear hysteretic dielectric response to an electric field. The motivation stems from the notion that the screened Coulomb potential interaction between the graphene and the charge impurities present on the substrate surface, which is responsible for limiting of the carrier mobilities, can be suppressed by using substrates with high κ. An example of this was provided by the study of S. Sonde $\hat{e}t$. al., which shows that the enhanced mobility observed in graphene/SiC compared to graphene/SiO$_2$ is due to better dielectric screening of the charged impurities by SiC over SiO$_2$ as a result of SiC having higher κ compared to SiO$_2$ and also due to lesser surface polar phonon scattering observed in graphene/SiC.[235]

The other main factors that contribute towards the interest in ferroelectric materials
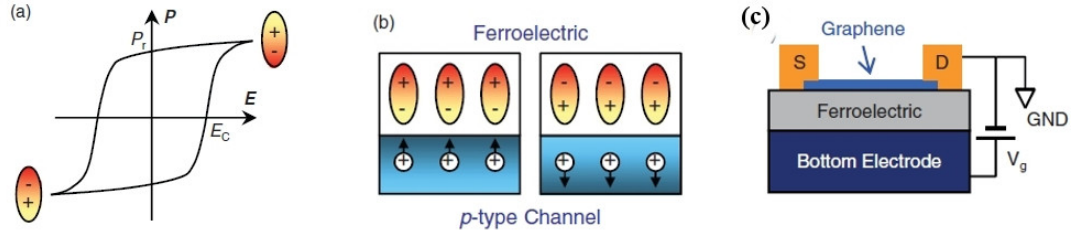
Figure 1.12: Schematics of (a) the ferroelectric polarization versus applied electric field ($P - E$) hysteresis loop; (b) ferroelectric field effect induced charge carrier accumulation (left) and depletion (right) in a p-type conducting channel; (c) Schematics of (a) a graphene FET with a ferroelectric back-gate(Figure adopted from Ref[231])

as a gate dielectric is the fact that ferroelectric materials possess two, sometimes more , nonvolatile polarization states. By applying an electric field greater than the coercive field, switching between the different polarization states can be initiated as can be seen from Figure 1.12(a). Thus when using ferroelectric materials as FET gate, charge carriers can be accumulated or depleted from the conduction channel in response to the polarization field, depending on the direction of polarization and the carrier type (refer Figure 1.12(b)). This results in nonvolatile changes in channel resistance which is essential for designing nonvolatile memory storage devices and charge sensors. In addition ferroelectric materials also possess high doping capacity. For example in many ferroelectric perovskite-oxides , the polarization value can reach 50-100 $\mu C cm^{-2}$ which can induce carrier densities upto $10^{14} cm^{-2}$, a magnitude higher than conventional dielectric substrates.[236]

In graphene based FET (refer Fig 1.12(c)) with ferroelectric gates, polarization field induced doping of graphene with a high density of electron or holes depending on the polarization direction is observed. This results in shifting of the Dirac point which is used as an indicator to describe the effect of ferroelectric polarization on conductivity.[236, 237]

However, the advantages of using ferroelectric substrates over conventional substrates remains a highly contested issue. Studies have shown that while using ferroelectric materials can enhance carrier mobilities over conventional substrates in the low temperature regime as in the cases of single as well as few layer graphene devices prepared on Pb(Zr,Ti)O_3 (PZT)[237–239] and (Ba,Sr)TiO_3 (BSTO) films [240], the room temperature mobility invariably drops within the range of 1000-5000 cm^{2}V^{-1}s^{-1} for single layer graphene devices[240–242]. The presence of soft phonon modes, which give ferroelectric materials their ferroelectric property, can cause the remote substrate optical (RSO) phonon modes to contribute significantly towards the carrier mobility which

washes away the advantage of better screening of charged impurities due to high κ.[243]

On the other hand, the high sensitivity of graphene towards charge modulation at the interface, have lead to the application of graphene FET's based on ferroelectric materials as highly promising charge sensors for the detection of polarization of the adjacent ferroelectric layer. Rajapitamahamuni *et. al.*,[240] have already demonstrated the use of such a sensor for examination of the dielectric constant, pyroelectric coefficient and ferroelectric polarization of BSTO thin films.

In chapter 5 we first summarize the experimental setup in which graphene FET was employed as a sensor to detect the out-of-plane ferroelectric polarization at the surface of $SrTiO_3$(STO). Motivated by the experimental findings, we then discuss the setup and results of our theoretical investigation of the graphene-STO model using density functional theory to determine the out-of-plane dipole moments at the STO surface. In addition we also look at the effect of an electric field and the role played by graphene on the surface polarization of STO.

1.4.4 Graphene Nanomesh

Graphene nanomesh (GNM) is a two-dimensional structural derivative of graphene having semiconducting properties. Experimental studies have reported that graphene nanomesh FET devices can support currents 100 times greater than GNR devices with a comparable on-off ratio that can be tuned depending on the structural parameters.[244] The tunability of the electronic properties along with it's thin film nature has lead to growing interest in graphene nanomeshes for practical device application.
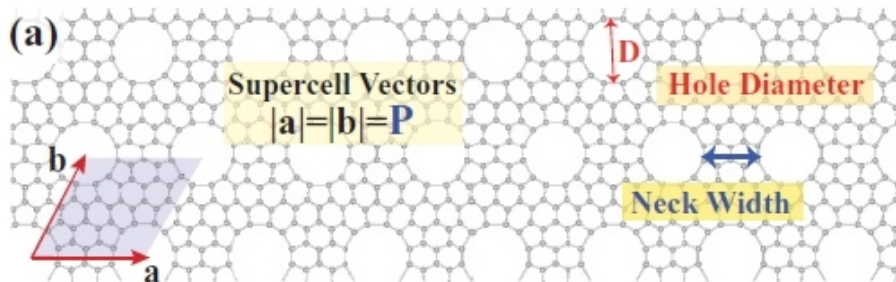
Figure 1.13: Stuctural Parameters of a graphene nanomesh (Figure adapted from Ref[245])

Graphene nanomesh can be obtained by removal of a large number of atoms from a large graphene sheet to create a periodic array of nano-sized holes as shown in Figure

1.13. The presence of these nano-holes results in the quantum confinement of the remaining graphitic structure. Thus a graphene nanomesh, also known as holey graphene, can be pictured as interconnected network of GNR's. The electronic properties of GNM are dependent on two critical structure parameters : (a) periodicity defined as the centre-to-centre distance between two neighboring nano-holes and (b) neck-width defined as the smallest edge-to-edge distance between two neighboring nano-holes. Synthesis of GNM's has been achieved by various techniques such as block copolymer lithography[244, 246], nanosphere lithography[247] and nanoimprint lithography[248] which also allow control of the aforementioned structural parameters and hence the electronic properties. Experimental studies report[243, 244] that GNM's are semiconductors with the opening of the band-gap showing inverse dependency on the neck-width (W_{nw}) which is analogous to the case of graphene nanoribbons. Liang $et.al.$,[243] also provided a scaling rule for the dependence of band-gap (E_g) on the neck-width given by $E_g = \alpha/W_{nw}$ where α is a coefficient with the unit of nm. eV. In keeping with the analogy with GNR's, the nano-holes themselves are characterized by the presence of armchair and zigzag edges though the influence of edge character on the electronic properties of GNM's have yet to be observed.

While experimental observation predict semiconducting behavior for all GNM's fabricated till date, theoretical investigation into the dependence of electronic properties on the lattice parameters, shape, size as well as edge character of nano-holes provide a more complex picture.[245, 249–254]

In 2009, W. Liu $et.al.$ studied GNM's with triangular (T-GNH) and rhombus nanoholes (R-GNH) having zigzag and armchair edges based on the tight-binding model(TB) in order to investigate the band gap dependence on the lattice size (L) and hole size (l).[250] The study showed that for zigzag R-GNH (T-GNH) the E_g increases monotonically with increasing l while decreasing monotonically with increasing L as shown in Figure 1.14. It was also observed that for both T-GNH and R-GNH the scaling rule for $E_g \propto \sqrt{N_{rem}}/N_{total}$, where N_{rem} is the number of removed carbon atoms and N_{tot} is the total number of carbon atoms in the defect-free lattice, holds true. In contrast, for armchair T-GNH (R-GNH) for a given L, the band gap E_g has an oscillatory increasing dependence with the increasing l with a period of 3, the qualitative behavior being analogous to armchair GNR's.[110, 255] Conversely, increasing L for a given l causes E_g to decrease monotonically.

The oscillatory behavior of E_g with a period of 3 was also found for GNM's with zigzag-edged hexagonal and rhombohedral holes by F Ouyang $et.al.$, while studying the sensitivity of E_g to the neck width W of the GNM's.[251] Thus of the total systems
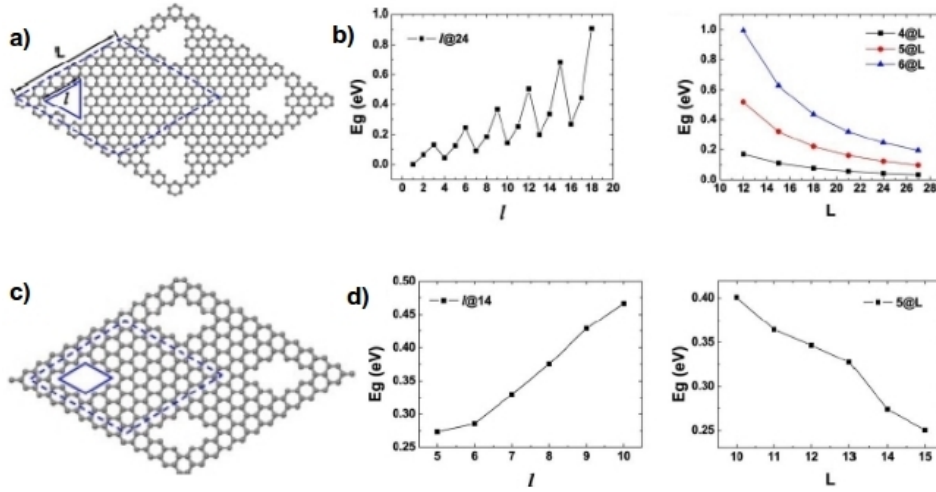
Figure 1.14: (a),(c) The structure of triangular (T-GNH) and rhombus (R-GNH) nanohole geometries. The grey balls indicate the carbon atoms. The solid and dashed blue lines denote the size of the nanohole in terms of side length l and of the lattice by length of the unit cell L.(b) Armchair T-GNH : Band gap E_g vs l for fixed value of $L = 24$ (left) and Band gap E_g vs L for fixed $l = 4, 5, 6$ (right).(d) Zigzag R-GNH : Band gap E_g vs l for fixed value of $L = 14$ (left) and Band gap E_g vs L for fixed $l = 5$ (right). (Figure adapted from Ref[250])

studied, only half were found to be semiconducting for the hexagonal hole systems while only one-third were found to be semiconducting for the rhombohedral hole systems. A similar periodicity of 3 was once again observed by W. Oswald and Z. Wu[253] for the dependence of E_g on the lattice vectors P and Q along the armchair and zigzag directions of the lattice. Their study carried out on zigzag-edged hexagonal holes arranged in a rectangular pattern in a graphene lattic showed that increasing Q caused the GNM to transition from semimetallic for $Q = 3m + 1$ and $Q = 3m + 2$ (m is an integer) to semiconducting for $Q = 3m$. In the case of semiconducting GNM's, increasing P led to a reduction of E_g without any modification of the band structure features.

Thus, the sensitivity of the GNM band gap E_g towards the structural parameters opens up the possibility of band gap engineering in GNM for various applications. While the landscape of electronic properties offered by GNM's is diverse, it becomes even richer when magnetism is taken into consideration.

As in the case of GNR's, the character of the edge at the hole perimeter determines the magnetic nature of the GNM's. The localized states present at the zigzag edge due to the unsaturated C bonds produce a flat band at the Fermi energy in a non-magnetic calculation which is removed on addition of spin polarization. This opens a spin-split

gap (E_s) in addition to the existing electronic gap E_g as shown in Figure 1.15. The spins show a parallel alignment if the zigzag edges are at angles 0° or 120° . Conversely, the spins show anti-parallel alignment if the zigzag edges are at angles 60° or 120°.
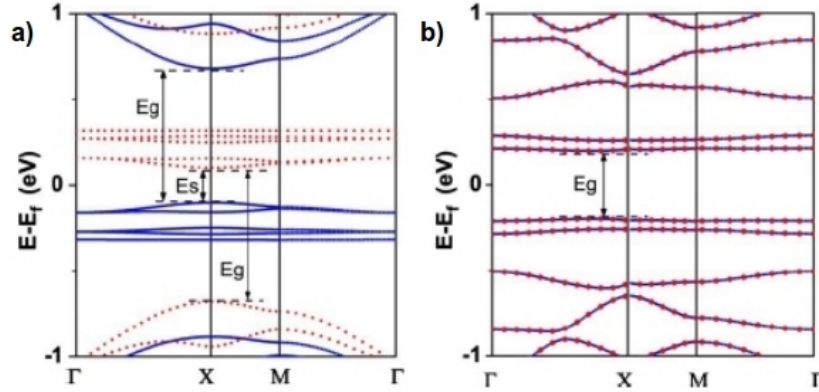
Figure 1.15: a)Spin-polarized band structure of zigzag triangular (T-GNH) nanohole geometry. Red dot and blue line denote spin-up and -down bands in the FM ground state; E_g and E_s are the band gap and spin-splitting gap, respectively. b) Spin-polarized band structure of zigzag rhombus (R-GNH) nanohole geometry. Spin bands are degenerate in the AFM ground state. (Figure adapted from Ref[250]).

Keep this in mind, W. Liu *et.al*[250] found that GNM's with triangular holes have a ferromagnetic (FM) ground state, while GNM's with rhombohedral holes have an anti-ferromagnetic (AFM) ground state as can be seen from the spin-polarized band structures for both the geometries given in Figure 1.15. An detailed study within the *ab-initio* calculation framework on magnetic properties of GNM's was carried out by H-X Yang *et. al*[256] by taking into account the sublattice symmetry of graphene. The study showed that the magnetic behavior of GNM's is dependent on the difference $\Delta_{AB} = |B - A|$ between the number of removed A and B sites to form the hole. For $\Delta_{AB} = 0$ i.e equal A and B sites are removed, GNM's with zigzag-type hole edges exhibit anti-ferromagnetic ground states while GNM's with armchair-type hole edges show a nonmagnetic ground state. However, for $\Delta_{AB} \neq 0$, the GNM's studied showed stable ferromagnetic/ferrimagnetic ground states, implying that magnetism in GNM's can be tuned by varying Δ_{AB}. Moreover, an increase in the spin-splitting gap E_s with increasing Δ_{AB} was also observed which could be exploited for possible applications in spintronics.

The possibility of manipulation of the electronic and magnetic properties make GNM a versatile material for multiple technologies such as nanoelectronics[244, 248], gas sensing[257, 258], electrodes for supercapacitors and batteries[259–261], catalysis[262, 263], spintronics[264, 265], etc. In recent years, proposed methods for achieving stable

and controlled doping of GNM's are being extensively researched which is crucial for the use of GNM's in graphene-based electronics and spintronic devices. Recently, A. A. Maarouf *et.al.*[266] proposed a method wherein controlled passivation of the hole edges followed by chemical doping gave rise to p- and n- doped structures. In a similar spirit, alternate holey two-dimensional structures based on graphene such as the recently synthesized semiconducting nitrogenated-holey graphene[267], are also being researched for their electronic, magnetic, mechanical and thermal properties. A brief background of these materials will be covered in chapter 6 of our thesis.

In chapter 6, we look at two graphene-based holey 2-D structures *viz* nitrogenated holey-graphene and a proposed fluorine-passivated holey graphene. We aim to study the electronic and magnetic properties of these system subject to chemical doping by $3d$ transition-metal atoms.

In the concluding section of this introductory chapter, a brief overview discussing of the remaining chapters of the present thesis is provided.

1.5 Overview of the Thesis

- **Chapter 2**: In this chapter we provide an overview of the primary tools of our work. The materials described in the thesis were generally investigated theoretically within the framework of density functional theory which takes into all the structural and chemical aspects of the material. The details of the basic formalism of density functional theory are provided in the chapter. We also discuss the various basis sets that have been employed for solving the density functional theory hamiltonian. Systems with inherent strong electron-electron correlations for which the density functional theory falls short, were investigated by the model Hamiltonian approach and exact diagonalization method. The description of Lanzcos method for exact diagonalization is also provided in this chapter.

- **Chapter 3** : Using density functional theory we investigated the effect of metal-atom adsorption on the electronic properties of bilayer graphene with the aim to understand formation of local magnetic moments within the system. We have chosen three representative atoms sodium (Na), copper (Cu) and iron (Fe) which belong to the alkali metal and transition metal group. The nature of bonding, the electronic density of states as well as local moment formation is studied systematically for the case of single metal atom adsorption on bilayer graphene. The effect

of an external electric field in regards to the tunability of the magnetic moments is also investigated for all the three cases. Additionally, the case of two Fe atoms adsorbed on bilayer graphene in dimer configuration is also investigated with the aim to study the exchange coupling and it's tunability with respect to applied external electric field.

- **Chapter 4**: Using the extended Hubbard model which takes into account inter-site Coulomb interactions V, the electronic and magnetic properties of nanographene was studied. The exact diagonalization of this model Hamiltonian was used to study the many-body instabilities driven electronic, magnetic and thermodynamic properties. The effect of doping (n) on the properties was also investigated. For our purpose we chose two nanoflakes one with triangular geometry and other with linear stripe geometry. In this way, the effect of geometry was also considered in our study. Our aim was to provide a complete magnetic phase diagram in $n - V$ space for the nanoflakes. The evolution of average charge $\langle n_i \rangle$, average spin $\langle m_i \rangle$, charge-charge correlations and spin-spin correlations as well as finite temperature properties such as magnetization and specific heat with respect to variations in the value of V and n were also extensively studied with the aim to develop a basis for better understanding of the effects of strong electron-electron correlations in nanographene for future studies.

- **Chapter 5**: It has been predicted that while bulk strontium titanate ($SrTiO_3$) cannot stabilize a ferroelectric state, the $SrTiO_3$ (001) surface may host out-of-plane dipole moment due to surface reconstruction resulting in spontaneous electric polarization being exhibited. In this chapter we have investigated, by first principle calculations, the origins behind the formation of out-of-plane dipole moments and thus electric polarization at the TiO_2 terminated surface of $SrTIO_3$ (001). Furthermore, motivated by recent experiments where out-of-plane surface polarization was found at the interface of graphene and $SrTiO_3$, we have also investigated the effect the presence of graphene has on the surface polarization by considering a graphene-$SrTiO_3$ heterostructure geometry which mimics the experimental setup. The effect of an external electric field applied normal to the graphene-$SrTiO_3$ geometry and it's directionality on the surface polarization was also studied with the aim of tuning the electric polarization by external means.

- **Chapter 6** : Employing density functional theory we studied the electronic properties of nitrogenated holey-graphene (C_2N) system and a proposed C_2CF system

obtained by substitution of N atoms in the C_2N geometry with a C-F molecule. With the expectation of promoting local magnetic moment formation, the embedding of single as well as a pair of transition metal (TM) atoms within the C_2N and C_2CF frame was explored for the choice of scandium (Sc) atom. In this regards, the effect of the differential nature of interaction between Sc-N atoms and Sc-F atoms on the site positioning, electronic structure and magnetism was examined. The investigation will extend in future to probe the possibility of manipulating said properties by external means and for the choice of different TM atoms.

- **Chapter 7**: In this last chaper, a concise summary of the main results presented in this thesis is provided along with a future outlook.

1.6 Bibliography

[1]   P. C. Hohenberg *Physical Review*, vol. 158, p. 383, 1967.

[2]   N. D. Mermin *Physical Review*, vol. 176, p. 250, 1968.

[3]   P. Miró, M. Audiffred, and T. Heine *Chemical Society Reviews*, vol. 43, p. 6537, 2014.

[4]   K. S. Novoselov, A. K. Geim, S. V. Morozov, D. Jiang, Y. Zhang, S. V. Dubonos, I. V. Grigorieva, and A. A. Firsov *Science*, vol. 306, p. 666, 2004.

[5]   K. S. Novoselov, A. K. Geim, S. V. Morozov, D. Jiang, M. I. Katsnelson, I. V. Grigorieva, S. V. Dubonos, and A. A. Firsov *Nature*, vol. 438, p. 197, 2005.

[6]   Y. Zhang, Y.-W. Tan, H. L. Stormer, and P. Kim *Nature*, vol. 438, p. 201, 2005.

[7]   A. K. Geim and K. S. Novoselov *Nature Materials*, vol. 6, p. 183, 2007.

[8]   A. A. Balandin, S. Ghosh, W. Bao, I. Calizo, D. Teweldebrhan, F. Miao, and C. N. Lau *Nano Letters*, vol. 8, p. 902, 2008.

[9]   S. Ghosh, I. Calizo, D. Teweldebrhan, E. P. Pokatilov, D. L. Nika, A. A. Balandin, W. Bao, F. Miao, and C. N. Lau *Applied Physics Letters*, vol. 92, p. 151911, 2008.

[10] I. Calizo, A. A. Balandin, W. Bao, F. Miao, and C. N. Lau *Nano Letters*, vol. 7, p. 2645, 2007.

[11] A. A. Balandin *Nature Materials*, vol. 10, p. 569, 2011.

[12] P. R. Wallace *Physical Review*, vol. 71, p. 622, 1947.

[13] B. Partoens and F. M. Peeters *Physical Review B*, vol. 74, p. 075404, 2006.

[14] A. H. Castro Neto, F. Guinea, N. M. R. Peres, K. S. Novoselov, and A. K. Geim *Reviews of Modern Physics*, vol. 81, p. 109, 2009.

[15] K. Watanabe, T. Taniguchi, and H. Kanda *Nature Materials*, vol. 3, p. 404, 2004.

[16] N. Ooi, A. Rairkar, L. Lindsley, and J. B. Adams *Journal of Physics: Condensed Matter*, vol. 18, p. 97, 2006.

[17] K. F. Mak, C. Lee, J. Hone, J. Shan, and T. F. Heinz *Physical Review Letters*, vol. 105, p. 136805, 2010.

[18] S. Lebègue and O. Eriksson *Physical Review B*, vol. 79, p. 115409, 2009.

[19] Y. Ding, Y. Wang, J. Ni, L. Shi, S. Shi, and W. Tang *Physica B Condensed Matter*, vol. 406, p. 2254, 2011.

[20] C. Ataca, H. Şahin, and S. Ciraci *The Journal of Physical Chemistry C*, vol. 116, p. 8983, 2012.

[21] B. Sipos, A. F. Kusmartseva, A. Akrap, H. Berger, L. Forró, and E. Tutiš *Nature Materials*, vol. 7, p. 960, 2008.

[22] N. E. Staley, J. Wu, P. Eklund, Y. Liu, L. Li, and Z. Xu *Physical Review B*, vol. 80, p. 184505, 2009.

[23] M. Chhowalla, H. S. Shin, G. Eda, L.-J. Li, K. P. Loh, and H. Zhang *Nature Chemistry*, vol. 5, p. 263, 2013.

[24] F. Wang, Y. Zhang, C. Tian, C. Girit, A. Zettl, M. Crommie, and Y. R. Shen *Science*, vol. 320, p. 206, 2008.

[25] R. R. Nair, P. Blake, A. N. Grigorenko, K. S. Novoselov, T. J. Booth, T. Stauber, N. M. R. Peres, and A. K. Geim *Science*, vol. 320, p. 1308, 2008.

[26] Q. H. Wang, K. Kalantar-Zadeh, A. Kis, J. N. Coleman, and M. S. Strano *Nature Nanotechnology*, vol. 7, p. 699, 2012.

[27] C. Lee, X. Wei, J. W. Kysar, and J. Hone *Science*, vol. 321, p. 385, 2008.

[28] S. Bertolazzi, J. Brivio, and A. Kis *ACS Nano*, vol. 5, p. 9703, 2011.

[29] M. Ghorbani-Asl, S. Borini, A. Kuc, and T. Heine *Physical Review B*, vol. 87, p. 235434, 2013.

[30] F. Schwierz *Nature Nanotechnology*, vol. 5, p. 487, 2010.

[31] F. Bonaccorso, Z. Sun, T. Hasan, and A. C. Ferrari *Nature Photonics*, vol. 4, p. 611, 2010.

[32] W. Choi, N. Choudhary, G. H. Han, J. Park, D. Akinwande, and Y. H. Lee *Materials Today*, vol. 20, p. 116, 2017.

[33] G. R. Bhimanapati, Z. Lin, V. Meunier, Y. Jung, and *et.al. ACS Nano*, vol. 9, p. 11509, 2015.

[34] A. Splendiani, L. Sun, Y. Zhang, T. Li, J. Kim, C.-Y. Chim, G. Galli, and F. Wang *Nano Letters*, vol. 10, p. 1271, 2010.

[35] G. Eda, H. Yamaguchi, D. Voiry, T. Fujita, M. Chen, and M. Chhowalla *Nano Letters*, vol. 11, p. 5111, 2011.

[36] Y. Wang, Z. Shi, Y. Huang, Y. Ma, C. Wang, M. Chen, and Y. Chen *The Journal of Physical Chemistry C*, vol. 113, p. 13103, 2009.

[37] Q. Ke and J. Wang *Journal of Materiomics*, vol. 2, p. 37, 2016.

[38] M. Pumera, Z. Sofer, and A. Ambrosi *Journal of Materials Chemistry A*, vol. 2, p. 8981, 2014.

[39] M. A. Bissett, S. D. Worrall, I. A. Kinloch, and R. A. Dryfe *Electrochimica Acta*, vol. 201, p. 30, 2016.

[40] C. R. Dean, A. F. Young, I. Meric, C. Lee, L. Wang, S. Sorgenfrei, K. Watanabe, T. Taniguchi, P. Kim, K. L. Shepard, and J. Hone *Nature Nanotechnology*, vol. 5, p. 722, 2010.

[41] E. H. Hwang, S. Adam, and S. Das Sarma *Physical Review B*, vol. 76, p. 195421, 2007.

[42] S. Das Sarma, S. Adam, E. H. Hwang, and E. Rossi *Reviews of Modern Physics*, vol. 83, p. 407, 2011.

[43] E. V. Castro, K. S. Novoselov, S. V. Morozov, N. M. R. Peres, J. M. B. L. Dos Santos, J. Nilsson, F. Guinea, A. K. Geim, and A. H. C. Neto *Physical Review Letters*, vol. 99, p. 216802, 2007.

[44] Y. Zhang, T.-T. Tang, C. Girit, Z. Hao, M. C. Martin, A. Zettl, M. F. Crommie, Y. R. Shen, and F. Wang *Nature*, vol. 459, p. 8203, 2009.

[45] C. H. Lui, Z. Li, K. F. Mak, E. Cappelluti, and T. F. Heinz *Nature Physics*, vol. 7, p. 944, 2011.

[46] K. Tang, R. Qin, J. Zhou, H. Qu, J. Zheng, R. Fei, H. Li, Q. Zheng, Z. Gao, and J. Lu *The Journal of Physical Chemistry C*, vol. 115, p. 9458, 2011.

[47] S.-M. Choi, S.-H. Jhi, and Y.-W. Son *Nano Letters*, vol. 10, p. 3486, 2010.

[48] B. R. K. Nanda and S. Satpathy *Physical Review B*, vol. 80, p. 165430, 2009.

[49] T.-Y. Yang, J. Balakrishnan, F. Volmer, A. Avsar, M. Jaiswal, J. Samm, S. R. Ali, A. Pachoud, M. Zeng, M. Popinciuc, G. Güntherodt, B. Beschoten, and B. Özyilmaz *Physical Review Letters*, vol. 107, p. 047206, 2011.

[50] C. Ertler, S. Konschuh, M. Gmitra, and J. Fabian *Physical Reviews B*, vol. 80, p. 041405, 2009.

[51] N. Tombros, C. Jozsa, M. Popinciuc, H. T. Jonkman, and B. J. van Wees *Nature*, vol. 448, p. 571, 2007.

[52] L. Sun, J. Yan, D. Zhan, L. Liu, H. Hu, H. Li, B. K. Tay, J.-L. Kuo, C.-C. Huang, D. W. Hewak, P. S. Lee, and Z. X. Shen *Physical Review Letters*, vol. 111, p. 126801, 2013.

[53] Z. Y. Zhu, Y. C. Cheng, and U. Schwingenschlögl *Physical Review B*, vol. 84, p. 153402, 2011.

[54] N. Zibouche, A. Kuc, J. Musfeldt, and T. Heine *Annalen der Physik*, vol. 526, p. 395, 2014.

[55] L. Cai, J. He, Q. Liu, T. Yao, L. Chen, W. Yan, F. Hu, Y. Jiang, Y. Zhao, T. Hu, Z. Sun, and S. Wei *Journal of the American Chemical Society*, vol. 137, p. 2622, 2015.

[56] S. Datta and B. Das *Applied Physics Letters*, vol. 56, p. 665, 1990.

[57] L. P. Biró, P. Nemes-Incze, and P. Lambin *Nanoscale*, vol. 4, p. 1824, 2012.

[58] V. Huc, N. Bendiab, N. Rosman, T. Ebbesen, C. Delacour, and V. Bouchiat *Nanotechnology*, vol. 19, p. 455601, 2008.

[59] A. Shukla, R. Kumar, J. Mazher, and A. Balan *Solid State Communications*, vol. 149, p. 718, 2009.

[60] C. Berger, Z. Song, T. Li, X. Li, A. Y. Ogbazghi, R. Feng, Z. Dai, A. N. Marchenkov, E. H. Conrad, P. N. First, and W. A. de Heer *The Journal of Physical Chemistry B*, vol. 108, p. 19912, 2004.

[61] E. Rollings, G.-H. Gweon, S. Zhou, B. Mun, J. McChesney, B. Hussain, A. Fedorov, P. First, W. de Heer, and A. Lanzara *Journal of Physics and Chemistry of Solids*, vol. 67, p. 2172, 2006.

[62] A. Reina, X. Jia, J. Ho, D. Nezich, H. Son, V. Bulovic, M. S. Dresselhaus, and J. Kong* *Nano Letters*, vol. 9, p. 3087, 2009.

[63] X. Li, W. Cai, J. An, S. Kim, J. Nah, D. Yang, R. Piner, A. Velamakanni, I. Jung, E. Tutuc, S. K. Banerjee, L. Colombo, and R. S. Ruoff *Science*, vol. 324, p. 1312, 2009.

[64] A. N. Obraztsov *Nature Nanotechnology*, vol. 4, p. 212, 2009.

[65] Y. Hernandez, V. Nicolosi, M. Lotya, F. M. Blighe, Z. Sun, S. de, I. T. McGovern, B. Holland, M. Byrne, Y. K. Gun'ko, J. J. Boland, P. Niraj, G. Duesberg, S. Krishnamurthy, R. Goodhue, J. Hutchison, V. Scardaci, A. C. Ferrari, and J. N. Coleman *Nature Nanotechnology*, vol. 3, p. 563, 2008.

[66] S. Łoś, L. Duclaux, L. Alvarez, Ł. Hawełek, S. Duber, and W. Kempiński *Carbon*, vol. 55, p. 53, 2013.

[67] T. Ohta, A. Bostwick, T. Seyller, K. Horn, and E. Rotenberg *Science*, vol. 313, p. 951, 2006.

[68] S. Y. Zhou, D. A. Siegel, A. V. Fedorov, and A. Lanzara *Physical Review Letters*, vol. 101, p. 086402, 2008.

[69] A. C. Ferrari, J. C. Meyer, V. Scardaci, C. Casiraghi, M. Lazzeri, F. Mauri, S. Piscanec, D. Jiang, K. S. Novoselov, S. Roth, and A. K. Geim *Physical Review Letters*, vol. 97, p. 187401, 2006.

[70] A. C. Ferrari *Solid State Communications*, vol. 143, p. 47, 2007.

[71] K. I. Bolotin, K. J. Sikes, Z. Jiang, M. Klima, G. Fudenberg, J. Hone, P. Kim, and H. L. Stormer *Solid State Communications*, vol. 146, p. 351, 2008.

[72] V. P. Gusynin and S. G. Sharapov *Physical Review Letters*, vol. 95, p. 146801, 2005.

[73] K. S. Novoselov, Z. Jiang, Y. Zhang, S. V. Morozov, H. L. Stormer, U. Zeitler, J. C. Maan, G. S. Boebinger, P. Kim, and A. K. Geim *Science*, vol. 315, p. 1379, 2007.

[74] Y.-M. Lin, A. Valdes-Garcia, S.-J. Han, D. B. Farmer, I. Meric, Y. Sun, Y. Wu, C. Dimitrakopoulos, A. Grill, P. Avouris, and K. A. Jenkins *Science*, vol. 332, p. 1294, 2011.

[75] F. Schedin, A. K. Geim, S. V. Morozov, E. W. Hill, P. Blake, M. I. Katsnelson, and K. S. Novoselov *Nature Materials*, vol. 6, p. 652, 2007.

[76] S. Bae, H. Kim, Y. Lee, X. Xu, J.-S. Park, Y. Zheng, J. Balakrishnan, T. Lei, H. Ri Kim, Y. I. Song, Y.-J. Kim, K. S. Kim, B. Özyilmaz, J.-H. Ahn, B. H. Hong, and S. Iijima *Nature Nanotechnology*, vol. 5, p. 574, 2010.

[77] K. S. Kim, Y. Zhao, H. Jang, S. Y. Lee, J. M. Kim, K. S. Kim, J.-H. Ahn, P. Kim, J.-Y. Choi, and B. H. Hong *nature*, vol. 457, p. 706, 2009.

[78] X. Wang, L. Zhi, and K. Müllen *Nano Letters*, vol. 8, p. 323, 2008.

[79] X. Cai, L. Lai, Z. Shen, and J. Lin *Journal of Materials Chemistry A*, vol. 5, p. 15423, 2017.

[80] X. Huang, X. Qi, F. Boey, and H. Zhang *Chemical Society Reviews*, vol. 41, p. 666, 2012.

[81] M. Takahashi, P. Turek, Y. Nakazawa, M. Tamura, K. Nozawa, D. Shiomi, M. Ishikawa, and M. Kinoshita *Physical Review Letters*, vol. 67, p. 746, 1991.

[82] M. Tamura, Y. Nakazawa, D. Shiomi, K. Nozawa, Y. Hosokoshi, M. Ishikawa, M. Takahashi, and M. Kinoshita *Chemical Physics Letters*, vol. 186, p. 401, 1991.

[83] P.-M. Allemand, K. C. Khemani, A. Koch, F. Wudl, K. Holczer, S. Donovan, G. Gruner, and J. D. Thompson *Science*, vol. 253, p. 301, 1991.

[84] P. Esquinazi, D. Spemann, R. Höhne, A. Setzer, K.-H. Han, and T. Butz *Physical Review Letters*, vol. 91, p. 227201, 2003.

[85] D. M. Edwards and M. I. Katsnelson *Journal of Physics Condensed Matter*, vol. 18, p. 7209, 2006.

[86] O. V. Yazyev and M. I. Katsnelson *Physical Review Letters*, vol. 100, p. 047209, 2008.

[87] B. Trauzettel, D. V. Bulaev, D. Loss, and G. Burkard *Nature Physics*, vol. 3, p. 192, 2007.

[88] J. Fischer, B. Trauzettel, and D. Loss *Physical Review B*, vol. 80, p. 155401, 2009.

[89] O. V. Yazyev *Nano Letters*, vol. 8, p. 1011, 2008.

[90] M. V. Kamalakar, C. Groenveld, A. Dankert, and S. P. Dash *Nature Communications*, vol. 6, p. 6766, 2015.

[91] M. Sepioni, R. R. Nair, S. Rablen, J. Narayanan, F. Tuna, R. Winpenny, A. K. Geim, and I. V. Grigorieva *Physical Review Letters*, vol. 105, p. 207205, 2010.

[92] S. Sorella and E. Tosatti *EPL (Europhysics Letters)*, vol. 19, p. 699, 1992.

[93] L. M. Martelo, M. Dzierzawa, L. Siffert, and D. Baeriswyl *Zeitschrift fur Physik B Condensed Matter*, vol. 103, p. 335, 1997.

[94] Y. Shibayama, H. Sato, T. Enoki, and M. Endo *Physical Review Letters*, vol. 84, p. 1744, 2000.

[95] T. Enoki and K. Takai *Solid State Communications*, vol. 149, p. 1144, 2009.

[96] P. Esquinazi, A. Setzer, R. Höhne, C. Semmelhack, Y. Kopelevich, D. Spemann, T. Butz, B. Kohlstrunk, and M. Lösche *Physical Review B*, vol. 66, p. 024429, 2002.

[97] J. Červenka, M. I. Katsnelson, and C. F. J. Flipse *Nature Physics*, vol. 5, p. 840, 2009.

[98] E. H. Lieb *Physical Review Letters*, vol. 62, p. 1201, 1989.

[99] O. V. Yazyev and L. Helm *Physical Review B*, vol. 75, p. 125408, 2007.

[100] H. González-Herrero, J. M. Gómez-Rodríguez, P. Mallet, M. Moaied, J. J. Palacios, C. Salgado, M. M. Ugeda, J.-Y. Veuillen, F. Yndurain, and I. Brihuega *Science*, vol. 352, p. 437, 2016.

[101] O. V. Yazyev *Physical Review Letters*, vol. 101, p. 037203, 2008.

[102] J. J. Palacios, J. Fernández-Rossier, and L. Brey *Physical Review B*, vol. 77, p. 195428, 2008.

[103] V. M. Pereira, F. Guinea, J. M. B. Lopes dos Santos, N. M. R. Peres, and A. H. Castro Neto *Physical Review Letters*, vol. 96, p. 036801, 2006.

[104] M. M. Ugeda, I. Brihuega, F. Guinea, and J. M. Gómez-Rodríguez *Physical Review Letters*, vol. 104, p. 096804, 2010.

[105] Y. Zhang, S.-Y. Li, H. Huang, W.-T. Li, J.-B. Qiao, W.-X. Wang, L.-J. Yin, K.-K. Bai, W. Duan, and L. He *Physical Review Letters*, vol. 117, p. 166801, 2016.

[106] K. Nakada, M. Fujita, G. Dresselhaus, and M. S. Dresselhaus *Physical Review B*, vol. 54, p. 17954, 1996.

[107] V. Barone, O. Hod, and G. E. Scuseria *Nano Letters*, vol. 6, p. 2748, 2006.

[108] M. Ezawa *Physical Review B*, vol. 73, p. 045432, 2006.

[109] L. Brey and H. A. Fertig *Physical Review B*, vol. 73, p. 235411, 2006.

[110] Y.-W. Son, M. L. Cohen, and S. G. Louie *Physical Review Letters*, vol. 97, p. 216803, 2006.

[111] K.-i. Sakai, K. Takai, K.-i. Fukui, T. Nakanishi, and T. Enoki *Physical Review B*, vol. 81, p. 235417, 2010.

[112] Y. Kobayashi, K.-i. Fukui, T. Enoki, K. Kusakabe, and Y. Kaburagi *Physical Review B*, vol. 71, p. 193406, 2005.

[113] T. Enoki, S. Fujii, and K. Takai *Carbon*, vol. 50, p. 3141, 2012.

[114] V. L. J. Joly, M. Kiguchi, S.-J. Hao, K. Takai, T. Enoki, R. Sumii, K. Amemiya, H. Muramatsu, T. Hayashi, Y. A. Kim, M. Endo, J. Campos-Delgado, F. López-Urías, A. Botello-M
endez, H. Terrones, M. Terrones, and M. S. Dresselhaus *Physical Review B*, vol. 81, p. 245428, 2010.

[115] G. Z. Magda, X. Jin, I. Hagymási, P. Vancsó, Z. Osváth, P. Nemes-Incze, C. Hwang, L. P. Biró, and L. Tapasztó *Nature*, vol. 514, p. 608, 2014.

[116] M. Y. Han, B. Özyilmaz, Y. Zhang, and P. Kim *Physical Review Letters*, vol. 98, p. 206805, 2007.

[117] M. C. Lemme, D. C. Bell, J. R. Williams, L. A. Stern, B. W. H. Baugher, P. Jarillo-Herrero, and C. M. Marcus *ACS Nano*, vol. 3, p. 2674, 2009.

[118] L. Tapasztó, G. Dobrik, P. Lambin, and L. P. Biró *Nature Nanotechnology*, vol. 3, p. 397, 2008.

[119] X. Li, X. Wang, L. Zhang, S. Lee, and H. Dai *science*, vol. 319, p. 1229, 2008.

[120] J. Campos-Delgado, J. M. Romo-Herrera, X. Jia, D. A. Cullen, H. Muramatsu, Y. A. Kim, T. Hayashi, Z. Ren, D. J. Smith, Y. Okuno, *et al. Nano Letters*, vol. 8, p. 2773, 2008.

[121] R. M. Jacobberger, B. Kiraly, M. Fortin-Deschenes, P. L. Levesque, K. M. McElhinny, G. J. Brady, R. R. Delgado, S. S. Roy, A. Mannix, M. G. Lagally, *et al. Nature communications*, vol. 6, p. 8006, 2015.

[122] L. Jiao, X. Wang, G. Diankov, H. Wang, and H. Dai *Nature Nanotechnology*, vol. 5, p. 321, 2010.

[123] L. Jiao, L. Zhang, X. Wang, G. Diankov, and H. Dai *Nature*, vol. 458, p. 877, 2009.

[124] M. Fujita, K. Wakabayashi, K. Nakada, and K. Kusakabe *Journal of the Physical Society of Japan*, vol. 65, p. 1920, 1996.

[125] K. Wakabayashi, M. Fujita, H. Ajiki, and M. Sigrist *Physical Review B*, vol. 59, p. 8271, 1999.

[126] Y. Miyamoto, K. Nakada, and M. Fujita *Physical Review B*, vol. 59, p. 9858, 1999.

[127] Y. Hao, Y. Wang, L. Wang, Z. Ni, Z. Wang, R. Wang, C. K. Koo, Z. Shen, and J. T. Thong *small*, vol. 6, p. 195, 2010.

[128] C. H. Lui, Z. Li, Z. Chen, P. V. Klimov, L. E. Brus, and T. F. Heinz *Nano Letters*, vol. 11, p. 164, 2010.

[129] W. Norimatsu and M. Kusunoki *Physical Review B*, vol. 81, p. 161410, 2010.

[130] C. Cong, T. Yu, K. Sato, J. Shang, R. Saito, G. F. Dresselhaus, and M. S. Dresselhaus *ACS Nano*, vol. 5, p. 8760, 2011.

[131] L. Gao *Graphene and 2D Materials*, vol. 1, 2014.

[132] Y. Zhang, T.-T. Tang, C. Girit, Z. Hao, M. C. Martin, A. Zettl, M. F. Crommie, Y. R. Shen, and F. Wang *Nature*, vol. 459, p. 820, 2009.

[133] E. V. Castro, K. Novoselov, S. Morozov, N. Peres, J. L. Dos Santos, J. Nilsson, F. Guinea, A. Geim, and A. C. Neto *Physical Review Letters*, vol. 99, p. 216802, 2007.

[134] T. Ohta, A. Bostwick, T. Seyller, K. Horn, and E. Rotenberg *Science*, vol. 313, p. 951, 2006.

[135] A. Avetisyan, B. Partoens, and F. Peeters *Physical Review B*, vol. 81, p. 115432, 2010.

[136] J. Nilsson, A. H. Castro Neto, F. Guinea, and N. M. R. Peres *Physical Review B*, vol. 78, p. 045405, 2008.

[137] M. Aoki and H. Amawashi *Solid State Communications*, vol. 142, p. 123, 2007.

[138] K. Tang, R. Qin, J. Zhou, H. Qu, J. Zheng, R. Fei, H. Li, Q. Zheng, Z. Gao, and J. Lu *The Journal of Physical Chemistry C*, vol. 115, p. 9458, 2011.

[139] M. Koshino *Physical Review B*, vol. 81, p. 125304, 2010.

[140] K. F. Mak, J. Shan, and T. F. Heinz *Physical Review Letters*, vol. 104, p. 176404, 2010.

[141] M. Craciun, S. Russo, M. Yamamoto, J. B. Oostinga, A. Morpurgo, and S. Tarucha *Nature Nanotechnology*, vol. 4, p. 383, 2009.

[142] W. Bao, L. Jing, J. Velasco Jr, Y. Lee, G. Liu, D. Tran, B. Standley, M. Aykol, S. Cronin, D. Smirnov, *et al. Nature Physics*, vol. 7, p. 948, 2011.

[143] E. McCann *Physical Review B*, vol. 74, p. 161403, 2006.

[144] E. V. Castro, K. S. Novoselov, S. V. Morozov, N. M. R. Peres, J. M. B. Lopes dos Santos, J. Nilsson, F. Guinea, A. K. Geim, and A. H. Castro Neto *Journal of Physics Condensed Matter*, vol. 22, p. 175503, 2010.

[145] F. Zhang, B. Sahu, H. Min, and A. H. MacDonald *Physical Review B*, vol. 82, p. 035409, 2010.

[146] E. Yu, D. Stewart, and S. Tiwari *Physical Review B*, vol. 77, p. 195406, 2008.

[147] B. N. Szafranek, D. Schall, M. Otto, D. Neumaier, and H. Kurz *Nano Letters*, vol. 11, p. 2640, 2011.

[148] W. J. Yu, L. Liao, S. H. Chae, Y. H. Lee, and X. Duan *Nano Letters*, vol. 11, p. 4759, 2011.

[149] F. Yavari, C. Kritzinger, C. Gaire, L. Song, H. Gulapalli, T. Borca-Tasciuc, P. M. Ajayan, and N. Koratkar *small*, vol. 6, p. 2535, 2010.

[150] R. Quhe, J. Ma, Z. Zeng, K. Tang, J. Zheng, Y. Wang, Z. Ni, L. Wang, Z. Gao, J. Shi, *et al. Scientific reports*, vol. 3, p. 1794, 2013.

[151] S. Ghosh, W. Bao, D. L. Nika, S. Subrina, E. P. Pokatilov, C. N. Lau, and A. A. Balandin *Nature materials*, vol. 9, p. 555, 2010.

[152] D. Singh, J. Y. Murthy, and T. S. Fisher *Journal of Applied Physics*, vol. 110, p. 044317, 2011.

[153] H. Goto, A. Kanda, T. Sato, S. Tanaka, Y. Ootuka, S. Odaka, H. Miyazaki, K. Tsuk-agoshi, and Y. Aoyagi *Applied Physics Letters*, vol. 92, p. 212110, 2008.

[154] O. V. Yazyev *Reports on Progress in Physics*, vol. 73, p. 056501, 2010.

[155] S. Dutta and S. K. Pati *Journal of Materials Chemistry*, vol. 20, p. 8207, 2010.

[156] S. S. Datta, D. R. Strachan, S. M. Khamis, and A. C. Johnson *Nano Letters*, vol. 8, p. 1912, 2008.

[157] X. Wang, Y. Ouyang, X. Li, H. Wang, J. Guo, and H. Dai *Physical Review Letters*, vol. 100, p. 206803, 2008.

[158] N. G. Shang, P. Papakonstantinou, M. McMullan, M. Chu, A. Stamboulis, A. Potenza, S. S. Dhesi, and H. Marchetto *Advanced functional materials*, vol. 18, p. 3506, 2008.

[159] J. Cai, P. Ruffieux, R. Jaafar, M. Bieri, T. Braun, S. Blankenburg, M. Muoth, A. P. Seitsonen, M. Saleh, X. Feng, *et al. Nature*, vol. 466, p. 470, 2010.

[160] H. Huang, D. Wei, J. Sun, S. L. Wong, Y. P. Feng, A. C. Neto, and A. T. S. Wee *Scientific reports*, vol. 2, p. 983, 2012.

[161] D. Geng, B. Wu, Y. Guo, L. Huang, Y. Xue, J. Chen, G. Yu, L. Jiang, W. Hu, and Y. Liu *Proceedings of the National Academy of Sciences*, 2012.

[162] N. Hong, S. Nie, L. Song, Q. Tai, P. Zhang, B. Wang, X. Qian, and Y. Hu *Materials Letters*, vol. 65, p. 2707, 2011.

[163] K. Wakabayashi, M. Fujita, H. Ajiki, and M. Sigrist *Physical Review B*, vol. 59, p. 8271, 1999.

[164] J. Fernández-Rossier *Physical Review B*, vol. 77, p. 075430, 2008.

[165] Y.-W. Son, M. L. Cohen, and S. G. Louie *Nature*, vol. 444, p. 347, 2006.

[166] L. Pisani, J. Chan, B. Montanari, and N. Harrison *Physical Review B*, vol. 75, p. 064418, 2007.

[167] E. C. Stoner *Proceedings of the Royal Society of London Series A*, vol. 165, p. 372, 1938.

[168] E.-J. Kan, Z. Li, J. Yang, and J. Hou *Applied Physics Letters*, vol. 91, p. 243116, 2007.

[169] H. Raza and E. C. Kan *Physical Review B*, vol. 77, p. 245434, 2008.

[170] J. Jung and A. H. MacDonald *Physical Review B*, vol. 79, p. 235433, 2009.

[171] K. Sawada, F. Ishii, M. Saito, S. Okada, and T. Kawai *Nano Letters*, vol. 9, p. 269, 2008.

[172] D. Gunlycke, J. Li, J. Mintmire, and C. White *Applied Physics Letters*, vol. 91, p. 112108, 2007.

[173] O. Hod, V. Barone, J. E. Peralta, and G. E. Scuseria *Nano Letters*, vol. 7, p. 2295, 2007.

[174] Y.-W. Tan, Y. Zhang, K. Bolotin, Y. Zhao, S. Adam, E. Hwang, S. D. Sarma, H. Stormer, and P. Kim *Physical Review Letters*, vol. 99, p. 246803, 2007.

[175] J. Yan and M. S. Fuhrer *Physical Review Letters*, vol. 107, p. 206601, 2011.

[176] S. Cho and M. S. Fuhrer *Physical Review B*, vol. 77, p. 081402, 2008.

[177] E. Rossi, S. Adam, and S. D. Sarma *Physical Review B*, vol. 79, p. 245423, 2009.

[178] J.-H. Chen, C. Jang, S. Xiao, M. Ishigami, and M. S. Fuhrer *Nature Nanotechnology*, vol. 3, p. 206, 2008.

[179] E. Hwang and S. D. Sarma *Physical Review B*, vol. 77, p. 115449, 2008.

[180] S. Fratini and F. Guinea *Physical Review B*, vol. 77, p. 195415, 2008.

[181] M. Ishigami, J. Chen, W. Cullen, M. Fuhrer, and E. Williams *Nano Letters*, vol. 7, p. 1643, 2007.

[182] S. Morozov, K. Novoselov, M. Katsnelson, F. Schedin, D. Elias, J. A. Jaszczak, and A. Geim *Physical Review Letters*, vol. 100, p. 016602, 2008.

[183] J. Martin, N. Akerman, G. Ulbricht, T. Lohmann, J. v. Smet, K. Von Klitzing, and A. Yacoby *Nature Physics*, vol. 4, p. 144, 2008.

[184] P. Sutter, J. T. Sadowski, and E. Sutter *Physical Review B*, vol. 80, p. 245411, 2009.

[185] M. Gao, Y. Pan, L. Huang, H. Hu, L. Zhang, H. Guo, S. Du, and H.-J. Gao *Applied Physics Letters*, vol. 98, p. 033101, 2011.

[186] E. Cazzanelli, T. Caruso, M. Castriota, A. Marino, A. Politano, G. Chiarello, M. Giarola, and G. Mariotto *Journal of Raman Spectroscopy*, vol. 44, p. 1393, 2013.

[187] H. Zhang, Q. Fu, Y. Cui, D. Tan, and X. Bao *The Journal of Physical Chemistry C*, vol. 113, p. 8296, 2009.

[188] S. Marchini, S. Günther, and J. Wintterlin *Physical Review B*, vol. 76, p. 075429, 2007.

[189] Y. Pan, H. Zhang, D. Shi, J. Sun, S. Du, F. Liu, and H.-j. Gao *Advanced Materials*, vol. 21, p. 2777, 2009.

[190] J. Coraux, M. Engler, C. Busse, D. Wall, N. Buckanie, F.-J. M. Zu Heringdorf, R. Van Gastel, B. Poelsema, T. Michely, *et al. New Journal of Physics*, vol. 11, p. 023006, 2009.

[191] J. Coraux, T. N. Plasa, C. Busse, T. Michely, *et al. New Journal of Physics*, vol. 10, p. 043033, 2008.

[192] M. Kralj, I. Pletikosić, M. Petrović, P. Pervan, M. Milun, C. Busse, T. Michely, J. Fujii, I. Vobornik, *et al. Physical Review B*, vol. 84, p. 075427, 2011.

[193] J. Lahiri, T. Miller, L. Adamska, I. I. Oleynik, and M. Batzill *Nano Letters*, vol. 11, p. 518, 2010.

[194] R. Addou, A. Dahal, P. Sutter, and M. Batzill *Applied Physics Letters*, vol. 100, p. 021601, 2012.

[195] G. Odahara, S. Otani, C. Oshima, M. Suzuki, T. Yasue, and T. Koshikawa *Surface Science*, vol. 605, p. 1095, 2011.

[196] G. Odahara, S. Otani, C. Oshima, M. Suzuki, T. Yasue, and T. Koshikawa *Surface Science*, vol. 605, p. 1095, 2011.

[197] T. C. Nguyen, M. Otani, and S. Okada *Physical Review Letters*, vol. 106, p. 106801, 2011.

[198] X. Fan, W. Zheng, V. Chihaia, Z. Shen, and J.-L. Kuo *Journal of Physics: Condensed Matter*, vol. 24, p. 305004, 2012.

[199] Y. Y. Wang, Z. H. Ni, T. Yu, Z. X. Shen, H. M. Wang, Y. H. Wu, W. Chen, and A. T. Shen Wee *The Journal of Physical Chemistry C*, vol. 112, p. 10637, 2008.

[200] H. Zi-Pu, D. Ogletree, M. Van Hove, and G. Somorjai *Surface Science*, vol. 180, p. 433, 1987.

[201] P. Khomyakov, G. Giovannetti, P. Rusu, G. v. Brocks, J. Van den Brink, and P. J. Kelly *Physical Review B*, vol. 79, p. 195425, 2009.

[202] C. Busse, P. Lazić, R. Djemour, J. Coraux, T. Gerber, N. Atodiresei, V. Caciuc, R. Brako, S. Blügel, J. Zegenhagen, *et al. Physical Review Letters*, vol. 107, p. 036101, 2011.

[203] R. Brako, D. Šokčević, P. Lazić, and N. Atodiresei *New Journal of Physics*, vol. 12, p. 113016, 2010.

[204] S. Bleikamp, P. J. Feibelman, T. Michely, *et al. Physical Review Letters*, vol. 97, p. 215501, 2006.

[205] K. V. Emtsev, F. Speck, T. Seyller, L. Ley, and J. D. Riley *Physical Review B*, vol. 77, p. 155303, 2008.

[206] A. Mattausch and O. Pankratov *Physical Review Letters*, vol. 99, p. 076802, 2007.

[207] F. Varchon, R. Feng, J. Hass, X. Li, B. N. Nguyen, C. Naud, P. Mallet, J.-Y. Veuillen, C. Berger, E. H. Conrad, *et al. Physical Review Letters*, vol. 99, p. 126805, 2007.

[208] P. W. Sutter, J.-I. Flege, and E. A. Sutter *Nature materials*, vol. 7, p. 406, 2008.

[209] D.-e. Jiang, M.-H. Du, and S. Dai *The Journal of chemical physics*, vol. 130, p. 074705, 2009.

[210] D. Martoccia, M. Björck, C. Schlepütz, T. Brugger, S. Pauli, B. Patterson, T. Greber, and P. Willmott *New Journal of Physics*, vol. 12, p. 043028, 2010.

[211] S. Marchini, S. Günther, and J. Wintterlin *Physical Review B*, vol. 76, p. 075429, 2007.

[212] V. Karpan, G. Giovannetti, P. Khomyakov, M. Talanana, A. Starikov, M. Zwierzycki, J. Van Den Brink, G. Brocks, and P. J. Kelly *Physical Review Letters*, vol. 99, p. 176602, 2007.

[213] G. Bertoni, L. Calmels, A. Altibelli, and V. Serin *Physical Review B*, vol. 71, p. 075402, 2005.

[214] Y. Gamo, A. Nagashima, M. Wakabayashi, M. Terai, and C. Oshima *Surface Science*, vol. 374, p. 61, 1997.

[215] A. Dahal and M. Batzill *Nanoscale*, vol. 6, p. 2548, 2014.

[216] T. Aizawa, R. Souda, Y. Ishizawa, H. Hirano, T. Yamada, K.-i. Tanaka, and C. Oshima *Surface Science*, vol. 237, p. 194, 1990.

[217] A. Shikin, D. Farıas, V. Adamchuk, and K.-H. Rieder *Surface science*, vol. 424, p. 155, 1999.

[218] T. Aizawa, Y. Hwang, W. Hayami, R. Souda, S. Otani, and Y. Ishizawa *Surface science*, vol. 260, p. 311, 1992.

[219] A. Shikin, G. Prudnikova, V. Adamchuk, F. Moresco, and K.-H. Rieder *Physical Review B*, vol. 62, p. 13202, 2000.

[220] J. Chen, G. Zhang, and B. Li *Nanoscale*, vol. 5, p. 532, 2013.

[221] Z.-Y. Ong and E. Pop *Physical Review B*, vol. 84, p. 075471, 2011.

[222] S. Koniakhin, O. Utesov, I. Terterov, and A. Nalitov *Physical Review B*, vol. 95, p. 045418, 2017.

[223] Y. Shi, X. Dong, P. Chen, J. Wang, and L.-J. Li *Physical Review B*, vol. 79, p. 115402, 2009.

[224] Y.-J. Kang, J. Kang, and K.-J. Chang *Physical Review B*, vol. 78, p. 115404, 2008.

[225] M. Gao, Y. Pan, C. Zhang, H. Hu, R. Yang, H. Lu, J. Cai, S. Du, F. Liu, and H.-J. Gao *Applied Physics Letters*, vol. 96, p. 053109, 2010.

[226] S. Y. Zhou, G.-H. Gweon, A. Fedorov, d. First, PN, W. De Heer, D.-H. Lee, F. Guinea, A. C. Neto, and A. Lanzara *Nature materials*, vol. 6, p. 770, 2007.

[227] S. Sung, S. Kim, P. Lee, J. Kim, M. Ryu, H. Park, K. Kim, B. I. Min, and J. Chung *Nanotechnology*, vol. 28, p. 205201, 2017.

[228] C. Enderlein, Y. Kim, A. Bostwick, E. Rotenberg, and K. Horn *New Journal of Physics*, vol. 12, p. 033014, 2010.

[229] A. Varykhalov, M. Scholz, T. K. Kim, and O. Rader *Physical Review B*, vol. 82, p. 121101, 2010.

[230] M. Hasegawa, K. Nishidate, T. Hosokai, and N. Yoshimoto *Physical Review B*, vol. 87, p. 085439, 2013.

[231] S. G. Kwon and M. H. Kang *Journal of the Korean Physical Society*, vol. 61, p. 589, 2012.

[232] J. Warmuth, A. Bruix, M. Michiardi, T. Hänke, M. Bianchi, J. Wiebe, R. Wiesendanger, B. Hammer, P. Hofmann, and A. A. Khajetoorians *Physical Review B*, vol. 93, p. 165437, 2016.

[233] H. Vita, S. Böttcher, K. Horn, E. Voloshina, R. Ovcharenko, T. Kampen, A. Thissen, and Y. S. Dedkov *Scientific reports*, vol. 4, p. 5704, 2014.

[234] J. Brede, J. Sławińska, M. Abadia, C. Rogero, J. E. Ortega, I. Piquero-Zulaica, J. Lobo-Checa, A. Arnau, and J. I. Cerdá *2D Materials*, vol. 4, p. 015016, 2016.

[235] S. Sonde, F. Giannazzo, C. Vecchio, R. Yakimova, E. Rimini, and V. Raineri *Applied Physics Letters*, vol. 97, p. 132101, 2010.

[236] X. Hong *Journal of Physics: Condensed Matter*, vol. 28, p. 103003, 2016.

[237] A. Lipatov, A. Fursina, T. H. Vo, P. Sharma, A. Gruverman, and A. Sinitskii *Advanced Electronic Materials*, vol. 3, p. 1700020, 2017.

[238] X. Hong, A. Posadas, K. Zou, C. Ahn, and J. Zhu *Physical Review Letters*, vol. 102, p. 136808, 2009.

[239] C. Baeumer, S. P. Rogers, R. Xu, L. W. Martin, and M. Shim *Nano Letters*, vol. 13, p. 1693, 2013.

[240] A. Rajapitamahuni, J. Hoffman, C. Ahn, and X. Hong *Nano Letters*, vol. 13, p. 4374, 2013.

[241] W. Jie, Y. Y. Hui, N. Y. Chan, Y. Zhang, S. P. Lau, and J. Hao *The Journal of Physical Chemistry C*, vol. 117, p. 13747, 2013.

[242] S. Raghavan, I. Stolichnov, N. Setter, J.-S. Heron, M. Tosun, and A. Kis *Applied Physics Letters*, vol. 100, p. 023507, 2012.

[243] A. Konar, T. Fang, and D. Jena *Physical Review B*, vol. 82, p. 115452, 2010.

[244] J. Bai, X. Zhong, S. Jiang, Y. Huang, and X. Duan *Nature Nanotechnology*, vol. 5, p. 190, 2010.

[245] H. Şahin and S. Ciraci *Physical Review B*, vol. 84, p. 035452, 2011.

[246] M. Kim, N. S. Safron, E. Han, M. S. Arnold, and P. Gopalan *Nano Letters*, vol. 10, p. 1125, 2010.

[247] A. Sinitskii and J. M. Tour *Journal of the American Chemical Society*, vol. 132, p. 14730, 2010.

[248] X. Liang, Y.-S. Jung, S. Wu, A. Ismach, D. L. Olynick, S. Cabrini, and J. Bokor *Nano Letters*, vol. 10, p. 2454, 2010.

[249] T. G. Pedersen, C. Flindt, J. Pedersen, N. A. Mortensen, A.-P. Jauho, and K. Pedersen *Physical Review Letters*, vol. 100, p. 136804, 2008.

[250] W. Liu, Z. Wang, Q. Shi, J. Yang, and F. Liu *Physical Review B*, vol. 80, p. 233405, 2009.

[251] F. Ouyang, S. Peng, Z. Liu, and Z. Liu *ACS Nano*, vol. 5, p. 4023, 2011.

[252] A. Zhang, H. F. Teoh, Z. Dai, Y. P. Feng, and C. Zhang *Applied Physics Letters*, vol. 98, p. 023105, 2011.

[253] W. Oswald and Z. Wu *Physical Review B*, vol. 85, p. 115431, 2012.

[254] H. Jippo, M. Ohfuchi, and C. Kaneta *Physical Review B*, vol. 84, p. 075467, 2011.

[255] Z. Wang, Q. Li, H. Zheng, H. Ren, H. Su, Q. Shi, and J. Chen *Physical Review B*, vol. 75, p. 113406, 2007.

[256] H.-X. Yang, M. Chshiev, D. W. Boukhvalov, X. Waintal, and S. Roche *Physical Review B*, vol. 84, p. 214404, 2011.

[257] R. K. Paul, S. Badhulika, N. M. Saucedo, and A. Mulchandani *Analytical chemistry*, vol. 84, p. 8171, 2012.

[258] A. Esfandiar, N. J. Kybert, E. N. Dattoli, G. Hee Han, M. B. Lerner, O. Akhavan, A. Irajizad, and A. Charlie Johnson *Applied Physics Letters*, vol. 103, p. 183110, 2013.

[259] J. Yan, Z. Fan, W. Sun, G. Ning, T. Wei, Q. Zhang, R. Zhang, L. Zhi, and F. Wei *Advanced Functional Materials*, vol. 22, p. 2632, 2012.

[260] Z. Fan, J. Yan, G. Ning, T. Wei, L. Zhi, and F. Wei *Carbon*, vol. 60, p. 558, 2013.

[261] X. Zhu, X. Song, X. Ma, and G. Ning *ACS applied materials & interfaces*, vol. 6, p. 7189, 2014.

[262] X. Lv, W. Lv, W. Wei, X. Zheng, C. Zhang, L. Zhi, and Q.-H. Yang *Chemical Communications*, vol. 51, p. 3911, 2015.

[263] T. Palaniselvam, H. B. Aiyappa, and S. Kurungot *Journal of Materials Chemistry*, vol. 22, p. 23799, 2012.

[264] J. Haruyama *Electronics*, vol. 2, p. 368, 2013.

[265] T. G. Pedersen, C. Flindt, J. Pedersen, N. A. Mortensen, A.-P. Jauho, and K. Pedersen *Physical Review Letters*, vol. 100, p. 136804, 2008.

[266] A. A. Maarouf, R. A. Nistor, A. Afzali-Ardakani, M. A. Kuroda, D. M. Newns, and G. J. Martyna *Journal of chemical theory and computation*, vol. 9, p. 2398, 2013.

[267] J. Mahmood, E. K. Lee, M. Jung, D. Shin, I.-Y. Jeon, S.-M. Jung, H.-J. Choi, J.-M. Seo, S.-Y. Bae, S.-D. Sohn, *et al. Nature communications*, vol. 6, p. 6486, 2015.

In this chapter we discuss the different methods and techniques used in our investigation of the electronic and magnetic properties of graphene-based systems. Depending on the physical specifications of the system under study we have chosen either the *ab-initio* density functional techniques or the model Hamiltonian approach which were solved using exact diagonalization scheme. Though the various methods may differ in the approaches used for their formulation, the objective is exactly same *viz* the solution of the fundamental many-body Hamiltonian which describes all forms of matter. We, thus, open the discussion by stating the the many-body Hamiltonian, following which we provide details of the various methods that were primarily used for the studies presented in the thesis.

2.1   The Many Body Hamiltonian

Matter is made up of atoms and the properties of matter are a result of the various interactions between the atoms. According to quantum mechanical theory, the microscopic behavior of an ensemble of atoms can be described by a system of electrons and nuclei, the constituent elements of an atom, interacting *via* electrostatic (Coulombic) forces. Hence, in general any form of matter, whether it be solid or liquid or gaseous, can be represented by the many-body Hamiltonian given by

$$(2.1) \quad \hat{H} = -\sum_{I}^{N_a} \frac{\hbar^2}{2M_I}\nabla_I^2 - \sum_{i}^{N_e} \frac{\hbar^2}{2m_i}\nabla_i^2 + \frac{e^2}{2}\sum_{I=1}^{N_a}\sum_{J\neq I}^{N_a}\frac{Z_I Z_J}{|R_I - R_J|} + \frac{e^2}{2}\sum_{i=1}^{N_e}\sum_{j\neq i}^{N_e}\frac{1}{|r_i - r_j|} - e^2\sum_{I=1}^{N_a}\sum_{i=1}^{N_e}\frac{Z_I}{|R_I - r_i|}$$

where $\{R_I\}, I = 1, \cdots, N_a$ are the set of N_a nuclear coordinates and $\{r_i\}, i = 1, \cdots, N_e$ are the set of N_e electron coordinates. M_I and m_i are the nuclear and electron masses carrying charges Z_I and e respectively.

In principle, the Schrödinger equation given by

$$(2.2) \qquad\qquad\qquad \hat{H}\hat{\psi}(\mathbf{r}, \mathbf{R}) = E\hat{\psi}(\mathbf{r}, \mathbf{R})$$

provides an exact description for the many-body system of electrons and nuclei, where $\hat{H}$ is the Hamiltonian of Eqn (2.1), $\mathbf{r} = \{r_i\}$ and $\mathbf{R} = \{R_I\}$ and $\hat{\psi}$ represents the total many-body wave-function. Therefore, it is expected that by solving the Schrödinger equation within the full quantum mechanical framework, all the properties of the system can be obtained. In reality, however, solving the Schrödinger's equation using either analytical methods or numerical approaches is non trivial since one has to deal with $3N_a + 3N_e$ coupled degrees of freedom which makes Eqn (2.1) very difficult to solve except for a few simple cases such as the isolated hydrogen atom.

One of the crucial role of computational materials science is the development of simulation techniques that allows one to tackle the many-body Schrödinger's equation in practice and provide reliable results for the properties of a broad range of materials. In principle this can be achieved mainly in two ways

1. By applying some sensible approximations such as the Born-Oppenheimer Approximation and Independent electron approximation that allow the full many-body wave-function $\hat{\psi}_n$ to be decoupled and hence makes Eqn (2.1) tractable enough to be solvable in practice by various methods such as Hartree[1],Hartree-Fock[2], Density Functional Theory[3, 4],etc.

2. By replacing the electronic part of the full many-body Hamiltonian by a model Hamiltonian which contains only the dominant effects along with the significant single particle orbitals which play a significant role in determining the specific property under study. These models include the likes of Hubbard model[5, 6], Heisenberg model[7], etc. which are solved by numerical techniques such as exact diagonalization (ED).

As the density functional theory (DFT) of the first approach and the exact diagonalizaton scheme (ED) of the second approach have been our primary tools of investigations, the subsequent sections are dedicated to the details of both the approaches.

2.1.1 The Born-Oppenheimer Approximation

The Born-Oppenheimer Approximation[8] was one of the first successful attempts to simplify the many-body Hamiltonian problem described in Eqn (2.1). It took advantage of the fact that since the nuclear mass is significantly heavier (~ 2000 times) compared to electron mass, the nuclear motion is significantly slower than the electron motion. Thus, one can assume the nuclei to be stationary relative to the electrons which move around it. This allows for the decoupling of the electron and nuclear degrees of freedom resulting in the electron and nuclear problems being solved independently. Thus, the many body Hamiltonian of can be rewritten as

$$\hat{H} = H_{electron} + H_{nuclei} \tag{2.3}$$

$$= [\hat{T}_e + \hat{V}_{ee} + \hat{V}_{ne}] + [\hat{T}_{nn} + \hat{V}_{nn}] \tag{2.4}$$

where $\hat{T}_e$ and $\hat{V}_{ee}$ are the kinetic and potential energy operators for the electrons, $\hat{V}_{ne}$ is the potential energy operator due to the interaction between electrons and nucleus, $\hat{T}_{nn}$ and $\hat{V}_{nn}$ are the kinetic and potential energy operators for the nuclei.

As the nuclei are fixed, their kinetic energy can be ignored while the potential energy due to the nuclear-nuclear interactions can be assumed to be constant. The constant nuclear potential energy term $\hat{V}_{nn}$ is called Madelung energy and can be calculated classically.

By solving the electron part of the Schrödinger equation one obtains the electron total energy $E_{electron}$ and the electron wave-function $\psi_{electron}$, which explicitly depends on the electron coordinates and where the nuclear coordinates appear as mere parameters. Thus the total energy of the system can be written as the sum of electron energy and constant nuclear energy as

$$E_{total} = E_{electron} + E_{nuclei} \tag{2.5}$$

2.1.2 The Independent Electron Approximation

Even with the simplification obtained on application of the Born-Oppenheimer approximation, Eqn (2.3) still remains a many-body eigenvalue problem corresponding to the electron degrees of freedom and therefore difficult to solve. For example for an iron atom with N_e = 26 electrons, the total electron wave-function is dependent on 78 (26 × 3) variables. Even by restricting the tabulation of the total electron wave-function to 10 points per variable, it would require storing and processing of 10^{78} numbers. Even if each number was assigned to a single atom, the number of atoms in the entire solar system would be insufficient for storing such a huge set of numbers.

The independent electron approximation allows for further simplification of Eqn (2.3) by mapping the problem of many interacting electron system onto a system of non-interacting electrons moving in an effective potential due to all other electrons. In this way the many electron eigenvalue problem can be decoupled into an exactly equivalent set of effective single electron equations which can then be solved independently. In order to achieve this mapping, two distinct formulations have been put forth over the years *viz* (a) the wave-function based approaches of the Hartree[1], Hartree-Fock[2] formalism and (b) the density functional theory based approaches[3, 4] respectively.

The wave-function based approaches suffer from the drawback of being computationally expensive for even small systems and very quickly become computationally prohibitive as the system size increases. In contrast density functional theory is simpler and computationally tractable compared to wave-function based approaches and has become the preferred method for obtaining solutions of the the many-body Hamiltonian problem for a variety of extended and complex systems. The following section is thus dedicated to discuss the formalism of density functional theory.

2.2 Density Functional Theory

Density functional theory has become the cornerstone for computational materials science having being successfully applied to a vast class of materials. It's root can be traced back to the Thomas-Fermi theory proposed in 1927[9, 10], where the basic idea was to replace the many-body wave-function $\psi(\mathbf{r})$ which is a function of $3N$ variables, N being the number of electrons, by the electron density $\rho(\mathbf{r})$ given by

$$(2.6) \qquad \rho(\mathbf{r}) = N \int \psi(r_1, r_2, \cdots, r_N) \psi^*(r_1, r_2, \cdots, r_N) dr_1 dr_2 \cdots dr_N$$

as the fundamental variable. The Thomas-Fermi theory however suffered from serious drawbacks primarily due to the fact that the approximations for the kinetic energy of electrons as well as errors in the exchange energy were unable to sustain bound states. It was thus discarded. It was not until 1964, when Hohenberg and Kohn put forth two crucial theorems[3] that provided a practical approach for reducing the many-electron problem to an effective one-electron problem. The two Hohenberg-Kohn theorems are the back-bone of modern density functional theory.

2.2.1 The Hohenberg-Kohn Theorems

The two Hohenberg-Kohn theorems state that

Theorem 1: The external potential $V(\mathbf{r})$ is uniquely determined by the ground state electron charge density $\rho_o(\mathbf{r})$.

Proof of theorem 1: Let us assume that the ground state of two N-electron systems is characterized by two different external potentials $v_1(\mathbf{r})$ and $v_2(\mathbf{r})$ (differing by more than an additive constant). Let us further assume, that the corresponding two wave-functions ψ_1 and ψ_2 yield the same ground state electron charge density $\rho_0(\mathbf{r})$. Thus the Schrödinger equation for the two N-electron system is given by

$$\begin{aligned} \hat{H}_1 \hat{\psi}_1 &= E_1 \hat{\psi}_1 \\ \hat{H}_2 \hat{\psi}_2 &= E_2 \hat{\psi}_2 \end{aligned}$$

(2.7)

On using the variational principle, one may obtain the energy expression as

$$E_1 = \langle \hat{\psi}_1 | H_1 | \hat{\psi}_1 \rangle < \langle \hat{\psi}_2 | H_2 | \hat{\psi}_2 \rangle \tag{2.8}$$

$$= \langle \hat{\psi}_2 | H_2 | \hat{\psi}_2 \rangle + \langle \hat{\psi}_1 | H_1 - H_2 | \hat{\psi}_1 \rangle \tag{2.9}$$

$$< E_2 + \int d r \rho(\mathbf{r}) [v_1(\mathbf{r}) - v_2(\mathbf{r})] \tag{2.10}$$

On interchange of suffixes one obtains

$$E_2 < E_1 + \int d r \rho(\mathbf{r}) [v_2(\mathbf{r}) - v_1(\mathbf{r})] \tag{2.11}$$

By summing the two inequalities Eqn (2.10) and Eqn (2.11) we face a contradiction

$$E_1 + E_2 < E_2 + E_1 \tag{2.12}$$

57

Thus, the assumption that two different external potentials gives the same ground state electron charge density is wrong. Hence, the given ground state charge density $\rho_0(\mathbf{r})$ uniquely determines the external potential and thus the Hamiltonian of the many-electron system. Furthermore, the ground state expectation value of any observable $\hat{A}$ is a unique functional of the ground state electron charge density.

Theorem 2: This theorem is a variational principle that asserts that the ground state energy can be regarded as a functional of the charge density, $E[\rho(\mathbf{r})]$. The charge density that minimizes the total energy is the ground state charge density $\rho_0(\mathbf{r})$.

Proof of theorem 2: Let us consider the many-body Hamiltonian $\hat{H} = \hat{T} + \hat{V} + \hat{V}_{ext}$ where $\hat{T}$ is the kinetic energy, $\hat{V}$ is the electron-electron interaction and $\hat{V}_{ext}$ is the external potential. Let ψ be the ground state wavefunction. For a given electron charge density $\rho(\mathbf{r})$, the total energy can be expressed as

$$
\begin{aligned}
E[\rho] &= \langle \psi[\rho] | \hat{H} | \psi[\rho] \rangle \\
&= \langle \psi[\rho] | \hat{T} + \hat{V} | \psi[\rho] \rangle + \langle \psi[\rho] | \hat{V}_{ext} | \psi[\rho] \rangle \\
&= F[\rho] + \int \rho(\mathbf{r}) \hat{V}_{ext}(\mathbf{r}) d\mathbf{r}
\end{aligned}
$$

By applying the Rayleigh-Ritz variational principle to electron charge density we obtain

$$
(2.13) \qquad F[\rho(\mathbf{r})] + \int \rho(\mathbf{r}) \hat{V}_{ext}(\mathbf{r}) d\mathbf{r} = E[\rho(\mathbf{r})] \geq E_0[\rho_0(\mathbf{r})] = \langle \psi | \hat{H} | \psi \rangle
$$

This implies that the ground state properties of an interacting N electron system is completely determined by the electron charge density $\rho(\mathbf{r})$ and the problem is reduced to finding the $\rho(\mathbf{r})$ which minimizes the energy functional $E[\rho(\mathbf{r})]$. It is worth noting that the above theorem restricts density functional theory to the study of ground state properties only.

It is obvious from Eqn (2.13) that the exact analytical form of the functional $F[\rho(\mathbf{r})]$, which contains all the many body effect, is crucial for the determination of $E[\rho(\mathbf{r})]$. Since the exact analytical form of the functional $F[\rho(\mathbf{r})]$ is not known, the reduction of the problem proved to be of little practical use. It was only a year later, that Kohn-Sham specifically addressed the issue and provided the formalism that lead to development of modern DFT.

2.2.2 The Kohn-Sham Equations and formulation of modern DFT

In 1965, Kohn and Sham [4] presented a formulation based on the Hohenberg-Kohn theorems which provided an approximation of the kinetic energy functional $\hat{T}(\rho)$ for the interacting electron system in terms of a non-interacting electron system having the same ground state charge density $\rho(\mathbf{r})$.

The total energy for system of N interacting electrons with charge density $\rho(\mathbf{r})$ can be written as

$$E[\rho] = F[\rho] + \int \hat{V}_{ext}(\mathbf{r})\rho(\mathbf{r})d\mathbf{r} \tag{2.14}$$

with the universal functional $F[\rho]$ for the system given by

$$F[\rho] = T[\rho] + V_H[\rho] + E_{xc}[\rho] \tag{2.15}$$

where $T[\rho]$ is the kinetic energy of the interacting electron, $V_H[\rho]$ is the electrostatic Coulomb energy of electrons or the Hartree term and $E_{xc}[\rho]$ contains all the exchange and correlations effects. Within the Kohn-Sham formulation, by replacing the exact kinetic energy functional $T[\rho]$ by that of the non-interacting electrons having the same charge density, the exchange-correlation term $E_{xc}[\rho]$ could be redefined as

$$E_{xc}[\rho] = E_{xc}^{exact}[\rho] + T[\rho] - T_s[\rho] \tag{2.16}$$

where $T_s[\rho]$ represents the kinetic energy of non-interacting electrons.

These approximations to the kinetic and exchange-correlation functionals allow for the mapping of the many interacting electron system onto an exactly equivalent system of non-interacting electrons moving in an effective potential due to all other electrons and having the same $\rho(\mathbf{r})$. Thus the interacting many-electron problem is reduced to solving a set of self-consistent non-interacting one-electron equations known as Kohn-Sham equations.

For a system of N non-interacting electrons the ground state charge density can be represented as a sum over one electron orbitals ϕ_i (the Kohn-Sham orbitals) as follows

$$\rho(\mathbf{r}) = \sum_{i}^{N} |\phi_i|^2 \tag{2.17}$$

Then, the total energy functional for this non-interacting electron system can be written as

$$(2.18) \quad E_{KS}[\rho] = T_s[\rho(\mathbf{r})] + \int \hat{V}_{ext}(\mathbf{r})\rho(\mathbf{r})d\mathbf{r} + \frac{1}{2}\frac{e^2}{4\pi\epsilon_0}\int\int\frac{\rho(\mathbf{r})\rho(\mathbf{r}')}{|\mathbf{r}-r'|}d\mathbf{r}d\mathbf{r}' + E_{xc}[\rho(\mathbf{r})]$$

and the corresponding Hamiltonian is given by

$$(2.19) \quad \hat{H}_{KS} = -\frac{\hbar^2}{2m}\nabla^2 + V_{eff}(\mathbf{r})$$

where

$$(2.20) \quad V_{eff}(\mathbf{r}) = V_{ext}(\mathbf{r}) + \frac{1}{2}\frac{E^2}{4\pi\epsilon_0}\int\frac{\rho(\mathbf{r}')}{|\mathbf{r}-r'|}d\mathbf{r}' + \frac{\delta E_{xc}}{\delta\rho(\mathbf{r})}$$

$$= V_{ext} + V_{Hartree} + V_{xc}$$

Thus using Eqn (2.18), (2.19) and (2.20) one can find the the one-electron orbitals ϕ_i, which minimize the energy and satisfy the following set of one-electron Schrödinger-like equations

$$(2.21) \quad \left[-\frac{\hbar^2}{2m}\nabla^2 + V_{eff}(\mathbf{r};\rho)\right]\phi(\mathbf{r}) = \epsilon_i\phi_i(\mathbf{r})$$

From Eqn (2.21) it should be noted that the above set of one-electron equations can be solved if the effective potential V_{eff} is known. However, to know V_{eff} we have to know the charge density $\rho(\mathbf{r})$ and that means knowing the set of orbitals ϕ_i which are the solutions of the Kohn-Sham equations. Thus the Kohn-Sham equations need to be solved self-consistently by applying iterative methods as follows

1. Start with an initial guess for the charge density $\rho(\mathbf{r})$.

2. Calculate the corresponding $V_{eff}(\mathbf{r};\rho)$ and solve the Eqn (2.21) with appropriate boundary condition to obtain the total energy ϵ_i and the one-electron orbitals ϕ_i

3. From the ϕ_i , calculate the new charge density and repeat the iterative process until convergence is reached. The convergence is self-consistently achieved, when the output charge density differs from the input charge density by a preassigned small value.

A flowchart summarizing the above steps is given in Figure 2.1.
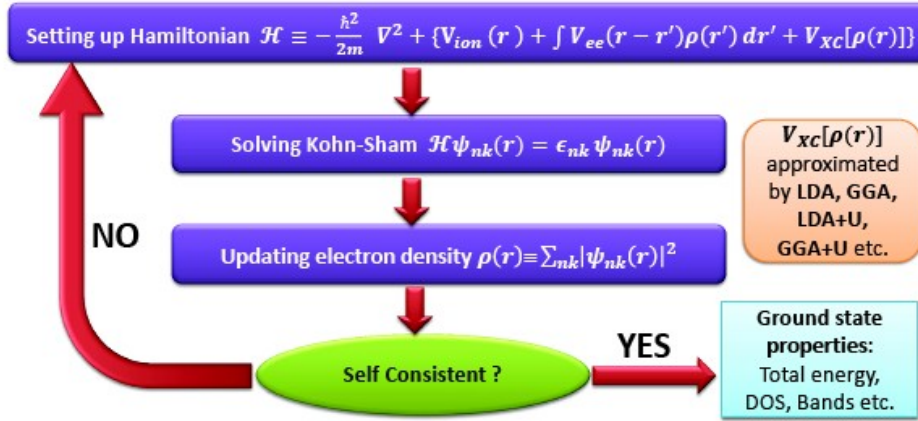
Figure 2.1: Flowchart illustrating the iterative procedure to solve the Kohn-sham equations.

2.2.3 Exchange-Correlation Functional

While the Kohn-Sham theory is exact in principle, it suffers a major drawback due to the ill-defined exchange-correlation energy term. In reality, as the exact expression for exchange-correlation energy E_{xc} is not known, the effective potential V_{eff} itself becomes an unknown quantity. Hence to solve the set of Kohn-Sham equations, approximations to the exchange-correlation functional are needed. Of the various approximations formulated over the years, the local density approximation (LDA) and generalized gradient approximation (GGA) are the most commonly used and the same have been used for our studies.

Local Density Approximation (LDA)

Local Density Approximation (LDA) is one of the simplest approximation for the exchange correlation energy. It was introduced by Kohn and Sham in 1965[4]. The central idea of the approximation relies on the assumption that the exchange-correlation energy is a functional that depends only on the local value of electron charge density.

Under the above assumption, the exchange-correlation energy of an inhomogeneous electron system having the charge density $\rho(\mathbf{r})$ at any point $\mathbf{r}$ in space, can be considered equal to the exchange-correlation energy of a homogeneous electron gas having the same electron charge density $\rho(\mathbf{r})$.

Within the LDA approximation, the exchange-correlation functional has the following

form

$$(2.22) \qquad E_{xc}[\rho(\mathbf{r})] = \int \epsilon_{xc}^{LDA}[\rho(\mathbf{r})]\rho(\mathbf{r})d\mathbf{r}$$

where the choice of $\epsilon_{xc}^{LDA}[\rho(\mathbf{r})]$ is taken to be the exchange-correlation energy density of the homogeneous electron gas of density $\rho(\mathbf{r})$. $\epsilon_{xc}^{LDA}[\rho(\mathbf{r})]$ can be further separated into the exchange and correlation contributions

$$(2.23) \qquad \epsilon_{xc}^{LDA}[\rho(\mathbf{r})] = \epsilon_{x}^{LDA}[\rho(\mathbf{r})] + \epsilon_{c}^{LDA}[\rho(\mathbf{r})]$$

For an homogeneous electron gas, the exchange energy $\epsilon_x^{LDA}[\rho(\mathbf{r})]$ is known exactly and is given by Dirac's expression

$$(2.24) \qquad \epsilon_x^{LDA}[\rho(\mathbf{r})] = -\frac{3}{4}(\frac{3}{\pi})^{1/3}\rho^{1/3} = -\frac{3}{4}(\frac{9}{4\pi^2})^{1/3}\frac{1}{r_s} = -\frac{0.058}{r_s}$$

where $r_s = (3/4\pi\rho)^{1/3}$ is the mean inter-electron distance.

On the other hand the functional form of the correlation density, $\epsilon_c^{LDA}[\rho(\mathbf{r})]$ is unknown. In 1980, Ceperley and Adler[11] provided an accurate estimate of $\epsilon_c^{LDA}[\rho(\mathbf{r})]$ for the homogeneous electron gas by numerical quantum Monte-Carlo simulations. The resultant exchange-correlation (XC) functional was later on parameterized by Perdew and Zunger[12], Perdew and Wang[13], etc and are now known as LDA functionals.

The LDA approximation is expected to work well for systems where the charge density varies slowly in space. However in some cases where the electron density is inhomogeneous and the approximation is expected to fail, the LDA gives surprisingly good results.[14] This can be attributed to two facts. First, the LDA underestimates the exchange energy and overestimates the correlation energy which leads to a cancellation of errors. Secondly, the electron-electron interaction is dependent only on the spherical average of the exchange-correlation hole and not on it's detailed shape.

However, while the LDA approximation provides reasonable results for structural, elastic and vibrational properties it cannot accurately predict activation energy barriers and is known to overestimate the binding energies.

Generalized Gradient Approximation (GGA)

The generalized gradient approximation (GGA) is the next step towards the improvement of the LDA XC functional. While GGA retains the core features of LDA, it also takes into

account the spatial variations in the charge density which are important. The exchange correlation energy within the GGA approximation can be written as

(2.25)
$$E_{xc}^{GGA} = \int \epsilon_{xc}[\rho(\mathbf{r}), |\nabla\rho(\mathbf{r})|]\rho(r)d\mathbf{r}$$
$$= \int \epsilon_{xc}[\rho(\mathbf{r})]F_{xc}[\rho(\mathbf{r}), \nabla\rho(\mathbf{r})]\rho(\mathbf{r})d\mathbf{r}$$

where the functional F_{xc} is called the enhancement factor. The functional F_{xc} can have different forms and depending on the choice of the functional form of F_{xc}, a variety of GGA functionals are available for use such as Langreth-Mehl(LM)[15], Perdew-Wang (PW86, PW91)[16, 17], Perdew-Burke-Ernzerhof(PBE)[18], etc. In the present thesis, PBE GGA exchange-correlation functional bee mostly used, which is briefly described below.

PBE exchange-correlation functional

The PBE exchange-correlation energy functional is given by

(2.26)
$$E_{xc}^{PBE} = \int \epsilon_x^{LDA}[\rho(\mathbf{r})]F_{xc}(\rho,\zeta,s)\rho(\mathbf{r})d\mathbf{r}$$

where ρ is the local density , ζ is the relative spin-polarization and

$$s = \frac{|\nabla\rho(r)|}{2k_F\rho}$$

is the dimensionless density gradient. The enhancement factor F_{xc} has the form

$$F_{xc}(s) = 1 + \kappa - \frac{\kappa}{1 + \mu s^2/\kappa}$$

where κ and μ are empirically fitted to a database of ionization energies.

The correlation contribution to the energy is written as

(2.27)
$$E_C^{PBE} = \int [\epsilon_c^{LDA}(\rho,\zeta) + H(\rho,\zeta,t)]\rho(\mathbf{r})d\mathbf{r}$$

with

(2.28)
$$H(\rho,\zeta,t) = (\frac{e^2}{a_0})\gamma\phi^3 ln\{1 + \frac{\beta\gamma^2}{t}[\frac{1 + At^2}{1 + At^2 + At^4}]\}$$

here

(2.29)
$$t = \frac{|\nabla\rho(\mathbf{r})|}{2\phi k_s\rho}$$

is the dimensional density gradient, and

$$k_s = (\frac{4k_F}{\pi a_0})$$

is the Thomas-Fermi screening wave number.

$$\phi(\zeta) = \frac{[(1+\zeta)^{2/3} + (1-\zeta)^{2/3}]}{2}$$

is a spin scaling factor. The function A has the form

$$A = \frac{\beta}{\gamma}[\frac{exp(-\epsilon_c^{LDA}[\rho])}{\gamma\phi^3(e^2/a_0)} - 1]^{-1}$$

Though the GGA is improvement over LDA in terms of predicting the binding energies, electronic and magnetic properties of the materials, it does have a few drawbacks. The GGA approximation cannot describe the Van-der Waals interaction. It is also known to overestimate the electric polarization for polar materials[19]. Finally, GGA as well as LDA fail for materials where strong electron-electron correlations play a crucial role in determining the properties.

2.2.4   Basis Sets

To solve the Kohn-Sham equations, a choice of an appropriate basis set to expand the one-electron Kohn-Sham orbitals is necessary. The choice of basis set is dependent on the attributes of the system under study. Over the years, various basis set methods have been developed for prediction of the electronic properties of solids with reasonable accuracy. Depending on the choice of the basis sets the methods can be classified in two sets

1. **Fixed Basis Set Methods**: In this approach, the Kohn-Sham orbitals are expanded in terms of energy independent basis sets or fixed basis sets as in the tight binding model using linear combination of atomic orbitals (LCAO)[20], the orthogonalized plane wave-pseudopotential methods[21, 22], etc.

2. **Partial Wave Methods**: In this approach, the Kohn-Sham orbitals are expanded in terms energy and potential dependent all-electron partial wave basis sets as in the Korrimga-Kohn-Rostoker (KKR)[23, 24] and the augmented plane wave (APW)[25] methods.

The linearized form of KKR and APW *viz* the linear muffin tin orbital method (LMTO)[26] and the linearized augmented plane wave method (LAPW)[25] respectively combines the attractive features of both, the simplicity of the energy independent fixed basis set methods and the accuracy of the partial wave methods.

In this thesis we have used two types of basis set methods for geometry optimization and electronic structure calculations. These are

1. Plane wave basis set - pseudo potential method within the projected augmented wave (PAW) scheme.

2. The all electron linearized augmented plane wave (LAPW) method.

A brief description of these methods is provided below.

Plane Wave Based Pseudopotential method

Plane Wave Basis Set

According to Bloch's theorem, the wave function of an electron moving in a potential generated by a periodic lattice can be written as a product of a plane wave $e^{i\mathbf{k}.r}$ and a function $u_{\mathbf{k}}(\mathbf{r})$ that has the periodicity of the lattice. Thus we can write

$$(2.30) \qquad \psi_{\mathbf{k}}(\mathbf{r}) = e^{i\mathbf{k}.r} u_{\mathbf{k}}(\mathbf{r})$$

Furthermore the cell periodic part $u_{\mathbf{k}}(\mathbf{r})$ of the electron wave-function can be expanded using a basis set of plane waves whose wave vectors are the reciprocal lattice vectors of the crystal. Thus,

$$(2.31) \qquad u_{\mathbf{k}}(\mathbf{r}) = \sum_{\mathbf{G}} c_{i,\mathbf{G}} e^{i\mathbf{G}.r}$$

where the reciprocal lattice vectors $\mathbf{G}$ are defined by $\mathbf{G}.l = 2\pi m$ for all l where l is a lattice vector and m is an integer. Therefore the full electron wave-function can be written as

$$(2.32) \qquad \psi_{\mathbf{k}}(\mathbf{r}) = \sum_{\mathbf{G}} c_{i,\mathbf{k}+G} e^{i(\mathbf{k}+G).\mathbf{r}}$$

Thus, the electron wave-function at each $\mathbf{k}$ point can be expanded as linear combination of discrete plane waves.

Pseudopotential Method

The electronic states of a system can be divided into two categories *viz* (a) the localized core states, which lie deep in energy and (b) the valence/conduction states which are spatially delocalized or spread out and are higher in energy. The core states are tightly bound to the nucleus and within the core, the potential is spherically symmetric which is reflected in the angular dependence of the core state wave function $\psi_{\mathbf{k}}$. Furthermore, the imposition of orthogonality with the valence state implies that $\psi_{\mathbf{k}}$ shows rapid oscillations. Therefore, an accurate description of the core state wave functions $\psi_{\mathbf{k}}$ requires a very large number of plane-waves and is the primary drawback of using the plane-wave basis set.

To alleviate the problem, the concept of pseudopotential, whose basis lie in the orthogonalized plane wave method proposed by C. Herring, was introduced.[27, 28] The pseudopotential approximation takes advantage of the fact that electrons in the core state do not play a significant role in determining the physical properties of materials such as chemical bonding , electronic structure , etc. Instead, these electrons partially screen the nucleus and thereby form an inert core along with the nucleus. Thus the atom can be represented as an ionic core that interacts with the valence electrons *via* a strong ionic potential. This allows separation of the core states and valence states, which is exploited in the pseudopotential approach by removing the core electrons and replacing the strong ionic potential by a weaker effective pseudopotential. The valence electrons are then described by a set of pseudo wave functions which are acted on by the effective pseudopotential. The pseudopotential and pseudo wave functions are constructed in such a way that they are identical to the true potential and true wave function, respectively beyond a certain cut-off radius.

The steps for generation of the pseudopotential are summarized below.

1. The all electron (AE) free atom Kohn-Sham radial equation is given by

    $$(2.33) \qquad \left[-\frac{1}{2}\frac{d^2}{dr^2} + \frac{l(l+1)}{2r^2} + V_{eff}^{AE}[\rho^{AE}(\mathbf{r})] \right] \mathbf{r} R_{nl}^{AE}(\mathbf{r}) = \epsilon_{nl}^{AE}(\mathbf{r}) R_{nl}^{AE}(\mathbf{r})$$

    where R_{nl}^{AE} is the radial part of the all electron wave-function with angular momentum l. Within the spherical assumption of the Hartree and exchange-correlation potential, the effective potential V_{eff}^{AE} is written as

    $$(2.34) \qquad V_{eff}^{AE}[\rho^{AE}(\mathbf{r})] = -\frac{Z}{r} + V_{Hartree}[\rho^{AE}(\mathbf{r})] + V_{xc}[\rho^{AE}(\mathbf{r})]$$
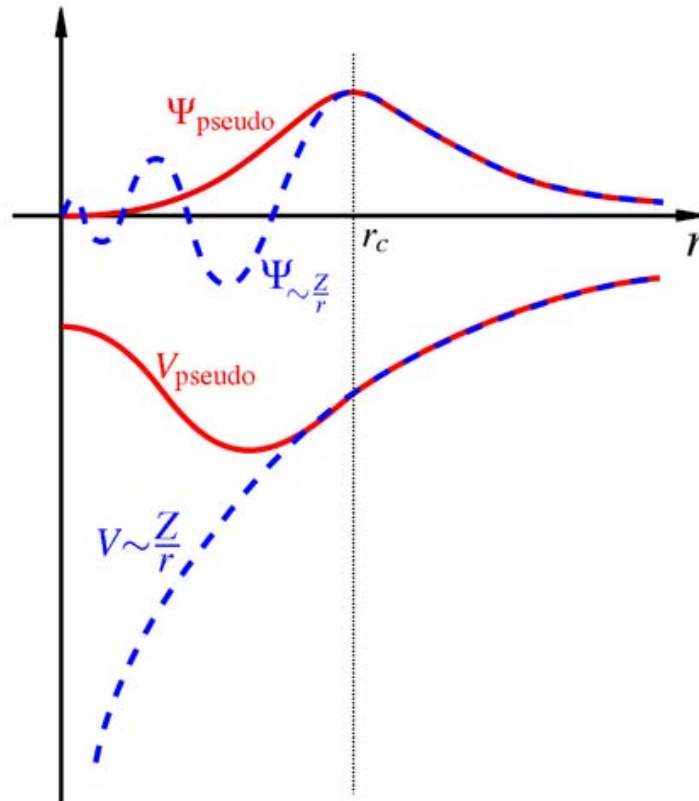
Figure 2.2: Comparison of a wave-function in the Coulomb potential of the nucleus (dashed) to the one in the pseudo-potential (solid). The real and the pseudo wave-function and potentials match above a certain cutoff radius. Figure adapted from Wikipedia.

For a given distribution of electrons in the atomic energy levels the free atom Kohn-Sham radial equation is then solved to obtain the radial wave function R_{nl}^{AE}. This is the reference configuration.

2. Generate the pseudo wave function R_{nl}^{PS} corresponding to R_{nl}^{AE} subject to the conditions:

   a) The pseudo wave-function should be node-less inside the core region of certain radius r_c

   b) The pseudo wave-function should be identical to the true all electron (AE) wave function beyond a certain cutoff distance i.e $R_{nl}^{PS} = R_{nl}^{AE}$ for $r \geq r_c$

3. From the obtained pseudo wave-function, the pseudopotential can be constructed by inverting the radial Kohn-Sham equation for the pseudo wave-function and the

valence electron charge density given by

$$(2.35) \qquad V_{l,scr}^{PS} = \epsilon_l^{PS} - \frac{l(l+1)}{2r^2} + \frac{1}{2rR_l^{PS}(r)} \frac{d^2}{dr^2}[\mathbf{r}R_l^{PS}(\mathbf{r})]$$

The pseudopotential $V_{l,scr}^{PS}$ thus obtained takes into account the screening effect of the valence electrons. In order to obtain the final form of the pseudopotential, one subtracts the Hartree and exchange-correlation potentials calculated only for the valence electrons as follows

$$(2.36) \qquad V_l^{PS} = V_{l,scr}^{PS} - V_{Hartree}[\rho^{PS}(\mathbf{r})] - V_{xc}[\rho^{PS}(\mathbf{r})]$$

A major drawback of the plane-wave pseudopotential method is that all information of the true wave-function close to the nuclei is lost which can play an important role in determining certain physical properties such as hyperfine splitting , electric field gradients, etc. Within the pseudopotential method this problem can be addressed by the use of the projected augmented wave (PAW) method proposed by P. Blöchl.[29] A different approach is the on the all electron approach of the linearized augmented plane wave method based on the choice of partial wave functions as basis sets. Both methods are discussed in the following sections.

Linearized Augmented Plane Wave (LAPW) Formalism

The linearized augmented plane wave (LAPW) formalism is a modification of the augmented plane wave (APW) method proposed by Slater[30, 31]. From solid state physics, it is understood that in regions far away from the nuclei the electrons behave as almost free particles and can be described by plane waves. On the other hand in regions close to the nuclei, the electrons get localized at the nuclei site and therefore are more accurately described by atomic-like functions. In APW method, this allows one to partition the system space into two parts *viz* the 'muffin-tin" (MT) spheres centered at each atom site and the remaining region called interstitial.

A MT sphere (S_a) is a sphere of radius R_a constructed around each atom. These MT spheres are chosen so that they do not overlap and fill the space to maximal extent. The remaining space outside the spheres is called interstitial region (IS). Within the MT spheres the potential is approximated to be spherically symmetric while in the interstitial region it is considered to be constant.

The APW basis functions are then defined as

$$(2.37) \qquad \phi_G^k(r,\epsilon) = \begin{cases} \frac{1}{\sqrt{\Omega}} e^{i(k+G).r} & \text{for } r \in IS \\ \sum_{l,m} A_{lm}^{a,k+G} \varphi_l^a(r,\epsilon) Y_m^l(\theta',\phi') & \text{for } r \in S_a \end{cases}$$

The position r inside the spheres is given with respect to the center of each sphere. φ_l^a is the solution to the radial Schrödinger equation for an isolated atom a with respect to the energy parameter ϵ. The coefficients $A_{lm}^{a,k+G}$ are determined by the requirement that the wave-functions have to be continuous at the boundary of the MT spheres. Thus by matching the plane waves outside the sphere to the function inside the sphere at the boundary the value of $A_{lm}^{a,k+G}$ can be obtained. In principle, since the expansion of the plane wave term of Eqn (2.37) contains a series of infinite terms, an infinite number of $A_{lm}^{a,k+G}$ can be found such that two functions can be matched. For practical purposes however a truncation at some value of l_{max} is required. A reasonably good condition is given by $R_a G_{max} = l_{max}$ where G_{max} provides the cut-off for the plane wave expansion.

Since φ_l^a depends on energy, so does the resultant Hamiltonian matrix H. Thus, solving the secular equation to obtain the energy eigenvalues becomes a non-linear problem which is computationally more expensive and non trivial. In order to solve this issue of energy dependence of the Hamiltonian matrix H, linearized methods were proposed by Anderson[32] and Koelling and Arbman[33]. Within the Anderson formalism, the linearized augmented plane waves (LAPW) were given by

$$(2.38) \qquad \phi_G^k(r,\epsilon) = \begin{cases} \frac{1}{\sqrt{\Omega}} e^{i(k+G).r} & \text{for } r \in IS \\ \sum_{l,m} A_{lm}^{a,k+G} \varphi_l^a(r',\epsilon_v) + B_{lm}^{a,k+G} \dot{\varphi}_l^a(r',\epsilon_v) Y_m^l(\theta',\phi') & \text{for } r \in S_a \end{cases}$$

where the coefficients $A_{lm}^{a,k+G}$ and $B_{lm}^{a,k+G}$ can be determined by matching the two functions at the sphere boundary in terms of value as well as slope.

Projector Augmented Wave (PAW) Formalism

It was in 1994 that P. Blöchl [29] proposed the projector augmented wave (PAW) formalism as a means to unify the accuracy obtained by an all-electron (AE) calculation and the computational efficiency of the plane-wave pseudopotential method. Within this formalism the drawback arising due to oscillations of valence-state wave-functions is addressed by transforming the physical wave-functions $\psi_n(r)$ into smooth auxiliary wave-functions $\tilde{\psi}_n(r)$ that can be represented in a plane wave expansion. This is achieved by defining a linear transformation operator T as

(2.39)
$$\hat{T} = 1 + \sum_a \hat{T}^a$$

where $\hat{T}^a$ only acts in the augmentation spheres.

Augmentation spheres are constructs similar to the muffin-tin spheres defined around each atoms i and have a radius $|r - R^a| < r_c^a$, where r_c^a is the cut-off radius, a is the atom site index and R^a is the position of the atoms i.

Then transformation $\hat{T}$ maps the smooth auxiliary wave-functions onto the true wave-functions by

(2.40)
$$\psi_n(r) = \hat{T}\tilde{\psi}_n(r)$$

In order to evaluate the form of the operator $\hat{T}$, one considers the all electron partial wave basis functions $|\phi_i^a\rangle$. Let $|\tilde{\phi}_i^a\rangle$ be the auxiliary partial wave such that outside the augmentation spheres they are identical to the all electron partial wave basis functions i.e

$$|\phi_i^a\rangle = |\tilde{\phi}_i^a\rangle \; \forall |r - R^a| > r_c^a$$

Then,

(2.42)
$$|\phi_i^a\rangle = \hat{T}|\tilde{\phi}_i^a\rangle$$

(2.43)
$$|\phi_i^a\rangle = (1 + \sum_{a'} \hat{T}^{a'})|\tilde{\phi}_i^a\rangle$$

(2.44)
$$|\phi_i^a\rangle = (1 + \hat{T}^a)|\tilde{\phi}_i^a\rangle$$

The above implies that

(2.45)
$$\hat{T}^a|\tilde{\phi}_i^a\rangle = |\phi_i^a\rangle - |\tilde{\phi}_i^a\rangle$$

(2.46)
$$= \sum_j (|\phi_j^a\rangle - |\tilde{\phi}_j^a\rangle)\langle \tilde{p}_j^a|\tilde{\phi}_i^a\rangle$$

where $\langle \tilde{p}_j^a|$ is the projector operator statisfying the condition $\langle \tilde{p}_j^a|\tilde{\phi}_i^a\rangle = \delta_{i,j}$

Then the operator $\hat{T}$ can be written as

(2.47)
$$\hat{T} = 1 + \sum_j (|\phi_j^a\rangle - |\tilde{\phi}_j^a\rangle)\langle \tilde{p}_j^a|\tilde{\phi}_i^a\rangle$$

Thus, $\psi_n(r)$ can be reconstructed from $\tilde{\psi}_n(r)$ on operating $\hat{T}$ as

$$(2.48) \qquad \psi_n(r) = \tilde{\psi}_n(r) + \sum_j (|\phi_j^a\rangle - |\tilde{\phi}_j^a\rangle)\langle \tilde{p}_j^a|\tilde{\psi}_n^r\rangle$$

The smooth auxiliary wave-function $\tilde{\psi}_n(r)$ is identical to the all-electron wavefunctions $\psi_n(r)$ outside the augmented spheres. The auxiliary partial waves $|\tilde{\phi}_i^a\rangle$ are chosen such that they form the basis for $\tilde{\psi}_n(r)$ within the augmented sphere. Therefore one can write

$$(2.49) \qquad \tilde{\psi}_n(r) = \sum_i C_{ni}^a |\tilde{\phi}_i^a\rangle$$

Furthermore, it can be shown that the all-electron wave function $\psi_n(r)$ can be expanded in terms of all-electron partial waves $|\phi_i^a\rangle$ using the exactly the same coefficents C_{ni}^a.

The PAW formalism as implemented within the Vienna Ab-initio Simulation Package by Kresse and Joubert,[34] has been primarily used for the work described within this thesis.

Various properties of materials such as it's electronic structure, carrier concentration, electric polarization, etc are gate dependent. In order to study these properties in an experiment requires the material to be used in gated geometry under the influence of an applied external electric field. On the other hand computational modeling of such an external electric field within the periodic set-up of density functional simulations is not straightforward. In the next section, we briefly describe the modeling of such an external electric field used in our simulations to investigate gate-dependent magnetism and polarization.

2.2.5 Application of an External Electric Field

Application of constant external electric field , whose potential U_{ext} is given by a linear monotonic function, breaks the periodicity of the lattice system. The eigenstates, therefore, cannot be represented as Bloch states. To preserve the underlying periodicity of the lattice, the external electric field is setup by the application of a periodic sawtooth potential given by[35, 36]
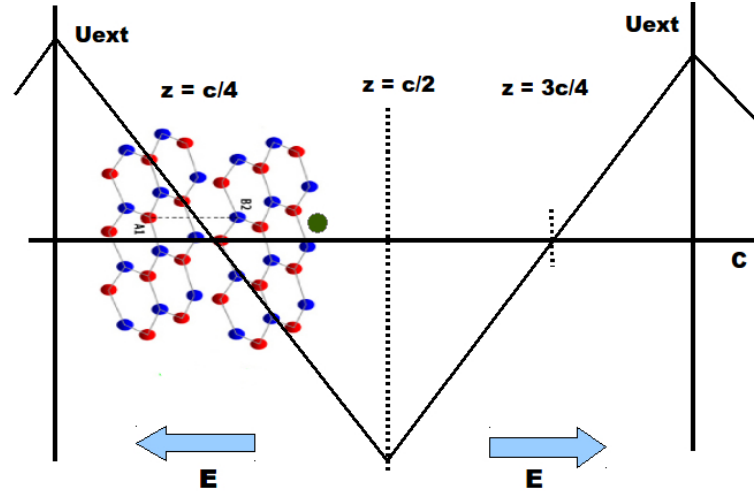
Figure 2.3: Setup of periodic sawtooth potential within the DFT calculations. The system is placed such that it sees a linear potential.

$$U_{ext} = U_0 \frac{8}{\pi^2} \sum_n \frac{1}{n^2} cos[nz\frac{2\pi}{c}]$$

$$n = 1, 3, 5, \cdots, 2m - 1$$

where c is the lattice parameter in z direction. U_{ext}, then has a translational symmetry of some superlattice, and yet "regions of interest" in each supercell, will perceive a linear potential i.e an electric field constant in space as shown in Figure 2.3.

While it is very successful in describing correctly the properties and physics of many materials, the density functional theory approach is a single electron approximation, where the electron-electron correlations are treated in a mean field manner. However, this mean field approximation breaks down in the limit of strong electron-electron correlations which can significantly affect the properties of the studied materials. Thus, the density functional theory cannot accurately describe strongly correlated systems. In order to study such systems, one therefore must turn to the many body Hamiltonian approach, where various numerical methods such as the Monte-Carlo techniques, exact diagonalization schemes, etc are utilized to solve the Hamiltonian to obtain the required eigenvalues and eigenfunctions. In the present thesis we have used the exact diagonalization method within the framework of Lanczos algorithm to solve the pertinent many body Hamiltonian the details of which are discussed in the remaining sections of the chapter. We have followed the prescription described in Ref[37], Ref[38]

2.3 Exact Diagonalization Method using Lanczos Algorithm

Exact Diagonalization (ED) alludes to computation of the eigenvalues and eigenvectors of the appropriate Hamiltonian matrix describing a system. ED method differs from other computational techniques due to it's exactness *i.e.* it is not approximated in any way. A typical ED scheme can be summarized as follows

1. Choosing a model Hamiltonian which can appropriately describe the physical system.

2. Constructing a suitable many particle basis set.

3. Using the constructed basis set to build the Hamiltonian matrix.

4. To diagonalize the Hamiltonian matrix using suitable methods to obtain the many body ground-state and excited states.

5. Use the obtained eigenvectors to compute various properties.

In this section we describe the ED scheme typically used to solve the Hubbard model Hamiltonian for a given lattices of N sites having the form

$$H = -t \sum_{\langle i,j \rangle, \sigma} [c^{\dagger}_{i,\sigma} c_{j,\sigma} + h.c.] + U \sum_i n_{i,\uparrow} n_{i,\downarrow}$$

where $c^{\dagger}_{i,\sigma}$ and $c_{i,\sigma}$ are operators which create and annihilate an electron with spin σ at site i respectively and 'h.c' stands for it's hermitian conjugate counterpart. t is the nearest neighbor hopping term and the notation $\langle .,. \rangle$ denotes that only nearest-neighbor interactions are included. The term U represents the repulsive on-site Coulomb interaction and is a short-range interaction term.

2.3.1 Choice of Basis sets

In order to diagonalize any matrix, it is first necessary to estimate the dimension of the matrix. For the Hubbard model defined on a lattice of N sites, they are 4 spin states per site $\{|0\rangle, |\uparrow\rangle, |\downarrow\rangle, |\uparrow\downarrow\rangle\}$. Therefore total number of states i.e the size of the basis set for the

Hubbard model is equal to 4^N which will be the dimension of the Hamiltonian matrix. The exponential scaling of the matrix dimension with the number of sites does not allow handling of large cluster sizes and is a major drawback of the ED scheme.

Economical computation of the Hamiltonian matrix is possible by choosing an appropriate basis set which reduces the dimension of the matrix. This can be done by taking advantage of the common symmetries usually encountered in many models including the Hubbard model. These symmetries, embedded in the conservation laws are: the conservation of total charge $\hat{N}_e$, the conservation of total spin in the z direction $i.e.$ $\hat{S}^z_{tot}$ as well as the translational and rotational symmetries. As a result of exploiting the conservation of charge and spin, the commutation relations can be written as

$$[\hat{H}, \hat{S}^z_{tot}] = [\hat{H}, \hat{S}^2_{tot}] = [\hat{H}, \hat{N}_e] = 0$$

In addition these operators also obey the commutation relations

(2.50)
$$[\hat{S}^2_{tot}, \hat{S}^z_{tot}] = [\hat{S}^z_{tot}, \hat{N}_e] = [\hat{N}_e, \hat{S}^2_{tot}] = 0$$

This implies that the eigenvalues of $\hat{H}$, $\hat{S}^z_{tot}$, $\hat{N}_e$ and $\hat{S}^2_{tot}$ are simultaneous eigenvalues given by the energy E, the total spin along the z-direction S^z, the total charge n_e and $S(S+1)$ where S is the total spin of the system, respectively. Thus the basis size for the Hubbard model reduces to ${}^N C_{N_\uparrow} \times {}^N C_{N_\downarrow}$ where N is the total number of sites, $N_\uparrow$ is the total number of up-electrons and $N_\downarrow$ is the total number of down electrons. The translational and rotational symmetries can be used to further reduce the basis size and hence the dimension of the matrix.

Numerical Representation of the Basis set

For easier handling of the basis set, the matrix elements of the many particle basis set is resolved into two arrays, one for the spin up ($M^\uparrow$) part and the other for the spin down ($M^\downarrow$) part. Such a resolution is possible because operators like the kinetic energy operator ($c_i^\dagger c_j$) do not mix spins. Furthermore, a lowering of memory cost and faster computation of matrix elements can be achieved by coding the basis set numerically in an "integer representation" corresponding to a sequence of bits. The details behind the construction of such an integer representation is provided below.

Instead of using the standard two spin values $\sigma = \pm\frac{1}{2}$ we use integers $n_i^\uparrow$ and $n_j^\downarrow$ $\in \{0, 1\}$ to indicate whether the site $i(j)$ is occupied or not with $\uparrow$ electron or $\downarrow$ electron. Thus the basis set can be represented as a sequence of $n_i^\uparrow$ ($n_j^\downarrow$) which can be identified

state	↑	↓	↑	↓	↑	↓	↑	↓	↑	↓	
site label	1	2	3	4	5	6	7	8	9	10	
bit label	0	1	2	3	4	5	6	7	0	1	2
↑ part	1	1	0	1	0	1	0	1	0	1	0	Int. Rep.:(-85,2)
↓ part	1	0	1	0	1	0	1	0	1	0	1	Int. Rep.:(85,5)
byte label	1	1	1	1	1	1	1	1	2	2	2

Table 2.1: Representation of a basis state in byte and bit variables. The third row specifies the bit variable within given byte (specified in the last row)

with the bit-pattern of an integer number. We demonstrate this by providing a concrete example summarized in Table 2.1.

Let us consider an anti-ferromagnetic state on a lattice of 10 sites. The state is given $|\uparrow\downarrow\uparrow\downarrow\uparrow\downarrow\uparrow\downarrow\uparrow\downarrow\rangle$. Then, the $|\uparrow\rangle$ and $|\downarrow\rangle$ of the state can be represented as a string of integers $n_i^{\uparrow}$, $n_j^{\downarrow} \in \{0,1\}$ as shown in rows 4 and 5 of Table 2.1 where each integer is regarded as bit. The sequence of integers(bits) is then stored to an integer array of data-type BYTE *i.e.* any element of this array is a byte. From convention it is known, that a single byte is equal to 8 bits. Thus, it follows that for a 10 site lattice model, the basis set represented by 10 bits requires two byte elements for it's storage as noted from the last row of Table 2.1. Furthermore, it is possible to map each byte element to an integer $I = \sum_{i=1}^{8} n_i 2^{i-1}$ representing a 8-bit pattern. Let us consider $|\downarrow\rangle$ part the given anti-ferromagnetic state. For storage purposes, the corresponding 10-bit pattern (refer row 5 of Table 2.1) is split into two 8-bit patterns given by $n_1 = 01010101$ and $n_2 = 00000101$, with each 8-bit pattern stored as a byte array element labeled by index 1 and 2 (refer last row of Table 2.1). Each of the two 8-bit pattern will have a corresponding integer representation I_1 and I_2. For $n_2 = 00000101$, I_2 is given by $I_2 = 0 \times 2^7 + 0 \times 2^6 + 0 \times 2^5 + 0 \times 2^4 + 0 \times 2^3 + 1 \times 2^2 + 0 \times 2^1 + 1 \times 2^0 = 5$. Similarly, $I_1 = 85$ for n_1 bit-pattern. Thus the $|\downarrow\rangle$ part of the given anti-ferromagnetic state has an integer representation $(I_1, I_2) = (85,5)$. Following the same procedure the integer representation of the $|\uparrow\rangle$ part is given by (-85,2).

In this way all basis states and their integer representation can be formulated. A point to note, the zeroth bit of the first byte for each state is set to 1 so as to differentiate between a state with no electrons and the number zero.

The constructed basis states are then stored as columns of an array *viz* an array for the $|\uparrow\rangle$ part ($M^{\uparrow}$) and an array for the $|\downarrow\rangle$ part ($M^{\downarrow}$). The total basis state is subsequently given by the *direct* product of columns of $M^{\uparrow}$ and $M^{\downarrow}$ array. All that remains then is to sort the full basis set in an ascending (or descending) order. This is done by sorting the

$|\uparrow\rangle$ part in ascending order and making corresponding changes in the $|\downarrow\rangle$ part. Whenever repetition of $|\uparrow\rangle$ is encountered, the $|\downarrow\rangle$ part is further re-sorted in ascending order.

Symmetrized Basis Set

Application of lattice symmetries such as translation and rotation to the constructed basis sets can be used to further reduce the memory storage. Let us consider the example of translation symmetry in order to understand the process.

Let G be the group of all spatial symmetries for the given lattice system. Then, the set of translational symmetries TG is a subgroup of G. Since TG is an abelian group it has only one-dimensional irreducible representations labeled by wave vector $\mathbf{k}$. The set of allowed wave vectors can be derived from the geometry of the lattice. The character of this representation is given by

$$\chi_{\mathbf{k}}(t) = exp(i\mathbf{k}.\mathbf{T}(t)), \forall t \in T,$$

where $\mathbf{T}(t)$ denotes the translation vector associated with the element t. Then the configurations $|c\rangle$ in Hilbert space can be symmetrized as follows

$$symm_{\mathbf{k}}(|c\rangle) = \frac{1}{N_{c\mathbf{k}}} \sum_{t \in T} \chi_{\mathbf{k}}(t) |(t)(c)\rangle,$$

Thus, the states as constructed above are invariant under the symmetry operations and can be considered as generalized Blöch waves. The normalization factor has to be separately ascertained for each state $symm_{\mathbf{k}}(|c\rangle)$, in particular if more symmetries are implemented.

The construction of the symmetrized S^z basis sets is coded according to the following scheme

1. Loop over all configurations $|c\rangle$ with correct S^z_{tot}.

2. Within the loop generate class($|c\rangle$) = $\{g(|c\rangle)|\forall g \in TG\}$

3. If $|c\rangle$ corresponds to the smallest numerical integer representation in the class($|c\rangle$), register $|c\rangle$ with the calculated normalization factor.

The registered state is known as the "representative state" of class$\{|c\rangle\}$ and the dimension of the targeted subspace is reduced to the number of registered states.

2.3.2 Construction of the Hamiltonian Matrix

In order to setup the Hamiltonian matrix H it is necessary to calculate the matrix elements in the symmetrized S^z basis set. For this purpose it is assumed that the action of the Hamiltonian on a given representative state $|\phi\rangle$ is to generate a new configuration $|m\rangle$ having some amplitude a i.e.

$$H|\phi\rangle = a|m\rangle \tag{2.51}$$

Note, the state $|m\rangle$ need not be a representative state. Define $|m_0\rangle$ as the representative state of class ($|m\rangle$). Let g_n be a symmetry operation which maps the state $|m\rangle$ to state $|m_0\rangle$. Then, it has been proven that matrix element can be given as [37]

$$\langle m_0|H|\phi\rangle = \sqrt{\frac{N_{m_0\mathbf{k}}}{N_{\phi\mathbf{k}}}} \chi_{\mathbf{k}}(g_n)a \tag{2.52}$$

On solving the above equation the elements of the Hamiltonian matrix H can be generated. Within a computer program this can be achieved by implementing efficient schemes required to find $|m_0\rangle$ and it's index in the list of representative states like a simple look-up table or a binary search of the representative states.

Since the resultant matrix is a sparse matrix containing only a small number of matrix elements with distinct non-zero values, the memory required for storage of the matrix can be minimized by choosing an appropriate sparse matrix format, where the non-zero matrix elements are stored in the form of a *pointer* to a distinct value.

2.3.3 Lanczos Algorithim

In the final step we describe the Lanczos Algorithm[38] to solve the eigenvalue problem given a basis and Hamiltonian operator. The eigenvalue problem is formulated as

$$H|\psi\rangle = E|\psi\rangle$$

The Lanczos method circumvents the issues regarding calculation and storage of large matrices by constructing a basis in Krylov space $|\phi_0\rangle, H|\phi_0\rangle, H^2|\phi_0\rangle, \cdots, H^n|\phi_0\rangle$ that leads to a tridiagonal form of H. The procedure is described as below.

At the start of the first step, let $|\phi_0\rangle$ be an arbitrary normalized vector which we assume is not an eigenvalue of H. Let $|\phi_0\rangle$ satisfies the orthonormality condition

(2.54)
$$\langle \phi_0 | \phi_0 \rangle = 1$$

Let $|\phi_1\rangle$ be a new vector defined by

(2.55)
$$H|\phi_0\rangle = a_0|\phi_0\rangle + b_1|\phi_1\rangle$$

subject to the orthonormality conditions

(2.56)
$$\langle \phi_0 | \phi_1 \rangle = 0 \quad \text{and} \quad \langle \phi_1 | \phi_1 \rangle = 1.$$

Thus the left-hand side of above equation is known, and a_0, b_1 and $|\phi_1\rangle$ have to be determined. On multiplying by $\langle \phi_0|$ from the left of above equation, a_0 can be determined as

(2.57)
$$a_0 = \langle \phi_0 | H | \phi_0 \rangle$$

By subtracting the now known $a_0|\phi_0\rangle$ from Eqn (2.55) we obtain

(2.58)
$$b_1|\phi_1\rangle = (H - a_0)|\phi_0\rangle$$

Then on multiplying Eqn (2.58) from left by $\langle \phi_1|$ and imposing the orthonormality condition we get

(2.59)
$$b_1^2 = [(H - a_0)|\phi_0\rangle]^\dagger [(H - a_0)|\phi_0\rangle]$$

Since the inner product is positive definite, $b_1^2 \geq 0$. If $b_1^2 > 0$, then for convenience b_1 is taken to be the positive square-root of b_1^2 so that $|\phi_1\rangle$ can be determined as

(2.60)
$$|\phi_1\rangle = (H - a_0)|\phi_0\rangle / b_1$$

Next, the general Lanczos step is considered. In this step we assume that a set of orthonormal states $\{|\phi_0\rangle, |\phi_1\rangle, \cdots, |\phi_n\rangle\}$ with real parameters $\{a_0, a_1 \cdots, a_{n-1}\}$ and

$\{b_0, b_1 \cdots, b_n\}$ such that no b is zero. We can now determine $|\phi_{n+1}\rangle$, a_n and b_{n+1} by using recursion relation

$$(2.61) \qquad H|\phi_n\rangle = a_n|\phi_n\rangle + b_{n+1}|\phi_{n+1}\rangle + b_n|\phi_{n-1}\rangle$$

Calculation $H|\phi_n\rangle$ and projecting out the components $|\phi_n\rangle$ and $|\phi_{n-1}\rangle$ as in the first step , we obtain

$$(2.62) \qquad a_n = \langle\phi_n|H|\phi_n\rangle \quad \text{and} \quad b_n = \langle\phi_n|H|\phi_{n-1}\rangle$$

Solving for the new vector $|\phi_{n+1}\rangle$ we get

$$(2.63) \qquad b_{n+1}|\phi_{n+1}\rangle = (H - a_n)|\phi_n\rangle - b_n|\phi_{n-1}\rangle$$

b_{n+1}^2 is obtained by normalizing $|\phi_{n+1}\rangle$ which yields the positive square root b_{n+1} which in turn gives

$$(2.64) \qquad |\phi_{n+1}\rangle = [(H - a_n)|\phi_n\rangle - b_n|\phi_{n-1}\rangle]/b_{n+1}$$

$|\phi_{n+1}\rangle$ is orthogonal to $|\phi_n\rangle$ and $|\phi_{n-1}\rangle$ by construction and is normalized to one. That $|\phi_{n+1}\rangle$ is orthogonal to the states $|\phi_{n-2}\rangle, \cdots, |\phi_0\rangle$ is straightforward to show.

In summary the Lanczos algorithm can be outlined as

- Choose an arbitrary normalized starting vector $|\phi_0\rangle$

- Enforcing the conditions that $b_0 = 0$ and $|\phi_{-1}\rangle = 0$, at each iteration determine $a_n = \langle\phi_n|H|\phi_n\rangle$ and b_n^2 by normalizing the new vector obtained by following the recursion relations

$$b_1|\phi_1\rangle = H|\phi_0\rangle - a_0|\phi_0\rangle$$
$$b_{n+1}|\phi_{n+1}\rangle = (H - a_n)|\phi_n\rangle - b_n|\phi_{n-1}\rangle$$

Thus, in this basis representation the it can be shown that the resultant Hamiltonian matrix takes the tridiagonal form

$$(2.65) \qquad H = \begin{bmatrix} a_0 & b_1 & 0 & 0 & \dots \\ b_1 & a_{1)} & b_2 & 0 & \dots \\ 0 & b_2 & a_2 & b_3 & \dots \\ 0 & 0 & b_3 & a_3 & \dots \\ \vdots & \vdots & \vdots & \vdots & \end{bmatrix}$$

Once the tridiagonal form is obtained the matrix can be easily diagonalized by using standard routines.[39]

The advantage of Lanczos algorithm lies in the fact that the extreme eigenvalues, eigenvalues with the largest or smallest modulus, of the tridiagonal matrix Eqn (2.65) rapidly converges to the extreme values of H for a finite N. However the number of iterations required to completely diagonalize the matrix is equal to the size of the Hilbert space and therefore computationally expensive.

2.3.4 Computation of Expectation Values

ED approach is also a useful to compute expectation values of relevant operators such as the momentum distribution $\langle n(k)\rangle$, $\langle S_i^z S_j^z\rangle$, etc.

The eigenvectors obtained by Lanczos method can be written in the terms of the symmetrized, translationally invariant basis sets $|\phi_m(k)\rangle$ as

$$(2.66) \qquad |\psi(k)\rangle = \sum_m^{N_{class}} b_m |\phi_m(k)\rangle$$

$$(2.67) \qquad = \sum_m^{N_{class}} b_m \left[\frac{1}{\sqrt{N_m}} \sum_{t=0}^{N_m-1} e^{ikt} |m,t\rangle \right]$$

where, b_m's are the coefficients determined by the Lanczos procedure. N_{class} are the number of classes of the complete basis under translation symmetry operation. N_m is the number of members in a class m and $|m,t\rangle$ denotes the tth translation of the stored representative state $|m,0\rangle$.

The basis states are subject to the normalization conditions given by

$$(2.68) \qquad \langle \phi_m|\phi_n\rangle = \delta_{mn} \; ; \; \langle m,t|n,t'\rangle = \delta_{mn}\delta_{tt'} \; ; \; \sum_m^{N_{class}} |b_m^2| = 1$$

Then, the expectation value of an operator $\hat{G}$ in $|\psi(k)\rangle$ is given by

$$(2.69) \qquad \langle\psi|\hat{G}|\psi\rangle = \sum_{m,n} \sum_{t,t'} \frac{b_m^* b_n}{\sqrt{N_m N_n}} e^{ikt} e^{ikt'} \langle m,t|n,t'\rangle$$

If $\hat{G}$ is a diagonal operator then only the terms $m = n$ and $t = t'$ contribute and Eqn (2.68) reduces to

$$(2.70) \qquad \langle\psi|\hat{G}|\psi\rangle = \sum_{m,t} \frac{|b_m^2|}{N_m} \langle m,t|\hat{G}_{diag}|m,t\rangle$$

Eqn (2.69) is straightforward to evaluate.

If $\hat{G}$ is an off diagonal operator say for example $c^\dagger_{i,\sigma} c_{i,\sigma}$ then Eqn (2.68) is rewritten in a translationally invariant form given by

$$(2.71) \qquad \langle \hat{G}(r,\sigma) \rangle \equiv \frac{1}{N_{site}} \sum_i \langle c^\dagger_{i,\sigma} c_{i,\sigma} \rangle$$

This is true for all the off diagonal operators and computation of the expectation value of Eqn (2.70) is similar to the evaluation of the Hamiltonian operator and Eqn (2.51). As is true for Eqn (2.51), the correct evaluation of the normalization factor ($\sqrt{N_m/N_n}$) is crucial for computation of the off diagonal expectation value.

2.4 Bibliography

[1] D. R. Hartree *Proceedings of the Cambridge Philosophical Society*, vol. 24, p. 89, 1928.

[2] V. Fock *Zeitschrift fur Physik*, vol. 61, p. 126, 1930.

[3] P. Hohenberg and W. Kohn *Physical Review*, vol. 136, p. 864, 1964.

[4] W. Kohn and L. J. Sham *Physical Review*, vol. 140, p. 1133, 1965.

[5] J. Hubbard *Proceedings of the Royal Society of London Series A*, vol. 276, p. 238, 1963.

[6] M. C. Gutzwiller *Physical Review Letters*, vol. 10, p. 159, 1963.

[7] P. W. Anderson *Physical Review*, vol. 79, p. 350, 1950.

[8] M. Born and R. Oppenheimer *Annalen der Physik*, vol. 389, p. 457, 1927.

[9] L. H. Thomas *Proceedings of the Cambridge Philosophical Society*, vol. 23, p. 542, 1927.

[10] E. Fermi *Rend. Accad. Naz. Lincei*, vol. 6, p. 602607, 1927.

[11] D. M. Ceperley and B. J. Alder *Physical Review Letters*, vol. 45, p. 566, 1980.

[12] J. P. Perdew and A. Zunger *Physical Review B*, vol. 23, p. 5048, 1981.

[13] J. P. Perdew and Y. Wang *Physical Review B*, vol. 45, pp. 13244–13249, 1992.

[14] R. O. Jones and O. Gunnarsson *Reviews of Modern Physics*, vol. 61, p. 689, 1989.

[15] D. C. Langreth and M. J. Mehl *Physical Review Letters*, vol. 47, p. 446, 1981.

[16] J. P. Perdew and W. Yue *Physical Review B*, vol. 33, p. 8800, 1986.

[17] J. P. Perdew and Y. Wang *Physical Review B*, vol. 45, p. 13244, 1992.

[18] J. P. Perdew, K. Burke, and M. Ernzerhof *Physical Review Letters*, vol. 77, p. 3865, 1996.

[19] Y. Umeno, B. Meyer, C. Elsässer, and P. Gumbsch *Physical Review B*, vol. 74, p. 060101, 2006.

[20] J. C. Slater and G. F. Koster *Physical Review*, vol. 94, p. 1498, 1954.

[21] D. Vanderbilt *Physical Review B*, vol. 41, p. 7892, 1990.

[22] G. Kresse and J. Hafner *Journal of Physics Condensed Matter*, vol. 6, p. 8245, 1994.

[23] J. Korringa *Physica*, vol. 13, p. 392, 1947.

[24] J. Korringa *Physics Reports*, vol. 238, p. 341, 1994.

[25] T. L. Loucks, *Augmented Plane Wave Method*.
New York: W A Benjamin, 1967.

[26] O. K. Andersen and O. Jepsen *Physical Review Letters*, vol. 53, p. 2571, 1984.

[27] C. Herring *Physical Review*, vol. 57, p. 1169, 1940.

[28] C. Herring and A. G. Hill *Physical Review*, vol. 58, p. 132, 1940.

[29] P. E. Blöchl *Physical Review B*, vol. 50, p. 17953, 1994.

[30] J. C. Slater *Physical Review*, vol. 51, p. 846, 1937.

[31] J. C. Slater *Advances in Quantum Chemistry*, vol. 1, p. 35, 1964.

[32] O. K. Andersen *Physical Review B*, vol. 12, p. 3060, 1975.

[33] D. D. Koelling and G. O. Arbman *Journal of Physics F Metal Physics*, vol. 5, p. 2041, 1975.

[34] G. Kresse and D. Joubert *Physical Review B*, vol. 59, p. 1758, 1999.

[35] R. Resta and K. Kunc *Physical Review B*, vol. 34, p. 7146, 1986.

[36] J. Stahn, U. Pietsch, P. Blaha, and K. Schwarz *Physical Review B*, vol. 63, p. 165205, 2001.

[37] A. Nandgaonkar, *Static and Dynamical Properties of Correlated Systems*.
PhD thesis, Department of Physics, University of Pune, 2004.

[38] J. K. Cullum and R. A. Willoughby, "Lanczos algorithims for large symmetric eigenvalue computations volume i: Theory," in *Progress in Scientific Computing*, Birkhauser Boston, 1984.

[39] W. H. Press, S. A. Teukolsky, W. T. Vetterling, and B. P. Flannery, "Numerical recipes the art of scientific computing," Cambridge University Press, 3 ed., 2007.

FIELD TUNABLE MAGNETISM OF AN ADATOM ON BILAYER GRAPHENE*

3.1   Introduction and Motivation

As discussed previously in Chapter 1, magnetism in graphene-based system is of considerable interest from a technological viewpoint. Magnetic graphene provides an opportunity to engineer ultra-thin 2-D magnetic materials which can enhance our current information storage capabilities, give rise to high Curie temperature magnetism as well as have potential applications for spintronics. However, since systems such as pristine graphene and few layer graphene (FLG) are known to be non-magnetic, the introduction of magnetic moments is a crucial requirement for imposing magnetic order in such graphene-systems, the end expectation being able to achieve tunbale magnetism controlled by external means such as gate voltage, strain, etc.

In this regard, adsorbate-induced magnetism in graphene has been well-studied in literature by theory as well as experiment. Theoretically, the adsorption of an atom (an adatom) on the surface of graphene gives rise to sub-lattice imbalance within the system which may lead to the stabilization of localized magnetic states in accordance with Lieb's theorem[1]. Predicted in 2007 by O. Yazyev and L. Helm,[2] magnetism induced by the adsorption of hydrogen atoms on graphene is a landmark case in this regard, with

several experimental and computational studies[2–8] providing evidence in support of the claim. In a recent investigation Herrero *et.al.*, using scanning tunneling microscope (STM) were able to visualize a single hydrogen atom adsorbed on graphene and measure the magnetic moment induced due to it.[8]

In recent years, the synthesis of graphene on metal substrates has prompted studies focusing on metal atom-graphene interactions as metallic impurities introduced during the growth process can have a significant effect on the electronic and magnetic properties of graphene. Furthermore, on consideration that magnetic materials in general tend to be metals, interactions between metal adatoms and graphene is of considerable interest in investigating graphene magnetism. A comprehensive review by Liu *et al* [9] discusses extensively the experimental and computational studies related to the growth morphologies of metal adatoms adsorbed on various substrate supported graphene sheets. In recent years, scanning tunneling microscopy (STM) experiments has been used to study the adsorption behaviour of TM adatoms on substrate supported graphene [10–14]. Of particular interest are the $3d$ transition metal (TM) atoms as they possess large localized magnetic moments. Using a combination of STM and x-ray magnetic circular dichroism (XMCD), T. Eelbo *et.al.*[10] have studied the magnetic cobalt(Co), iron(Fe) and nickel (Ni) adatoms on graphene/SiC which show that Fe and Co adatoms are found in a high-spin ground state with sizable magnitude of spin and orbital moments, while the Ni adatoms are nonmagnetic. A similar investigation by F. Donati *et.al.* [12] for Co adatoms on graphene/Pt(111) using STM spin-excitation spectroscopy found a magnetic moment of 2.2 μ_B localized on the Co adatoms along with large magnetic anisotropy.

The experimental results are also supported by the vast literature based on *ab-initio* studies based on adsorption-induced magnetism of graphene by metal atoms encompassing a broad range from alkali-metal to transition-metal (TM) atoms [15–27]. These first principle investigations show that the mechanism driving the metal adatom-induced magnetism is charge transfer between graphene and the atom adsorbed on the surface of graphene. The directionality of the charge transfer is determined by the positioning of the highest occupied molecular orbital (HOMO) and the lowest occupied molecular orbital (LUMO) of the adatom and the Fermi level of graphene. Charge is transferred from adatom to graphene if the HOMO of adatom is positioned above the Fermi level of graphene while it is reversed if the LUMO of adatom is positioned below the Fermi level of graphene. The studies also show that the magnitude of charge transfer crucially depends on the chemical interaction as well as the relative work function between metal atoms and graphene[28].

These chemical interactions between metal adatoms and graphene have been extensively studied *via ab-initio* calculations in the context of binding energies, nature of bonding, electronic properties and magnetism.[15, 16, 19, 23, 27]. In this context, K. T. Chan *et.al.*[23] as well as X. Liu *et.al.* [27] have provided a comprehensive systematic study of different adatoms including alkali, simple and transition-metal atoms adsorbed on graphene within the framework of density functional theory. The studies show that the interaction between metal adatoms and graphene is highly dependent on the distance between metal adatom and graphene surface and adatom positioning which affects bonding character between the adatom and graphene. It was noted that interactions between alkali-metals and graphene are mostly ionic in character and does not drastically affect the lattice and electronic states of the graphene layer while noble metals, group IV metals and $3d$ transition-metal, demonstrate strong covalent bonding with graphene resulting from strong hybridization between adatom and graphene electronic states. Metal adatoms belonging to group III exhibit mixed ionic and covalent bonding character. Though results from the numerous computational studies performed may vary and not be consistent, some adatoms such as Co and Fe are consistently shown to promote formation of magnetic moments when adsorbed on graphene while alkali metal adatoms such as Al or Na are shown to have either zero or tiny net magnetic moments.

Metal adatoms on graphene have also been studied in the context of Kondo physics[14, 15, 29, 30]. Recently, J. Ren *et. al* reported the first experimental observation of Kondo effect caused by Co adatoms deposited on graphene/Ru(0001) system[14]. Furthermore, the same study also found that the Kondo effect can be tuned by the ripples induced in graphene by the substrate. A first principles calculation by T. Wehling *et. al*[15] demonstrated that depending on the positioning of the magnetic adatoms, the Kondo effect in graphene is affected by the spin-orbit coupling.

Thus, from the above discussion it can be seen that placement of adatoms on graphene may lead to formation of induced local moments within the system. Given that the adatoms do not introduce structural distortions within graphene, the adsorption in most cases being a reversible process and that the positioning of these adatoms can be controlled precisely in experiments by making use of the STM tip, adsorption of atoms on graphene is an effective option to induce graphene magnetism. However, the adatom-graphene system does suffer from certain drawbacks which hinders it's viability for potential applications. One of the major disadvantage is the uncertainty in opening of a band-gap on adsorption of the atoms. In cases where band-gap opening is achieved, it cannot be controlled by external means. Similarly, while changing the carrier

concentration of graphene by gating can affect the formation of induced local magnetic
moments within the system, the precise tuning of these magnetic moments which is
crucial for spintronic applications cannot be achieved within the adatom-graphene model.

In this regard, the disadvantages of the adatom-graphene system can be overcome
by adatom-few layer graphene (FLG) system which exploits the fact that FLG systems
offer an extra tuning parameter. Employing the adatom-FLG system in a dual gate
geometry allows one to control separately the chemical potential on each of the layers
as well as tune the potential of the individual layers by applying an external potential
perpendicular to the system. This provides various advantages over the adatom-graphene
system such as (a) controlling the chemical potential can modify the carrier concentration
in each of the individual layers, (b) application of an electric field normal to the system
breaks the inversion symmetry, which opens a band-gap dependent on the potential
difference (bias) generated due to the top and bottom layers being held at different
potentials[31–34] (c) leads to modification of the FLG quasiparticle wavefunctions which
significantly affects the hybridization between FLG and the adatom (d) as the adatom
position lies close to the top-layer, the application of electric field also results in shifting
the adatom energy levels by an amount proportional to the bias between the top and
bottom layers. Thus, by applying an external electric field perpendicular to adatom-FLG
system one can effectively tune the band gap as well as the adatom energy states relative
to the FLG energy states simultaneously. This opens up the possibility of gaining control
over the local magnetic moments. Furthermore, since the interaction between the adatom
states and FLG quasiparticle states possesses a band and momentum dependence, it
is expected that overall magnetic phase diagram for the adatom-FLG system is much
richer than that of adatom-graphene due to the differences in the low-energy dispersion
characteristics.

In the current chapter, the rich picture of magnetism offered on consideration of
adatom-FLG system is explored within the context of the adatom-bilayer graphene
(BLG) system. Due to it's relevance to the current study, a brief review of literature on
the electronic and magnetic properties of bilayer graphene is provided in the following
section, subsequent to which the details of our investigation are discussed.

3.1.1 Bilayer Graphene

Bilayer graphene (BLG) (refer Figure 3.1) is the simplest generalization of few-layer
graphene where multiple graphene layers are coupled together *via* Van der Waal's in-
teraction as discussed in chapter 1. Bilayer graphene is a semimetal though unlike

graphene it shows a parabolic dispersion near the Fermi energy as is observed from the bandstructure in Figure 3.1.[32, 35]. Bilayer graphene also retains many of the unique features of single-layer graphene like high carrier mobility [36], high eletrical and thermal conductivity [36–38], gate-tunable carrier density[39–41], etc. The presence of two graphene layers gives rise to the possibility of individually tuning the potential on each of the two layers of BLG thereby breaking the inversion symmetry between the two layers. Employing this feature to open band-gaps dependent on an external bias in bilayer graphene (BLG) as well as few layer graphene (FLG) has been discussed theoretically in the context of tight-binding models[35, 42, 43]. The first direct observation of such a tunable band-gap in BLG is credited to T. Ohta *et. al* who employed angle-resolved photoemission spectroscopy (ARPES) to study epitaxial BLG on silicon carbide [41]. Since then band gaps in BLG as well as FLG's have been probed in various experiments using single-gated or dual-gated devices and employing different methods such as photoemission[41], magnetotransport[44], infrared spectroscopy[45–49], scanning tunneling microscopy (STM)[50] and more. Results from optical measurements as well as first principle investigations estimate the band-gap in BLG to be ~ 0.3 eV[48, 49, 51].
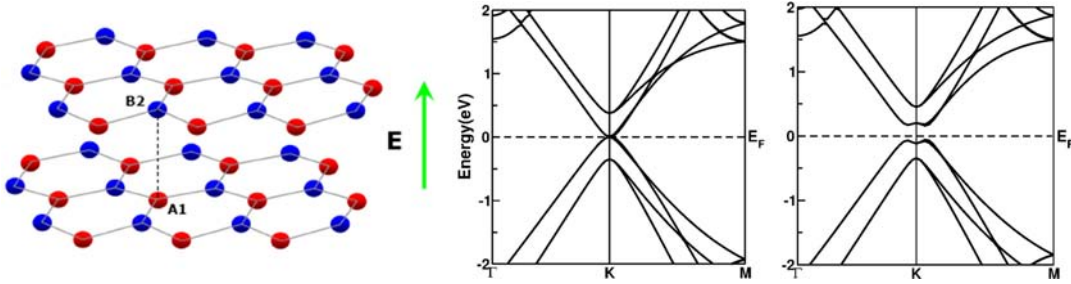
Figure 3.1: Figure shows a schematic showing $\tilde{A}B$ stacked bilayer graphene with the direction of the electric field shown by green arrow (left panel) and the band structure of isolated BLG in absence (middle panel) and in presence of an external electric field of strength U_{ext} = 1 eV (right panel).

Ohta *et. al* also demonstrated that by manipulating the carrier concentration within each of the two graphene layers of BLG may provide control over the electronic structure of BLG.[41] Confirmation was provided by E. V. Castro *et al* who demonstrated control of the bandgap *via* doping by potassium (K) atom.[44] This has generated interest in investigating modification of the electronic structure of BLG through chemical functionalization and metal atom doping. The relevance of such studies is of importance as similar to the case of graphene, substrate supported BLG show signatures of metallic atoms being deposited on BLG during the growth process[52–55] and hence the need for

better understanding of metal adatom-BLG interaction.

Unfortunately, in contrast to available literature on metal atom-doped graphene, research on metal atom-BLG interaction is very limited and mostly investigated within the scope of theoretical and computational methods. T. P. Hardcastle *et. al* studied the adsorption of Al, Cr and Au on single-, bi- and trilayer graphene using DFT and STM.[56] The binding energies and migration activation barriers of the adatoms were calculated. It was observed that the migration activation barrier for the adatoms were smaller than or within an order of magnitude of $k_B T$ demonstrating that adatom mobility on graphene surfaces is high. Recently, electronic and magnetic properties of isolated Mo adatom substitutionally doped in epitaxial bilayer graphene supported on 4H-SiC(0001) was investigated by low temperature STM as well as first principles calculation and it was found doping by Mo is of n-type and that a magnetic moment $\sim 2\ \mu_B$ is introduced in the BLG per Mo adatom.[57] *Ab-inito* calculations on metal adatoms doped on BLG as well as FLG show that similar to graphene alkali metals tend to form ionic bond with the graphene layers while the $3d$ TM atoms and noble metals exhibit covalent bonding. The limited studies on TM metal atoms show that doping by Mn atoms leads to formation of local moments close to $2\ \mu_B$ while Pt atoms adsorbed on vacancy site of BLG possess magnetic moments $\sim 1.2\ \mu_B$.[58, 59]

In the past few years, theoretical model Hamiltonian studies has been carried out on the topic of magnetic impurities on bilayer graphene.[60–63] in regards to it's effect on the electronic structure and magnetism. Furthermore interactions between the magnetic impurities has also been studied in the context of Freidel oscillations and Ruderman-Kittel-Kasuya-Yoshida (RKKY) interactions.[64–66] The RKKY interaction also has been investigated *via* first-principles calculation for the case Fe adatoms on graphene.[67] A comprehensive study within the framework of the Anderson-impurity model was carried out by M. Killi *et al* in regards to the local momement formation as well as it's control.[63] It was shown that presence of adatoms on bilayer graphene modifies the BLG electronic states. The dependence of the electronic structure on varying the chemical potential as well as on varying gate-bias was also studied. The significant observation that gate-bias shifts the adatom energy states lead to the crucial finding of local adatom magnetic moments being turned on or off by applying external electric fields. The effect of an external electric field on the RKKY interaction was also explored in the study.

Motivated by the theoretical results and the interesting prospect of tuning the adatom energy states relative to the BLG states by an external electric field, in the present chapter we discuss the results obtained from our first principles investigation of metal

adatoms on bilayer graphene and the effect of external electric field. As first principles calculation takes into account all the structural aspects, the site preference of the adatom and the chemical aspects correctly it is our belief that the study provides a more realistic insight and verification of the predications made by the model studies. In the current chapter, we investigate the formation of local magnetic moment within the adatom-BLG system and it's manipulation by an external electric field *via* first principles within the framework of DFT for a choice of three adatoms *viz* the alkali metal atom sodium (Na) and the transition metal atoms, copper (Cu) and iron (Fe). It was found that magnetsim of the adatom-BLG system in the absence of eletric field depends on the choice of adatom which characterizes the bonding between adatom and BLG. Application of an external electric field was found to have a significant impact on the local moment formation. A electric field applied perpendicular to BLG was found to switch on magnetism in the case of Na adatom and switch off magnetism in the case of Cu adatom. For the case of Fe adatom an external electric field was found to modulate the charge and spin states of the adatom over a wide range. Furthermore, it was found that the magnetic exchange coupling between two Fe adatoms could also be manipulated by application of small electric fields.

3.2 Computational Details

To investigate the structural, electronic and magnetic properties of adatoms placed on BLG both in absence and presence of an electric field, a first principles calculation within the framework of density functional theory (DFT) was carried out in two choice of basis sets: (a) the plane wave pseudopotential method as implemented within the Vienna *Ab Initio* Package (VASP)[68, 69] and (b) the full-potential linearized augmented plane-wave (FLAPW) method as implemented in WIEN2K[70]. Structural optimization was carried out within the local density approximation (LDA) with a kinetic energy cutoff of 500 eV. Projected Augmented Wave (PAW) potentials were used.[71, 72] All the forces were converged to within 0.01 eV/Å.

To quantify the change in nature of bonding between the adatom and graphene layers, we computed the hybridization index as well as the charge transfer for the adatom-BLG system, brief details of which is given below.

Hybridization Index H_{hyb}

The hybridization index is defined as[73, 74]

$$(3.1) \qquad H_{hyb} = \sum_k \sum_i w^{ad}_{i,k,l} w^{C}_{i,k,p}$$

where $w^{ad}_{i,k,l}$ and $w^{C}_{i,k,p}$ are the projections of the ith Kohn-Sham orbital at the kth point of the Brillouin zone (BZ) onto a spherical harmonic corresponding to the lth orbital centred at the adatom and that to the p spherical harmonic centred at the nearest-neighbour C atom in the graphene layers respectively.

Charge transfer Δq

The charge transfer is defined as[23]

$$(3.2) \qquad \Delta\rho(r) = \rho_{ad-BLG}(r) - \rho_{ad}(r) - \rho_{BLG}(r)$$

where $\rho_{ad-BLG}(r)$, $\rho_{ad}(r)$, $\rho_{BLG}(r)$ are the charge densities of the adatom-BLG system, the adatom without BLG and isolated BLG respectively. In order to have a single quantitative estimate (Δq), the xy plane averaged $\Delta\bar{\rho}(z)$ was integrated from the two graphene layers to the midpoint between the averaged z coordinate of the top layer of BLG and the z coordinate of the adatoms.

Subsequently, we have also carried out a) Γ-point phonon calculations as well as nudged elastic band (NEB) calculations in order to explain the transition from the ferromagnetic (FM) state and ferrimagnetic (FiM) state as well as to determine the transition barrier between the two states for the case of Fe dimer on BLG, the computational considerations of which are given below.

Phonon Calculation

In the case of Fe dimer on BLG, the Γ-point phonon calculations based on the finite-difference method was performed on the Fe dimer-BLG subsystem of the Fe_2/BLG/SiO_2 system. To minimize the computational effort, the Fe atoms along with the C atoms belonging to the rings hosting said Fe atoms were allowed to move. Motion was restricted for the other atoms.

Nudged Elastic Band Calculation

For the nudged elastic band (NEB)[75] calculation, the minimum energy path between the ferromagnetic (FM) and ferrimagnetic (FiM) spin configuration was sampled using climbing-image nudged elastic band method (CI-NEB).[76] A set of five intermediate structures was distributed along the path connecting the FM and FiM configuration. The intermediate structures are connected *via* elastic spring, and each of them is fully relaxed in the hyperspace, perpendicular to the path.

3.3 Results and Discussion

Adatom Site Preference

Adatom positioning on BLG plays a crucial role in the formation of local magnetic moment as it dictates the nature of bonding between the adatom and BLG. Hence, the determination of a favourable adsorbtion site which depends on the choice of the adatom is an important first step of our investigation. As such we model the adatom on BLG by placing one metal (Na, Cu and Fe) adatom on a 4 × 4 BLG supercell, which amounts to a coverage of 1 adatom per 64 C atoms. A vacuum of 16Å was added perpendicular to the BLG in order to avoid interactions between bilayers of neighbouring supercells, due to periodic boundary conditions. Dictated by the geometry of the top graphene layer of BLG, we have considered three adsoprbiton sites of high symmetry as shown in Figure 3.2: the hollow (H) site at the center of the hexagon ring, the bridge (B) site at the midpoint of the carbon-carbon bond and the top (T) site directly above the carbon atom. To ascertain the site preference for the choice of adatom (Na, Cu and Fe) we evaluate the adatom adsorption energy E_{ad}[23] defined as

$$(3.3) \qquad\qquad E_{ad} = E_a + E_{bg} - E_{abg}$$

where E_a is the energy of isolated atom, E_{bg} is the energy of isolated BLG and E_{abg} is the total energy of the adatom-BLG system. Table 3.1 lists the adsorption energy calculated for the three adatoms Na, Cu and Fe adsorbed at the three different sites. The preferred site is estimated by the largest adsorption energy. In addition Table 3.1 also lists the adatom vertical height (h_{ad}) defined as the difference in z coordinate of the adatom and the average z coordinate of the carbon atoms constituting the top layer of
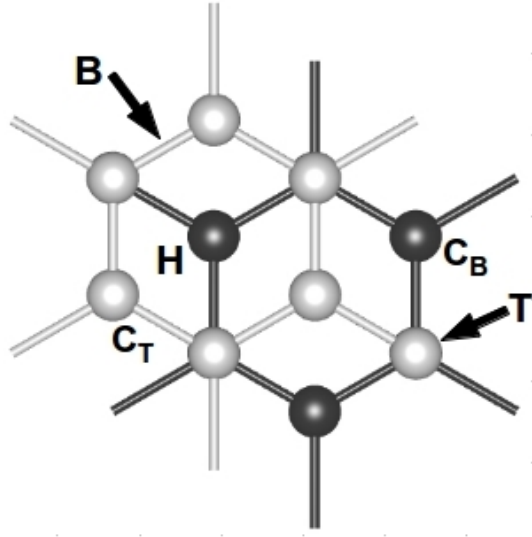
Figure 3.2: The high symmetry adsorption sites of BLG *viz* the hollow site (H), the top
site (T) and the bridge site (B) are marked with black arrows. C_T (light grey balls) and
C_B (dark grey balls) correspond to the carbon atoms belonging to the top and bottom
graphene layers of BLG respectively

BLG, and the distance (d_{ad-c}) between the adatom and the nearest-neighbour carbon
atoms.

From the Table 3.1, we surmise that while Na and Fe prefer the hollow (H) site,
Cu prefers the bridge (B) site over the top (T) site by ∼ 30 meV. Furthermore, we note
that though Na and Fe prefer to sit at the H site, h_{ad} for Fe adatom is found to be
comparatively smaller than for Na adatom, indicating at a change in the nature of
bonding between adatom and BLG as one progresses from alkali metal to transition
metal.

On a closer inspection of the electron configuration of Na ([Ne]3s^1), Cu ([Ar]3d^{1}04s^1)
and Fe ([Ar]3d^{6}4s^2), we note that the chemistry of these adatoms with BLG is governed
by the single half filled s orbital in the case Na and Cu adatoms and the partially-filled
d orbitals in the case of Fe adatom. As such the formation of local magnetic moments
and the effects of electric field were examined in the context of a single orbital *vs* multi
orbital scenario, the results of which are discussed in the following sections. Going a step
further, we investigate the magnetic state of two Fe adatoms placed on BLG and explore
the possibility of manipulating the magnetic exchange coupling through control of the
RKKY interaction between them *via* an electric field.

Atom	Site	E_{ad} (eV)	d_{ad-c} Å	h_{ad}
	H	1.302	2.56	2.117
Na	B^*	—	—	—
	T	1.063	2.39	2.339
	H^*	—	—	—
Cu	B	0.646	2.065	2.011
	T	0.616	1.98	2.196
	H	2.084	2.055	1.439
Fe	B^*	—	—	—
	T	1.135	1.84	1.626

Table 3.1: The structural properties of single metal adatom adsorbed on bilayer graphene. The properties noted are adatom absorption energy E_{ad}, adatom-carbon distance d_{ad-c}, height of adatom from the top graphene sheet h_{ad} $i.e.$, adsorption height for the ground state structure. The result for bridge site of Fe adatom and Na adatom is not shown as during relaxation the adatom tends to move to the hollow site from the bridge site. For similar reasons, the hollow site of Cu adatom is not shown as the adatom tends to move to bridge site from hollow site

3.3.1   Single Orbital Picture: The Case of Na and Cu Adatoms

Preliminary to the study of magnetism and the effect of electric field on it, it is of value to inspect the non-spin-polarized electronic structure of the adatom+BLG system in the absence of electric field, in order to gain insight about the nature of bonding between adatom and BLG and the role it plays in the formation of local magnetic moments within the system.

Nature of bonding

Figure 3.3 shows the non-spin-polarized density of states (DOS) of the adatoms Na and Cu on BLG, in comparison to that of the isolated BLG. The left panels show the DOS projected onto the C atoms of BLG and the adatom states. For Na, projection only to the Na s state is shown, while for Cu projections to both s and d states is shown. The insets show the zoomed view of the total DOS around Fermi energy (E_F). In the right panels, projections onto the C atoms belonging to the top graphene layer and bottom graphene layer of the BLG have been shown separately, which highlights the asymmetry between the two layers brought about by adatom adsorption as well as the different hybridization character of the two adatoms with BLG.

  Analyzing the Na adatom case first, we find that the Na s state lies above E_F
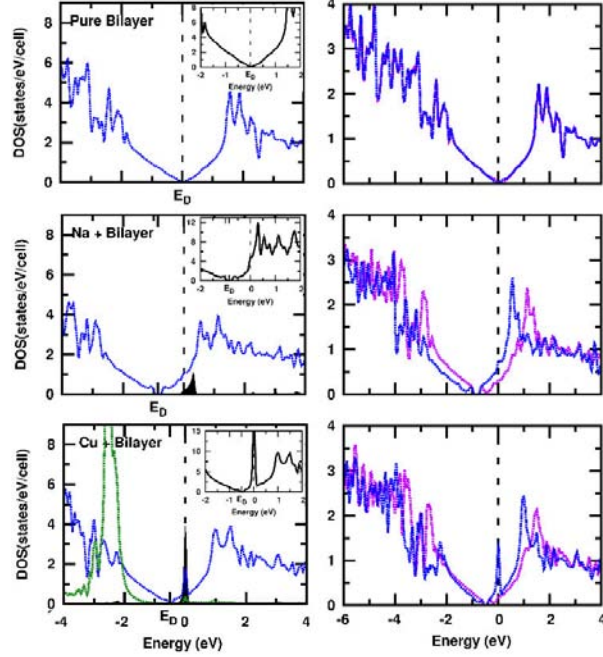
Figure 3.3: Non-spin-polarized density of states for isolated BLG, Na on BLG, Cu on BLG
(from top to bottom). The zero of the energy is set at LDA Fermi energy. The density of
states presented in left panels is projected to C p states (shown as blue/dark gray solid
line), adatom s state (filled area), and adatom d states (shown as green/light gray solid
line). The insets show the total DOS zoomed in region close to E_F. E_D marks the Dirac
point. The right panels show the individual projections to C p states belonging to top
(blue/dark gray line) and bottom (magenta/light gray line) layers of the BLG.

completely unoccupied, indicative of charge transfer between adatom and BLG. This
implies that the nature of bonding between Na and BLG is ionic in character and close
to one electron is transfered from the 3s state of Na to the top graphene layer. This
shifts E_F from the Dirac point E_D, which for the case of isolated BLG is same as E_F.
In addition, adsorption of Na atom also opens a gap ~ 0.16 eV at the E_D. The shape
of the graphene states remains unaltered compared to isolated BLG, indicating little
hybridization between Na and BLG, except for splitting between the states of the two
layers due to the asymmetric charge transfer to the top and bottom layer of BLG.

Switching focus to the case of Cu adatom, we observe that the Cu s state lies exactly
at E_F while the Cu d states lie about ≈ 2.6 meV below E_F as they are fully occupied. The
projected DOS corresponding to the top graphene layer of BLG is substantially modified
compared to isolated BLG with a peak right at E_F, pointing to the covalent nature of
bonding arising due to the hybridization between the Cu s states and the graphene
states, while the bottom layer is hardly influenced by the presence of the adatom. The

addition of Cu opens a gap of ~ 0.1 eV at E_D , which is smaller than that due to Na adatom because of the increased covalency of Cu, compared to Na.
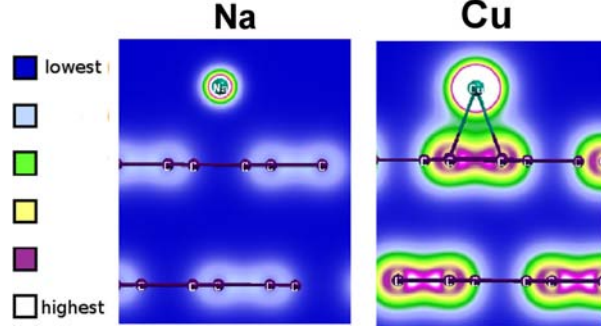
Figure 3.4: The charge density calculated for the Na on BLG, Cu on BLG. The blue and white color represent the lowest and highest contour values [in $e^-/\mathring{A}^3$], respectively, with four intermediate contour values, as shown by the side.

Atom Orbital	BLG Orbital	Hybridization Index	Charge Transfer
Na 3s	bottom layer p	0.012	0.136
	top layer p	0.047	0.645
Cu 4s	bottom layer p	0.021	0.013
	top layer p	0.389	0.026

Table 3.2: Calculated hybridization index and the charge transfer between the adatom and the nearest-neighbor C atom belonging to graphene layers for chosen orbitals.

The change in the nature of bonding between Na and Cu adatoms with BLG, is made evident from the charge density plots of Figure 3.4, projected on the xz plane. The shape of the charge density around the adatom suggests that the participating orbital in the bonding is the s orbital for both Na and Cu. Table 3.2 provides numerical estimates for the charge transfer Δq and the hybridization index H_{hyb}, which is measure of the change in the nature of bonding between the adatom and BLG. From the table we can surmise that the covalent character of the binding of adatom to the graphene layers is relatively strengthened when moving from Na to Cu.

Magnetism

As noted in the previous section, the non-spin-polarized DOS for Cu adatom shows a
highly peaked density of states at E_F, which according to Stoner's criteria [77] indicates
instability towards a magnetic solution. Consequently, the spin-polarized calculation
was performed for Na on BLG and Cu on BLG. From the estimates of the magnetic
moments shown in Table 3.3, we observe a rather small moment (≈ 0.2 μ_B) for Na on
BLG with a tiny moment on the Na site. Conversely, a rather large moment of ≈ 0.95
μ_B was found for Cu on BLG, which is close to the 1 μ_B expected for a single unpaired
electron ($S = 1/2$) in Cu 4s. This is a consequence of the covalent nature of bonding of
Cu s and the nearest-neighbour carbon atoms of the graphene layer with small or no
transfer of electron from the adatom. The computed electronic structure in such a case is
close to the scenario of the Anderson impurity model. The unpaired electron from the
adatom is mostly contained in the sharply peaked DOS at E_F with a small bandwidth,
supporting the formation of the local moment. On the other hand, for Na on BLG, the net
magnetic moment being much smaller than the expected 1 μ_B for the single unpaired
electron in the Na 3s shell, is due to the fact that the transferred electron gets distributed
among the C atoms making up the graphene layers which provide an sp-bonded wide
bandwidth that is unable to support local moment.

Effect of an Electric Field

Since the formation of magnetic moments is dependent on the relative positioning of the
adatom energy levels with respect to that of C energy levels, it is an expectation that
the magnetic moments thus formed maybe tuned by an external electric field applied
perpendicular to the BLG layers. We thus, carried out calculations in the presence of
finite electric field defined in terms of $U_{ext} = e \times E^z_{ex} \times d$, where E^z_{ex} is the external electric
field along the z direction and d being the interlayer separation of BLG (set at 3.31 Å).
The non-spin-polarized density of states projected onto the adatom states and C atoms on
BLG, for various different values of the external electric field is shown in Figure 3.5. The
left panels are for Na on BLG and the right panels are for Cu on BLG. Focusing on the
Na case first, we find that application of the electric field moves the position of the Na s
level to lower energy, and for the choice of $U_{ext} = 3$ eV, the half-filled Na s level lies right
at E_F, making the situation comparable to Cu on BLG in the absence of electric field,
$U_{ext} = 0$ eV. From Table 3.3, the calculated magnetic moment is found to be as large as
0.95 μ_B for $U_{ext} = 3$ eV , which is very close to the fully polarized value of $1\mu_B$ arising out
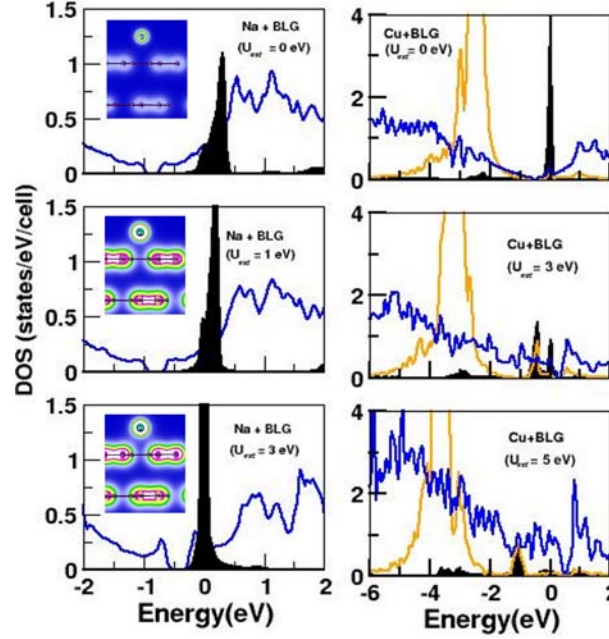
Figure 3.5: Non-spin-polarized density of states for Na on BLG (left panels) and Cu on BLG (right panels) for increasing values of external electric field. The density of states is projected to C states (shown as blue/dark gray, solid lines), adatom s state (filled area), and adatom d states (shown as orange/thin light gray, solid line). For better visibility of adatom s states, the C states have been scaled down by a factor of 4. The insets in left panels show the charge density plots for Na on BLG for corresponding values of applied electric field. The contour values are as in Fig. 3.4

of one unpaired electron. The plot of charge density demonstrates the evolution in the nature of bonding of the Na adatom on BLG from ionic to covalent like upon application of electric field, which further solidifies it's comparison to the case of Cu on BLG for $U_{ext} = 0$ eV.

In contrast, for Cu on BLG the application of electric field moves the peak corresponding to the Cu $4s$ away from E_F, thus making it more occupied due to charge transfer from the graphene layers to Cu s. This is reflected in the computed magnetic moment shown in Table 3.3, which drops from a value of 0.95 μ_B for $U_{ext} = 0$ eV to 0.68 μ_B for $U_{ext} = 3$ eV to a tiny value of 0.03 μ_B for $U_{ext} = 5$ eV. The Cu d states also show a downward shift upon the application of electric field, remaining always fully occupied.

The schematic shown in Figure 3.6, illustrates the movement of Na s and Cu s levels upon increasing value of the external electric field. While for Na on BLG, the increasing external field moves the Na s level closer to E_F, making it from empty to half-filled and hence promoting the formation of magnetic moment, for Cu on BLG the electric field

Site	Na+bilayer			Cu+bilayer		
	Magnetic Moment			Magnetic Moment		
U_{ext}	0eV	1eV	3eV	0eV	3eV	5eV
	0.0001	0.0006	0.0020	0.0079	0.0013	0.0001
	0.0002	0.0005	0.0020	0.0080	0.0010	0.0000
	0.0002	0.0004	0.0020	0.0050	0.0180	0.0001
C(nn)	0.0004	0.0005	0.0036	0.0049	0.0137	0.0001
	0.0003	0.0006	0.0037	0.0083	0.0011	0.0025
	0.0003	0.0007	0.0037	0.0084	0.0009	0.0001
	0.0001	0.0001	0.0005	0.0002	0.0017	0.0001
Adatom	0.023	0.043	0.325	0.695	0.453	0.0017
Interstial	0.165	0.204	0.605	0.198	0.164	0.0252
In Cell	0.187	0.251	0.951	0.949	0.685	0.032

Table 3.3: Calculated magnetic moments (in μ_B) at the adatom site, at the neighboring C atoms to the adatom, at the interstitial, and the total magnetic moment within the cell, calculated for various different values of external electric field. Interstitial refers to the region in between atom-centered muffin-tin spheres, used in the LAPW calculation.

shifts the Cu s level away from E_F, making it from half-filled to filled state, thereby quenching the magnetic moment on the adatom.

3.3.2   Multi Orbital Picture : The Case of Fe Adatom

The single-orbital picture of Na and Cu adatoms on BLG presented in the preceding section leads to a rather simple picture regarding the formation of local magnetic moment and their control, where the local adatom moment can be switched "off" (Cu adatom) or switched "on" (Na adatom). Conversely, in the following discussion we illustrate that the multi-orbital scenario of Fe adatom placed on BLG lends a layer of complexity which can be exploited to control the charge and spin states of the adatom.

For our investigation a single Fe adatom was placed on 6 × 6 supercell of BLG. It is to be noted from the preceding discussions, that the strength of the electric field predicted by DFT for switching on and off the magnetism in the case Na and Cu adatoms respectively is rather large and presumably originates partly due to stronger screening in DFT. As such, in order to obtain more reliable values of electric field and also the motivation to mimic experiments as closely as possible, the Fe/BLG system was mounted on a 3 × 3 × 5 supercell of O-terminated α-quartz SiO_2 dielectric substrate. The last few layers of SiO_2 were kept fixed to mimic the effect of a substrate.
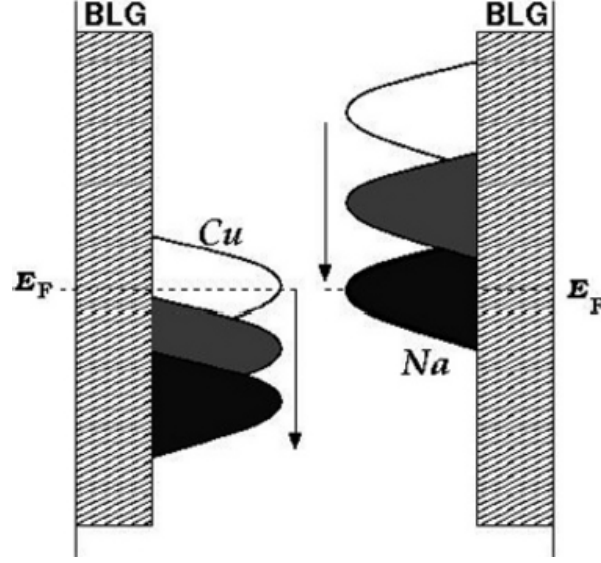
Figure 3.6: Schematic diagram showing the movement of Cu s state and Na s state on BLG, upon application of increasing electric field. The direction of increase of electric field in two cases is shown with arrows.

Nature of Bonding

As in the previous case, we commence by discussing the nature of bonding between the Fe adatom and BLG/SiO$_2$ in the absence of an external electric field. The non-spin-polarized density of states projected on to the Fe d states (top left panel) and the C p states of the top and bottom layer of BLG (top right panel) are shown in Figure 3.7.

The Fe d states show a three-peaked pattern arising from the preference of the Fe adatom to sit on the H site of BLG. The C_{6v} symmetry of the H site lifts the five-fold degeneracy of the d levels and decomposes into two inequivalent two-dimensional irreducible E_1 (d_{yz}, d_{xz}) and E_2 ($d_{x^2-y^2}$, d_{xy}) states, and one one-dimensional A_1 ($d_{3z^2-r^2}$) state. The A_1 state appears between the E_1 and E_2 states with a crystal field splitting, $\epsilon_{E_2} - \epsilon_{E_1} \sim$ -1.0 eV and $\epsilon_{A_1} - \epsilon_{E_1} \sim$ -0.7 eV .

It is noted that the Fe s state is completely unoccupied, the charge being redistributed to Fe d-C p states. The E_1 doublet state lies at E_F, while the E_2 doublet state and A_1 singlet state are completely filled and lie below E_F which indicates a nominal valence configuration of $3d^8 4s^0$ for the Fe adatom. The noticeably strong hybridization between the Fe d and C p states significantly modifies the electronic structure of both the top and bottom layers of BLG, washing out the Dirac point completely. The nature of hybridization between the Fe d states and C p states can be seen from the charge density plots provided in the bottom panel of Figure 3.7. Thus, the bonding between Fe adatom and BLG is
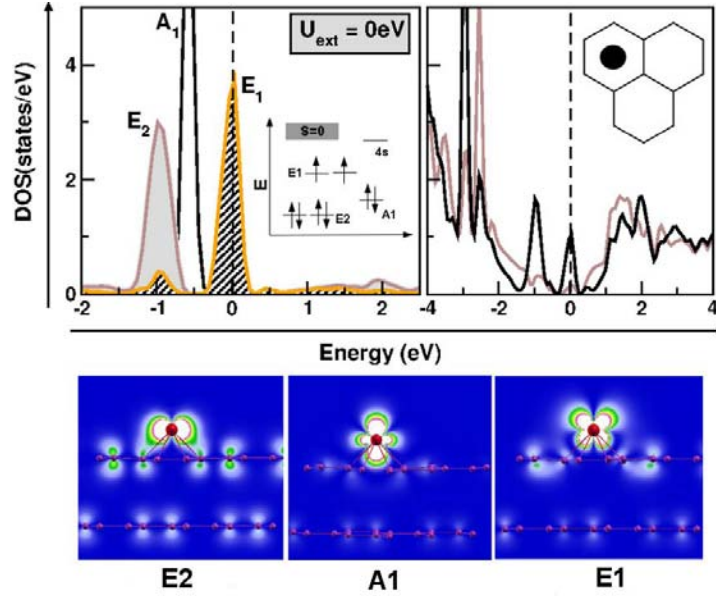
Figure 3.7: Top panel: Non spin-polarized density of states for Fe adatom projected onto
the Fe d manifold and the C p_z orbital (right) of the top graphene layer and bottom
graphene layer of BLG is shown. Bottom panel: The charge density plots showing the
bonding between the E_2, A_1 and E_1 orbitals with the top graphene layer is shown.

strongly covalent, with a greater degree of covalency compared to Cu adatom on BLG
due to the shorter vertical height of the Fe adatom in comparison to Cu adatom (see
Table 3.1) and the different site preference for the Fe adatom (H site) and the Cu adatom
(B site).

Magnetism

The high density of states at E_F indicates a magnetic solution for Fe adatom on BLG/SiO$_2$
according to Stoner's criteria. A spin-polarized calculation found the system to stabilize
in the $S = 1$ state with a total moment of 2 μ_B in the unit cell as noted in Table 3.4. The
magnetism arises from the two unpaired electrons ($S = 1$) residing in the E_1 orbital in
the crystal field split configuration, $E_2(\uparrow\downarrow\uparrow\downarrow) A_1(\uparrow\downarrow) E_1(\uparrow\uparrow)4s^0$. The E_1 ($\uparrow\uparrow$) configuration
leads to an orbitally quenched situation with the effect of spin-orbit coupling (SOC) being
minimal. The S = 1 state in the d^8 configuration has been discussed in the context of Co
on SLG[15] and for such a scenario, a rather high Kondo temperature has been predicted.
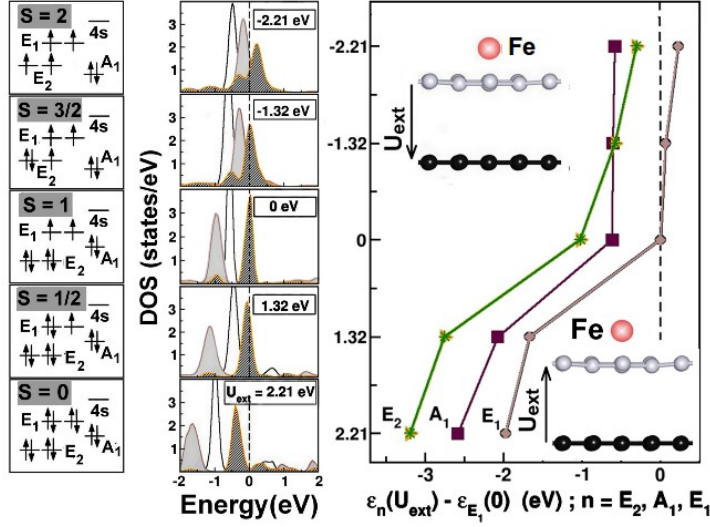
Figure 3.8: Middle panel: The non spin-polarized LDA density of states for single Fe adatom on BLG/SiO$_2$ projected onto Fe-E_2 (light shaded), Fe-E_1 (dark shaded) and Fe-A_1 (unshaded) states, corresponding to different applied electric field. The strength of the electric field is defined as $U_{ext} = e \times E^z_{ext} \times d$, where E^z_{ext} is the external electric field along the direction perpendicular to BLG and d is the intralayer separation of BLG ($\sim$ 3.31 Å). The direction of the electric field is considered to be positive while applied along the +z direction (bottom to the top layer of BLG), and vice versa. The zero of the energy is set at Fermi energy in each panel. Left panel: The corresponding nominal occupancies of Fe d states are shown by side which determine the charge and spin state of Fe. Right panel:The energy positions of E_2, E_1 and A_1 states measured with respect to the position of E_1 at zero electric field.

Effect of Electric Field

Application of the external electric field appreciably tunes the energy states of the Fe adatom with respect to the BLG states leading to formation of new charge and spins states. Figure 3.8 depicts the effect of the external electric field on the adatom density of states. On applying the electric field in the +z direction (directed from bottom to top layer of BLG), the Fe d states rearrange with respect to BLG states such that charge transfer takes place from BLG to Fe d states.

Thus, depending on the strength of the external electric field, the Fe d states become progressively filled thereby stabilizing in a $3d^9 4s^0$, $S = 1/2$ state for $U_{ext} = 1.32$ eV and a nonmagnetic $S = 0$ state with a completely filled d state with a nominal valence configuration of $3d^{10} 4s^0$ for $U_{ext} = 2.21$ eV of the Fe adatom. Switching the electric field to opposite direction, pointing along the $-z$ axis, reverses the direction of charge transfer *i.e.* from Fe adatom to BLG. Conversely, depending on the field strength the charge on

U_{ext} eV	Charge State	Orbital Moment (μ_B)	Spin Moment (μ_B)
-2.21	d^6	0.014	3.793
-1.32	d^7	0.238	2.928
0.00	d^8	0.015	1.942
1.32	d^9	0.219	0.970
2.21	d^{10}	0.002	0.030

Table 3.4: Calculated values of spin and orbital magnetic moments at Fe site for different values of electric field.

the Fe adatom gets progressively depleted leading to formation of $3d^7 4s^0$, $S = 3/2$ state and $3d^6 4s^0$, $S = 2$ states for U_{ext} = -1.32 eV and -2.21 eV. Reversing the electric field has the additional effect of switching the ordering of A_1 and E_2 energy levels (right panel of Fig 3.8). Due to its $d_{3z^2-r^2}$ symmetry the A_1 orbital has a strong bonding with the C p_z orbital and thus moves only marginally when the electric field is applied along the $-z$ direction. In contrast, the relatively loosely bonded E_2 and E_1 states appreciably move in energy, and the movement is found to be larger for E_2 and E_1.

The d^9 and d^7 configurations are expected to be orbitally active, with unpaired electron in the E_1 and E_2 state respectively and thus a check was done to study the plausible effect of spin-orbit coupling (SOC). Table 3.4 gives the calculated orbital and spin moments for the Fe adatom. For the d^{10}, d^8 and d^6 configurations the orbital moments are found to be tiny (~ 0.01 μ_B or less) which is expected. In contrast, the contribution of the orbital moment is quite significant (0.22-0.24 μ_B) for d^9 and d^7 configuration with the orbital moment pointing in the same direction as the spin moment.

3.3.3   Manipulation of Magnetic Exchange Coupling: The Case of Fe dimer

In order to investigate the nature of magnetic interaction between adatoms on BLG, two Fe adatoms were placed at the centers of adjacent hexagon rings along the zigzag direction on BLG/SiO$_2$ as shown in Figure 3.9. The Fe dimer-like configuration of the Fe$_2$/BLG/SiO$_2$ system was studied in the absence as well as in the presence of electric field for both parallel as well as anti-parallel alignment of Fe spins.
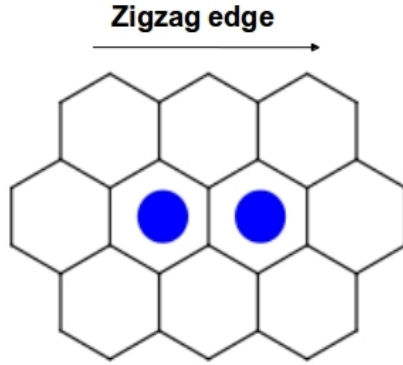
Figure 3.9: The schematic shows the arrangement of the two Fe adatoms (blue circles) atop the top graphene layer of BLG. The bottom layer is not shown for convenience

Magnetism

The optimized geometries for both the parallel and anti-parallel spin configurations of the Fe_2/BLG/SiO_2 system in the absence of electric field are shown in left panel of Figure 3.10. The parallel or ferromagnetic (FM) configuration of Fe spins was found to be the ground state over the anti-parallel spin configuration by ~ 0.26 eV. For the ferromagnetic ground state, the local magnetic moment per Fe adatom was found to be 2.6 μ_B with both Fe atoms being at the same height (1.66 Å) from the BLG plane. A total spin of $S = 3$ was found for the Fe_2/BLG/SiO_2 system. In contrast, the anti-parallel arrangement of Fe spins yields a rather surprising and interesting result. As shown in Figure 3.10 for the anti-parallel spin configuration, the heights of the Fe atoms above BLG turned out to be different *i.e.* 1.66 Å and 1.38 Å respectively, as one of the Fe atom is pushed towards the BLG plane. Due to the difference in heights the up and down Fe atoms couple differently with the BLG, and the different hybridization between Fe d and C p states promotes the formation of different local moments *i.e.* 2.69 μ_B and -0.91 μ_B. Thus the Fe dimer stabilizes into a ferrimagnetic (FiM) configuration with a net moment of 2 μ_B for Fe_2/BLG/SiO_2 system, rather than a fully compensated anti-ferromagnetic state due to significant magnetostructural deformation.

The evidence of such strong magnetostructural coupling within the Fe_2/BLG/SiO_2 system becomes very apparent on computation of the phonon spectra for both FM and FiM states of the Fe dimer as shown in the right panel of Figure 3.10. The calculated Γ-point phonon shows notable softening of the phonon modes (indicated by arrows in figure) upon change in the magnetic configuration of the Fe dimer. An analysis of the displacement vectors corresponding to the soft phonon modes (representative one shown
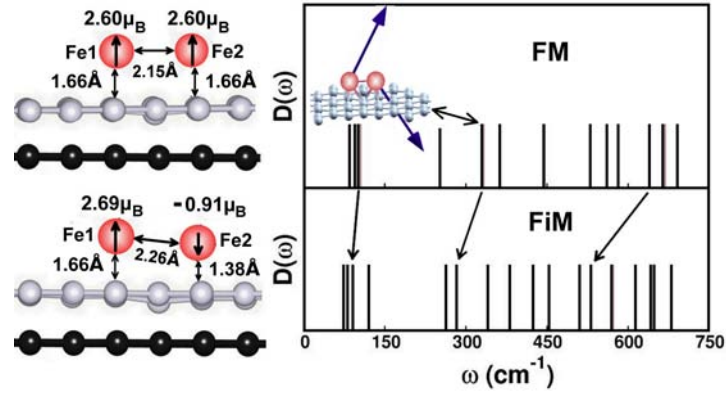
Figure 3.10: Left panels:The side view of the optimized structure of the Fe dimer on BLG/SiO$_2$ in FM (top) and FiM (bottom) alignment of Fe spins. Only the Fe$_2$/BLG is shown and SiO$_2$ is omitted for clarity. Right panel: The corresponding Γ-point phonon spectra D(ω) plotted as a function of frequency ω. The displacement vectors corresponding to the mode at ~258 cm^{-1} are shown in the inset of the top panel

in the inset of Figure 3.10) indicate that the movement of the Fe atoms is primarily along the $+z$ and $-z$ directions, along with some in-plane components. The above emphasizes the existence of strong spin-phonon coupling within the system being the root cause for the observed magnetostructural deformation that needs to be investigated further.

Effect of Electric Field

As discussed in the previous section, the change in spin alignment of the Fe dimer is accompanied by a change in spin direction as well as a strong asymmetric structural change giving rise to different local Fe moments. In order to estimate the energy barrier between the FM and FiM spin alignments, a nudged elastic band (NEB) calculation was carried out, the results of which are shown in the left panel of Figure 3.11. It is observed that the FiM has a shallow minima which is separated from the FM ground state by an energy barrier of ~ 0.27 eV, which is almost equal to the energy difference(~ 0.26 eV) between these two magnetic states. This rouses the expectation that it may be possible to tune the magnetic configuration from FM to FiM by an external electric field by manipulating the energy states of the delocalized electrons of the BLG which mediate the RKKY interaction. The effect of electric field on the RKKY interaction between local moments placed on BLG has been studied in the context of model Hamiltonian calculation.[63] The study predicts that both the magnitude as well as the sign of the RKKY interaction can be manipulated on application of an external electric field.

Moreover, the change in sign occurs over a narrow range of electric field and for a particular field direction.
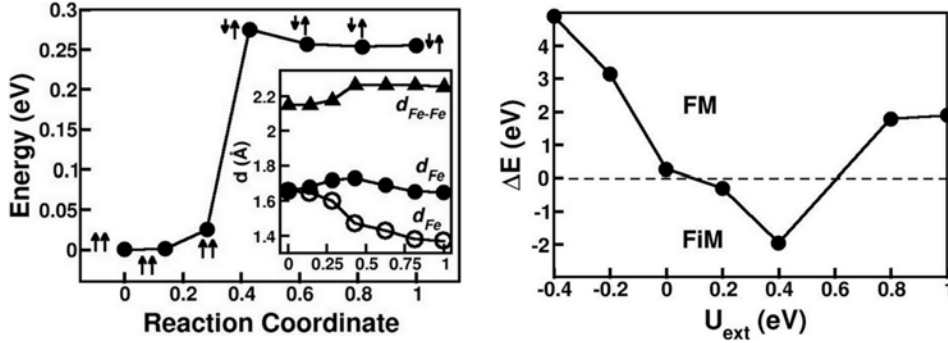
Figure 3.11: Left panel: Energy plotted as a function of reaction coordinate connecting the Fe dimer on BLG/SiO_2 in FM and FiM configurations, which involves a change in alignment and magnitude of the Fe moments as well as the geometry. The inset shows the evolution of the bond length in the Fe-Fe dimer (triangular symbols); the height of Fe1(Fe2) from the top layer of BLG is shown in the open circle (closed circle) as a function of the reaction coordinate. Right panel: The energy difference between FM and FiM configurations of Fe spins as a function of applied electric field.

The right panel of Figure 3.11 shows the energy difference between FM and FiM configurations of the Fe dimer on BLG, as a function of the external electric field from our *ab-initio* calculations. It is observed that the FiM state with the asymmetric structure indeed becomes the ground state over the FM state for small range of electric field, U_{ext} = +0.2 eV to +0.4 eV. The reentrant FM configuration is observed on increasing the electric field strength beyond +0.4 eV. Furthermore, switching of exchange coupling is not observed when the direction of the external electric field is reversed, rather further stabilization of the FM state is observed.

The conclusions of our *ab-initio* calculations are in remarkable agreement with the model calculation which conclusively indicate the RKKY interaction to be the driving mechanism behind the magnetic exchange.

3.4 Conclusion

We have investigated through first-principle calculations, the adsorption of an alkali metal adatom such as Na and transition-metal adatoms such as Cu and Fe on bilayer graphene (BLG), with the aim of studying formation of local moment and it's manipulation by an external electric field. The study encompasses the geometric properties,

bonding properties, electronic structure and magnetic properties of adatoms on BLG. The
importance of orbital physics in determining the magnetic properties is also explored in
the context of single-orbital cases such as Na and Cu, for which it is the s orbital of the
adatom that plays a key role in magnetism, as well as multi-orbital cases like Fe where
it is the d orbital manifold of the adatom which plays the key role.

Our study concludes, that ionic bonding between Na and BLG disfavors formation
of a local moment, while the covalent nature of bonding with minimal charge transfer
between adatom and BLG, as in the case of Cu and Fe, promotes the formation of
a local magnetic moment. Application of an external electric field perpendicular to
bilayer graphene moves the adatom energy states relative to the graphene states thereby
completely changing scenario. In the single-orbital scenario of Na and Cu adatoms, this
leads to a change in the character of adatom-BLG bonding from ionic to more covalent-
like and vice versa which results in swicthing "on" of adatom magnetism in the case of
Na and switching "off" of adatom magnetism in the case of Cu.

In the multi-orbital scenario of Fe adatom on BLG, the application of an external
electric field can modulate the charge and spin states of the Fe atom over a wide range
depending on the strength and direction of the electric field. States ranging from $3d^6$,
$S = 2$ to $3d^{10}$, $S = 0$ were observed for the Fe adatom resulting from the rearrangement of
the Fe d states with respect to that of the C p states of BLG depending on the magnitude
of electric field and direction of charge transfer. The realization of the unusual valence
and spin states of the Fe adatom on BLG should be interesting to produce orbitally
controlled Kondo effect as well as other spintronic applications.

The manipulation of the magnetic exchange coupling between two local moments
placed on BLG, was studied in the case of Fe dimer on BLG. For Fe dimer on BLG, the
parallel Fe spin configuration was found to be the ground state over the anti-parallel
spin configuration. The anti-parallel alignment of Fe spins was accompanied by strong
magnetostructural coupling resulting in the formation of an uncompensated ferrimag-
netic (FiM) state over the fully compensated anti-ferromagnetic state. The application of
an electric field allowed for the tuning of the magnetic exchange coupling to be switched
from the Fe-Fe FM coupling to FiM coupling due to the manipulation of the RKKY
interaction *via* the modification of the electronic states of the delocalized electrons of the
BLG.

Thus, the theoretical finding of external electric field controlled tuning of the mag-
netic moments as well as magnetic exchange coupling discussed in this chapter are of
considerable interest and should motivate and promote future experiments.

3.5 Bibliography

[1] E. H. Lieb *Physical Review Letters*, vol. 62, p. 1201, 1989.

[2] O. V. Yazyev and L. Helm *Physical Review B*, vol. 75, p. 125408, 2007.

[3] J. O. Sofo, G. Usaj, P. S. Cornaglia, A. M. Suarez, A. D. Hernández-Nieves, and C. A. Balseiro *Physical Review B*, vol. 85, p. 115405, 2012.

[4] D. C. Elias, R. R. Nair, T. M. G. Mohiuddin, S. V. Morozov, P. Blake, M. P. Halsall, A. C. Ferrari, D. W. Boukhvalov, M. I. Katsnelson, A. K. Geim, and K. S. Novoselov *Science*, vol. 323, p. 610, 2009.

[5] K. M. McCreary, A. G. Swartz, W. Han, J. Fabian, and R. K. Kawakami *Physical Review Letters*, vol. 109, p. 186604, 2012.

[6] D. W. Boukhvalov, M. I. Katsnelson, and A. I. Lichtenstein *Physical Review B*, vol. 77, p. 035427, 2008.

[7] A. J. M. Giesbers, K. Uhlířová, M. Konečný, E. C. Peters, M. Burghard, J. Aarts, and C. F. J. Flipse *Physical Review Letters*, vol. 111, p. 166101, 2013.

[8] H. González-Herrero, J. M. Gómez-Rodríguez, P. Mallet, M. Moaied, J. J. Palacios, C. Salgado, M. M. Ugeda, J.-Y. Veuillen, F. Yndurain, and I. Brihuega *Science*, vol. 352, p. 437, 2016.

[9] X. Liu, Y. Han, J. W. Evans, A. K. Engstfeld, R. J. Behm, M. C. Tringides, M. Hupalo, H.-Q. Lin, L. Huang, K.-M. Ho, D. Appy, P. A. Thiel, and C.-Z. Wang *Progress In Surface Science*, vol. 90, p. 397, 2015.

[10] T. Eelbo, M. Waśniowska, P. Thakur, M. Gyamfi, B. Sachs, T. O. Wehling, S. Forti, U. Starke, C. Tieg, A. I. Lichtenstein, and R. Wiesendanger *Physical Review Letters*, vol. 110, p. 136804, 2013.

[11] Z. J. Wang, A. Dong, M. Wei, Q. Fu, and X. Bao *Applied Physics Letters*, vol. 104, p. 181604, 2014.

[12] F. Donati, Q. Dubout, G. Autès, F. Patthey, F. Calleja, P. Gambardella, O. V. Yazyev, and H. Brune *Physical Review Letters*, vol. 111, p. 236801, 2013.

[13] M. Gyamfi, T. Eelbo, M. Waśniowska, and R. Wiesendanger *Physical Review B*, vol. 84, p. 113403, 2011.

[14] J. Ren, H. Guo, J. Pan, Y. Y. Zhang, X. Wu, H.-G. Luo, S. Du, S. T. Pantelides, and
H.-J. Gao *Nano Letters*, vol. 14, p. 4011, 2014.

[15] T. O. Wehling, A. V. Balatsky, M. I. Katsnelson, A. I. Lichtenstein, and A. Rosch
Physical Review B, vol. 81, p. 115427, 2010.

[16] T. O. Wehling, A. I. Lichtenstein, and M. I. Katsnelson *Physical Review B*, vol. 84,
p. 235110, 2011.

[17] L. Hu, X. Hu, X. Wu, C. Du, Y. Dai, and J. Deng *Physica B Condensed Matter*,
vol. 405, p. 3337, 2010.

[18] M. Wu, C. Cao, and J. Z. Jiang *New Journal of Physics*, vol. 12, p. 063020, 2010.

[19] C. Cao, M. Wu, J. Jiang, and H.-P. Cheng *Physical Review B*, vol. 81, p. 205424,
2010.

[20] Y. Mao, J. Yuan, and J. Zhong *Journal of Physics Condensed Matter*, vol. 20,
p. 115209, 2008.

[21] R. Varns and P. Strange *Journal of Physics Condensed Matter*, vol. 20, p. 225005,
2008.

[22] B. Uchoa, C.-Y. Lin, and A. H. Castro Neto *Physical Review B*, vol. 77, p. 035420,
2008.

[23] K. T. Chan, J. B. Neaton, and M. L. Cohen *Physical Review B*, vol. 77, p. 235430,
2008.

[24] Y. Sanchez-Paisal, D. Sanchez-Portal, and A. Ayuela *Physical Review B*, vol. 80,
p. 045428, 2009.

[25] H. Sevinçli, M. Topsakal, E. Durgun, and S. Ciraci *Physical Review B*, vol. 77,
p. 195434, 2008.

[26] A. V. Krasheninnikov, P. O. Lehtinen, A. S. Foster, P. Pyykkö, and R. M. Nieminen
Physical Review Letters, vol. 102, p. 126807, 2009.

[27] X. Liu, C. Z. Wang, Y. X. Yao, W. C. Lu, M. Hupalo, M. C. Tringides, and K. M. Ho
Physical Review B, vol. 83, p. 235411, 2011.

[28] G. Giovannetti, P. A. Khomyakov, G. Brocks, V. M. Karpan, J. van den Brink, and P. J. Kelly *Physical Review Letters*, vol. 101, p. 026803, 2008.

[29] D. Jacob and G. Kotliar *Physical Review B*, vol. 82, p. 085423, 2010.

[30] L. Li, Y.-Y. Ni, Y. Zhong, T.-F. Fang, and H.-G. Luo *New Journal of Physics*, vol. 15, p. 053018, 2013.

[31] A. A. Avetisyan, B. Partoens, and F. M. Peeters *Physical Review B*, vol. 79, p. 035421, 2009.

[32] J. Nilsson, A. H. Castro Neto, F. Guinea, and N. M. R. Peres *Physical Review B*, vol. 78, p. 045405, 2008.

[33] K. Tang, R. Qin, J. Zhou, H. Qu, J. Zheng, R. Fei, H. Li, Q. Zheng, Z. Gao, and J. Lu *The Journal of Physical Chemistry C*, vol. 115, p. 9458, 2011.

[34] C. H. Lui, Z. Li, K. F. Mak, E. Cappelluti, and T. F. Heinz *Nature Physics*, vol. 7, p. 944, 2011.

[35] B. Partoens and F. M. Peeters *Physical Review B*, vol. 74, p. 075404, 2006.

[36] C. R. Dean, A. F. Young, I. Meric, C. Lee, L. Wang, S. Sorgenfrei, K. Watanabe, T. Taniguchi, P. Kim, K. L. Shepard, and J. Hone *Nature Nanotechnology*, vol. 5, p. 722, 2010.

[37] A. A. Balandin *Nature Materials*, vol. 10, p. 569, 2011.

[38] S. Ghosh, W. Bao, D. L. Nika, S. Subrina, E. P. Pokatilov, C. N. Lau, and A. A. Balandin *Nature Materials*, vol. 9, p. 555, 2010.

[39] K. S. Novoselov, E. McCann, S. V. Morozov, V. I. Fal'Ko, M. I. Katsnelson, U. Zeitler, D. Jiang, F. Schedin, and A. K. Geim *Nature Physics*, vol. 2, p. 177, 2006.

[40] K. S. Novoselov, A. K. Geim, S. V. Morozov, D. Jiang, Y. Zhang, S. V. Dubonos, I. V. Grigorieva, and A. A. Firsov *Science*, vol. 306, p. 666, 2004.

[41] T. Ohta, A. Bostwick, T. Seyller, K. Horn, and E. Rotenberg *Science*, vol. 313, p. 951, 2006.

[42] E. McCann *Physical Review B*, vol. 74, p. 161403, 2006.

[43] E. V. Castro, K. S. Novoselov, S. V. Morozov, N. M. R. Peres, J. M. B. Lopes dos
     Santos, J. Nilsson, F. Guinea, A. K. Geim, and A. H. Castro Neto *Journal of
     Physics Condensed Matter*, vol. 22, p. 175503, 2010.

[44] E. V. Castro, K. S. Novoselov, S. V. Morozov, N. M. R. Peres, J. M. B. L. Dos Santos,
     J. Nilsson, F. Guinea, A. K. Geim, and A. H. C. Neto *Physical Review Letters*,
     vol. 99, p. 216802, 2007.

[45] L. M. Zhang, Z. Q. Li, D. N. Basov, M. M. Fogler, Z. Hao, and M. C. Martin *Physical
     Review B*, vol. 78, p. 235408, 2008.

[46] A. B. Kuzmenko, I. Crassee, D. van der Marel, P. Blake, and K. S. Novoselov *Physical
     Review B*, vol. 80, p. 165406, 2009.

[47] A. B. Kuzmenko, E. van Heumen, D. van der Marel, P. Lerch, P. Blake, K. S.
     Novoselov, and A. K. Geim *Physical Review B*, vol. 79, p. 115441, 2009.

[48] K. F. Mak, C. H. Lui, J. Shan, and T. F. Heinz *Physical Review Letters*, vol. 102,
     p. 256405, 2009.

[49] Y. Zhang, T.-T. Tang, C. Girit, Z. Hao, M. C. Martin, A. Zettl, M. F. Crommie, Y. R.
     Shen, and F. Wang *Nature*, vol. 459, p. 820, 2009.

[50] A. Deshpande, W. Bao, Z. Zhao, C. N. Lau, and B. J. LeRoy *Applied Physics Letters*,
     vol. 95, p. 243502, 2009.

[51] H. Min, B. Sahu, S. K. Banerjee, and A. H. MacDonald *Physical Review B*, vol. 75,
     p. 155115, 2007.

[52] J. Zheng, Y. Wang, L. Wang, R. Quhe, Z. Ni, W.-N. Mei, Z. Gao, D. Yu, J. Shi, and
     J. Lu *Scientific Reports*, vol. 3, p. 2081, 2013.

[53] Q. Wang, L. Wei, M. Sullivan, S.-W. Yang, and Y. Chen *RSC Advances*, vol. 3, p. 3046,
     2013.

[54] W. Chen, P. Cui, W. Zhu, E. Kaxiras, Y. Gao, and Z. Zhang *Physical Review B*, vol. 91,
     p. 045408, 2015.

[55] K. M. McCreary, K. Pi, A. G. Swartz, W. Han, W. Bao, C. N. Lau, F. Guinea, M. I.
     Katsnelson, and R. K. Kawakami *Physical Review B*, vol. 81, p. 115453, 2010.

[56] T. P. Hardcastle, C. R. Seabourne, R. Zan, R. M. D. Brydson, U. Bangert, Q. M. Ramasse, K. S. Novoselov, and A. J. Scott *Physical Review B*, vol. 87, p. 195430, 2013.

[57] W. Wan, H. Li, H. Huang, S. L. Wong, L. Lv, Y. Gao, and A. T. S. Wee *ACS Nano*, vol. 8, p. 970, 2014.

[58] Y. Mao and J. Zhong *Nanotechnology*, vol. 19, p. 205708, 2008.

[59] Y. Tang, H. Zhang, Z. Shen, M. Zhao, Y. Li, and X. Dai *RSC Advances*, vol. 7, p. 33208, 2017.

[60] J. Nilsson and A. H. Castro Neto *Physical Review Letters*, vol. 98, p. 126801, 2007.

[61] C. Bena *Physical Review Letters*, vol. 100, p. 076601, 2008.

[62] J. H. Sun, F. M. Hu, H. K. Tang, and H. Q. Lin *International Journal of Modern Physics B*, vol. 27, p. 1362039, 2013.

[63] M. Killi, D. Heidarian, and A. Paramekanti *New Journal of Physics*, vol. 13, p. 053043, 2011.

[64] S. Saremi *Physical Review B*, vol. 76, p. 184430, 2007.

[65] M. Sherafati and S. Satpathy *Physical Review B*, vol. 83, p. 165425, 2011.

[66] E. H. Hwang and S. Das Sarma *Physical Review Letters*, vol. 101, p. 156802, 2008.

[67] X. Liu, C. Z. Wang, M. Hupalo, W.-C. Lu, P. A. Thiel, K. M. Ho, and M. C. Tringides *Physical Review B*, vol. 84, p. 235446, 2011.

[68] G. Kresse and J. Hafner *Physical Review B*, vol. 47, p. 558, 1993.

[69] G. Kresse and J. Furthmüller *Physical Review B*, vol. 54, p. 11169, 1996.

[70] P. Blaha, K. Schwarz, G. K. H. Masden, D. Kvasnicka, and J. Luitz, "Wien2k, an augumented planewave + local orbitals program for calculating crystal properties," in *Wien2k, An Augumented PlaneWave + Local Orbitals Program for Calculating Crystal Properties* (K. Schwarz, ed.), Technische Universitiät Wien, Vienna, 2001.

[71] P. E. Blöchl *Physical Review B*, vol. 50, p. 17953, 1994.

[72] G. Kresse and D. Joubert *Physical Review B*, vol. 59, p. 1758, 1999.

[73] H. Häkkinen, M. Moseler, and U. Landman *Physical Review Letters*, vol. 89,
p. 033401, 2002.

[74] H. Häkkinen, B. Yoon, U. Landman, X. Li, H.-J. Zhai, and L.-S. Wang *The Journal
of Physical Chemistry A*, vol. 107, p. 6168, 2003.

[75] G. Henkelman and H. Jónsson *Journal of Chemical Physics*, vol. 113, p. 9978, 2000.

[76] G. Henkelman, B. P. Uberuaga, and H. Jónsson *Journal of Chemical Physics*,
vol. 113, p. 9901, 2000.

[77] E. C. Stoner *Proceedings of the Royal Society of London Series A*, vol. 165, p. 372,
1938.

MAGNETISM DRIVEN BY LONG-RANGE COULOMB INTERACTION IN GRAPHENE NANOFLAKES*

4.1   Background

Nanographene systems are finite-sized form of graphene and include systems such as graphene nanoflakes and graphene nanoribbons, which are the 0D and quasi-1D forms of graphene, respectively. In contrast to graphene, which is non-magnetic, experiments have reported magnetism in nanographene.[1–5] The magnetic nature of nanographene systems stems from the presence of edge states as a result of the unsaturated p_z orbitals which are created on termination of the graphene sheet. Various studies have also shown that the magnetic properties of graphene nanoribbons are size dependent and therefore tunable [1, 2, 6–11]. In this regard, graphene nanoflakes have garnered particular attention as unlike graphene nanoribbons, their magnetic properties are also shape dependent. The dependence of graphene nanoflake electronic structure on size and shape results in their electronic and magnetic properties spanning from molecular to 2D. The growing interest in graphene nanoflakes due to their potential applications to future technologies have prompted studies, both at theoretical and experimental level, to investigate the electronic and magnetic properties of these systems.

It is known from solid-state physics, that magnetic ordering in materials arises due to "correlated" motions of electrons. Therefore, the inclusion of electron-electron interactions which take into account these correlations becomes necessary for studying the onset of magnetism within materials. In this regard, the standard Hubbard model has proven to be quite robust in explaining the properties of many magnetic materials involving the d- or f- block elements such as transition metal oxides. Interestingly, it has also been successful in explaining magnetism of sp^2 carbon materials like graphene and graphene based materials where each carbon atom contributes one p_z orbital and a single π electron per site.

The one orbital extended Hubbard model[12] is defined as

$$H = -t \sum_{\langle i,j \rangle, \sigma} [c_{i,\sigma}^\dagger c_{j,\sigma} + h.c.] + U \sum_i n_{i,\uparrow} n_{i,\downarrow} + V \sum_{\langle i,j \rangle, \sigma, \sigma'} n_{i,\sigma} n_{j,\sigma'}$$

where $c_{i,\sigma}^\dagger$ and $c_{i,\sigma}$ are operators which create and annihilate an electron with spin σ at site i respectively and '$h.c.$' stands for it's hermitian conjugate counterpart. t is the nearest neighbor hopping term and the notation $\langle .,. \rangle$ denotes that only nearest-neighbor interactions are included. The electron correlations are introduced through the terms U and V. The term U represents the repulsive on-site Coulomb interaction and is a short-range interaction term. For graphene systems, this implies that two electrons interact only if they occupy the same p_z orbital of the same atom. The term V represents the repulsive inter-site Coulomb interaction term and, unlike U it is a long-range interaction term. Since the strength of the V term is much weaker than that of U, it is generally neglected except in some special instances where it plays an important role that will be discussed in the subsequent sections. Dropping of the V term reduces the above Hamiltonian to the standard Hubbard Hamiltonian.

For an appropriate value of U/t it has been shown that the mean-field Hubbard model calculation reproduces closely the results from first principles calculations for graphene with $U/t \sim 1.0\text{-}1.5$ providing best fitting for DFT results[7, 13, 14]. Likewise, the one orbital Hubbard model can also be used to explain the magnetism observed due to presence of localized edge states in graphene nanoflakes.

In the subsequent sections we discuss in brief the magnetism in graphene nanoflakes based on the Hubbard model, it's limitations and the need for models beyond the standard Hubbard model. Following the discussion a outline of our study is provided.

4.1.1 Magnetism in Graphene Nanoflakes
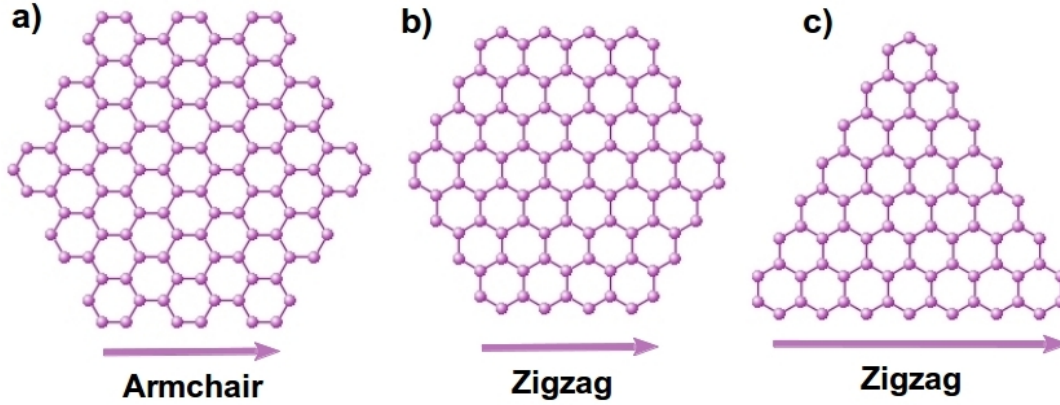
Figure 4.1: Figure shows representative geometries for the three graphene nanoflake systems (a) Armchair hexagonal nanoflake, (b) Zigzag hexagonal nanoflake and (c) Zigzag triangular nanoflake

In order to understand the magnetic behavior of graphene nanoflakes, three cases are discussed; (a) hexagonal nanoflake with armchair edge, (b) hexagonal nanoflake with zigzag edge and (c) triangular nanoflake with zigzag edge (see Fig 4.1).[15, 16] Figure 4.2 shows the energy spectrum (top panels) and density of states (bottom panel) for these three cases of graphene nanoflakes at half-filling. For all the three cases, an energy gap is observed in the energy spectrum, with the zigzag hexagonal nanoflake having a smaller energy gap compared to the other two. Of particular interest, is the existence of highly degenerate zero energy state for the zigzag triangular nanoflake. Graphene being a bipartite lattice can be decomposed into two sublattices A and B such that each atom of sublattice A is connected to atoms of sublattice B only and vice versa. The degeneracy of the zero energy state is then given by the sublattice imbalance $|N_A - N_B|$ where N_A (N_B) is the number of atoms belonging to A (B) sublattice. For the both hexagonal nanoflakes, armchair and zigzag, the sublattice imbalance is zero and hence no degenerate zero energy states are found. This is not the case for the zigzag triangular nanoflake where $|N_A - N_B|$ is not zero and therefore leads to high degeneracy of the zero energy states.

The energy states at/near the Fermi (zero) energy for the zigzag nanoflakes correspond to the localized edge states which are a generic property of zigzag edges [5, 8, 10, 17, 18] On the other hand, no such edge state exists in the case of armchair edges. This edge effect is clearly seen in the density of states (DOS) plots (bottom panel of figure 4.2) where the localized edge states, give rise to a narrow peak at the Fermi energy E_F in the case of zigzag nanoflakes while for the armchair nanoflake the DOS resembles that

of a pristine graphene sheet. The unequal contribution to the DOS at E_F for the zigzag
nanoflakes is due to the presence of degenerate zero-energy states in the triangular
nanoflake over the hexagonal nanoflake.
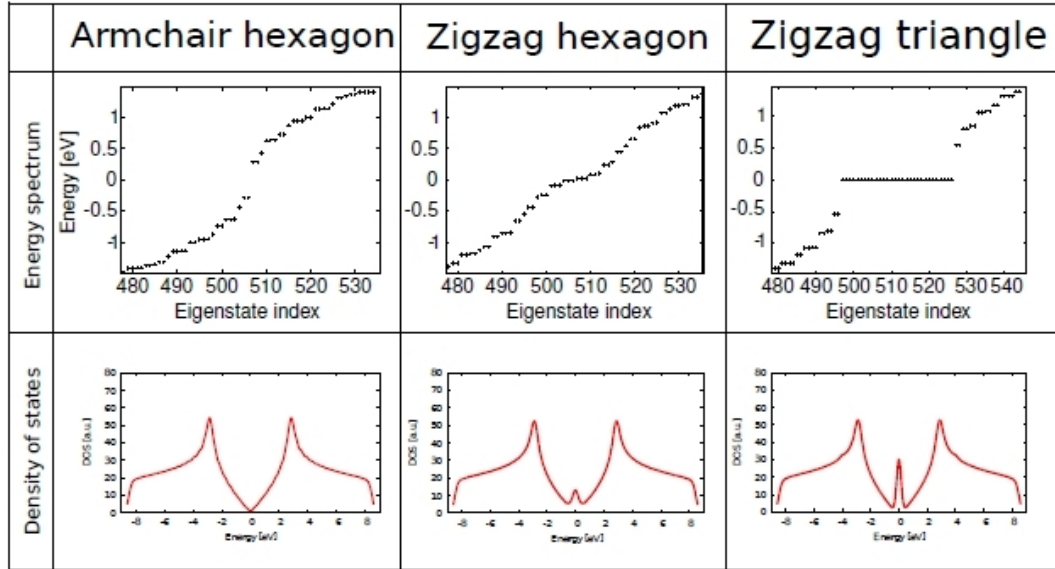
Figure 4.2: Comparison between the energy spectrum (top panel) and the density of
states (bottom panel) for the three nanoflake geometries.(Adopted from Ref.[15])

The presence of peaked DOS at E_F suggests that onset of magnetism in the nanoflake
system is determined by the Stoner criteria [19] which points to the competition between
exchange energy gain due to exchange splitting ($\frac{U}{2}\sum_i n_i^2$) of the electronic states and the
kinetic energy penalty associated with the spin polarization of the system. Thus, the
system is stabilized by spin polarization of the zero-energy states for any $U > 0$ with a
total magnetic moment given by Lieb's theorem [20] as $S = \frac{1}{2}|N_A - N_B|$ and the alignment
of spins dictated by Hund's rule.

This implies that the zigzag triangular nanoflake has a finite total moment whereas
both the hexagonal nanoflakes have net zero moment. Furthermore, spin polarization
also opens a spin gap within the zero energy states for the zigzag triangular nanoflake.
The localized edge states for the zigzag nanoflakes give rise to ferromagnetic ordering
within each edge as shown in Figure 4.3. However for a zigzag hexagonal nanoflake,
the carbon atoms belonging to neighboring edges belong to different sublattices and
therefore opposite spin orientation between neighboring edges, giving rise to an anti-
ferromagnetic order. For the zigzag triangular lattice, the carbon atoms belonging to
neighboring edges belong to same sublattice which leads to a ferromagnetic ordering

Hexagonal Nanoflake   **Triangular Nanoflake**
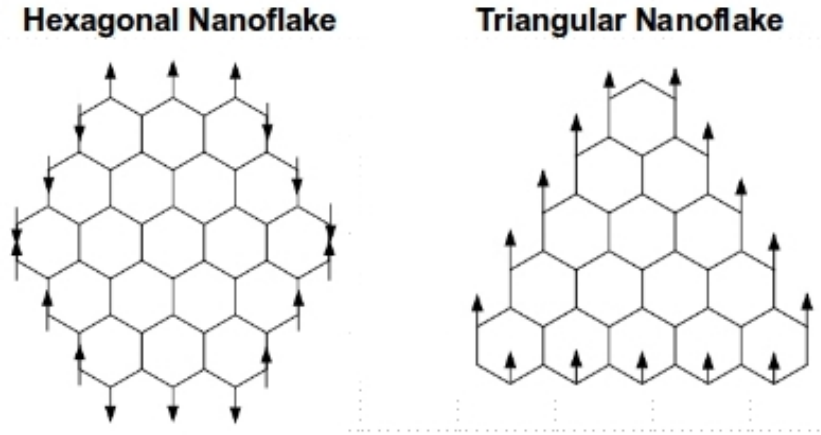
Figure 4.3: The alignment of spins at the zigzag edges of the hexagonal nanoflake and triangular nanoflake.

between the neighboring edges. The armchair nanoflakes posses no such edge states and therefore no local spin ordering.

4.1.2 Importance of Electron-Electron Interactions Beyond On-site Interaction(U)

It is apparent that the Hubbard model which takes into account the electron-electron correlation *via* the short range Coulomb interaction term U, provides a meaningful picture for the magnetic behavior of graphene nanoflakes. However, it is to be noted that the discussion of the preceding section holds only for graphene nanoflakes at half-filling as a consequence of the validity of Lieb's theorem. Away from half-filling the electron-electron correlation can become strong enough to cause the breakdown of the Lieb's theorem which require us to search beyond the standard Hubbard model for the sake of completeness.

One straightforward way to achieve this would be the introduction of correlations associated with the long-range part of the Coulomb interaction which consist of terms related to the inter-site Coulomb repulsion (V), direct exchange (F), Coulomb assisted hopping (X) and simultaneous hopping of two electrons (Y) processes. In 1988, D. K Campbell *et.al.*,[21, 22] provided estimates for the mentioned correlated terms for the isolated benzene system as: $U \sim 19$ eV, $V \sim 9$ eV , $X \sim 3$ eV and $F/Y \sim 1/2$ eV. It is worthwhile to note that though the strength of the inter-site Coulomb repulsion V is much smaller than the U term to have any effect in most cases, it is substantial enough

119

that it may introduce energy splittings in systems having nearly degenerate states and
therefore cannot be completely ignored.

The role of long-ranged Coulomb interactions in pristine graphene have been stud-
ied and it is debatable whether these interactions might lead to the occurrence of
strongly correlated phases like insulators[23, 24] or graphene remains weakly corre-
lated. Theoretically, an anti-ferromagnetic insulating ground state has been predicted
for pristine graphene for on-site repulsive Coulomb interaction exceeding at critical
value $U_{AFM} >> 4t - 5t$ from quantum monte carlo (QMC) studies and $U_{AFM} > 2.2t$ for
Hartree-Fock theory [25–27]. For values of U between $U_{SL} = 3.5t$ and U_{AFM}, a gapped
spin liquid has also been predicted.[28] On the other hand, ferromagnetism in pristine
graphene has not been experimentally observed for temperatures upto 2K.[29]

However, ferromagnetic ordering has been observed experimentally in nanographene
[1, 2], disordered graphite samples [30, 31] and at grain boundaries of highly oriented
pyrolitic graphite (HOPG) [32]. The observation of ferromagnetic ordering in these
systems hints at correlation effects beyond U as ferromagnetism, in general, is not a
property of the Hubbard model. This might prove to be true especially in the case of
nanographene where finite size effects lead to stronger correlations.

Estimates of Coulomb interaction parameters for pristine graphene that could be
used to construct a generalized Hubbard model were recently reported by T. Wehling *et.*
al..[33] The study carried out within the framework of constrained random phase approx-
imation (CRPA) [34] estimated the on-site Coulomb interaction (U) to be of strength $3.4t$
and a inter-site Coulomb interaction (V) of strength $2.0t$, t being the nearest-neighbor
effective hopping. While, the estimated strength of the on-site Coulomb interaction
puts graphene between two quantum phase transitions, parametrically separating the
zero-gap situation of graphene from the gapped solution of a spin liquid, the most crucial
finding of the study is the importance of the intersite Coulomb interaction V. The sizable
estimate reported for V, puts graphene in close proximity to competing spin-density- and
charge-density-wave phases.

Thus, the electronic and magnetic behavior of graphene-based systems is a result
of the delicate balance maintained between U and V. Furthermore, as the interplay
between the charge and spin degrees of freedom of the p_z orbital crucially depends on
the strength of these electron-electron Coulomb interaction terms, even a small deviation
in U and V can introduce many-body instabilities within the system which may furnish
a rich magnetic phase diagram.

120

4.1.3 Brief Outline of Present Study

In the present work we investigate the role of the intersite Coulomb repulsion term V in driving the electronic, magnetic and thermodynamic properties in graphene nanoflakes by solving the extended Hubbard within the exact diagonalization scheme. This is achieved by

- choosing nanosized graphene which increases the importance of correlations due to finite-size effects

- by explicitly dealing with the effect of correlations brought about by the inclusion of V within the extended Hubbard model

- by considering a range of V/U ratios

- by doping the nanoflakes, which is expected to trigger further instabilities.[35, 36]

For our exact diagonalization study we consider graphene nanoflakes where three benzene rings are connected to each other *via* edge sharing in two ways : a) a zigzag trigonal nanodisk and b) a zigzag linear nanostripe.

The electron filling n is varied about the half-filled situation generating both electron and hole doping which can be experimentally achieved by application of a gate voltage. It has also been suggested that the ratio V/U can be tuned by putting graphene nanoflakes on different dielectric substrates [33]. Since we expect the strength of the on-site Coulomb repulsion to be less affected by the environment of the dielectric substrate, the U was kept fixed to $3.4t$ and V was varied.

The present study, thus, provides a complete phase diagram in terms of the inter-site Coulomb interaction V and electron filling n for the two geometries of the nanoflakes. Besides the exact low-energy spectrum, we also compute the average charge and magnetic moment for each site as well as the spin-spin and charge-charge correlations across the sites in the ground state. Furthermore, the temperature-dependent physical properties like magnetization and specific heat are also studied.

It is hoped that our extensive study forms a basis and prompts further investigations into correlation-driven instabilities in graphene nanodisks and nanoribbons.

4.2 Computational Details

Given the importance of electron-electron correlations beyond on-site for nanographene
system as discussed in section 4.1.2, we have chosen the extended Hubbard model as our
model Hamiltonian. The extended Hubbard model is given by

$$(4.1) \qquad H = - \sum_{\langle i,j \rangle, \sigma} [t_{ij} c^{\dagger}_{i,\sigma} c_{j,\sigma} + h.c.] + U \sum_{i} n_{i,\uparrow} n_{i,\downarrow} + V \sum_{\langle i,j \rangle, \sigma, \sigma'} n_{i,\sigma} n_{j,\sigma'}$$

where i is the site index, which runs from 1 to N_s, N_s being the number of sites
within the nanoflake. The operators $c^{\dagger}_{i,\sigma}$, $c_{i,\sigma}$ and the paramters t_{ij}, U and V have the
same meaning as defined in section 4.1. Thus, the geometry of the system is completely
specified by the connectivity matrix t_{ij}, U and V.

The exact many-body wave-function is expanded in the S_z basis sets, where $S_z = (n_\uparrow - n_\downarrow)/2$ is the z component of the total spin and $n_\uparrow(n_\downarrow)$ represents the number of
up(down) electrons.

The Hamiltonian matrix is constructed for all S_z sectors $i.e.$ from S_z^{max} with $n_\uparrow = n$ to
$S_z^{min} = 0$ or $1/2$. Finally, the resultant matrix is diagonalized by Lanczos procedure to
obtain the ground and the lowest few eigenstates and eigenvectors.

Using the procedure described in section 2.3.4 we calculate the expectation values of
relevant operators viz $\langle E \rangle$, $\langle n_i \rangle$, $\langle m_i \rangle$, $\langle S_i^z \rangle$, $\langle S_i^z S_j^z \rangle$. These expectation values are then
used to evaluate the pertinent quantities such as

- Average charge : $\frac{n}{N_s}$

- Magnetic moment : $(\langle n_\uparrow \rangle - \langle n_\downarrow \rangle)$

- Spin-Spin correlation : $\langle S_i^z S_j^z \rangle - \langle S_i^z \rangle \langle S_j^z \rangle$

For the evaluation of finite temperature properties such as specific heat ($\langle C_v \rangle_T$) and
magnetization ($\langle m \rangle_T$) we follow the procedure described below.

Finite Temperature Properties

The low-temperature thermodynamic properties were evaluated within the boundaries
of the canonical ensemble. If $\hat{O}$ represents the operator of interest, then by the means of
the partition function Z given by

(4.2)
$$Z = \sum_I e^{-\beta \epsilon_I}$$

where ϵ_I is the eigenstate of I with eigenvector ψ_I, the thermal average ($\langle \hat{O} \rangle$) of the operator $\hat{O}$ is defined as

(4.3)
$$\langle \hat{O} \rangle_T = \frac{\sum_I e^{-\beta \epsilon_I} \langle \psi_I | \hat{O} | \psi_I \rangle}{\sum_I e^{-\beta \epsilon_I}}$$

where $\beta = 1/k_B T$ and $\langle \psi_I | O | \psi_I \rangle$ is the quantum mechanical expectation value in the state I, which can be evaluated as shown in section 2.3.4. Thus we obtain

(4.4)
$$\text{Average Magnetization } \langle m \rangle_T = \frac{\sum_I e^{-\beta \epsilon_I} \langle \psi_I | m_i | \psi_I \rangle}{\sum_I e^{-\beta \epsilon_I}}$$

(4.5)
$$\text{Average energy } \langle \epsilon \rangle_T = \frac{\sum_I e^{-\beta \epsilon_I} \langle \psi_I | \epsilon_i | \psi_I \rangle}{\sum_I e^{-\beta \epsilon_I}}$$

(4.6)
$$\text{Specific Heat } \langle C_v \rangle_T = \left[\frac{\langle \epsilon^2 \rangle_T - \langle \epsilon \rangle_T^2}{(k_B T)^2} \right] k_B$$

4.3   Results and Discussion

As shown in Figure 4.4 we consider two graphene nanoflake geometries denoted by NF13 and NF14 for our exact diagonalization study. The NF13 geometry consists of three benzene rings connected to each other *via* edge sharing in a triangular fashion leading to a nanodisk geometry with 13 sites. On the other hand the NF14 geometry is a finite-sized nanostripe geometry obtained by connecting the three benzene rings next to each other *via* edge sharing in a linear fashion and consists of 14 sites.

The underlying D_{3h} and D_{2h} symmetries of the NF13 and NF14 nanoflakes lead to four different inequivalent classes of carbon C sites with different connectivities as listed in Table 1. The distribution of the C sites in different inequivalent classes having different coordination and neighbor environment plays a crucial role in modulating the charges at different sites and determining the magnetic behavior of these nanoflakes which we discuss in the following sections.

Group	13 sites	14 sites
A	1,5,9 (2)	1,7,8,14(2)
B	2,4,6,10,12 (2)	2,6,9,13(2)
C	3,7,11 (3)	3,5,10,12 (3)
D	13 (3)	4,11 (2)

(a) NF13   (b) NF14   (c) Table 1
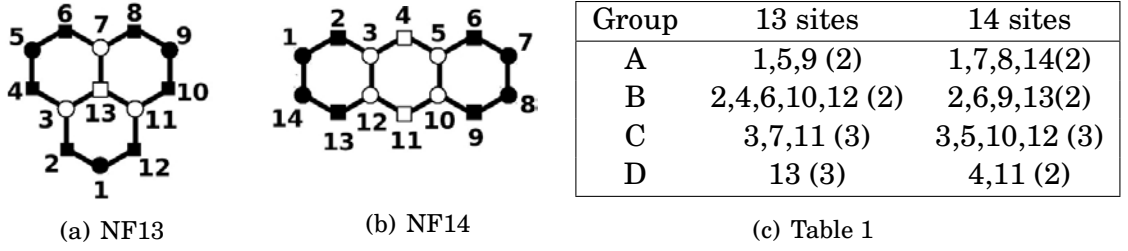
Figure 4.4: Geometries of (a) 13-site and (b) 14 site nanographene constructed by linking three benzene rings. The C atoms have been numbered for the sake of identification of atoms. For easy identification, the atoms belonging to groups A,B,C and D are marked as closed circles, closed squares, open circles and open squares respectively. (c) Table 1 provides the site indices for different groups of sites for 13- and 14-site geometry. The number within the parentheses is the coordination number of the sites belonging to a specific group

4.3.1 Magnetic Phase Diagram

We begin by discussing the magnetic phase diagram in n-V space given where n is the electron filling and V is the nonlocal inter-site Coulomb interaction. The phase diagram is obtained by varying V over a wide range of values viz $0.0t$, $0.57t$, $1.0t$, $1.57t$, $2.0t$. Similarly the electron filling n is also varied over a wide range of values from 3 to 24 for NF13 and from 3 to 26 for NF14, spanning from an extreme dilute limit to an extreme populated limit. The ground state is characterized in terms of solutions with net-magnetic-moment and zero-magnetic-moment. A point to note, the zero-magnetic-moment solution corresponds to the lowest magnetic moment solution which is 0 μ_B for the case of even electron filling and 1 μ_B the case of the odd electron filling, arising from the single unpaired electron. Hence for the odd electron filling case, net-magnetic-moment solutions are the solutions with magnetic moment higher than 1 μ_B. By taking into account the above considerations, the magnetic phase diagram obtained in n-V space is given in Figure 4.5 for the NF13 (upper panel) and NF14 (lower panel) geometries. The net-magnetic-moment solutions are colored differently to distinguish them from the zero-magnetic-moment solutions.

On considering the NF13 case, we find that for the filling of 13 electrons $i.e.$ the half-filled situation, the ground state is a zero-magnetic-moment state. For both electron and hole doping, isolated regions with ground states having net-magnetic-moment are observed in the phase space. For $V = 0$ all the zero-magnetic-moment ground states are anti-ferromagnetic (AFM) in nature. The existence of isolated magnetic regions for $V = 0$ can be explained on the basis of the effective one-electron description of the electronic
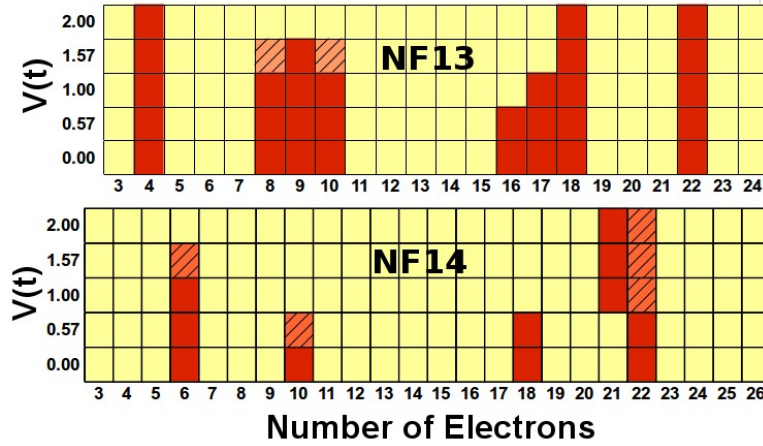
Figure 4.5: Magnetic phase diagram for NF13 (upper panel) and NF14 (lower panel) obtained by varying V and n. The solutions with net and zero magnetic moment are colored red and yellow, respectively. Solutions with near degeneracy(energy difference $\leq$ $0.001t$) are shown as hatched areas.

structure and Stoner criteria. A finite V, however favors charge disproportionation which affects the spin-spin correlations in a non-trivial way which will be discussed in the following sections. As such, introduction of a finite V can stabilize or suppress solutions of net magnetic moments depending on the occupancy and strength of V, stressing the formation of many-body-instabilities. The nanoflake geometry also has a substantial effect on the phase diagram, as discerned from the NF14 case. We observe fewer examples of net magnetic-moment solutions suggesting that the nanostripe like geometry disfavors magnetic structures with net magnetic moment.

In the following sections we discuss the effect of the competition between U and V on the charge distribution and spin-spin correlations in detail for the case of NF13. The case of NF14 is then discussed in comparison to NF13 to examine the geometric effect. Finally, we probe the finite-temperature properties of both the nanoflakes.

4.3.2 The Interplay between U and V: The Case of NF13 nanoflake

Due to the presence of four inequivalent classes of sites, it is of interest to analyze the charge and spin distributions among these four site classes in the ground state. In order to facilitate a better understanding we present a semiquantitative pictorial view of charge and spin distributions with the following display scheme. The charge on a

given site is shown as a sphere with three different possible colors, *viz*., white, red, and cyan. Cyan indicates the average charge ($\bar{n} = n/N_s$), red indicates charge depletion (CD), and white corresponds to charge accumulation (CA) with respect to the average charge. The size of the sphere is proportional to the value of the charge. The magnetic moment ($\langle n_\uparrow \rangle - \langle n_\downarrow \rangle$) is shown as an arrow, the height being proportional to its absolute value.

Charge Modulation and Spin Distribution

The top panel of figure 4.6 shows the charge and spin distribution for the NF13 nanoflake at half filling (13 e^-) for the entire range of V values, while the bottom panel shows the distribution for a fixed value of $V = 1.5t$ for a filling of $17e^-$, $18e^-$, $19e^-$.

As per expectation, for the case of half filling and $V = 0$, the total charge is equally distributed on all the sites i.e., one electron per site. The effect of the central site situated in the middle of the otherwise zigzag ring, is seen in the spin distribution. The odd number of electrons at half filling gives rise to an uncompensated ferrimagnetic character which is reflected in the spin distribution. All the sites belonging to group B have the largest spin moments, whereas sites belonging to group C and D having connectivity 3 have much smaller spin moments. Thus, it is noted that the spin distribution is dominated by geometry *via* the single particle states.

Effect of nonlocal Coulomb interaction V

Switching on the nonlocal inter-site Coulomb interaction V leads to several interesting observations. The significance of the inter-site Coulomb repulsion is clearly discernible on examining the top panel of Figure 4.6. Increasing V value leads to a charge-disproportionated situation, with unequal charges at different sites, thus stabilizing charge-density-wave like instabilities. The choice of V greatly dictates the pattern of charge disproportionation which is strongly driven by the interplay between the U and V. The local correlation U disfavors charge accumulation at a given site, while the nonlocal nearest-neighbor interaction V favors charge disproportionation between neighboring sites, even at the cost of charge accumulation at a given site.

The strong dependence on V can be clearly seen from the fact that even a moderate positive value of V can lead to substantial changes in the charge pattern obtained at $V = 0$. For $V = 0.57t$, we find that the central site (group D) has a charge of $\bar{n}$, while the neighboring sites *i.e.*, the group C sites, are all charge depleted in order to minimize the energy cost arising due to the V term. This leaves us with choices of group A and group
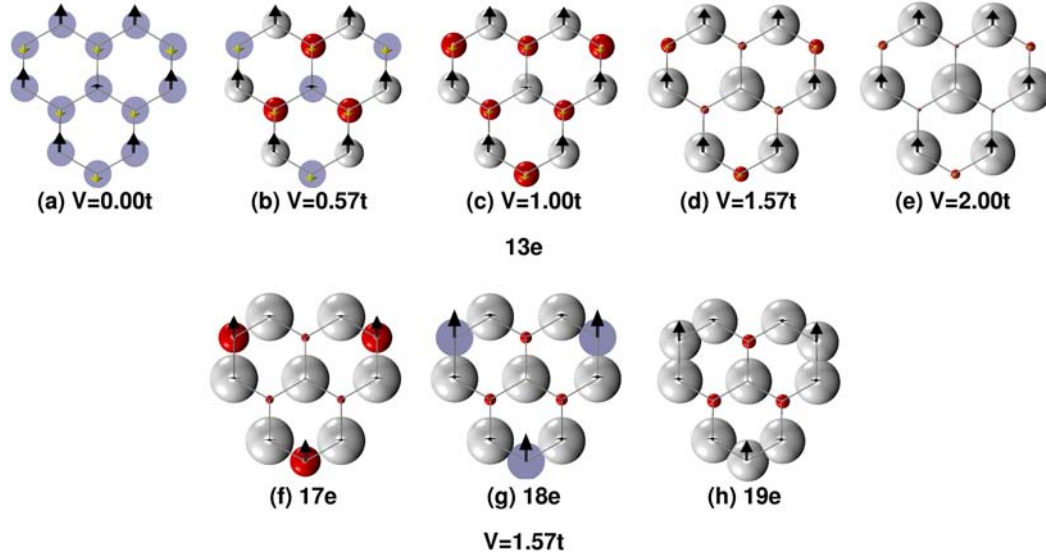
Figure 4.6: The charge and magnetic moments at different sites for NF13. The red, white and cyan spheres represent sites with depleted charge, accumulated charge and average charge respectively. Top panel: Filling of $13e^-$ and V values of 0, $0.57t$, $1.00t$, $1.57t$ and $2.00t$. Bottom panel: Filling of $17e^-$, $18e^-$ and $19e^-$ for fixed V value of $1.57t$.

B sites having charge $\bar{n}$ and CA, respectively, giving rise to a charge density pattern ...CA-$\bar{n}$-CD-CA... along the zigzag ring.

The dominance of V over U is further emphasized on increasing V to $1.00t$ leading to a significant change in the charge distribution where no site has average charge, instead each site has either charge accumulation (CA) or charge depletion (CD). This gives rise to a charge-density pattern of ...CA-CD-CA-CD... along the zigzag ring, with the central site being the charge accumulated site. Further increase in the value of V to $1.57t$ or $2.00t$ makes the charge-accumulation effect even stronger, at the cost of making alternate sites on the ring nearly empty.

The spin distribution is also dramatically altered with the emergence of the charge-density wave like structure due to effect of V. Increasing the value of V causes the central site to become doubly occupied and as a consequence loose its magnetic moment. The depletion of charge from all down electron sites *i.e.*, group A and group C, redistributes the magnetic moment on sites in group B.

Effect of electron filling n

From examination of the bottom panel of Figure 4.6 it is noted that for a given fixed and large value of V, the charge disproportionation becomes stronger with increased electron filling. This leads to an interesting evolution of charge-density pattern with changing filling. The charge plots in the bottom panel of Figure 4.6 are given for a representative case of $V = 1.57t$ for a filling of 17, 18 and 19 electrons. These plots can be compared to that shown in (d) of the top panel for a filling of 13 electrons. A dramatic change in the charge and spin distribution is observed on addition of four electrons with respect to the half-filled ($13e^-$) case. The extra electrons accumulate on group B sites making them doubly occupied and thereby destroying all the spin moments. As a consequence the spin moments are localized only on the three sites in group A.

Further increase of electron filling affects the charge distribution of group A sites mostly as distribution to other sites is prohibited by V. Thus the added electrons are mostly spread among the sites in group A with the charge distribution pattern evolving from the charge depletion ($17e^-$) case to the average charge ($18e^-$) case to the charge accumulation ($19e^-$) case. Interestingly, it is noted that a combination of large electron filling (e.g. $19e^-$) and large V drives the system to an unusual trimerized phase, with trimerization at the three corners.

Spin-Spin Correlations

The bottom panel of Figure 4.7 provides a pictorial representation for the spin-spin correlations between all possible pair of sites for the representative case of $17e^-$ for different values of V, along with the corresponding charge distribution(top panel) given for reference. The anti-ferromagnetic and ferromagnetic correlations are shown with two different colored bonds, white and red, respectively. The thickness of the bonds is proportional to the strength of the correlation, and only the dominant correlations are shown. The locations of the magnetic moments in the plot of spin-spin correlation are shown with red balls, the size of ball being proportional to the size of the magnetic moment $\langle S_z^i \rangle$.

From the analysis of the magnetic phase diagram we know that the solutions are magnetic for $V = 0$, $0.57t$ and $1.00t$ with a net moment of $3\mu_B$, while only a default moment of $1\mu_B$ is observed for $V = 1.57t$ and $2.00t$. We note that there exists strong anti-ferromagnetic correlations on the ring, together with ferromagnetic correlations even for the net-magnetic-moment solutions. On increasing the value of V, the anti-
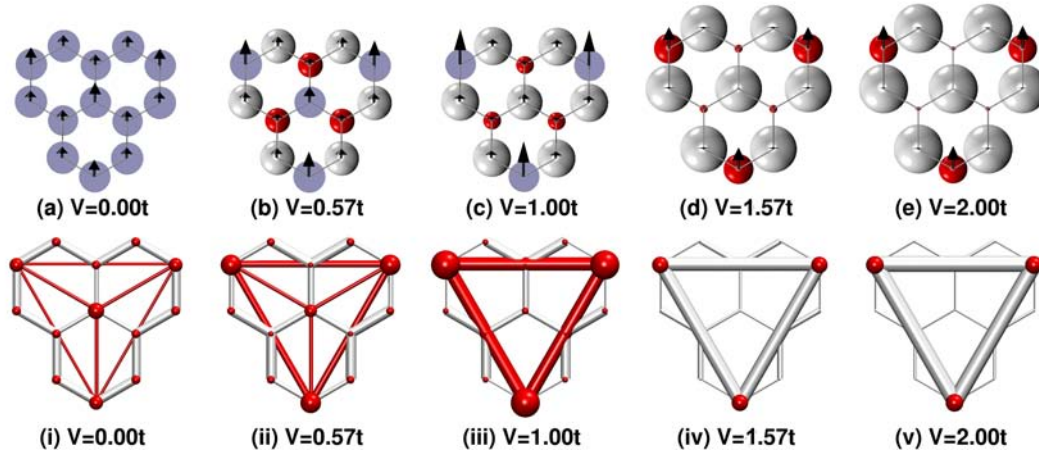
Figure 4.7: Spin-Spin correlation functions (bottom panel) for NF13, for $17e^-$ filling and various different values of V. The corresponding charge distributions are shown in the top panel. The anti-ferromagnetic and ferromagnetic correlations are shown by white and red bonds respectively

ferromagnetic correlations on the ring become spatially inhomogeneous. Interestingly, while the anti-ferromagnetic correlations are short ranged, the ferromagnetic correlations are of long-range nature and connect the sites with appreciable localized moment, which evident by comparing the figures for $V = 0.57t$ and $1.00t$. The origin of the long-range natured ferromagnetic correlations can be explained by examining the change in charge distribution at the central site D with V. From the discussion in the previous section, we know that the nature of charge distribution at the central site changes drastically on changing V value from $0.57t$ to $1.00t$. For our representative case, this causes the charge distribution at the central site to evolve from state with $\bar{n}$ to a charge accumulated state evident from the charge plots presented in the top panel of Figure 4.7. This causes reduction of the local moment at the central site D, destroying the ferromagnetic correlation between central site D and those in group A. This, in turn, leads to strong inter-site ferromagnetic correlations within group A.

A change of V from $1.00t$ to $1.57t$ or more causes the magnetic phase to change from magnetic with long-range ferromagnetic correlations to the default moment phase with long-range anti-ferromagnetic correlations, as shown in (iv) and (v) of the bottom panel in Fig. 4.7. It is to be noted that the long-range anti-ferromagnetic interaction between the three sites in group A forming a triangle would lead to frustration. A pertinent question concerns the origin of the long-range anti-ferromagnetic correlations. As has been already noted in the preceding section, increasing the electron filling with respect

to the half filled case make sites in group B doubly occupied. From the Figure 4.7 , it is
evident that the each site belonging to group A are separated by two doubly occupied sites
of group B, which suggests the presence of super-super-exchange-mediated long-range
anti-ferromagnetic interaction.
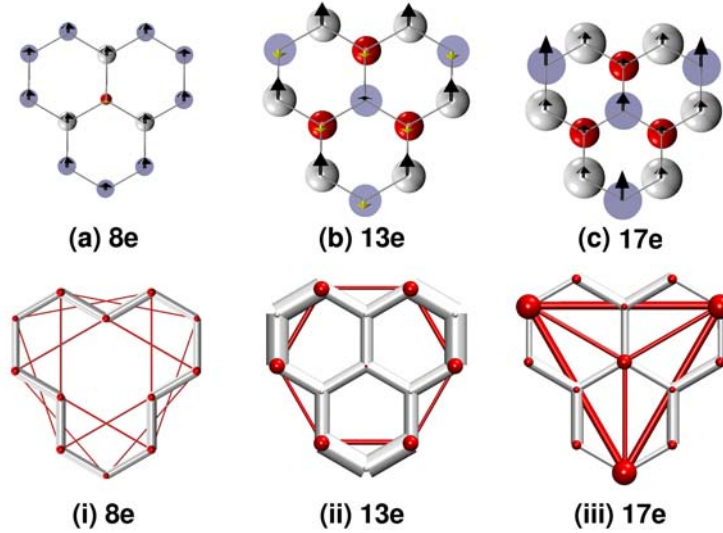
Figure 4.8: Spin-spin correlations (bottom panel) for NF13 for $V = 0.57t$ and different
values of e^- filling. The corresponding charge distributions are shown in the upper panel.

The Figure 4.8 shows the evolution of spin-spin correlation as a function of filling for
a fixed V of $0.57t$. The charge distributions are shown in the top panel for comparison.
We recall that the $8e^-$ as well as the $17e^-$ solutions are magnetic, while that of $13e^-$
has the default magnetic moment of $1\mu_B$. For a small electron filling of $8e^-$, the rather
dilute limit of the phase diagram, the magnetic moments are understandably small,
leading to weak correlation. Because of large charge depletion at the central site the
flake resembles the structure of a 12-site ring. Upon increasing the filling to $13e^-$,
strong nearest-neighbor anti-ferromagnetic correlations appear. A further increase of the
filling to $17e^-$ shifts the localized moments to sites in group A, setting up the triangular
ferromagnetic correlations connecting sites A as discussed earlier.

4.3.3   Effect of Geometry: The Case of NF14 nanoflake

In Figure 4.9, we show the representative charge distribution and spin-spin correla-
tion for NF14 geometry, for three different fillings $14e^-$, $21e^-$, and $22e^-$ for V = $1.00t$.
As already pointed out in the context of the magnetic phase diagram, the change in

geometry is found to have a significant effect on the details. This is also seen in the charge distribution and spin-spin correlation, for which the detailed nature of the charge disproportionation as well as the spin correlations are different from those of NF13 case.
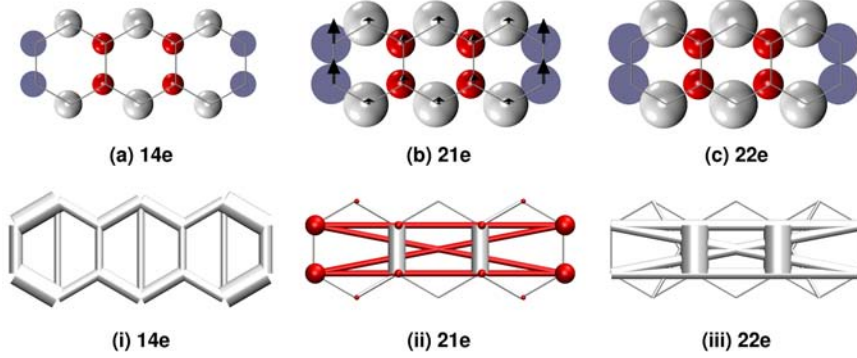
Figure 4.9: Charge distributions (top panel) and spin-spin correlations (bottom panel) for NF14, for $V = 1.0t$, and different values of e^- filling.

Among the chosen three representative cases, the $21e^-$ case is magnetic, while the remaining two, the half-filled $14e^-$ and highly electron-doped $22e^-$ case, have zero net moment. Inclusion of finite and moderately large V sets up a charge-density-wave pattern, which unlike that of NF13, show little variation in the pattern upon changing the filling. The filling pattern consists of charge accumulation at sites in groups B and D, while the nearest-neighbor sites in group C are charge depleted. Note that the edge sites in group A retain the average charge $\bar{n}$ irrespective of filling and the nonlocal Coulomb interaction. This is an effect of geometry. As found in NF13, U drives strong nearest-neighbor anti-ferromagnetic correlations. These correlations are seen to coexist with long-range ferromagnetic ones which connect sites in group A which have appreciable localized moments as evident from the plot (ii) in the bottom panel of Figure 4.9. For a filling of $22e^-$, we find that the solution with zero moment is nearly degenerate with that of finite moment. Remarkably, the zero-moment solution contains long-range anti-ferromagnetic correlation, similar to the long-range ferromagnetic correlations in the case of $21e^-$. Thus, although the generic features seen in NF13 and NF14 are similar in nature, the subtle effects of geometry make the charge distribution and magnetic correlation patterns richer in NF13 compared to NF14.

4.3.4 Finite Temperature Properties: Temperature dependent specific heat and magnetization

In the following, we discuss the results for the representative case of $8e^-$ filling in
NF13. Recalling the magnetic phase diagram, we note that for $8e^-$ filling, the solution
is magnetic for $V = 0$, $0.57t$ and $1.00t$, while for $V > 1.57t$ it becomes a zero-moment
solution nearly degenerate with the magnetic solution. The left panel in Figure 4.10
shows the ground state and a few excited-state eigenvalues for V = $0.57t$, $1.00t$, and $1.57t$
. The magnetic (zero-moment) character of the states is indicated by black (cyan) lines.
We find that for V = $0.57t$, although the doubly degenerate ground state is magnetic,
the next excited state is of zero-moment character. On increasing V to $1.0t$, the energy
separation between the two solutions decreases, and finally there is a crossover with the
zero-moment solution becoming the ground state for $V = 1.57t$. The middle and right
panels of Figure 4.10 show the computed specific heat and magnetization, respectively,
for the three V values; $0.57t$, $1.00t$, and $1.57t$.
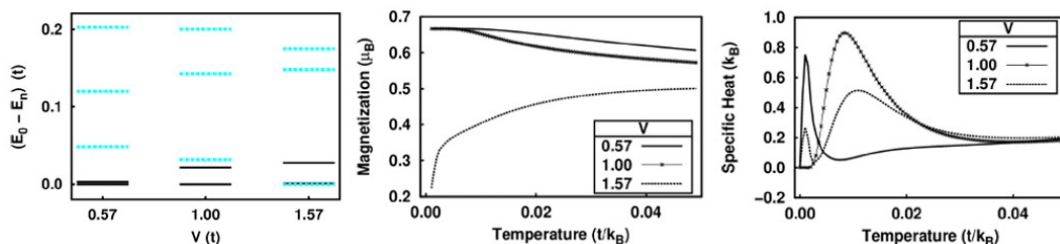
Figure 4.10: Eigenvalue spectrum (left panel), magnetization (middle panel) and specific
heat (right panel) for NF13, for filling of $8e^-$ and $V = 1.00t$. In the eigenvalue spectrum,
the magnetic (zero moment) solutions are shown as black, solid (cyan, dashed) lines.

For $V = 0.57t$ and $1.00t$, the low-temperature magnetic moment is finite (0.67 μ_B)
and decreases with temperature. The rate of decrease is dependent on the location of the
first excited state with zero magnetic moment, dictated by the precise value of V. Once
the crossover takes place the magnetic moment increases sharply from nearly zero at
very low temperature to about $0.5\mu_B$ within a few tens of kelvins. These results, arising
out of exact many-body calculations, support the recent DFT results and experimental
observations [37, 38], which suggest a change of magnetic state from the compensated
anti-ferromagnetic phase at low temperature to a ferromagnetic state with net magnetic
moment upon increasing temperature. The presence of a sharp peak in the specific heat
at low temperature is due to the near degeneracy of the first excited state to the ground
state. The location and the sharpness of the peak depends on the choice of V. With

increase of V from $0.57t$ to $1.00t$, the first excited state moves away from the ground state and as a result the peak shifts and broadens. Further increase of V to $1.57t$ brings back the first excited state close to the ground state resulting in a sharp peak at low temperature. The second broad peak, seen for $V = 1.57t$, arises due to the presence of a second excited state close to the first one. Our calculation demonstrates that the magnetization and specific heat at low temperature are sensitive to the value of V, and therefore may be tunable. The results for NF14 show a similar behavior for cases with low-lying states of contrasting magnetic behavior.

4.4 Conclusions

With the aim of studying the formation of many-body instabilities brought about by the delicate interplay of U and V, an exact diagonalization study of the extended Hubbard model was performed on nanographene systems. The presence of strong local and non-local electron-electron correlations in graphene was reported recently [33] and it was our expectation that with the reduction in system size the importance of these correlations would increase dramatically due to finite-size effects. Geometry plays an important role in determining various properties at nanosize scales. Thus, in order to take into account the effect of geometry we investigated two nanographene systems *viz* (a) the zigzag trigonal nanodisk and (b) the zigzag linear nanostripe geometries. The doping effect, which is speculated[35, 36] to trigger further instabilities, has also been studied by varying the electron filling over a wide range.

Our study showed that the presence of the strong nonlocal, inter-site Coulomb interaction V drives the system towards charge disproportionation leading to formation of charge density wave patterns which are strongly dependent on the doping level and precise value of V/U. The magnetic phase diagram in $n - V$ space was found to consist of isolated regions of net-magnetic-moment phases, separated by phases of zero-magnetic-moment character. It was further observed that changes in electron filling, as small as one electron or one hole, drives the transition between the zero- and net-magnetic moment phases. The nature of the magnetic ground state was found to be strongly dependent on doping even for same choice of V/U and same geometry. Curiously, states with finite non-zero magnetic moment show signature of strong anti-ferromagnetic fluctuation, which indicates a closeness to several many-body instabilities. Remarkably, the flake develops strong long-range ferromagnetic correlations which change to anti-ferromagnetic ones with a small change in V.

Our study also showed, pronounced differences in the behavior of many-body instabilities depending on the geometry of the graphene nanoflake. We found that linear nanostripe geometry disfavors structures with net magnetic moments. While the inclusion of V does setup a charge density wave pattern, in contrast to the trigonal nanodisk geometry, little variation is seen in the pattern on change in doping.

The low-temperature thermodynamic properties such as magnetization and specific heat were also examined. The behavior of these properties is governed by the many-body eigenvalue spectrum. An examination of the full many-body eigenvalue spectra revealed the presence of low-lying excited states of contrasting magnetic character compared to that of the ground state. We found that even a small change in V or temperature drives a crossover to the magnetic state. The magnetic crossover, triggered by transition between net-magnetic-moment and zero-magnetic-moment eigenstates, is signaled by a sharp peak in the specific heat which can be easily detected by experiments. Such a temperature-induced change in the magnetic state has already been observed [38]. It is our belief, that effect of the nonlocal, inter-site Coulomb interaction V on magnetism could be studied experimentally by putting the nanographene on different dielectric substrates, since doing so has been speculated to tune the ratio of the local to nonlocal Coulomb interaction.

4.5 Bibliography

[1] Y. Shibayama, H. Sato, T. Enoki, and M. Endo *Physical Review Letters*, vol. 84, p. 1744, 2000.

[2] T. Enoki and K. Takai *Solid State Communications*, vol. 149, p. 1144, 2009.

[3] J. Inoue, K. Fukui, T. Kubo, S. Nakazawa, K. Sato, D. Shiomi, Y. Morita, K. Ya-mamoto, T. Takui, and K. Nakasuji *Journal of the American Chemical Society*, vol. 123, p. 12702, 2001.

[4] G. Z. Magda, X. Jin, I. Hagymási, P. Vancsó, Z. Osváth, P. Nemes-Incze, C. Hwang, L. P. Biró, and L. Tapasztó *Nature*, vol. 514, p. 608, 2014.

[5] V. L. J. Joly, M. Kiguchi, S.-J. Hao, K. Takai, T. Enoki, R. Sumii, K. Amemiya, H. Muramatsu, T. Hayashi, Y. A. Kim, M. Endo, J. Campos-Delgado, F. López-Urías, A. Botello-Méndez, H. Terrones, M. Terrones, and M. S. Dresselhaus *Physical Review B*, vol. 81, p. 245428, 2010.

[6] M. Y. Han, B. Özyilmaz, Y. Zhang, and P. Kim *Physical Review Letters*, vol. 98, p. 206805, 2007.

[7] J. Fernández-Rossier and J. J. Palacios *Physical Review Letters*, vol. 99, p. 177204, 2007.

[8] M. Fujita, K. Wakabayashi, K. Nakada, and K. Kusakabe *Journal of the Physical Society of Japan*, vol. 65, p. 1920, 1996.

[9] S. Bhowmick and V. B. Shenoy *Journal of Chemical Physics*, vol. 128, p. 244717, 2008.

[10] K. Nakada, M. Fujita, G. Dresselhaus, and M. S. Dresselhaus *Physical Review B*, vol. 54, p. 17954, 1996.

[11] Y.-W. Son, M. L. Cohen, and S. G. Louie *Physical Review Letters*, vol. 97, p. 216803, 2006.

[12] P. Fazekas, "Lecture notes on electron correlation and magnetism," in *Modern Condensed Matter Physics - Vol. 5* (Y. L. I. Dzyaloshinski, S. Lundqvist, ed.), World Scientific Publishing, 1999.

[13] L. Pisani, J. A. Chan, B. Montanari, and N. M. Harrison *Physical Review B*, vol. 75, p. 064418, 2007.

[14] D. Gunlycke, D. A. Areshkin, J. Li, J. W. Mintmire, and C. T. White *Nano Letters*, vol. 7, p. 3608, 2007.

[15] B. Jaworowski, "Electronic properties of graphene nanostructures," Master's thesis, Wroclaw University of Technology, 7 2013.

[16] O. V. Yazyev *Reports on Progress in Physics*, vol. 73, p. 056501, 2010.

[17] Y. Kobayashi, K.-I. Fukui, T. Enoki, K. Kusakabe, and Y. Kaburagi *Physical Review B*, vol. 71, p. 193406, 2005.

[18] Y. Niimi, T. Matsui, H. Kambara, K. Tagami, M. Tsukada, and H. Fukuyama *Physical Review B*, vol. 73, p. 085421, 2006.

[19] E. C. Stoner *Proceedings of the Royal Society of London Series A*, vol. 165, p. 372, 1938.

[20] E. H. Lieb *Physical Review Letters*, vol. 62, p. 1201, 1989.

[21] D. K. Campbell, J. Tinka Gammel, and E. Y. Loh, Jr. *Physical Review B*, vol. 38, p. 12043, 1988.

[22] D. K. Campbell, J. Tinka Gammel, and E. Y. Loh, Jr. *Physical Review B*, vol. 42, p. 475, 1990.

[23] J. E. Drut and T. A. Lähde *Physical Review Letters*, vol. 102, p. 026802, 2009.

[24] I. F. Herbut *Physical Review Letters*, vol. 97, p. 146401, 2006.

[25] T. Paiva, R. T. Scalettar, W. Zheng, R. R. P. Singh, and J. Oitmaa *Physical Review B*, vol. 72, p. 085123, 2005.

[26] L. M. Martelo, M. Dzierzawa, L. Siffert, and D. Baeriswyl *Zeitschrift fur Physik B Condensed Matter*, vol. 103, p. 335, 1997.

[27] S. Sorella and E. Tosatti *EPL (Europhysics Letters)*, vol. 19, p. 699, 1992.

[28] Z. Y. Meng, T. C. Lang, S. Wessel, F. F. Assaad, and A. Muramatsu *Nature*, vol. 464, p. 847, 2010.

[29] M. Sepioni, R. R. Nair, S. Rablen, J. Narayanan, F. Tuna, R. Winpenny, A. K. Geim, and I. V. Grigorieva *Physical Review Letters*, vol. 105, p. 207205, 2010.

[30] P. Esquinazi, A. Setzer, R. Höhne, C. Semmelhack, Y. Kopelevich, D. Spemann, T. Butz, B. Kohlstrunk, and M. Lösche *Physical Review B*, vol. 66, p. 024429, 2002.

[31] P. Esquinazi, D. Spemann, R. Höhne, A. Setzer, K.-H. Han, and T. Butz *Physical Review Letters*, vol. 91, p. 227201, 2003.

[32] J. Červenka, M. I. Katsnelson, and C. F. J. Flipse *Nature Physics*, vol. 5, p. 840, 2009.

[33] T. O. Wehling, E. Şaşıoğlu, C. Friedrich, A. I. Lichtenstein, M. I. Katsnelson, and S. Blügel *Physical Review Letters*, vol. 106, p. 236805, 2011.

[34] F. Aryasetiawan, M. Imada, A. Georges, G. Kotliar, S. Biermann, and A. I. Lichtenstein *Physical Review B*, vol. 70, p. 195104, 2004.

[35] N. M. R. Peres, M. A. N. Araújo, and D. Bozi *Physical Review B*, vol. 70, p. 195122, 2004.

[36] S. Pathak, V. B. Shenoy, and G. Baskaran *Physical Review B*, vol. 81, p. 085431, 2010.

[37] M. Kabir and T. Saha-Dasgupta *Physical Review B*, vol. 90, p. 035403, 2014.

[38] L. Chen, L. Guo, Z. Li, H. Zhang, J. Lin, J. Huang, S. Jin, and X. Chen *Scientific Reports*, vol. 3, p. 2599, 2013.

Out-of-Plane Polarization at the interface of Graphene-Strontium Titanate Heterostructure*

5.1 Introduction

Ferroelectrics are materials that exhibit electric polarization due to spontaneous ordering of the electric dipole moments, the direction of which can be switched by the application of an external electric field. Ferroelectric materials are of importance due to their potential technological applications.

The most common and widely studied ferroelectric materials are the perovskite oxides. The perovskite oxide has a general chemical formula of ABO_3 where A and B are cations of different sizes and chemical valences, while O is oxygen anion which bonds with both A and B. The ABO_3 materials ideally crystallize in centrosymmetric lattice structure, at high temperatures, as shown in Figure 5.1, and are therefore paraelectric. However below a critical temperature T_c, the materials may start exhibiting ferroelectric behavior as a consequence of structural phase transition from high symmetry phase to one of low symmetry which breaks the centrosymmetry of the crystal.
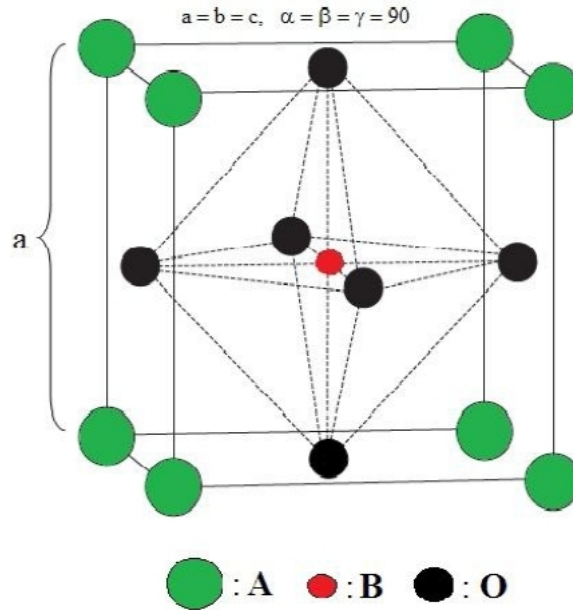
Figure 5.1: Ideal crystal structure (Space group $Pm\bar{3}m$) of a typical perovskite oxide material. The B cation is coordinated with 6 oxygen anions which form a BO_6 octahedra and the A cation has a maximal of 12 oxygen anions as it's nearest-neighbor. The BO_6 octahedra in bulk link together *via* corner sharing to form a three-dimensional octahedral network.

The deformation of the ABO_3 lattice structure at low temperatures is attributed to the softening of the low-frequency polar-phonon mode whose frequency approaches zero at T_c on cooling [1] and also as a consequence of hybridization between neighboring atoms which support displacive type (off-centering of the atoms) structural distortions within the systems.[2]

Ferroelectric perovskite oxides such as barium titanate ($BaTiO_3$), lead zirconium titanate (PZT), lead magnesium niobate (PMN), lead lanthanum zirconium titatnate (PLZT), lithium niobate ($LiNbO_3$), etc are widely used commercially, in their bulk forms as well as thin films, for a wide variety of applications such as highly efficient multi-layer ceramic capacitors[3, 4], pyroelectric detectors[5–7], transducers and actuators for microelectronic applications [8, 9], for electro-optical applications as thin film wave guides[10, 11] and thin film optical memory display[12], tunable microwave devices[13] and more.

A major research area of importance in ferroelectric material applications pertains exploiting the intrinsic ferroelectric property of switching between two stable polarization states by application of large enough electric field for non-volatile memory and

data storage applications such as ferroelectric random access memory (FRAM)[14, 15] and ferroelectric field effect transistor (FeFeT), where perovskite oxides serve as FET gates.[16–19]

Considering the significance of ferroelectric materials to the field of commercial technologies it is of equal importance to develop tools for characterization and precise measurements of the ferroelectric properties of these materials. In recent years the application of graphene field effect transistor with ferroelectric back gate has been researched for probing properties of ferroelectric materials.[20–25] One of the first use of graphene FET's as sensors was reported by A. Rajapitamahuni *et. al.*,[20] where graphene-perovskite oxide hybrid transistors were used to study and estimate the dielectric constant, pyroelectric coefficient as well as the ferroelectric polarization of barium strontium titanate (BSTO) thin films by analyzing the transfer characteristics of the FET device.
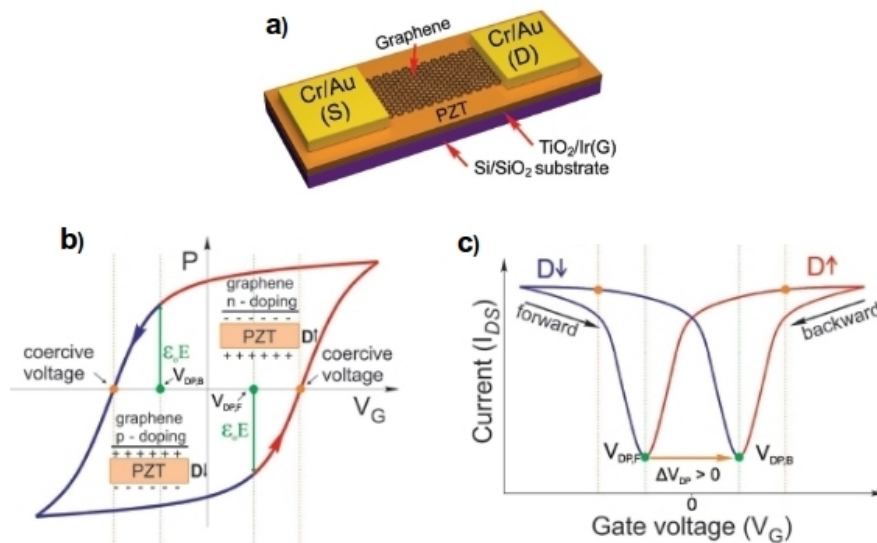
Figure 5.2: a) Schematic representation of two-terminal graphene-PZT (ferroelectric oxide) FeFET. b) Schematic representation of the dependence of polarization $\vec{P}$ on the gate voltage V_G. c) Observed anti-hysteresis in I_{DS}-V_G curve in graphene-PZT FeFeT. (The figure is adopted from Ref[25])

Figure 5.2 demonstrates the working of a typical graphene field effect transistor with a ferroelectric back gate and graphene as a conducting channel.[25] A schematic representation of the FET device is shown in Figure 5.2(a). The polarization direction depends on the direction of the applied back gate voltage V_G. For large positive values of V_G the polarization is oriented upwards while for large negative values of V_G the

polarization is oriented downwards. Figure 5.2(b) shows the dependence of the polarization $\vec{P}$ on V_G that shows hysteresis, which is a characteristic feature of ferroelectric materials. Application of back gate voltage V_G generates an electric field $\vec{E}$ which affects the polarization $\vec{P}$. The resulting electric displacemnet $\vec{D}$ given by $\vec{D} = \epsilon_0 \vec{E} + \vec{P}$ offsets the Fermi level of graphene causing conducting channel to be doped by electrons or holes depending on the polarization direction. As a consequence the channel resistance R and thus the current I_{DS} gets modified. The charge neutrality condition of the graphene channel characterized by minimum (maximum) conductivty(resistivity) is given by $\vec{D} = 0$ which is satisfied at $\vec{P} = -\epsilon_0 \vec{E}$. On tracing the hysteretic $\vec{P}$ vs V_G curve we note that this condition is satisfied for two values of the V_G (indicated by green dots) for which the conductivity attains minimum value and the two points are known as Dirac points V_{DP}. This implies that on measuring the variation I_{DS} or channel resistance (R) with respect to V_G, two Dirac points $V_{DP,F}$ and $V_{DP,B}$ should be observed for the forward sweep and the backward sweep of V_G as shown in Figure 5.2 (c). The extent of the (anti-)hysteresis, defined as $V_{DP,B} - V_{DP,F}$ is determined by the effect of the polarization on the conductivity(resistivity) of the graphene channel.

Recently A. Sahoo *et.al.*,[26] carried out an experimental study on ferroelectric polarization at the surface of strontium titanate ($SrTiO_3$). Though bulk $SrTiO_3$ (STO) is paraelectric at room temperature it approaches a incipient ferroelectric state at lower temperatures which is unstable with respect to quantum fluctuations.[27] This instability prohibits the formation of a long-range ferroelectric order in bulk STO. However surface terminations of STO along [100] direction allows hosting of out-of-plane dipole moments at the surface due to breaking of the inversion symmetry. Following the technquies similar to those prescribed by A. Rajapitamahuni *et.al.*,[18] a hybrid graphene-STO field effect transistor was used for direct evaluation of the electric polarization at the surface of STO.

Motivated by the experimental finding of Ref[26] we carried out a computational study *via* first principles method to probe the role of the surface geometry in inducing polarization at the surface of STO substrate within a graphene-$SrTiO_3$ heterostructure setup which mimics the graphene-STO field effect transistor geometry, the details of which are discussed in the current chapter.

We further investigated the influence of graphene layer on the surface geometry of the STO substrate as well as the effect of an external electric field on the surface polarization present at the interface of graphene and STO. In the subsequent section, we provide a brief background of the experimental results of Ref [26] which motivated

142

our theoretical investigation followed by the details about our study and finally the discussion of the results.

5.2   Experimental Background

The interface of graphene and $SrTiO_3$ was probed by a dual-gate single layer graphene (SLG) field effect transistor (FET) with hexagonal boron nitride ($h-$BN) as top gate and TiO_2 terminated $SrTiO_3$ (TiO_2-STO) as back gate. The schematic of the constructed dual gate SLG-FET transistor is shown in Figure 5.3(a)
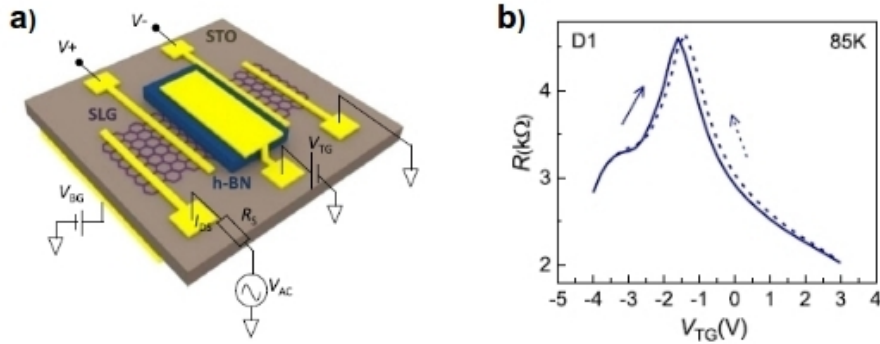
Figure 5.3: a) Schematic representation of dual-gated single-layer graphene (SLG) transistor on STO substrate with STO and $h-$BN as back and top gates respectively. b) The transfer characteristics with respect to top gate voltage V_{TG} at 85 K. The solid and dashed line depict the resistance of the graphene conducting channel with the forward and reverse sweeps of V_{TG} respectively. Figure adopted from Ref [26]

Transport and $1/f$ noise measurements were performed to obtain the resistance transfer characteristics with respect to the top gate ($h-$BN) as well as the back gate (TiO_2-STO). This allows for the a direct calibration of the graphene-STO interface relative to the conventional graphene-h-BN interface.

From transport measurements, the variance in resistance with respect to the front and reverse sweeps of the top gate voltage (V_{TG}) exhibits a negligible hysteric character due to the atomically clean, defect free nature of the interface between SLG and h-BN as shown in the plot of Figure 5.3(b).

On the other hand, the resistance transfer characteristic curve with respect to temperature and the back gate voltage (V_{BG}), as given in Figure 5.4(a,b), shows a strong anti-hysteresis at low temperatures ($< 200K$) and for a wide sweep range of V_{BG}. Such hysteretic behavior is typical of graphene FET's observed for various substrates and is

143

generally associated with the presence of impurity states due to surface defects such
as adsorbates, etc. However, it is observed from Figure 5.4 (c) that the extent of anti-
hysteresis, defined as the difference between the V_{CNP} for forward and backward sweeps
of the V_{BG}, is robust with variation of the V_{BG} sweep rate, suggesting that the surface
defects do not significantly affect the over-all hysteretic charcater. This leads to the
likelihood that the observed strong anti-hysteresis originates from different physical
mechanism.
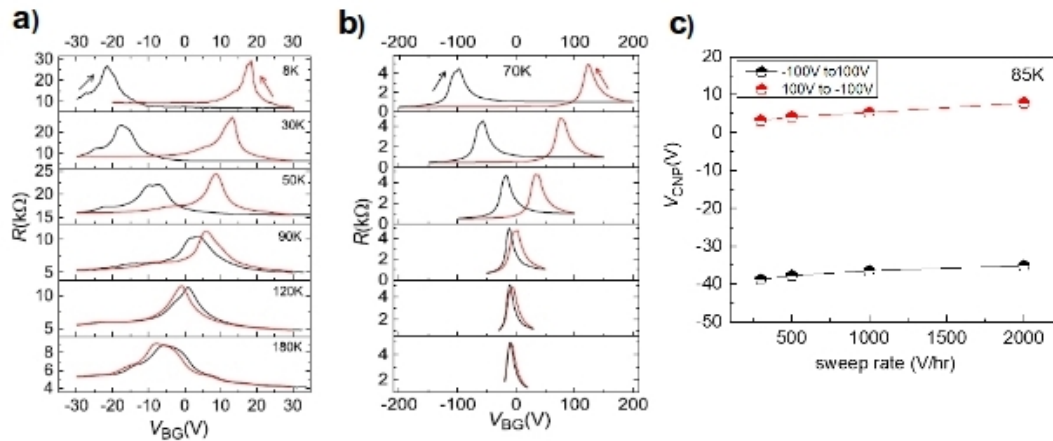
Figure 5.4: a) Anti-hysteresis in transfer characteristics with respect to back gate voltage
(V_{BG}) at different temperatures showing decrease in anti-hysteresis with increasing
temperature. b) Anti-hysteresis with respect to V_{BG} at temperature 70 K showing
decrease in anti-hysteresis with decreasing sweep range. c) The position of V_{CNP} at
different sweep rates of V_{BG} respectively. (Figure adopted from Ref [26])

Similarity of the observed transfer characteristic with those previously reported
for single- and multi-layer graphene on ferroelectric substrates [20, 21, 25] indicates
towards the possibility that the anti-hysteresis behavior originates from the presence
of electrostatically confined states at graphene-STO interface due to the formation of
surface dipole moments and thus out-of-plane surface polarization. These confined states
are called trap states as they trap, store and release charge from graphene periodically
as the V_{BG} is swept back and forth.

From the dependence of the hysteresis on temperature (ref Figure 5.4(a)) an esti-
mate of the energy barrier for the charge transfer from graphene to STO across the
interface was calculated. Equating this value to the electrostatic potential generated by
polarization field associated with the polarization of the STO given by $\Delta z P^2 A_{cell}/2\epsilon_0\epsilon_r$,
where A_{cell} is the area of TiO_2 surface unit cell yields a value of surface polarization as
$P \approx 13\mu C cm^{-2}$.

Further affirmation is provided by the 1/f noise measurement as the low frequency 1/f noise in the graphene channel resistance shows sensitivity to the surface dipoles. The origin of resistance noise i.e. the fluctuations in the resistance, $\frac{\langle\langle R^2\rangle\rangle}{R^2}$ is attributed to the noise in the trapping-detrapping rate of charge across the graphene-STO interface. The trapping-detrapping rate of charge and thus the 1/f noise is determined by the interracial potential barrier which can be strongly affected by the presence of out-of-plane surface polarization *via* the local effective electric field $\vec{E}_{eff}$. The dependence of 1/f noise on the out-of-plane surface polarization is reflected in the behavior of $\frac{\langle\langle R^2\rangle\rangle}{R^2}$ as a function V_{BG} which displays strong anti-hysteresis as shown in Figure 5.5(a,b)
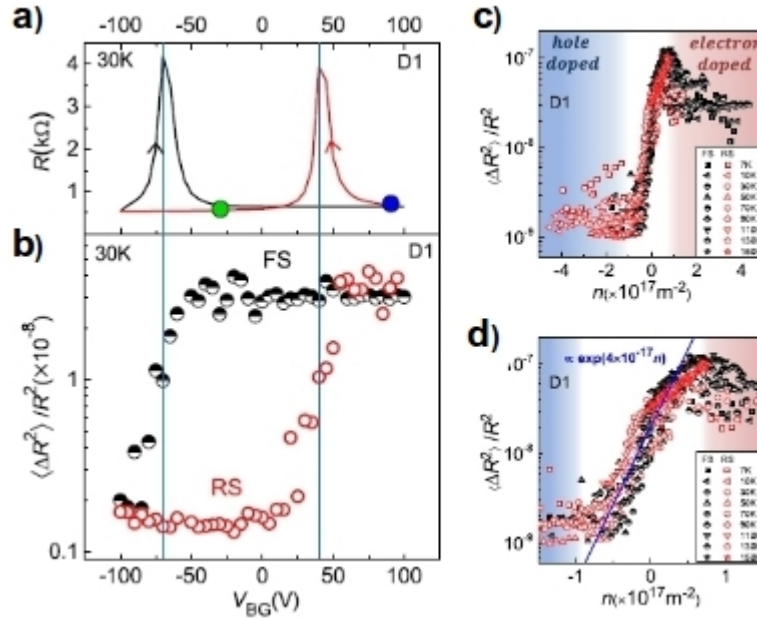
Figure 5.5: a) Anti-hysteresis in the resistance transfer characteristic of the graphene-STO FET at 30 K. b) Normalized 1/f noise $\frac{\langle\langle R^2\rangle\rangle}{R^2}$ of SLG on STO with forward sweep (FS) and reverse sweep (RS) of V_{BG} at 30 K, showing a very large magnitude on the right side of the charge neutrality point (CNP) and almost two magnitudes lower value on the left side of CNP for both FS and RS directions. c) Normalized 1/f noise $\frac{\langle\langle R^2\rangle\rangle}{R^2}$ vs carrier density (n) of the SLG channel at different temperatures from 7K to 150K showing a bistable feature in the electron-doped (red background) and hole-doped (blue background) regions for both FS and RS directions of V_{BG} d) The exponential fitting (blue line) of the noise magnitude near CNP provides the magnitude of interfacial polarization.(Figure adopted from Ref [26])

The magnitude of the surface polarization at the interface of graphene-STO can be estimated from the plot of $\frac{\langle\langle R^2\rangle\rangle}{R^2}$ as a function of carrier density n as shown in Figure

5.5(c,d). It is observed that the dependence of $\frac{\langle\langle R^2 \rangle\rangle}{R^2}$ on V_{BG} collapses on the same curve as a function of carrier density n irrespective of sweep directions or temperature. It is worth noting that since $n \propto \vec{E}_{eff}$, the monotonic variation in 1/f noise across the Dirac point is indicative of an unconventional microscopic origin dependent on the direction of $\vec{E}_{eff}$, rather than the magnitude. By exponential fitting of the experimental 1/f noise magnitude a quantitative estimate of about $12 \mu C cm^{-2}$ for the out-of-plane surface polarization was obtained which in agreement with that obtained from transport measurement.

While the above experiment shows that the observed anti-hysteresis in the transfer characteristics originates from the presence of locally confined trap states at the interface of graphene-STO as a consequence of the surface polarization at the STO surface rather than due to the impurity states, the determination of the microscopic origin that leads to formation of the surface dipole moments is beyond the scope of the experimental measurements.

In order to provide this fundamental insight we have performed simulations based on the density functional theory on the graphene-STO substrate heterostructures. Our study indicates that small displacements of the Sr and Ti atoms present within the surface layers results in the rumpling of the STO surface giving rise to surface dipole moments.

5.3   Computational Details

To simulate the graphene-STO system for a DFT study, modeling is necessary. The slab geometries for TiO_2 terminated $SrTiO_3$ (STO) substrate and graphene/STO (STO + Gr) systems were considered. The modeling was done in two different ways, referred as model-1 and model-2. The geometry of the two models is given in Figure 5.6. In both models, a $2 \times 2 \times 5$ supercell of cubic $SrTiO_3$ was considered, which was terminated at TiO_2 layer, along the [001] direction (z-direction). The STO substrate was separated from it's periodic image by a vacuum of 12 Å. The atomic positions in two bottom layers were kept fixed so as to mimic the substrate effect.

In model-1, an epitaxial registration between graphene and STO was assumed. Thus the lattice parameter of an 2×3 orthorhombic supercell of graphene was matched to that of STO substrate. This resulted in a compressive strain of 7.29 % along lattice parameter and a tensile strain of 6.77 % along in the graphene layer.

In model-2, we kept the inplane lattice parameters of STO substrate fixed. No

146
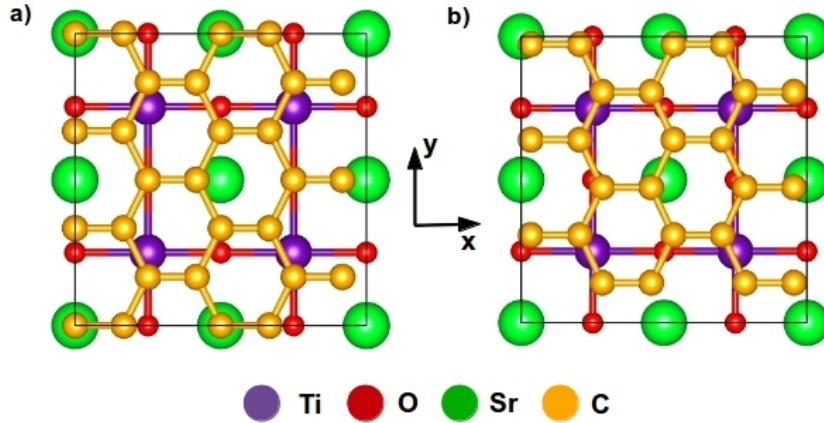
Figure 5.6: The top view of the initial geometry for a) model-1 and b) model-2

compressive or tensile strain was applied to the graphene sheet. Subsequently, structural optimization was carried out in three steps,

1. For the first step, all the layers of STO were kept fixed and only the graphene sheet was allowed to relax. For the graphene sheet, the relaxation was carried out only in the $x - y$ direction while being restricted in the z-direction. This allowed the in-plane lattice constant of the graphene sheet to adjust to that of the STO substrate without causing buckling of the sheet.

2. The second step is similar to the first step except that now the graphene sheet was allowed to be relaxed along the z-direction as well.

3. Keeping the bottom two layers of the STO substrate fixed to mimic the substrate effect, constrained relaxation of atomic coordinates of both the graphene sheet as well as the STO substrate was carried out.

Relaxation of the atomic coordinates for the TiO_2 terminated STO substrate and STO+Gr systems using DFT was carried out within the plane wave basis set as implemented in VASP[28, 29] with a kinetic energy cut-off of 500 eV. The projector augmented wave (PAW)[30, 31] potential was used and the generalized gradient approximation as parameterized by Perdew, Burke and Ernzheroff (PBE)[32] was considered for the exchange correlation. The DFT-D2 approach of Grimme[33] was used to take into account the Van-der Waals corrections. The Brillouin zone integrations were carried out over a Monkhorst-Pack grid of $4 \times 4 \times 2$ and the geometry was considered to be relaxed when the maximum force on the atoms converged to a value less than 0.01 eV/Å.

The scheme for the calculation of the polarization at the surface of STO substrate is
discussed below.

Calculation of Surface Polarization

To determine out-of-plane surface polarization $\bar{P}$ we followed the scheme implemented
by Vanderbilt *et.al.*, [34] based on calculating the dipole moment p^i on the i-th atomic
layer. This was done by identifying the nodes z_i at which $\int_{-c/2}^{z_i} \bar{\rho}(z)dz$ vanishes where
$\bar{\rho}(z) = \frac{1}{A} \int_A \rho(x,y,z)dxdy$; $\rho(x,y,z)$ being the screened charge density, c being the height
of the supercell, and A being the area of the surface unit cell.

The regions enclosed within the nodes are charge neutral and contain exactly one
SrO or TiO$_2$ atomic layer. The layer dipole moment p^i is given by $p^i = \int \bar{\rho}(z)dz$ where
the range of integration was restricted to the spacing between two nodes.

The dipole moment is largest for the surface layer due to the off-centric displacement
of the surface atoms being large. Since the atomic displacements die down rapidly as
we move away from the surface layer the dipole moment decreases correspondingly.
Thus modification of the surface polarization is primarily contributed to by the unit cell
enclosing the surface layers .

The net surface dipole moment p was then obtained by summing the individual dipole
moments of all the surface layers. Finally, the surface polarization $\bar{P}$ is given by $\bar{P} = \frac{p}{d}$
where d is the length of the unit cell.

5.4   Results and Discussion

We start our discussion, by analyzing the case of TiO$_2$ terminated SrTiO$_3$ in the absence
of graphene in order to provide a baseline reference for our further studies. Having done
so, we examine the case of graphene-STO system in the absence and presence of an
applied external field in regards to the effect on the surface polarization.

5.4.1   TiO$_2$ terminated STO in absence of graphene

From our DFT calculations, it is observed that termination of SrTiO$_3$ (STO) at the TiO$_2$
surface leads to buckling of the surface layers due to the atomic displacements of the
oxygen and metal atoms. As shown in Figure 5.7(a) and Figure 5.9(b), upon relaxation
the surface layers of the STO substrate gets somewhat rumpled due to the out-of-plane
(z) displacements of the Ti and Sr atoms, relative to the unrelaxed or ideal position
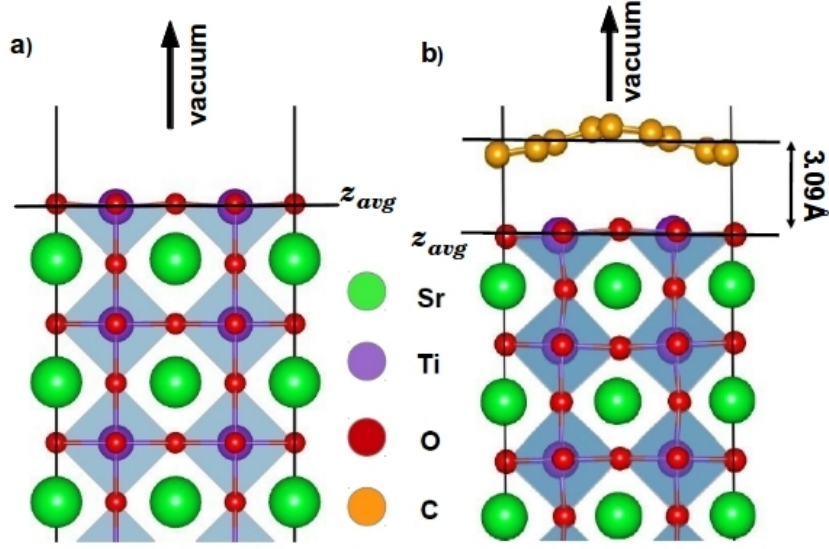
Figure 5.7: The optimized geometries for a) TiO_2 terminated STO in absence of graphene and b) TiO_2 terminated STO in presence of graphene. The Sr, Ti, O and C atoms are indicated by green, magenta, red and orange spheres, respectively. The black lines indicate the z-coordinate averaged over all atoms of the surface layer.

(marked as z_{ideal} in the Figure 5.9). Interestingly, the displacements of Ti and Sr atoms are directed oppositely as can be seen from Table 5.1. As noted from the sign, the Ti atoms (negative displacement) get pushed down towards the interior while the Sr atoms(positive displacement) get pulled up towards the surface. As a consequence the TiO_2 and SrO layers get rumpled which affects the interlayer spacing $\Delta d_{n+1,n}$ as shown in Figure 5.8.

	ΔzÅ	
	Ti	Sr
Opt. STO	-0.11	0.16
Opt. STO with SLG	-0.20	-0.01

Table 5.1: Average vertical displacement (Δz) of the Ti and Sr atoms at the surface of bare STO and STO with SLG

For the surface layers, it is observed that Δd_{21} is less than the corresponding bulk value due to the reduction in the interlayer spacing between the first and second surface layer while Δd_{23} is greater than the corresponding bulk value. This finding is consistent with the observed trends in other studies on slab geometries [34–37]. Furthermore it is also noted, that the off-centric displacements of the atoms decrease rapidly and thus,
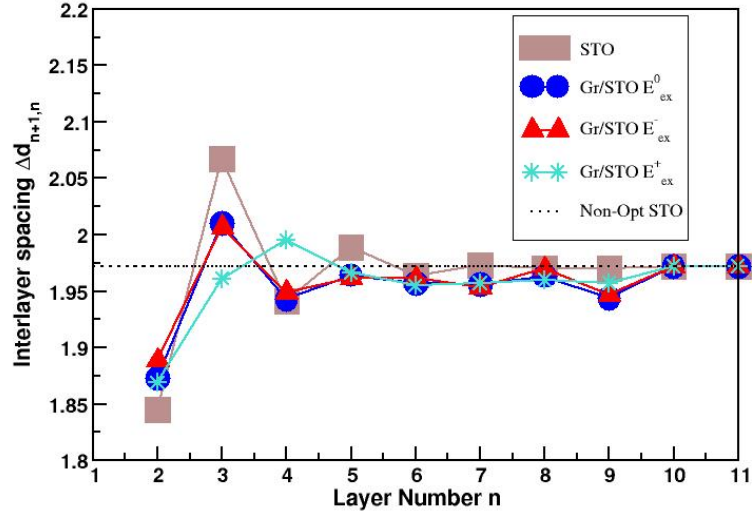
Figure 5.8: The interlayer spacing $\Delta d_{n+1,n}$ plotted against the layer number n counted down from the topmost layer marked as $n = 1$. Due to the off-centric movement of the atoms, the interlayer separation gets modified compared to that of bulk. The figure shows that the modification is largest for the first two layers (identified as surface layers) but decrease rapidly as one moves away from the surface.

the interlayer spacing approaches bulk value as we move inward away from the surface layers.

The buckling of the $SrTiO_3$ layers results in formation of dipole moments oriented along the z-direction, whose magnitude dies down rapidly as we move away from the surface corresponding to the reduction in the displacements of the atoms. Thus the contribution to surface polarization is dominated by the induced dipole moments at the surface layers viz $p^z(TiO_2)$ and $p^z(SrO)$ corresponding to the TiO_2 and the SrO surface layers. From Figure 5.9(b) we observe that $p^z(TiO_2)$ and $p^z(SrO)$ are oriented in opposite directions with $p^z(TiO_2) > p^z(SrO)$. This gives rise to a net surface polarization, directed towards the interior, $\bar{P}_{STO} = -13.89$ $\mu C/cm^2$. This is in good agreement with the result obtained by Vanderbilt $et.al.,$[34].

5.4.2   TiO$_2$ terminated STO in presence of graphene

As mentioned in Section 5.3, the modeling of the graphene-$SrTiO_3$ substrate system was done in two ways, model-1 and model-2. Our DFT calculations show that for both the
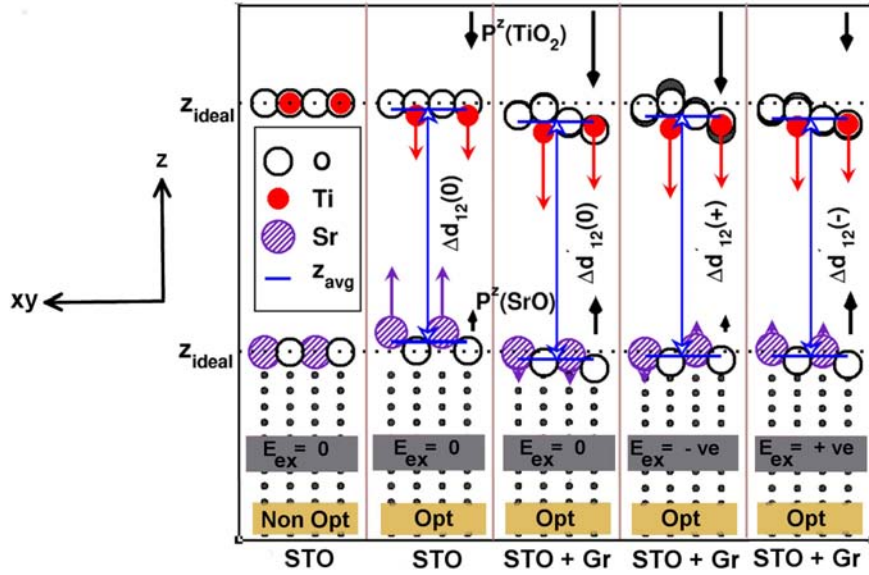
Figure 5.9: Schematic diagram of out-of-plane displacements of atoms beloning to the surface layers of the STO for five different cases a) the bulk (ideal) STO geometry b) Optimized bare STO geometry c) Optimized graphene+STO geometry d) Optimized graphene + STO geometry for negatively directed electric field $E_{-ve} = -1V/\text{Å}$. e) Optimized graphene + STO geometry for positively directed electric field $E_{+ve} = +1V/\text{Å}$. The y-axis denotes the displacements along the z-direction of the Sr, O and Ti atoms within the surface layers of the STO substrate. Only the top-most TiO_2 surface layer and the adjacent SrO layer are shown as they are the most greatly affected.

models graphene is physisorbed on $SrTiO_3$ substrate. The interlayer distance between graphene and $SrTiO_3$ (STO) substrate was found to be ~ 3.1 Å (cf. Figure 5.7(b)) which is consistent with the values obtained from previous studies of graphene physisorbed on metal substrates[38–41]. Thus graphene interacts with STO substrate mainly *via* Van der Waals interaction.

Graphene when deposited on STO substrate undergoes buckling which in turn also buckles the surface layers of STO as shown in Figure 5.7(b). In order to understand how the rumpling of the graphene sheet affects the surface polarization of the STO substrate, the case of model-1 is discussed as the added component of strain causes the graphene sheet to buckle significantly and thus alters the surface geometry of the STO substrate to greater degree.

The drastic influence on the surface geometry of STO substrate due to the presence of graphene, in the case of model-1, can be seen from Figure 5.9(c). The geometry of the surface layers is modified due to the rearrangement of the surface atoms compared to

that in absence of graphene (ref Figure 5.8).

The Ti atoms in the topmost TiO_2 layer get pushed further down towards the interior while the O atoms get displaced by different magnitudes depending on their positions relative to graphene. While for the present analysis we consider only out-of-plane (z-direction) movements, in-plane displacements are also observed in presence of graphene. Compared to the case in absence of graphene, the TiO_2 layer is much more rumpled (refer Table 5.1) resulting in larger value of the dipole moment, $p^z(TiO_2)$. In contrast, the displacements of Sr atoms belonging to SrO layer is suppressed (refer Table 5.1) while large displacements is observed for the O atoms in the SrO layer directed towards the interior. It should be noted that the displacements in SrO layer is practically insignificant compared to the case in absence of graphene. This leads to an overall enhancement of the net surface polarization in presence of graphene with $\bar{P}_{STO+Gr}$ = -34.90 μC/cm^2, compared to -13.89 μC/cm^2 in absence of graphene. The estimate of the surface polarization $\bar{P}_{STO+Gr}$ for the model-1 is larger by almost magnitude of two from the experimental estimate obtained from the transport and 1/f noise measurement as discussed in Section 5.2.

Comparatively, for the case of model-2 where no strain is applied to the graphene sheet, the degree of buckling of the graphene sheet is an order of magnitude smaller. Thus surface geometry of the STO substrate is affected to a lesser degree leading to a decreased value of surface polarization $\bar{P}_{STO+Gr}$ = -24 μC/cm^2 which is closer in magnitude to the experimental value.

Thus, the presence of graphene leads to enhancement of the polarization at the surface of STO, with the magnitude depending on the degree of buckling of the graphene sheet.

5.4.3 Influence of an external electric field on surface polarization

It is reasonable to assume that application of an external electric field along the positive z direction, would cause the negatively charged atoms to be pushed inward towards the bulk, while the positive ions will be pulled outward toward the surface. The reverse is expected to happen upon changing the orientation of the external electric field. As a consequence, the rumpling of the surface layers is expected to be strongly modified in the presence of an external electric field which affects the surface polarization.

From Figure 5.9 (d,e), it is clearly observed that presence of electric field influences

the atomic displacements and the calculated polarization values of the surface layers, leading to a strong asymmetry between positive and negative directions of electric fields.

As can be seen from Figure 5.9(e), in the case of positively directed electric field, we indeed find that relative to the graphene-STO case in absence of electric field (refer Figure 5.9 (c)), the positively charged Ti and Sr atoms are pulled toward the surface while the negatively charged O atoms are displaced inward towards the bulk. The change in the overall rumpling of the layers gives rise to surface dipole moments, $p^z(TiO_2)$ and $p^z(SrO)$ at TiO_2 and SrO layers that are found to be nearly equal in magnitude and oppositely directed, leading to near cancellation. The calculated polarization for an electric field of +1 V/Å turned out to be a tiny value of +2.286 $\mu C/cm^2$.

Reversing the direction of the electric field, leads to greater rumpling of the TiO_2 layer due to the larger displacements of the O ions (refer Figure 5.9 (d)). This causes a significant enhancement of the surface dipole moment $p^z(TiO_2)$ at TiO_2 layer. The application of negative electric field, on the other hand, makes the surface dipole moment $p^z(SrO)$ at SrO layer vanishingly small due to the oppositely directed atomic displacements of the Sr atoms which nearly nullifies the contribution of the SrO layers towards the surface polarization. Thus contribution to surface polarization $\bar{P}_{STO+Gr}$ dominantly comes from the TiO_2 layer and attains a large value of -66.39 $\mu C/cm^2$ for a considered electric field of -1 V/Å.

This leads us to conclude that there exists a strong asymmetry between the two stable polarization states on switching the direction of the electric field which is consistent with the experimental observations from 1/f noise measurements of resistance transfer characteristics.

5.5 Conclusion

Motivated by the recent experimental study where the out-of-plane surface polarization at the TiO_2 terminated surface of $SrTiO_3$ (100) crystal was measured by using graphene FET's as probe, we carried out a computational study within the framework of density functional theory on graphene-$SrTiO_3$ heterostructure geometry.

The modeling of the heterostructure was done in two ways. In model-1 assumption of an epitaxial registration, led the graphene to be strained. For model-2 no strain was applied to the graphene sheet. Keeping the in-plane lattice parameters of STO substrate fixed, the lattice constant of graphene was allowed to adjust to that of the substrate.

Our DFT calculations showed that buckling of the surface layers of TiO_2 terminated

STO, even in the absence of graphene, results in the formation of surface dipole moments along the z-direction. These out-of-plane surface dipole moments are a consequence of the off-centric displacements of the surface atoms which give rise to a net surface polarization $\vec{P} = -13.89\mu C/cm^2$.

The presence of graphene was observed to have a influence on the surface geometry of STO substrate. Buckling of the graphene layer causes the rearrangement of the surface atoms leading to the modification of the surface geometry. As a consequence the net polarization at the STO surface is enhanced and its magnitude was calculated to be $-34.90\mu C/cm^2$ and $-24\mu C/cm^2$ for model-1 and model-2 respectively. Our estimated values of surface polarization are larger than the experimentally obtained estimates. However, it should be noted that DFT is well-known to overestimate the polarization values.

Application of an external electric field leads to further modification of the surface geometry, dependent on the direction of the electric field. This results in a strong asymmetry in the calculated polarization values for the positive and negative directions of the electric field. For an electric field of strength +1 V/Å the estimated magnitude of polarization turned out to be tiny value of $+2.286\mu C/cm^2$. On reversing the electric field direction a rather large polarization value of $-66.39\mu C/cm^2$ was calculated for a field of -1 V/Å. The observed asymmetry between the two polarization states on switching direction of the electric field from our model simulations is consistent with the experimental observations reported in Ref [26].

5.6 Bibliography

[1] W. Cochran *Physical Review Letters*, vol. 3, p. 412, 1959.

[2] R. E. Cohen *Nature*, vol. 358, p. 136, 1992.

[3] D. Dimos and C. H. Mueller *Annual Review of Materials Science*, vol. 28, p. 397, 1998.

[4] I. H. Pratt *Proceedings of the IEEE*, vol. 59, p. 1440, 1971.

[5] K. Iijima, Y. Tomita, R. Takayama, and I. Ueda *Journal of Applied Physics*, vol. 60, p. 361, 1986.

[6] R. Takayama, Y. Tomita, K. Iijima, and I. Ueda *Journal of Applied Physics*, vol. 61, p. 411, 1987.

[7] R. Takayama and Y. Tomita *Journal of Applied Physics*, vol. 65, p. 1666, 1989.

[8] K. Uchino, S. Nomura, L. E. Cross, R. E. Newnham, and S. J. Jang *Journal of Materials Science*, vol. 16, p. 569, 1981.

[9] P. Muralt, R. G. Polcawich, and S. Trolier-McKinstry *MRS Bulletin*, vol. 34, p. 658, 2009.

[10] S. Miyazawa, S. Fushimi, and S. Kondo *Applied Physics Letters*, vol. 26, p. 8, 1975.

[11] S. Miyazawa, K. Sugii, and N. Uchida *Journal of Applied Physics*, vol. 46, p. 2223, 1975.

[12] S. L. Swartz *IEEE Transactions on Electrical Insulation*, vol. 25, p. 935, 1990.

[13] E. A. Nenasheva, A. D. Kanareykin, N. F. Kartenko, A. I. Dedyk, and S. F. Karmanenko *Journal of Electroceramics*, vol. 13, p. 235, 2004.

[14] J. F. Scott and C. A. Paz de Araujo *Science*, vol. 246, p. 1400, 1989.

[15] J. F. Scott, L. Kammerdiner, M. Parris, S. Traynor, and V. Ottenbacher *Journal of Applied Physics*, vol. 64, p. 787, 1988.

[16] S. Mathews, R. Ramesh, T. Venkatesan, and J. Benedetto *Science*, vol. 276, p. 238, 1997.

[17] J. Yu, Z. Hong, W. Zhou, G. Cao, J. Xie, X. Li, S. Li, and Z. Li *Applied Physics Letters*, vol. 70, p. 490, 1997.

[18] E. Tokumitsu, G. Fujii, and H. Ishiwara *Applied Physics Letters*, vol. 75, p. 575, 1999.

[19] Y. Watanabe *Applied Physics Letters*, vol. 66, p. 1770, 1995.

[20] A. Rajapitamahuni, J. Hoffman, C. H. Ahn, and X. Hong *Nano Letters*, vol. 13, p. 4374, 2013.

[21] X. Hong, J. Hoffman, A. Posadas, K. Zou, C. H. Ahn, and J. Zhu *Applied Physics Letters*, vol. 97, p. 033114, 2010.

[22] E. B. Song, B. Lian, S. Min Kim, S. Lee, T.-K. Chung, M. Wang, C. Zeng, G. Xu, K. Wong, Y. Zhou, H. I. Rasool, D. H. Seo, H.-J. Chung, J. Heo, S. Seo, and K. L. Wang *Applied Physics Letters*, vol. 99, p. 042109, 2011.

[23] W. Lee, O. Kahya, C. Tat Toh, B. Özyilmaz, and J.-H. Ahn *Nanotechnology*, vol. 24, p. 475202, 2013.

[24] C. Baeumer, S. P. Rogers, R. Xu, L. W. Martin, and M. Shim *Nano Letters*, vol. 13, p. 1693, 2013.

[25] A. Lipatov, A. Fursina, T. H. Vo, P. Sharma, A. Gruverman, and A. Sinitskii *Advanced Electronic Materials*, vol. 3, p. 1700020, 2017.

[26] A. Sahoo, D. Nafday, T. Paul, R. Ruiter, A. Roy, M. Mostovoy, T. Banerjee, T. Saha-Dasgupta, and A. Ghosh *npj 2D Materials and Applications*, vol. 2, 2018.

[27] K. A. Müller and H. Burkard *Physical Review B*, vol. 19, p. 3593, 1979.

[28] G. Kresse and J. Hafner *Physical Review B*, vol. 47, p. 558, 1993.

[29] G. Kresse and J. Furthmüller *Physical Review B*, vol. 54, p. 11169, 1996.

[30] P. E. Blöchl *Physical Review B*, vol. 50, p. 17953, 1994.

[31] G. Kresse and D. Joubert *Physical Review B*, vol. 59, p. 1758, 1999.

[32] J. P. Perdew, K. Burke, and M. Ernzerhof *Physical Review Letters*, vol. 77, p. 3865, 1996.

[33] S. Grimme *Journal of Computational Chemistry*, vol. 27, p. 1787, 2006.

[34] B. Meyer and D. Vanderbilt *Physical Review B*, vol. 63, p. 205426, 2001.

[35] J. Padilla and D. Vanderbilt *Surface Science*, vol. 418, p. 64, 1998.

[36] B. Meyer, J. Padilla, and D. Vanderbilt *Faraday Discussions*, vol. 114, p. 395, 1999.

[37] J. Padilla and D. Vanderbilt *Physical Review B*, vol. 56, p. 1625, 1997.

[38] H. Zi-Pu, D. Ogletree, M. V. Hove, and G. Somorjai *Surface Science*, vol. 180, p. 433, 1987.

[39] A. T. N'Diaye, S. Bleikamp, P. J. Feibelman, and T. Michely *Physical Review Letters*, vol. 97, p. 215501, 2006.

[40] C. Busse, P. Lazić, R. Djemour, J. Coraux, T. Gerber, N. Atodiresei, V. Caciuc, R. Brako, A. T. N'Diaye, S. Blügel, J. Zegenhagen, and T. Michely *Physical Review Letters*, vol. 107, p. 036101, 2011.

[41] P. Sutter, J. T. Sadowski, and E. Sutter *Physical Review B*, vol. 80, p. 245411, 2009.

ELECTRONIC AND MAGNETIC PROPERTIES OF TRANSITION-METAL EMBEDDED HOLEY GRAPHENE*

Manuscript under preparation

6.1 Introduction

In recent years, the 2-D graphene derivative, holey graphene has been extensively studied with regards to it's functionality for achieving graphene-based applications. As introduced in chapter 1, holey graphene or graphene nanomesh is obtained by introduction of well defined in-plane nano-holes sprinkled in an ordered fashion within the graphene sheet. The introduction of nano-holes in large number results in, (a) higher surface area which facilitates the cross-plane transport of particulate matter, (b) generation of high number of hole-edge atoms which provide active sites for increased interaction with adorbants, and (c) a significant modification of the graphene electronic properties due to quantum confinement of the remaining graphitic structure.

Synthesized holey graphene have been reported to show enhanced electrochemical performance with ultra high energy density, power density and specific capacity for supercapacitor applications [1] as well as high reversible capacity, superior high rate capability and long cycling stability for lithium ion battery applications.[2]

Theoretical studies based on MD simulations have also reported on the use of holey graphene as an ion separation membrane for selective segregation of cations and anions based on their size[3], as well as a molecular sieve for gas purification such as H_2 with superior selectivity over traditional membranes of silica and carbon[4] or as gas

separation membranes to separate atmospheric gases.[5] Moreover, it has been predicted
that holey graphene exhibits excellent water permeability which is higher by magnitude
than conventional reverse osmosis membranes making it an effective filter for separation
of NaCl salt from water.[6]

As discussed in chapter 1, holey graphene also shows good semiconducting properties
as a result of the quantum confinement of the graphitic backbone frame, which supports
the porous structure, to 1-D channels. Experimental reports already indicate that holey-
graphene based FET's can support currents 100 times greater than graphene nanoribbon
devices with comparable ON-OFF ratio. Various experimental and theoretical studies
have also showed that the magnitude of band gap opening in holey-graphene depends
inversely on the channel width which in turn depends on the size of nano-hole and the
lattice vectors which make it suitable candidate for band gap engineering applications.

Very recently, in 2015, Mahmood et. al., were able to successfully synthesize for the
first time a new 2-D holey-graphene derivative known as nitrogenated holey graphene
which consists of uniform distribution of holes and nitrogen atoms and has a C_2N
stoichometry.

Very recently, in 2015, Mahmood et. al., were able to successfully synthesize for the
first time a new 2-D holey-graphene derivative known as nitrogenated holey graphene
which consists of uniform distribution of holes and nitrogen atoms and has a C_2N
stoichometry.[7] Experimental studies have demonstrated that N-doped holey graphene
showed improved oxygen reduction reaction (ORR) performance[8] and also improved
ion adsorption resulting in decreased energy barriers for ion diffusion which in turn led
to higher capacity and rate performance in lithium ion batteries(LIB).[9] Furthermore,
it was reported that N, S co-doped porous graphene used as an electrode could deliver
higher power density of 116 kW Kg^{-1} and energy density of 322 W h kg^{-1} for LIB's.[10]
Computational studies have also reported that single- and double- sided N functionalized
holes behave as good sieves for helium isotope separation.[11, 12] Given the above, it is
expected that the novel 2-D porous material, C_2N will have tremendous applications in
the areas of gas storage, molecular sieving, supercapacitors and batteries.

Nitrogenated holey-graphene has also been shown to be a direct band gap semicon-
ductor with an experimental band gap of 1.96 eV which makes it a suitable candidate
for electronic device applications. C_2N based field effect transistors have already been
demonstrated to show a good ON/OFF ratio of 10^7.[7] The added benefit of having a
direct band gap implies that C_2N can also find applications in opto-electronic devices,
photocatalysis, etc.

Theoretical studies based on *ab initio* calculations have shown that the electronic properties of C_2N can be tuned from semiconducting to half-metallic by electron or hole doping over a wide range of doping concentrations.[13, 14] While pristine C_2N is found to be non-magnetic, the studies also show that the such electron or hole doping results in the stabilization of ferromagnetic order within the system which arises due to the spin-splitting of the electronic states at the valence band maximum for hole doped case and at the conduction band minimum for the electron doped case.[13–15] Furthermore, the study by Gong *et.al* also indicated that the magnetism in C_2N can be controlled by uniaxial strain and that for values of strain ∼ 10 % the magnetism completely vanishes.[13] Thus engineering of band gaps as well as control over magnetism by external means is possible for C_2N materials.

Passivation of the hole edges by H, F atoms can also provide an alternative way to improve the functionality of holey-graphene systems. In this chapter we have thus considered chemical modification of C_2N by replacing N by CF group.

Quite recently, the effect of embedding of $3d$ transition metal atoms within the holes of the C_2N geometry have also been extensively studied within the approach density functional theory.[16–18] in the context of their electronic and magnetic properties. Motivated by these studies, in addition to exploring the electronic structure of chemically modified holey graphene *viz* C_2CF, we has thus also explored the influence of the chemical modification on embedding of TM atom like scandium (Sc).

6.2 Computational Details

All the first principle calculations performed are based on density functional theory as implemented in the Vienna *Ab initio* Simulation Package (VASP).[19, 20] The projector augmented wave (PAW)[21, 22] potentials were used and the wavefunctions were expanded in a plane wave basis set with kinetic energy cut-off of 500 eV. All structural relaxation were carried out within the generalized gradient approximation (GGA)[23] as parameterized by Perdew-Burke-Ernzerhof (PBE).[4] In order to correctly describe the d-electrons of the transition metal atoms, an on-site Coulomb interaction $U = 4$ eV was applied to our calculations. A Monkhorst-Pack k-point mesh of $4 \times 4 \times 1$ was used. The structures were considered optimized within the convergence criteria of 0.01 eV/Å for the forces.

For our study two holey graphene systems were considered, a) the nitrogenated holey graphene (C_2N) monolayer system and b) the fluorine passivated holey graphene (C_2CF)

monolayer system. The C_2CF geometry was obtained by chemical modification of the C_2N geometry upon substitution of N atoms by the C-F molecule, leading to a resemblance with fluorine passivated graphene nanomesh geometry.

For studying embedding by transition (TM) metal atoms in both systems we have chosen to start with the scandium (Sc) atom. The site positioning for the TM atoms embedded in C_2N monolayer structure have been previously studied with differing results.[16, 17, 24] In particular for the scandium (Sc) atom the site position was reported to be at the center of the hole in Ref[16], while Ref[24] and Ref[17] report an off-centered position. The differing results could possibly arise due to the inclusion of the on-site Coulomb interaction U, which correctly describe the d-electrons of TM atoms in Ref[16] and which is absent in Ref[24], Ref[17]. Keeping in mind, that the positioning of the embedded atom can affect it's electronic properties, an U = 4 eV, similar to Ref[16] was applied to our calculations.
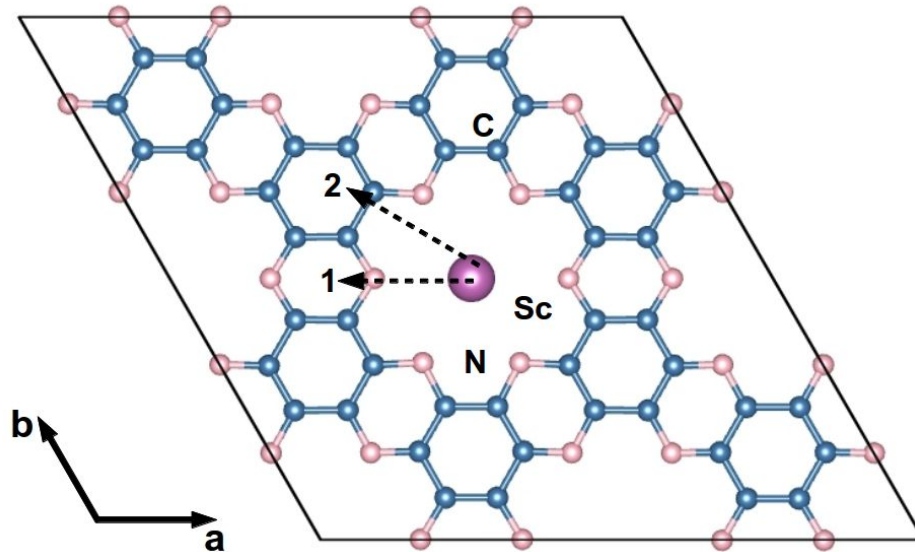
Figure 6.1: Schematic showing the displacement of Sc atom from the center along : direction 1 corresponding to displacement along x direction and direction 2 corresponding to displacement along x-y direction

In order to estimate the correct site positioning, the Sc atom was initially placed

at the center of the hole and subsequently kicked off-center step-by-step (with larger magnitudes in each step) along the the two directions as indicated in Figure 6.1. Thus, the Sc atom was placed at 5 positions along each of the two directions and for each position the structure was optimized.

6.3 Results and Discussion

We start our discussion by describing the geometry and electronic structure of the porous 2D C_2N and C_2CF monolayer sheets,

6.3.1 Pristine C_2N vs C_2CF

Geometry

The optimized crystal structure of monolayer pristine C_2N and C_2CF are shown in Figure 6.2. The 2D-honeycomb lattice of C_2N can be thought of as the benzene rings being bridged by pyrazine ring. This results into holes of radii r_H = 2.76 Å distributed uniformly in the monolayer sheet. The lattice constant (a_{lat}) of 8.33Å obtained after optimization agrees well with the previously reported values for C_2N.[7, 16, 17] The slight distortion of the benzene ring due to presence of the N atoms causes the alternate C-C bonds of the ring to be stretched by as much as 2.8 %. Our calculated values of 1.43 Å , 1.47 Å and 1.34 Å for the C-C(1), C-C(2) and C-N bond lengths (refer Figure 6.2 (a)) respectively, are also in accordance with previous results.[16, 17]
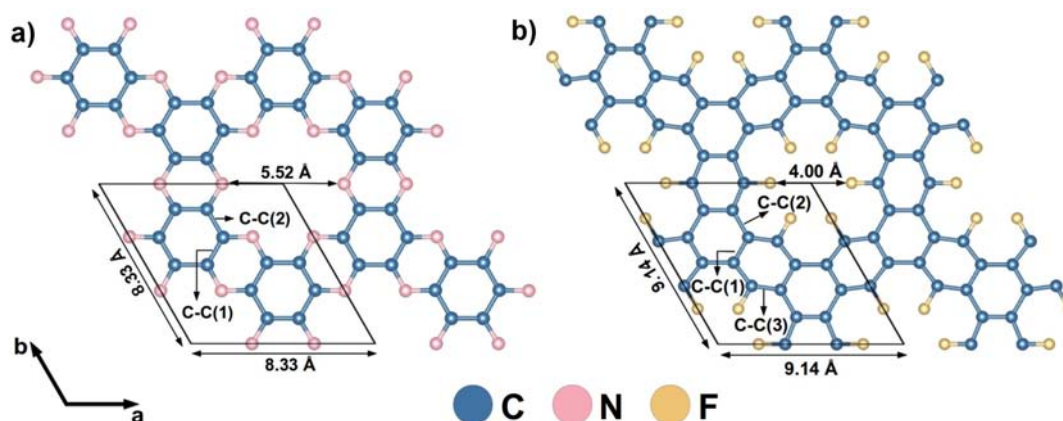
Figure 6.2: Geometry of a) pristine C_2N monolayer and b) pristine C_2CF monolayer. The box indicates the unit cell for the systems. The arrows indicate the unit-cell length and hole diameter ($2r_H$).

Similar to C_2N, the structure of C_2CF can be viewed as benzene rings being bridged
by a para-difluorobenzene ring instead of a pyrazine ring. The obtained a_{lat} of 9.14 Å is
9.72 % larger compared to that of pristine C_2N . The estimated values of the bond lengths,
as tabulated in Table 6.1, clearly show that the benzene rings get further distorted upon
substitution of the N atoms in C_2N by C-F molecule. Fluorine passivation causes the
hole size to decrease, with a reduced r_H value of 2.00 Å compared to 2.76 Å for C_2N. The
C-C(2) bond length is longer by 7.75 % over the C-C(1) bond length, which is greater than
the 2.8 % estimated for C_2N. This implies a higher deformation for the corresponding
benzene ring within the C_2CF geometry. Deformation of the para-difluorobenzene ring
causes the C-C bonds to be stretched by 3.4-3.8 % and the C-F bond to be compressed by
3.4 % with respect to the isolated molecule. That the calculated C-F bond length of 1.31
Å is smaller than the C-N bond length is expected due to the enhanced ionic character of
the C-F bond compared to the C-N bond, due to higher electro-negativity of fluorine than
nitrogen.

Bond length	C_2N	C_2CF
C-C (1)	1.429 Å	1.432 Å
C-C (2)	1.469 Å	1.543 Å
C-C (3)	-	1.445 Å
C-N(F)	1.336 Å	1.304 Å

Table 6.1: The table provides the optimized bond lengths for the pristine C_2N and C_2CF
structures.

Electronic Structure

The calculated electronic band structure and projected density of states (PDOS) for the
pristine C_2N and C_2CF sheets are shown in Figure 6.3. It is observed that both pristine
C_2N and pristine C_2CF are direct band gap semiconductors as both the valence band
maximum and conduction band minimum lie at the Γ-point. The band gap values were
calculated to be 1.64 eV and 1.25 eV for C_2N and C_2CF respectively. Our estimate of 1.64
eV for the C_2N band gap matches well with reported theoretical estimates,[7, 16, 17] but
is smaller than the 1.96 eV estimated by experiments[7]. Such a discrepancy is to be
expected as it is a well-known fact that DFT underestimates the band gap. The band gap
of 1.25 eV for pristine C_2CF is smaller than the pristine C_2N band gap.

An interesting point to note in the band structure of C_2N, is the existence of flat
bands at the valence band (VB) and conduction band (CB) edges. From the PDOS shown
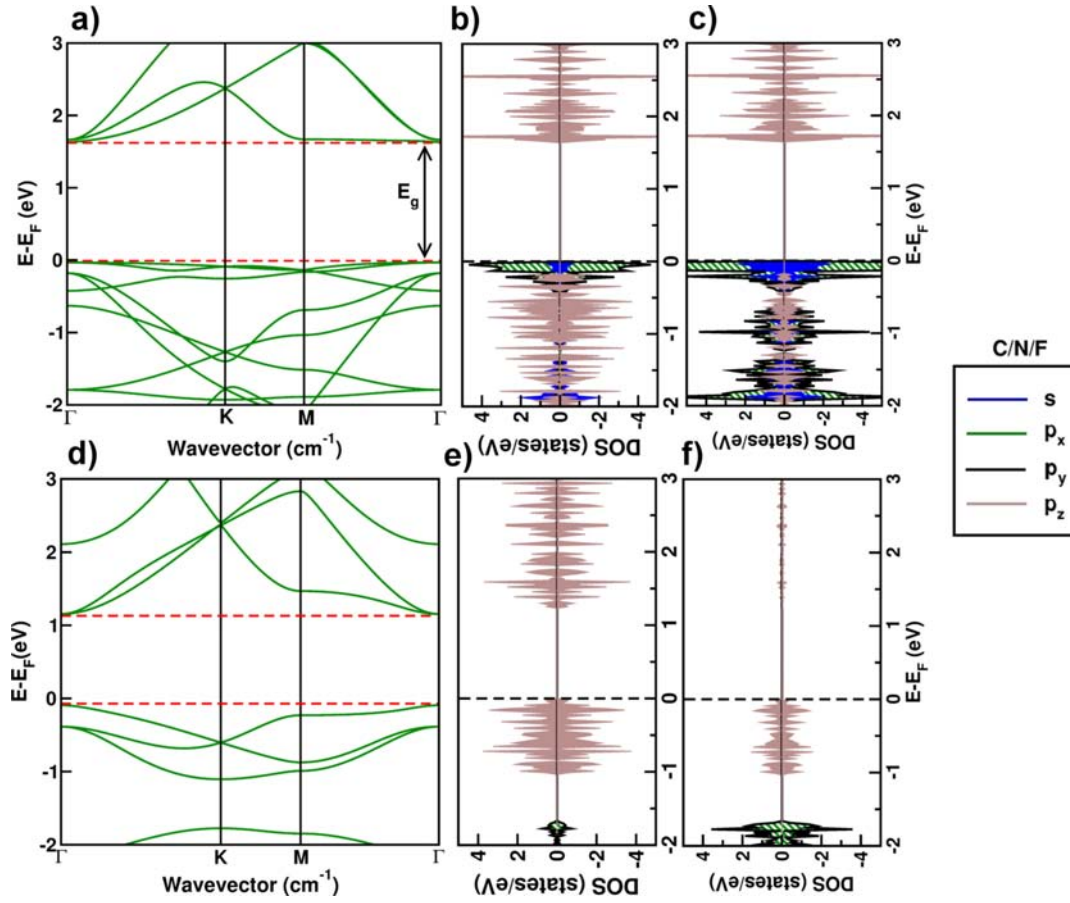
Figure 6.3: a), d): Band structure for pristine C_2N and C_2CF. E_g denotes the band gap. b), c): Density of states (DOS) projected on the s (blue), p_x (green hatched),p_y (black), p_z (brown shaded) states for C (panel b) and N (panel c) atoms. e), f): DOS project on the s,p_x, p_y, p_z states for C (panel e) and F(panel f).(Same color convention as in a).

in Figure 6.3 (b),(c), we note that the strong hybridization between the s, p_x and p_y orbitals of N and C atoms results in the formation of σ states which contribute to the valence band edge. The occurrence of the doubly degenerate flat band at the valence band edge is due to the presence of non-bonding σ states localized on each of the nitrogen atoms due to the lone pair of electrons. On the other hand, the flat band at the conduction edge stems from the π state arising from the localized p_z orbital of the nitrogen atom. These observations are consistent with previous studies[7, 16]. It has been suggested these flat bands near the edges can be tailored to induce useful functionalities.

The electronic band structure of pristine C_2CF is vastly different from that of pristine C_2N as observed from Figure 6.3 (d), specially the replacement of N by C-F removes the flat band at the VB and CB edges. The pristine C_2CF geometry bears similarity

with the hydrogen-passivated graphene nanomesh (GNM).[25, 26] An unpassivated
semiconducting GNM has unsaturated σ bonds localized on the carbon atoms located
at the hole perimeter. These unsaturated σ bonds give rise to mid-gap states in the
electronic structure. Passivation of the hole edges, by fluorine (F) in our case, saturates
the atomic orbitals resulting in the mid-gap states being shifted out of the gap. From
the PDOS plotted in Figure 6.3 (e),(f) we observe fluorine (F) bonds covalently with C
due to a strong hybridization between the fluorine p orbitals and the C sp^2 orbitals.
The p_z orbital of F is completely occupied and lies below the Fermi energy E_F set to
zero. Thus, unlike the case of pristine C_2N, the F atomic orbitals do not contribute
significantly to the valence band edge states. The major contribution to the valence
states and conduction states comes from dispersive π and π^* bands arising from the
conjugated system associated with benzene.

6.3.2 Embedded Transition Metal (TM) atoms in C_2N and C_2CF

Previous studies on embedding of $3d$ TM atoms in holey graphene systems reveal that
the electronic properties can depend significantly on the choice of the atom and site
positioning.[16, 17, 24] Depending on the choice of the embedded TM atom semiconduct-
ing, semi-metallic and metallic behaviors have been reported. The electronic properties
are also sensitive to site positioning, as in the example of Sc atom embedded in C_2N
where for the atom positioned at the center of the hole a semiconducting behavior was
reported[16] while for the off-centered position metallic behavior was reported.[17, 24].
As mentioned before, this differing result may arise from the inclusion or omission of the
on-site Coulomb interaction U beyond GGA in the exchange correlation approximation.
In the following section, we discuss the effect of embedding Sc atom in C_2N (Sc-C_2N)
and C_2CF (Sc-C_2CF) on the geometry, electronic and magnetic properties of the system.
Further more, we also investigate the case of Sc dimer embedded in adjacent holes of the
C_2N (Sc$_2$-C_2N) and C_2CF (Sc$_2$-C_2CF) geometries.

Single Sc atom embedded in C_2N and C_2CF

Geometry

To find the site positioning of the Sc atom, the procedure outlined in section 6.2 was
followed. The optimized geometries for Sc-C_2N and Sc-C_2CF are shown in Figure 6.4.
Our calculation show that for Sc-C_2N case, the Sc atom is found to stably sit at the

central site S_1 or at the off-centered sites S_2, S_3. In order to estimate which site is energy favorable, we calculated the binding energy (BE) defined as follows

(6.1)
$$E_b = E_{metal} + E_{C_2N} - E_{metal-C_2N}$$

where E_{metal}, E_{C_2N} and $E_{metal-C_2N}$ are the energy of isolated metal atom in the same volume, the energy of pristine C_2N and the energy of metal embedded-C_2N.
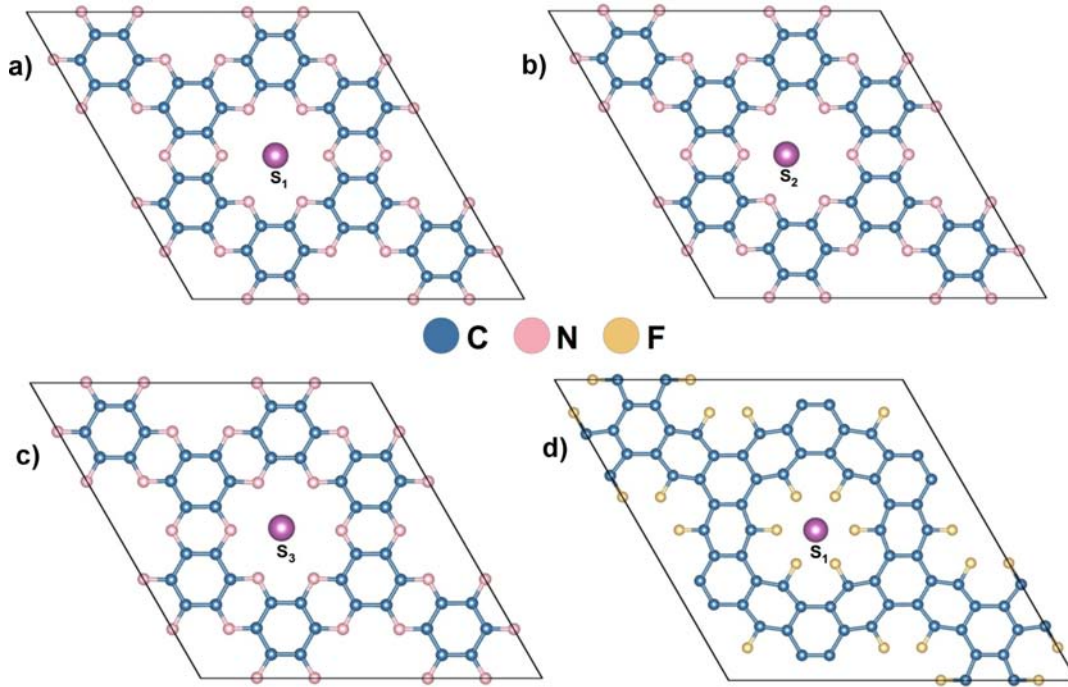
Figure 6.4: Optimized geometries for (a) centered Sc-C_2N geometry (site S_1), (b),(c) off-centered Sc-C_2N geometry (site S_1 and S_2) and (d) centered Sc-C_2CF geometry (site S_1).

From the estimates of the binding energies (BE) provided in Table 6.2, we note that Sc positioned on off-centered sites S_2 and S_3 have the same BE and therefore the same stability. However both S_2 and S_3 have a higher BE (7.04 eV) and are therefore more stable than Sc positioned on the central site S_1 (BE = 6.94 eV). Our findings are consistent with those of Ref[17, 24]. Thus, we note that the Sc atom prefers to sit in an off-centered position within the hole. Such an off-centering is possible due to the fact that size of Sc atom (covalent radius = 1.84 Å) is much smaller than size of the hole (r_H = 2.76 Å). The S_2 and S_3 sites have a lower symmetry than the S_1 site but allow for the Sc atom to form strong covalent bond with some of the neighboring N atoms, thereby increasing the stability of the structure.

System	Adsorption Site	BE (eV)	Magnetic moment μ_B	
			Sc atom	In Cell
Sc-C_2N	S_1	6.94 eV	0.55	3.00
	S_2	7.04 eV	0.72	1.42
	S_3	7.04 eV	0.72	1.92
Sc-C_2CF	S_1	1.57 eV	0.74	1.25

Table 6.2: The binding energy (BE) in eV, the magnetic moment (m) in μ_B and the Sc-N(F) bond lengths in Å for both the systems studied

In contrast for the Sc-C_2CF case, the size of the Sc atom is nearly equal to the size of the hole and as such off-centering of the Sc atom is not possible. Thus, the Sc atom prefers to sit at the central site S_1 as shown in Figure 6.4(d). The estimate of 1.57 eV for the BE (calculated as in equation 1) suggests that the Sc binds weakly to C_2CF compared to Sc-C_2N and hence is less stable. The relatively smaller value of the Sc-F bondlength (2.05 Å) over the Sc-N bondlength (2.48 Å) suggests that the Sc-F bonding is more ionic in character and hence responsible for the weaker binding of Sc to C_2CF.

Electronic Structure and Magnetic Properties

Figure 6.5 gives the density of states (DOS) as well as the magnetization density for the ground state geometry of Sc-C_2N and Sc-C_2CF geometries which, for the Sc-C_2N case is the Sc positioned on the S_3 site and for the Sc-C_2CF case is Sc positioned at S_1 site.

The DOS is projected onto the C p states, N(F) p states and the Sc d states. For Sc-C_2N we observe that the spin degenerate Sc d_{xz} and d_{yz} orbitals are occupied and lie $\sim$ 0.7 eV below the Fermi energy E_F while the $d_{x^2-y^2}$, d_{xy} and $d_{3z^2-r^2}$ orbital are unoccupied and lie above the E_F. The Sc d_{xz} and d_{yz} undergo a hybridization with N p_z orbitals to form covalent bonds. As these p_z orbitals in pristine-C_2N contribute to the flat band at the conduction band edge, the formation of covalent bonds with the Sc atom pushes the Fermi level E_F towards the conduction band making the system metallic. Furthermore, the asymmetry between the up-spin channel and down-spin channel suggests that the the ground state is magnetic and a local moment of about 0.72 μ_B was found on the Sc atom (refer Table 6.2).
From the magnetization density (refer Figure 6.5(c)) we note that small but finite moments are induced on the neighboring N atoms as a result of the covalent bonding between Sc and N.

On the other hand, we observe that the bond between Sc and C_2CF sheet is more ionic, with a charge being transfered to the C_2CF sheet due to high electro-negativity
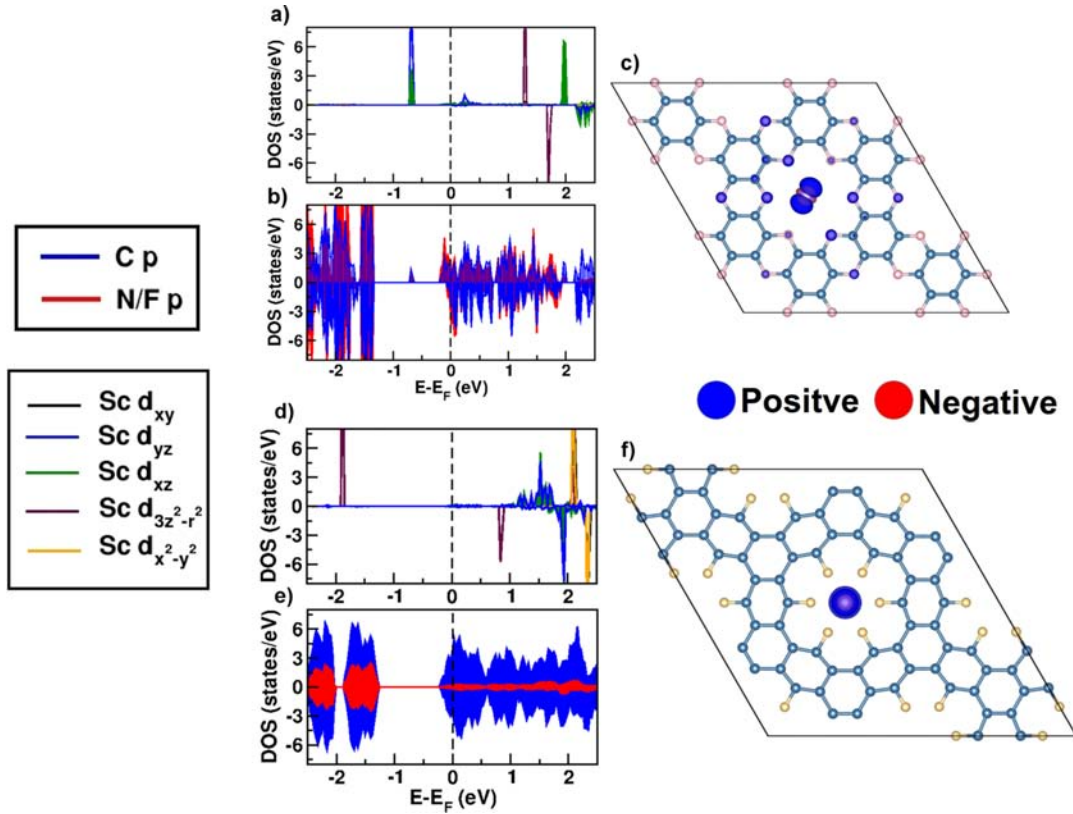
Figure 6.5: The figure shows PDOS and magnetization density for the ground state geometries of Sc-C$_2$N (a),b),c)) and Sc-C$_2$CF(d),e),f)). The panels (a),(b) give the DOS projected on the C, N p states and the Sc d states. The panels (d),(e) give the DOS projected on the C, F p states and the Sc d states for the Sc-C$_2$CF system. The panels (c), (f) give the magnetization density for the Sc-C$_2$N and Sc-C$_2$CF geometries at an isosurface vales of 0.005 e^-/Å^3. Blue color represents the up-spin densities and red color represent the down-spin densities in both the cases.

of fluorine. Since contribution to the valence and conduction bands arises from the dispersive π and $\pi*$ bands belonging to the benzene network, a transfer of charge results in the n-doping of the C$_2$CF system and pushes the E_F towards the conduction band making the system metallic. Similar to Sc-C$_2$N, the asymmetry between up-spin and down-spin channels leads to a magnetic ground state with a magnetic moment of 0.74 μ_B being found on the Sc atom. From the magnetization density (refer Figure 6.5(f)) it is noted, that no magnetic moment is induced on the neighboring F atoms implying that the charge transfered is delocalized over the entire C$_2$CF through the π network of benzene.

Thus, we note that embedding of the Sc atom in porous C$_2$N and C$_2$CF monolayer sheets cause the systems to transition from semiconducting to metallic.

169

Sc dimer embedded in C_2N and C_2CF
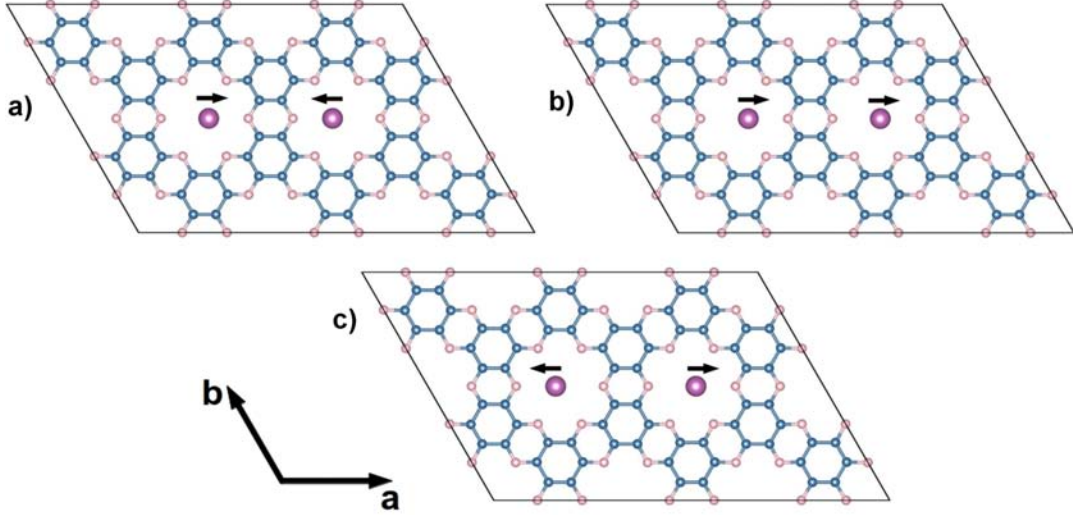
Figure 6.6: The initial configurations for Sc_2-C_2N geometry

Case of Sc_2-C_2N

Since the single Sc-atom embedded in C_2N prefers to sit in an off-centered position, the embedding of a pair of Sc atoms can be done in three ways as shown in Figure 6.6 *viz* a) the two Sc atoms are off-centered in opposite directions but towards each other, b) the two Sc atoms are off-centered in the same direction and c) the two Sc atoms are off-centered in opposite directions but away from each other. The distance between the two Sc atoms d_{Sc-Sc} for the three cases a), b), c) are 7.81 Å, 8.33 Å and 8.85 Å respectively. For all the three cases, the Sc atoms were off-centered along the x-direction.

Non-spin polarized geometry optimization on all the three cases causes them to converge in same geometry as shown in Figure 6.7(a). The converged geometry shows that the Sc atoms get additionally displaced along the y-direction and the displacements are oppositely directed for the two Sc atoms. This additional displacement makes the Sc-Sc distance 7.66 Å, smaller than the 7.81 Å. This is suggestive of the development of magnetic exchange coupling between the two Sc atoms. The coupling between the Sc atoms can be ferromagnetic (FM), where spins on the Sc atoms are aligned in parallel or anti-ferromagnetic (AFM), where the spins are oppositely directed. A spin-polarized geometry optimization considering both the spin configurations reveals that FM state is the ground state. The exchange energy $\Delta E = E_{AFM} - E_{FM}$ was found to be 9.3 meV.
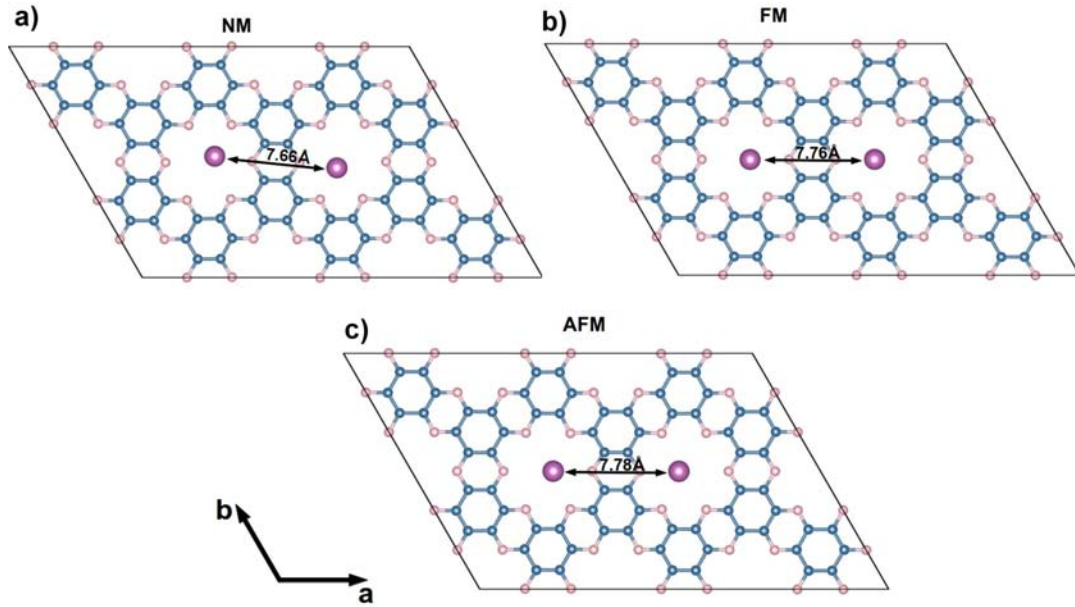
Figure 6.7: Optimized geometries for the Sc_2-C_2N geometry: (a) Non-magnetic state, (b) Ferromagnetic spin alignment state and (c) Anti-ferromagnetic spin alignment state. The arrows indicate the distance between the two Sc atoms, d_{Sc-Sc}.
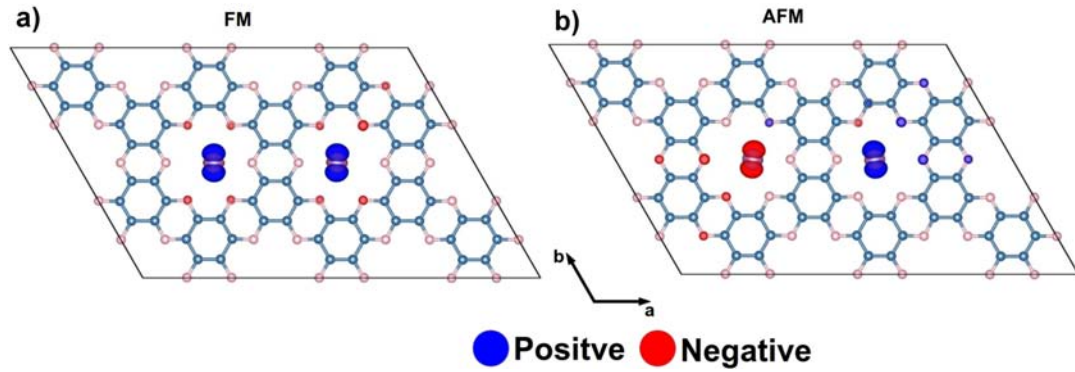
Figure 6.8: Magnetization density for (a) Ferromagnetic spin alignment state and (b) Anti-ferromagnetic spin alignment state. The isosurface was plotted for a value of 0.005 e^-/Å and up-spin and down-spin densities are given by blue and red color, respectively

In the optimized geometry considering the FM and AFM spin alignment of the Sc atoms (refer Figure 6.7 (b),(c)), the Sc-Sc distance is found to be 7.76 Å and 7.68 Å, respectively, both larger than the 7.66 Å found in the case of non-spin polarized situation. This in turn hints towards strong magnetostructural coupling as observed in the case of Fe dimer placed on BLG.[27] A magnetic moment of magnitude of 0.66 μ_B was found to develop on each Sc atom which is lower than the 0.72 μ_B observed for the single Sc

embedding. From the magnetization density plots shown in Figure 6.8 we note that the neighboring N atoms carry a small but finite magnetic moment with the spins oppositely directed with respect to the Sc-atom.

Case of Sc$_2$-C$_2$CF
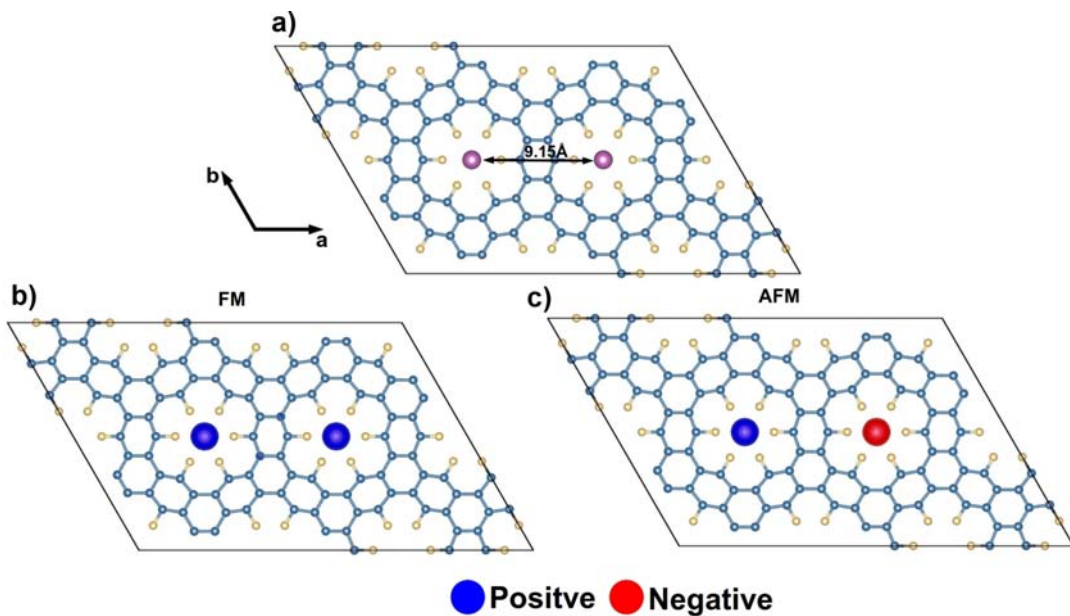
Figure 6.9: The figures shows (a) the optimized geometry for Sc$_2$-C$_2$CF and (b),(c) the magnetization density for the ferromagnetic and anti-ferromagnetic states, respectively. The same scheme as used in Figure 6.8 is employed.

In contrast to Sc$_2$-C$_2$N, the two Sc atoms were found to be in a centered position for the Sc$_2$-C$_2$CF geometry for both non-spin polarized and spin-polarized calculations. The spin-polarized optimized geometry is shown in Figure 6.9(a). The d_{Sc-Sc} = 9.16 Å for both FM and AFM spin configurations. Similar to the case of Sc$_2$-C$_2$N, the Sc atoms were found to be ferromagnetically coupled. The exchange energy ΔE was estimated to be 3.3 meV which is smaller than the 9.3 meV predicted for Sc$_2$-C$_2$N case. We observe from, the magnetization density given in Figure 6.9(b),(c), that unlike the Sc$_2$-C$_2$N case no magnetic moments are found on the neighboring fluorine atoms. The magnetic moment of 0.74 μ_B found on the Sc atom is same as that found for single Sc atom case.

6.4 Conclusion

Our study considering holey graphene of chemical composition C_2N and it's chemical modification C_2CF shows that the replacement of N by C-F molecule causes a significant narrowing of the band gap by removal of the unsaturated mid-gap states which were responsible for producing the flat bands at the conduction and valence band edges of C_2N. We further studied the influence of single TM and TM dimer embedding on these two systems. In particular, we considered the Sc atom as our choice of TM atom. The differential nature of the chemical bonding between Sc and N and that between Sc and F together with the difference of hole size in the two systems results into differential geometry, electronic structure, and magnetism of embedded in TM atoms in the two cases. In future, we would like to extend this analysis to other TM atoms.

6.5 Bibliography

[1]   Y. Zhu, S. Murali, M. D. Stoller, K. Ganesh, W. Cai, P. J. Ferreira, A. Pirkle, R. M.
      Wallace, K. A. Cychosz, M. Thommes, *et al. science*, vol. 332, p. 1537, 2011.

[2]   Z. Fan, J. Yan, G. Ning, T. Wei, L. Zhi, and F. Wei *Carbon*, vol. 60, p. 558, 2013.

[3]   K. Sint, B. Wang, and P. Král *Journal of the American Chemical Society*, vol. 130,
      p. 16448, 2008.

[4]   Y. Li, Z. Zhou, P. Shen, and Z. Chen *Chemical Communications*, vol. 46, p. 3672,
      2010.

[5]   S. Blankenburg, M. Bieri, R. Fasel, K. Müllen, C. A. Pignedoli, and D. Passerone
      Small, vol. 6, p. 2266, 2010.

[6]   D. Cohen-Tanugi and J. C. Grossman *Nano Letters*, vol. 12, p. 3602, 2012.

[7]   J. Mahmood, E. K. Lee, M. Jung, D. Shin, I.-Y. Jeon, S.-M. Jung, H.-J. Choi, J.-M.
      Seo, S.-Y. Bae, S.-D. Sohn, *et al. Nature communications*, vol. 6, p. 6486, 2015.

[8]   D. Yu, L. Wei, W. Jiang, H. Wang, B. Sun, Q. Zhang, K. Goh, R. Si, and Y. Chen
      Nanoscale, vol. 5, p. 3457, 2013.

[9]   J. Xu, Y. Lin, J. W. Connell, and L. Dai *Small*, vol. 11, p. 6179, 2015.

[10] Z.-L. Wang, D. Xu, H.-G. Wang, Z. Wu, and X.-B. Zhang *ACS Nano*, vol. 7, p. 2422,
      2013.

[11] A. W. Hauser and P. Schwerdtfeger *The Journal of Physical Chemistry Letters*, vol. 3,
      p. 209, 2012.

[12] A. W. Hauser, J. Schrier, and P. Schwerdtfeger *The Journal of Physical Chemistry C*,
      vol. 116, p. 10819, 2012.

[13] S. Gong, W. Wan, S. Guan, B. Tai, C. Liu, B. Fu, S. A. Yang, and Y. Yao *Journal of
      Materials Chemistry C*, vol. 5, p. 8424, 2017.

[14] J. Zhu, Y. Zhao, S. Zeng, and J. Ni *Physics Letters A*, vol. 381, p. 1097, 2017.

[15] Z. Liang, B. Xu, H. Xiang, Y. Xia, J. Yin, and Z. Liu *RSC Advances*, vol. 6, p. 54027,
      2016.

[16] J. Du, C. Xia, W. Xiong, X. Zhao, T. Wang, and Y. Jia *Physical Chemistry Chemical Physics*, vol. 18, p. 22678, 2016.

[17] D. Ma, Q. Wang, X. Yan, X. Zhang, C. He, D. Zhou, Y. Tang, Z. Lu, and Z. Yang *Carbon*, vol. 105, p. 463, 2016.

[18] Y. Yang, M. Guo, G. Zhang, and W. Li *Carbon*, vol. 117, p. 120, 2017.

[19] G. Kresse and J. Hafner *Physical Review B*, vol. 47, p. 558, Jan. 1993.

[20] G. Kresse and J. Furthmüller *Physical Review B*, vol. 54, p. 11169, Oct. 1996.

[21] P. E. Blöchl *Physical Review B*, vol. 50, p. 17953, Dec. 1994.

[22] G. Kresse and D. Joubert *Physical Review B*, vol. 59, p. 1758, Jan. 1999.

[23] J. P. Perdew, K. Burke, and M. Ernzerhof *Physical Review Letters*, vol. 77, p. 3865, Oct. 1996.

[24] M. M. Fadlallah, A. A. Maarouf, U. Schwingenschlögl, and U. Eckern *Journal of Physics: Condensed Matter*, vol. 29, p. 055301, 2016.

[25] K. Tada, J. Haruyama, H. Yang, M. Chshiev, T. Matsui, and H. Fukuyama *Physical Review Letters*, vol. 107, p. 217203, 2011.

[26] Y. Ding, Y. Wang, S. Shi, and W. Tang *The Journal of Physical Chemistry C*, vol. 115, no. 13, p. 5334, 2011.

[27] D. Nafday, M. Kabir, and T. Saha-Dasgupta *Physical Review B*, vol. 93, no. 4, p. 045433, 2016.

SUMMARY AND OUTLOOK

The non-magnetic, zero-gap semiconducting nature of graphene hinders it's practical usage in several applications despite it's highly sought after properties. Tailoring of the properties of graphene in order to fully utilize it's capabilities is an active area of research currently. In this regard the topic of graphene magnetism has generated considerable interest from the aspects of basic physics as well as future technologies such as spintronics. One of the major focus of the studies presented in this thesis, was the investigation of the magnetic properties of various graphene-based systems and it's manipulation by external means. The other focus area of the reported studies was how the sensitivity of the graphene electronic properties to external stimuli can be exploited to use graphene as a probe to study the properties of other materials. As showcased in chapter 3-6, we have investigated graphene-based systems belonging to four broad classes a) Few Layer Graphene , b) Graphene Nanoflakes , c) Graphene/Oxide heterostructures and d) Graphene Nanomesh. We have used first principles calculation within the framework of density functional theory (DFT) as well as model Hamiltonian approach in combination with exact digaonalization (ED) technique depending on their need in specific cases.

In the present chapter we present a concise summary of the main results obtained from our investigations discussed in the previous chapters and a brief discussion on the future directions that maybe undertaken.

7.1   Summary

7.1.1   Summary of Chapter 3

In this chapter we investigated the properties of adatom-bilayer graphene systems with emphasis on the formation of local magnetic moments and the control of the magnetic moments by an applied external electric field.

Our DFT study showed that the difference in the nature of adatom-BLG bonding between the alkali metal (Na) and transition metal (Cu,Fe) dictates the formation of local magnetic moments. We found that ionic bonding between Na adatom and BLG disfavors formation of local magnetic moment, while the covalent nature of bonding between Cu/Fe adatoms and BLG promotes the formation of local magnetic moment. We further showed that the application of an external electric field perpendicular to the adatom-BLG system tunes the adatom energy states relative to the BLG states causing a change in the nature of bonding between adatom and BLG which in turn directly affects the formation of local magnetic moment. The study also highlighted the key role played by orbital physics in the promotion of adatom magnetism. For the single-orbital case of Na and Cu adatoms where the s orbital plays a key role in magnetism, the application of an external electric field results in switching 'on' and 'off' of the magnetic moment. In contrast, the multi-orbital picture of the Fe adatom, where the d-orbital manifold plays a key role, offers an additional layer of complexity to the adatom magnetism scenario. Compared to the rather simple scenario of the single orbital case, the application of an external electric field results in the modulation of charge and spin states of the Fe adatom over a broad range dependent on the strength and directionality of the electric field. States ranging from $3d^6, S = 2$ to $3d^{10}, S = 0$ for the Fe adatom were observed which hitherto were inaccessible under normal conditions and therefore would be of interest in the context of Kondo physics. Motivated by the observations of local magnetic moment control by an external electric field, we further investigated the tunability of the exchange interaction between a pair of adatoms placed on BLG. Our calculations on a pair of Fe adatoms placed in a dimer-like configuration on BLG showed that the magnetic ground state corresponds to the parallel alignment of the Fe spins. However, of more interest was the observation of a strong magnetostructural coupling within the systems which leads to different geometric structure for the Fe dimer in parallel and anti-parallel spin states, which results in an uncompensated ferrimagnetic state for the Fe dimer over a fully compensated anti-ferromagnetic state. Furthermore, we found that the application of an external electric field can tune the RKKY interaction between the

pair of Fe atoms by modification of the electronic states of the mediating delocalized electrons of BLG. This leads to control over the Fe-Fe exchange interaction which can be switched from ferromagnetic coupling to ferrimagnetic coupling for an appropriate value of the electric field.

7.1.2 Summary of Chapter 4

In this chapter by employing exact diagonalization technique to solve the extended Hubbard model, we investigated the effects of the strong non-local electron-electron correlations *via* the inter-site Coulomb interaction term (V) on the magnetic and thermodynamic properties of graphene nanoflakes due to the formation of many-body instabilities. We considered two types of nanoflakes (a) the zigzag trigonal nanodisk and (b) the zigzag linear nanostripe in order to take into account the effect of geometry which plays a significant role in determining the properties at nanoflakes. Additionally, the effect of doping, which can cause further instabilities was also accounted for by modulating the electron filling (n) over a wide range. Our study, thus provided a complete magnetic phase diagram in $n - V$ space for the two different geometries.

Our investigations showed that the competition between the on-site Coulomb interaction (U) and the inter-site Coulomb interaction (V) drives the system towards charge disproportionation triggering the formation of charge density wave (CDW) patterns. We found that the formation of CDW depends significantly on the doping level and the precise value of V/U which promotes the development of strong long-range ferromagnetic correlations within the flake which can be made anti-ferromagnetic by changing the value of V. Thus, it was observed that the magnetic phase diagram in $n - V$ space consisted of isolated regions of net-magnetic-moment phases separated by phases having zero-magnetic-moment character with the nature of magnetic ground state being strongly dependent on electron filling. Our study also showed that a transition between zero- and net-magnetic-moment phases can be achieved by changing the electron filling by as little as one electron or one hole. On comparison of the $n - V$ phase diagram for the two nanoflake geometries, it was noted that the the linear nanostripe geometry disfavors structures with net-magnetic-moments which suggests that geometry also plays a role in determining the nature of the magnetic ground state.

Our investigations also showed that inclusion of inter-site Coulomb interaction V can affect the low-temperature thermodynamic properties such as magnetization and specific heat due the the presence of low-lying excited eigenstates of contrasting magnetic character compared to the ground state. It was observed that small changes in either

temperature or V results in a crossover to a magnetic state, triggered by transition between net-magnetic-moment and zero-magnetic-moment eigenstates. The magnetic crossover was found to be accompanied by a sharp peak in the specific heat which should be detectable by experiments. Our prediction may be validated by doping the flakes through gating and tuning the inter-site Coulomb interaction V by placing the flakes on different dielectric substrate.

7.1.3 Summary of Chapter 5

In this chapter, we carried out density functional theory based investigation on graphene-SrTiO$_3$ (STO) heterostructure geometry in order to study the influence of graphene on the out-of-plane surface polarization observed at the TiO$_2$-terminated surface of SrTiO$_3$ and the effect of an external electric field on the said surface polarization. The motivation for such a study stems from recent experimental studies where out-of-plane polarization at the surface of TiO$_2$-terminated surface of SrTiO$_3$(100) crystal was measured by utilizing graphene field effect transistor as a probe.

Our DFT calculations showed that the buckling of the surface layers of TiO$_2$-terminated SrTiO$_3$ caused by off-centric displacement of the surface atoms is mainly responsible for the formation of out-of-plane dipole moments at the surface and hence a finite surface polarization of $\vec{P} = -13.89 \mu\text{C/cm}^2$ even in the absence of graphene. It was observed that the introduction of graphene modifies the surface geometry of SrTiO$_3$ due to rearrangement of the surface atoms as consequence of graphene buckling. This results in an enhancement of the net surface polarization by almost an order of 2 in magnitude. Furthermore our study also shows that application of an external electric field leads to further alteration of the surface geometry depending on the directionality of the field. As a result, a strong asymmetry between the net surface polarization values is observed for positive and negative directions of the applied electric field. For an electric field of strength +1 V/Å the estimated magnitude of polarization was calculated to be tiny value of $+2.286 \mu\text{C/cm}^2$. However, on reversing the electric field direction a rather large polarization value of $-66.39 \mu\text{C/cm}^2$ was obtained for a field of -1 V/Å. The observed asymmetry between the two polarization states on switching direction of the electric field as found in our model simulations is consistent with the experimental observations.

7.1.4 Summary of Chapter 6

In this chapter we investigated the electronic and magnetic properties of nitrogenated holey-graphene (C_2N) and it chemical derivative C_2CF obtained by substitution of N atoms by C-F within the framework of density functional theory (DFT). Calculation of the electronic band structure for the C_2N and C_2CF geometry showed that both the systems are direct band gap semiconductors with band gaps of 1.64 eV and 1.25 eV respectively. The significant reduction in the band gap upon replacement of N atoms by C-F molecule was attributed to the removal of unsaturated localized states of the N atoms, responsible for the flat bands observed at the valence and conduction band edges of C_2N.

We also investigated the formation of the local magnetic moment for the cases of single TM atom and pair of TM atoms embedded within the C_2N and C_2CF systems. In particular we studied the case of Sc atom, our choice of TM atom, in terms of site positioning, electronic structure and magnetism when embedded in these two systems.

We found that the reduction in hole size as well as the differential nature of bonding between Sc and N atoms and that between Sc and F atoms leads to different preference of site positioning for the Sc atom within the two systems. For the C_2CF case, we found that the Sc atom prefers to sit in the centered position as a result of the decrease in hole size. In contrast, for the C_2N case, the off-centered position for the Sc atom was found to be more energetically favorable. From the electronic structure and spin-polarized calculation we observed that the embedding of Sc atom within the two system causes the system to exhibit metallic behavior instead of semiconducting with the formation of local magnetic moments close to 0.72 μ_B on the Sc atom.

Further calculations on embedding of a pair of Sc atoms showed that in both cases *viz* C_2N and C_2CF, the coupling between the two Sc atoms was found to be ferromagnetic with the exchange energy ΔE being equal to 9.3 meV and 3.3 meV. The chemical modification of holey graphene thus modulates the electronic structure of the system as well as modulates its functionality towards embedding of TM atoms.

7.2 Outlook

7.2.1 Adatom Assemblies on Few-layer Graphene

In the present thesis it has been shown by employing computational methods that adatom magnetism as well as the magnetic exchange coupling between a pair of adatoms placed on bilayer graphene (BLG) can be manipulated by external means such as an electric

field. First of all this, study should be extended beyond BLG to encompass adatom-few-layer graphene (FLG) systems as well. Secondly the study should be extended to adatom structure beyond a single or pair of adatoms.

Among the limited literature available on the subject of adatom magnetism in adatom-FLG systems, studies on the magnetic properties of adatom assemblies on FLG's such as linear atomic chains are almost non-existent. Theoretical studies based on spin lattice models suggest that for infinite one-dimensional (1-D) linear chains long-range ferro-magnetic order is prohibited.[1–3]. However these studies do not take into account the interaction between the 1-D nanostructures and the substrate on which it is grown. Experimental investigations on 1-D TM monoatomic linear chains grown on metal substrates show that the monoatomic chains consist of both short and long range fer-romagnetic order owing to the presence of large magnetic anisotropy energies.[4–8]. In particular, linear Fe monoatomic chains have garnered interest for nanoelectronic and spintronic applications. Using spin-polarized scanning tunneling microscope Eigler *et. al.*, demonstrated that Fe atomic chains on Cu_2N surfaces exhibit two switchable Néel AFM states[7], Khajetoorians *et.al.*,[8] constructed a atomic-spin based logic gate by utilizing AFM coupled Fe atomic chains placed on Cu(001) surface as spin leads for transferring signals from input to gate region and Menzel *et.al.*,[9] demonstrated vector spin chirality based information transfer for Fe chains on Ir(001) surface. These studies highlight the importance of substrate interactions in determining the magnetic order of these 1-D nanostructures. Theoretical simulations by Heinze *et.al.*, on $3d$ TM atom chains supported by metal substrate report that even a weak chain-substrate hybridization is sufficient to modify the magnetic coupling within the chains.[10]

Considering the fact that our studies show that for a pair of adatoms placed on BLG, the magnetic coupling between the adatoms can be tuned by external means, it would be interesting to study if the conclusion holds true even for a 1-D linear atomic chain placed on BLG/FLG, which can be regarded as an extended assembly of a pair of adatoms. However since the metal-metal interaction tends to be stronger than metal-graphene interaction, metal atoms tend to aggregate and form islands on graphene surface which makes patterning of metal atoms on graphene/BLG(FLG) sheets ex-perimentally difficult.[11–14] On the other hand, there are theoretical studies which speculate that such adatom assemblies can be stabilized on 2-D sheets by application of strain.[10, 15]. Futhermore, various studies have also shown that applying strain can tune the magnetic properties of defected graphene systems.[16–18] E.J. Santos *et.al.*, using first principle calculations have shown that magnetism in Ni-doped graphene can

be switched by applying an anisotropic strain.[19, 20]. More recently, B. Huang *et.al.*, showed that the spin-dependent hybridization between transition metal (TM) adatom d orbitals and graphene π orbitals can be affected by the presence of strain in the system and can therefore lead to tuning of the adatom magnetic states.[21]

Thus, as a future extension of our project on adatom-graphene assembly, our plan is to study the electronic and magnetic properties of such 1-D linear atomic chain assemblies and 2-D metal layers deposited on graphene/BLG(FLG) in order to investigate the possibility of strain controlled magnetism in these systems.

7.2.2 Intercalation of water between graphene and SrTiO$_3$ substrate

The structural, dynamical and thermodynamical properties of a fluid can be greatly affected relative to their bulk properties on confinement to nanoscale dimensions. In this regard, the study of water under nano-confinement has implications across various fields of science such as physics, chemistry, biology, etc. In cells, the confinement of water within the interstices between biomolecules can affect mechanisms regulating protein-folding[22–24], transference of molecules and ions across biological channels[25, 26], etc. Furthermore, factors such as the confinement geometry as well as the interactions between fluid-fluid or fluid-solid interfaces can modify the hydrogen bond networks which can significantly influence the wetting properties and adhesion between surfaces[27–30], dielectric properties of water[31–34] and may also lead to phase transitions.[35–39] Various studies have reported that confinement can promote freezing of water at room temperature as a result of entropy reduction.[39–42] Other studies suggest that application of electric field along with confinement can also affect the freezing temperature of water, known as electrofreezing, due to realignment of the water dipole moments which can result in rearrangement of the hydrogen bond network.[43–46] Qian *et. al.*, have showed that an lateral electric field can lead to formation of bilayer ice when water is confined between two walls with a fixed separation.[47] This is further supported by molecular dynamics study by Nie *et.al*, which show it is easier to freeze water when an electric field is applied parallel to confinement direction than when applied in perpendicular direction.[48] Electric field induced by charged surfaces can also cause the electrofreezing of water. D. Ehre *et.al.*, have reported positive and negatively charged surfaces of pyroelectric materials such as LaTiO$_3$ and SrTiO$_3$ can differently affect water freezing with positively charged surfaces promoting ice nucleation and

negatively charged surface reducing freezing temperatures.[49] Water layer adsorped on charged graphene was studied by Zhu *et. al.*, and phase transition of water from electromelting to electrofreezing was reported at room temperature with increase in charge values.[50] Investigation by D. Donadio *et.al.*, showed that for water confined between two non-polar planar surfaces the electronic charge density fluctuations occuring at the interface can affect the IR activity of the water molecules.[51] On the other hand, it was recently reported by Schlaich *et.al.*, that confinement of water molecules between two polar surfaces can lead to asymmetry in the dielectric response.[31]

In view of above, as an extension of the work reported in chapter 5, where out-of-plane surface polarization was found to be stabilized and enhanced at TiO_2 terminated surface of $SrTiO_3$ in the presence of graphene, we would like to take up investigation of water intercalated between graphene and $SrTiO_3$ surface. It is our expectation that the asymmetric confinement of water between a non-polar (graphene) and polar ($SrTiO_3$) surface would influence the properties of water such as structure, dielectric response in a manner different from those reported for symmetric confinement between non-polar and polar surfaces. Furthermore, keeping in mind the observation of a strong asymmetry in the electric field dependent polarization values at $SrTiO_3$ surface, it would also be of interest to study the effect of electric field on the freezing of the intercalated water.

7.2.3   Tunable magnetic properties of TM atoms embedded in holey graphene

In chapter 6, we presented the results for the case of Sc atom-C_2N system as part of our ongoing work to study the electronic and magnetic properties of TM atoms embedded in holey-graphene systems. In this regard, we also looked at the case of C_2CF system, which was obtained from C_2N by substitution of nitrogen atom with a C-F molecule, and the effect of such substitution on the magnetic properties of the embedded TM atom. We concluded that the embeddation of Sc atom within the C_2N/C_2CF system caused the system to transition from semiconducting behavior to metallic behavior along with the promotion of local magnetic moment on the Sc atom. As our next step, we wish to extend our analysis to other TM atoms. Furthermore we would also like to investigate the manipulation of these electronic and magnetic properties by suitable external means. Studies by Zhu *et.al.*, and Gong *et.al.*, on pristine C_2N monolayer have reported that tunable ferromagnetism and half-metallicity in these systems is possible by varying the carrier doping over a wide range.[52, 53] Ferromagnetism has also been

observed in porous graphene nanomesh where the hole edges have been terminated by hydrogen, whose structure is very close to that of C_2CF.[54] The electronic properties of C_2N can also be manipulated by the strain where studies have shown that increasing the uniaxial strain can lead to a monotonical decrease in the band gap while for a biaxial strain the band gap steadily increase with increasing strain upto 12 % after which it starts to decrease.[52, 55] Furthermore, investigation by Huang *et.al.*, have showed that the magnetic states of the TM atoms adsorbed on graphene can be modified by strain.[21] This has lead to our expectation of pursuing carrier doping and strain as suitable means for achieving manipulation of the magnetic properties in TM-C_2N and TM-C_2CF systems. It is our belief, that investigation of the tunability of the electronic and magnetic properties of these systems would be a fitting conclusion of our ongoing work which is in line with the core theme of the current thesis.

7.3   Bibliography

[1]   L. Landau and E. Lifshitz, "Statistical physics. course in theoretical physics," *London, Pergamon Press*, vol. 5, p. 482, 1959.

[2]   E. Ising *Zeitschrift für Physik*, vol. 31, p. 253, 1925.

[3]   N. D. Mermin and H. Wagner *Physical Review Letters*, vol. 17, p. 1133, 1966.

[4]   P. Gambardella, A. Dallmeyer, K. Maiti, M. Malagoli, W. Eberhardt, K. Kern, and C. Carbone *Nature*, vol. 416, p. 301, 2002.

[5]   L. Yan, M. Przybylski, Y. Lu, W. Wang, J. Barthel, and J. Kirschner *Applied Physics Letters*, vol. 86, p. 102503, 2005.

[6]   C. F. Hirjibehedin, C. P. Lutz, and A. J. Heinrich *Science*, vol. 312, p. 1021, 2006.

[7]   S. Loth, S. Baumann, C. P. Lutz, D. Eigler, and A. J. Heinrich *Science*, vol. 335, p. 196, 2012.

[8]   A. A. Khajetoorians, J. Wiebe, B. Chilian, and R. Wiesendanger *Science*, vol. 332, p. 1062, 2011.

[9]   M. Menzel, Y. Mokrousov, R. Wieser, J. E. Bickel, E. Vedmedenko, S. Blügel, S. Heinze, K. von Bergmann, A. Kubetzka, and R. Wiesendanger *Physical Review Letters*, vol. 108, p. 197204, 2012.

[10] Y. Mokrousov, G. Bihlmayer, S. Blügel, and S. Heinze *Physical Review B*, vol. 75, p. 104413, 2007.

[11] J. Zhou, Q. Sun, Q. Wang, and P. Jena *Physical Review B*, vol. 90, p. 205427, 2014.

[12] X. Liu, C.-Z. Wang, M. Hupalo, W.-C. Lu, P. A. Thiel, K.-M. Ho, and M. C. Tringides *Physical Review B*, vol. 84, p. 235446, 2011.

[13] S. M. Binz, M. Hupalo, X. Liu, C.-Z. Wang, W.-C. Lu, P. A. Thiel, K.-M. Ho, E. Conrad, and M. C. Tringides *Physical Review Letters*, vol. 109, p. 026103, 2012.

[14] X. Liu, C.-Z. Wang, H.-Q. Lin, M. Hupalo, P. A. Thiel, K.-M. Ho, and M. C. Tringides *Physical Review B*, vol. 90, p. 155444, 2014.

[15] J.-H. Liao, Y.-J. Zhao, J.-J. Tang, X.-B. Yang, and H. Xu *Physical Chemistry Chemical Physics*, vol. 18, p. 14244, 2016.

[16] A. Sharma, V. N. Kotov, and A. H. C. Neto *Physical Review B*, vol. 87, p. 155431, 2013.

[17] L. Kou, C. Tang, W. Guo, and C. Chen *ACS Nano*, vol. 5, p. 1012, 2011.

[18] E. Santos, S. Riikonen, D. Sánchez-Portal, and A. Ayuela *The Journal of Physical Chemistry C*, vol. 116, p. 7602, 2012.

[19] E. J. Santos, A. Ayuela, S. Fagan, J. Mendes Filho, D. Azevedo, A. Souza Filho, and D. Sánchez-Portal *Physical Review B*, vol. 78, p. 195420, 2008.

[20] E. J. Santos, A. Ayuela, and D. Sánchez-Portal *The Journal of Physical Chemistry C*, vol. 116, p. 1174, 2011.

[21] B. Huang, J. Yu, and S.-H. Wei *Physical Review B*, vol. 84, p. 075415, 2011.

[22] Y.-K. Cheng and P. J. Rossky *Nature*, vol. 392, p. 696, 1998.

[23] L. Hua, X. Huang, P. Liu, R. Zhou, and B. J. Berne *The Journal of Physical Chemistry B*, vol. 111, p. 9069, 2007.

[24] R. Zhou, X. Huang, C. J. Margulis, and B. J. Berne *Science*, vol. 305, p. 1605, 2004.

[25] V. J. van Hijkoop, A. J. Dammers, K. Malek, and M.-O. Coppens *The Journal of chemical physics*, vol. 127, p. 08B613, 2007.

[26] F. Zhu and K. Schulten *Biophysical journal*, vol. 85, p. 236, 2003.

[27] H. K. Christenson and P. M. Claesson *Science*, vol. 239, p. 390, 1988.

[28] D. Bratko, R. Curtis, H. Blanch, and J. Prausnitz *The Journal of Chemical Physics*, vol. 115, p. 3873, 2001.

[29] J. Israelachvili and H. Wennerström *Nature*, vol. 379, p. 219, 1996.

[30] Q. Du, E. Freysz, and Y. R. Shen *Physical Review Letters*, vol. 72, p. 238, 1994.

[31] A. Schlaich, E. W. Knapp, and R. R. Netz *Physical Review Letters*, vol. 117, p. 048001, 2016.

[32] I.-C. Yeh and M. L. Berkowitz *The Journal of chemical physics*, vol. 110, p. 7935, 1999.

[33] J. Marti, G. Nagy, E. Guardia, and M. Gordillo *The Journal of Physical Chemistry B*, vol. 110, p. 23987, 2006.

[34] F. Mikami, K. Matsuda, H. Kataura, and Y. Maniwa *ACS Nano*, vol. 3, p. 1279, 2009.

[35] C.-Y. Ruan, V. A. Lobastov, F. Vigliotti, S. Chen, and A. H. Zewail *Science*, vol. 304, p. 80, 2004.

[36] D. B. Asay and S. H. Kim *The Journal of Physical Chemistry B*, vol. 109, p. 16760, 2005.

[37] N. Giovambattista, P. J. Rossky, and P. G. Debenedetti *Physical Review E*, vol. 73, p. 041604, 2006.

[38] R. Zangi *Journal of Physics: Condensed Matter*, vol. 16, p. S5371, 2004.

[39] K. Jinesh and J. Frenken *Physical Review Letters*, vol. 101, p. 036101, 2008.

[40] R. Zangi and A. E. Mark *The Journal of Chemical Physics*, vol. 119, p. 1694, 2003.

[41] R. Zangi and A. E. Mark *Physical Review Letters*, vol. 91, p. 025502, 2003.

[42] K. Koga and H. Tanaka *The Journal of chemical physics*, vol. 122, p. 104711, 2005.

[43] X. Xia and M. L. Berkowitz *Physical Review Letters*, vol. 74, p. 3193, 1995.

[44] E.-M. Choi, Y.-H. Yoon, S. Lee, and H. Kang *Physical Review Letters*, vol. 95, p. 085701, 2005.

[45] H. Qiu and W. Guo *Physical Review Letters*, vol. 110, p. 195701, 2013.

[46] R. Zangi and A. E. Mark *The Journal of chemical physics*, vol. 120, p. 7123, 2004.

[47] Z. Qian and G. Wei *The Journal of Physical Chemistry A*, vol. 118, p. 8922, 2014.

[48] G.-X. Nie, Y. Wang, and J.-P. Huang *Frontiers of Physics*, vol. 10, p. 106101, 2015.

[49] D. Ehre, E. Lavert, M. Lahav, and I. Lubomirsky *Science*, vol. 327, p. 672, 2010.

[50] X. Zhu, Q. Yuan, and Y.-P. Zhao *Nanoscale*, vol. 6, p. 5432, 2014.

[51] D. Donadio, G. Cicero, E. Schwegler, M. Sharma, and G. Galli, "Electronic effects in the ir spectrum of water under confinement," *The Journal of Physical Chemistry B*, vol. 113, no. 13, pp. 4170–4175, 2009.

[52] J. Zhu, Y. Zhao, S. Zeng, and J. Ni *Physics Letters A*, vol. 381, p. 1097, 2017.

[53] S. Gong, W. Wan, S. Guan, B. Tai, C. Liu, B. Fu, S. A. Yang, and Y. Yao *Journal of Materials Chemistry C*, vol. 5, p. 8424, 2017.

[54] K. Tada, J. Haruyama, H. Yang, M. Chshiev, T. Matsui, and H. Fukuyama *Physical Review Letters*, vol. 107, p. 217203, 2011.

[55] S. Guan, Y. Cheng, C. Liu, J. Han, Y. Lu, S. A. Yang, and Y. Yao *Applied Physics Letters*, vol. 107, p. 231904, 2015.